NCAR/TN-503+STR
NCAR Technical Note

July 2013

Technical Description of version 4.5 of the Community Land Model (CLM)

Coordinating Lead Authors
Keith W. Oleson, David M. Lawrence

Lead Authors
Gordon B. Bonan, Beth Drewniak, Maoyi Huang, Charles D. Koven, Samuel Levis, Fang Li, William J. Riley, Zachary M. Subin, Sean C. Swenson, Peter E. Thornton

Contributing Authors
Anil Bozbiyik, Rosie Fisher, Colette L. Heald, Erik Kluzek, Jean-Francois Lamarque, Peter J. Lawrence, L. Ruby Leung, William Lipscomb, Stefan Muszala, Daniel M. Ricciuto, William Sacks, Ying Sun, Jinyun Tang, Zong-Liang Yang

NCAR Earth System Laboratory
Climate and Global Dynamics Division

NATIONAL CENTER FOR ATMOSPHERIC RESEARCH
P. O. Box 3000
BOULDER, COLORADO 80307-3000
ISSN Print Edition 2153-2397
ISSN Electronic Edition 2153-2400

NCAR TECHNICAL NOTES

http://library.ucar.edu/research/publish-technote

The Technical Notes series provides an outlet for a variety of NCAR Manuscripts that contribute in specialized ways to the body of scientific knowledge but that are not yet at a point of a formal journal, monograph or book publication. Reports in this series are issued by the NCAR scientific divisions, serviced by OpenSky and operated through the NCAR Library. Designation symbols for the series include:

EDD – Engineering, Design, or Development Reports
Equipment descriptions, test results, instrumentation, and operating and maintenance manuals.

IA – Instructional Aids
Instruction manuals, bibliographies, film supplements, and other research or instructional aids.

PPR – Program Progress Reports
Field program reports, interim and working reports, survey reports, and plans for experiments.

PROC – Proceedings
Documentation or symposia, colloquia, conferences, workshops, and lectures. (Distribution maybe limited to attendees).

STR – Scientific and Technical Reports
Data compilations, theoretical and numerical investigations, and experimental results.

The National Center for Atmospheric Research (NCAR) is operated by the nonprofit University Corporation for Atmospheric Research (UCAR) under the sponsorship of the National Science Foundation. Any opinions, findings, conclusions, or recommendations expressed in this publication are those of the author(s) and do not necessarily reflect the views of the National Science Foundation.

National Center for Atmospheric Research
P. O. Box 3000
Boulder, Colorado 80307-300

NCAR/TN-503+STR
NCAR Technical Note

July 2013

Technical Description of version 4.5 of the Community Land Model (CLM)

Coordinating Lead Authors
Keith W. Oleson, David M. Lawrence

Lead Authors
Gordon B. Bonan, Beth Drewniak, Maoyi Huang, Charles D. Koven, Samuel Levis, Fang Li, William J. Riley, Zachary M. Subin, Sean C. Swenson, Peter E. Thornton

Contributing Authors
Anil Bozbiyik, Rosie Fisher, Colette L. Heald, Erik Kluzek, Jean-Francois Lamarque, Peter J. Lawrence, L. Ruby Leung, William Lipscomb, Stefan Muszala, Daniel M. Ricciuto, William Sacks, Ying Sun, Jinyun Tang, Zong-Liang Yang

NCAR Earth System Laboratory
Climate and Global Dynamics Division

NATIONAL CENTER FOR ATMOSPHERIC RESEARCH
P. O. Box 3000
BOULDER, COLORADO 80307-3000
ISSN Print Edition 2153-2397
ISSN Electronic Edition 2153-2400

TABLE OF CONTENTS

LIST OF FIGURES

LIST OF TABLES

ACKNOWLEDGEMENTS

The authors would like to acknowledge the substantial contributions of the following members of the Land Model and Biogeochemistry Working Groups to the development of the Community Land Model since its inception in 1996: Benjamin Andre, Ian Baker, Michael Barlage, Mike Bosilovich, Marcia Branstetter, Tony Craig, Aiguo Dai, Yongjiu Dai, Mark Decker, Scott Denning, Robert Dickinson, Paul Dirmeyer, Jared Entin, Jay Famiglietti, Johannes Feddema, Mark Flanner, Jon Foley, Andrew Fox, Inez Fung, David Gochis, Alex Guenther, Tim Hoar, Forrest Hoffman, Paul Houser, Trish Jackson, Brian Kauffman, Silvia Kloster, Natalie Mahowald, Jiafu Mao, Lei Meng, Sheri Michelson, Guo-Yue Niu, Adam Phillips, Taotao Qian, Jon Radakovich, James Randerson, Nan Rosenbloom, Steve Running, Koichi Sakaguchi, Adam Schlosser, Andrew Slater, Reto Stöckli, Quinn Thomas, Mariana Vertenstein, Nicholas Viovy, Aihui Wang, Guiling Wang, Charlie Zender, Xiaodong Zeng, and Xubin Zeng.

The authors also thank the following people for their review of this document: Jonathan Buzan, Kyla Dahlin, Sanjiv Kumar, Hanna Lee, Danica Lombardozzi, Quinn Thomas, and Will Wieder.

Current affiliations for the authors are as follows:

K.W. Oleson, D.M. Lawrence, G.B. Bonan, S. Levis, S.C. Swenson, R. Fisher, E. Kluzek, J.-F. Lamarque, P.J. Lawrence, S. Muszala, and W. Sacks (National Center for Atmospheric Research); B. Drewniak (Argonne National Laboratory); M. Huang, L.R. Leung (Pacific Northwest National Laboratory); C.D. Koven, W.J. Riley, and J. Tang (Lawrence Berkeley National Laboratory); F. Li (Chinese Academy of Sciences); Z.M. Subin (Princeton University); P.E. Thornton and D.M. Ricciuto (Oak Ridge National

Laboratory); A. Bozbiyik (Bern University); C. Heald (Massachusetts Institute of Technology), W. Lipscomb (Los Alamos National Laboratory); Ying Sun and Z.-L. Yang (University of Texas at Austin)

1. Introduction

The purpose of this technical note is to describe the biogeophysical and biogeochemical parameterizations and numerical implementation of version 4.5 of the Community Land Model (CLM4.5). Scientific justification and evaluation of these parameterizations can be found in the referenced scientific papers (Chapter 27). This technical note and the CLM4.5 User's Guide together provide the user with the scientific description and operating instructions for CLM.

1.1 Model History

1.1.1 Inception of CLM

The early development of the Community Land Model can be described as the merging of a community-developed land model focusing on biogeophysics and a concurrent effort at NCAR to expand the NCAR Land Surface Model (NCAR LSM, Bonan 1996) to include the carbon cycle, vegetation dynamics, and river routing. The concept of a community-developed land component of the Community Climate System Model (CCSM) was initially proposed at the CCSM Land Model Working Group (LMWG) meeting in February 1996. Initial software specifications and development focused on evaluating the best features of three existing land models: the NCAR LSM (Bonan 1996, 1998) used in the Community Climate Model (CCM3) and the initial version of CCSM; the Institute of Atmospheric Physics, Chinese Academy of Sciences land model (IAP94) (Dai and Zeng 1997); and the Biosphere-Atmosphere Transfer Scheme (BATS) (Dickinson et al. 1993) used with CCM2. A scientific steering committee was formed to review the initial specifications of the design provided by

Robert Dickinson, Gordon Bonan, Xubin Zeng, and Yongjiu Dai and to facilitate further development. Steering committee members were selected so as to provide guidance and expertise in disciplines not generally well-represented in land surface models (e.g., carbon cycling, ecological modeling, hydrology, and river routing) and included scientists from NCAR, the university community, and government laboratories (R. Dickinson, G. Bonan, X. Zeng, Paul Dirmeyer, Jay Famiglietti, Jon Foley, and Paul Houser).

The specifications for the new model, designated the Common Land Model, were discussed and agreed upon at the June 1998 CCSM Workshop LMWG meeting. An initial code was developed by Y. Dai and was examined in March 1999 by Mike Bosilovich, P. Dirmeyer, and P. Houser. At this point an extensive period of code testing was initiated. Keith Oleson, Y. Dai, Adam Schlosser, and P. Houser presented preliminary results of offline 1-dimensional testing at the June 1999 CCSM Workshop LMWG meeting. Results from more extensive offline testing at plot, catchment, and large scale (up to global) were presented by Y. Dai, A. Schlosser, K. Oleson, M. Bosilovich, Zong-Liang Yang, Ian Baker, P. Houser, and P. Dirmeyer at the LMWG meeting hosted by COLA (Center for Ocean-Land-Atmosphere Studies) in November 1999. Field data used for validation included sites adopted by the Project for Intercomparison of Land-surface Parameterization Schemes (Henderson-Sellers et al. 1993) (Cabauw, Valdai, Red-Arkansas river basin) and others [FIFE (Sellers et al. 1988), BOREAS (Sellers et al. 1995), HAPEX-MOBILHY (André et al. 1986), ABRACOS (Gash et al. 1996), Sonoran Desert (Unland et al. 1996), GSWP (Dirmeyer et al. 1999)].

Y. Dai also presented results from a preliminary coupling of the Common Land Model to CCM3, indicating that the land model could be successfully coupled to a climate model.

Results of coupled simulations using CCM3 and the Common Land Model were presented by X. Zeng at the June 2000 CCSM Workshop LMWG meeting. Comparisons with the NCAR LSM and observations indicated major improvements to the seasonality of runoff, substantial reduction of a summer cold bias, and snow depth. Some deficiencies related to runoff and albedo were noted, however, that were subsequently addressed. Z.-L. Yang and I. Baker demonstrated improvements in the simulation of snow and soil temperatures. Sam Levis reported on efforts to incorporate a river routing model to deliver runoff to the ocean model in CCSM. Soon after the workshop, the code was delivered to NCAR for implementation into the CCSM framework. Documentation for the Common Land Model is provided by Dai et al. (2001) while the coupling with CCM3 is described in Zeng et al. (2002). The model was introduced to the modeling community in Dai et al. (2003).

1.1.2 CLM2

Concurrent with the development of the Common Land Model, the NCAR LSM was undergoing further development at NCAR in the areas of carbon cycling, vegetation dynamics, and river routing. The preservation of these advancements necessitated several modifications to the Common Land Model. The biome-type land cover classification scheme was replaced with a plant functional type (PFT) representation with the specification of PFTs and leaf area index from satellite data (Oleson and Bonan 2000; Bonan et al. 2002a, b). This also required modifications to parameterizations for vegetation albedo and vertical burying of vegetation by snow. Changes were made to

canopy scaling, leaf physiology, and soil water limitations on photosynthesis to resolve deficiencies indicated by the coupling to a dynamic vegetation model. Vertical heterogeneity in soil texture was implemented to improve coupling with a dust emission model. A river routing model was incorporated to improve the fresh water balance over oceans. Numerous modest changes were made to the parameterizations to conform to the strict energy and water balance requirements of CCSM. Further substantial software development was also required to meet coding standards. The resulting model was adopted in May 2002 as the Community Land Model (CLM2) for use with the Community Atmosphere Model (CAM2, the successor to CCM3) and version 2 of the Community Climate System Model (CCSM2).

K. Oleson reported on initial results from a coupling of CCM3 with CLM2 at the June 2001 CCSM Workshop LMWG meeting. Generally, the CLM2 preserved most of the improvements seen in the Common Land Model, particularly with respect to surface air temperature, runoff, and snow. These simulations are documented in Bonan et al. (2002a). Further small improvements to the biogeophysical parameterizations, ongoing software development, and extensive analysis and validation within CAM2 and CCSM2 culminated in the release of CLM2 to the community in May 2002.

Following this release, Peter Thornton implemented changes to the model structure required to represent carbon and nitrogen cycling in the model. This involved changing data structures from a single vector of spatially independent sub-grid patches to one that recognizes three hierarchical scales within a model grid cell: land unit, snow/soil column, and PFT. Furthermore, as an option, the model can be configured so that PFTs can share a single soil column and thus "compete" for water. This version of the model (CLM2.1)

was released to the community in February 2003. CLM2.1, without the compete option turned on, produced only round off level changes when compared to CLM2.

1.1.3 CLM3

CLM3 implemented further software improvements related to performance and model output, a re-writing of the code to support vector-based computational platforms, and improvements in biogeophysical parameterizations to correct deficiencies in the coupled model climate. Of these parameterization improvements, two were shown to have a noticeable impact on simulated climate. A variable aerodynamic resistance for heat/moisture transfer from ground to canopy air that depends on canopy density was implemented. This reduced unrealistically high surface temperatures in semi-arid regions. The second improvement added stability corrections to the diagnostic 2-m air temperature calculation which reduced biases in this temperature. Competition between PFTs for water, in which PFTs share a single soil column, is the default mode of operation in this model version. CLM3 was released to the community in June 2004. Dickinson et al. (2006) describe the climate statistics of CLM3 when coupled to CCSM3.0. Hack et al. (2006) provide an analysis of selected features of the land hydrological cycle. Lawrence et al. (2007) examine the impact of changes in CLM3 hydrological parameterizations on partitioning of evapotranspiration (ET) and its effect on the timescales of ET response to precipitation events, interseasonal soil moisture storage, soil moisture memory, and land-atmosphere coupling. Qian et al. (2006) evaluate CLM3's performance in simulating soil moisture content, runoff, and river discharge when forced by observed precipitation, temperature and other atmospheric data.

1.1.4 CLM3.5

Although the simulation of land surface climate by CLM3 was in many ways adequate, most of the unsatisfactory aspects of the simulated climate noted by the above studies could be traced directly to deficiencies in simulation of the hydrological cycle. In 2004, a project was initiated to improve the hydrology in CLM3 as part of the development of CLM version 3.5. A selected set of promising approaches to alleviating the hydrologic biases in CLM3 were tested and implemented. These included new surface datasets based on Moderate Resolution Imaging Spectroradiometer (MODIS) products, new parameterizations for canopy integration, canopy interception, frozen soil, soil water availability, and soil evaporation, a TOPMODEL-based model for surface and subsurface runoff, a groundwater model for determining water table depth, and the introduction of a factor to simulate nitrogen limitation on plant productivity. Oleson et al. (2008a) show that CLM3.5 exhibits significant improvements over CLM3 in its partitioning of global ET which result in wetter soils, less plant water stress, increased transpiration and photosynthesis, and an improved annual cycle of total water storage. Phase and amplitude of the runoff annual cycle is generally improved. Dramatic improvements in vegetation biogeography result when CLM3.5 is coupled to a dynamic global vegetation model. Stöckli et al. (2008) examine the performance of CLM3.5 at local scales by making use of a network of long-term ground-based ecosystem observations [FLUXNET (Baldocchi et al. 2001)]. Data from 15 FLUXNET sites were used to demonstrate significantly improved soil hydrology and energy partitioning in CLM3.5. CLM3.5 was released to the community in May, 2007.

1.1.5 CLM4

The motivation for the next version of the model, CLM4, was to (1) incorporate several recent scientific advances in the understanding and representation of land surface processes, (2) expand model capabilities, and (3) improve surface and atmospheric forcing datasets (Lawrence et al. 2011). Included in the first category are more sophisticated representations of soil hydrology and snow processes. In particular, new treatments of soil column-groundwater interactions, soil evaporation, aerodynamic parameters for sparse/dense canopies, vertical burial of vegetation by snow, snow cover fraction and aging, black carbon and dust deposition, and vertical distribution of solar energy for snow were implemented. Major new capabilities in the model include a representation of the carbon-nitrogen cycle (CLM4CN, see next paragraph for additional information), the ability to model land cover change in a transient mode, inclusion of organic soil and deep soil into the existing mineral soil treatment to enable more realistic modeling of permafrost, an urban canyon model to contrast rural and urban energy balance and climate (CLMU), and an updated biogenic volatile organic compounds (BVOC) model. Other modifications of note include refinement of the global PFT, wetland, and lake distributions, more realistic optical properties for grasslands and croplands, and an improved diurnal cycle and spectral distribution of incoming solar radiation to force the model in offline mode.

Many of the ideas incorporated into the carbon and nitrogen cycle component of CLM4 derive from the earlier development of the offline ecosystem process model Biome-BGC (Biome BioGeochemical Cycles), originating at the Numerical Terradynamic Simulation Group (NTSG) at the University of Montana, under the guidance of Prof. Steven Running. Biome-BGC itself is an extension of an earlier model,

Forest-BGC (Running and Coughlan, 1988; Running and Gower, 1991), which simulates water, carbon, and, to a limited extent, nitrogen fluxes for forest ecosystems. Forest-BGC was designed to be driven by remote sensing inputs of vegetation structure, and so used a diagnostic (prescribed) leaf area index, or, in the case of the dynamic allocation version of the model (Running and Gower, 1991), prescribed maximum leaf area index.

Biome-BGC expanded on the Forest-BGC logic by introducing a more mechanistic calculation of leaf and canopy scale photosynthesis (Hunt and Running, 1992), and extending the physiological parameterizations to include multiple woody and non-woody vegetation types (Hunt et al. 1996; Running and Hunt, 1993). Later versions of Biome-BGC introduced more mechanistic descriptions of belowground carbon and nitrogen cycles, nitrogen controls on photosynthesis and decomposition, sunlit and shaded canopies, vertical gradient in leaf morphology, and explicit treatment of fire and harvest disturbance and regrowth dynamics (Kimball et al. 1997; Thornton, 1998; Thornton et al. 2002; White et al. 2000). Biome-BGC version 4.1.2 (Thornton et al. 2002) provided a point of departure for integrating new biogeochemistry components into CLM4.

CLM4 was released to the community in June, 2010 along with the Community Climate System Model version 4 (CCSM4). CLM4 is used in CCSM4, CESM1, CESM1.1, and remains available as the default land component model option for coupled simulations in CESM1.2.

1.1.6 CLM4.5

The motivations for the development of CLM4.5 (the model version described in this Technical Description) were similar to those for CLM4: (1) incorporate several recent scientific advances in the understanding and representation of land surface

processes, (2) expand model capabilities, and (3) improve surface and atmospheric forcing datasets.

Specifically, several parameterizations were revised to reflect new scientific understanding and in an attempt to reduce biases identified in CLM4 simulations including low soil carbon stocks especially in the Arctic, excessive tropical GPP and unrealistically low Arctic GPP, a dry soil bias in Arctic soils, unrealistically high LAI in the tropics, a transient 20^{th} century carbon response that was inconsistent with observational estimates, and several other more minor problems or biases.

The main modifications include updates to canopy processes including a revised canopy radiation scheme and canopy scaling of leaf processes, co-limitations on photosynthesis, revisions to photosynthetic parameters (Bonan et al. 2011), temperature acclimation of photosynthesis, and improved stability of the iterative solution in the photosynthesis and stomatal conductance model (Sun et al. 2012). Hydrology updates include modifications such that hydraulic properties of frozen soils are determined by liquid water content only rather than total water content and the introduction of an ice impedance function, and other corrections that increase the consistency between soil water state and water table position and allow for a perched water table above icy permafrost ground (Swenson et al. 2012). A new snow cover fraction parameterization is incorporated that reflects the hysteresis in fractional snow cover for a given snow depth between accumulation and melt phases (Swenson and Lawrence, 2012). The lake model in CLM4 is replaced with a completely revised and more realistic lake model (Subin et al. 2012a). A surface water store is introduced, replacing the wetland land unit and permitting prognostic wetland distribution modeling, and the surface energy fluxes are

calculated separately (Swenson and Lawrence, 2012) for snow-covered, water-covered, and snow/water-free portions of vegetated and crop land units, and snow-covered and snow-free portions of glacier land units. Globally constant river flow velocity is replaced with variable flow velocity based on mean grid cell slope. A vertically resolved soil biogeochemistry scheme is introduced with base decomposition rates modified by soil temperature, water, and oxygen limitations and also including vertical mixing of soil carbon and nitrogen due to bioturbation, cryoturbation, and diffusion (Koven et al. 2013). The litter and soil carbon and nitrogen pool structure as well as nitrification and denitrification are modified based on the Century model and biological fixation is revised to distribute fixation more realistically over the year (Koven et al. 2013). The fire model is replaced with a model that includes representations of natural and anthropogenic triggers and suppression as well as agricultural, deforestation, and peat fires (Li et al. 2012a,b; Li et al. 2013a). The biogenic volatile organic compounds model is updated to MEGAN2.1 (Guenther et al. 2012).

Additions to the model include a methane production, oxidation, and emissions model (Riley et al. 2011a) and an extension of the crop model to include interactive fertilization, organ pools (Drewniak et al. 2013), and irrigation (Sacks et al. 2009). Elements of the Variable Infiltration Capacity (VIC) model are included as an alternative optional runoff generation scheme (Li et al. 2011). There is also an option to run with a multilayer canopy (Bonan et al. 2012). Multiple urban density classes, rather than the single dominant urban density class used in CLM4, are modeled in the urban land unit. Carbon (^{13}C and ^{14}C) isotopes are enabled (Koven et al. 2013). Minor changes include a switch of the C3 Arctic grass and shrub phenology from stress deciduous to seasonal

deciduous and a change in the glacier bare ice albedo to better reflect recent estimates. Finally, the carbon and nitrogen cycle spinup is accelerated and streamlined with a revised spinup method, though the spinup timescale remains long.

Finally, the predominantly low resolution input data for provided with CLM4 to create CLM4 surface datasets is replaced with newer and higher resolution input datasets where possible (see section 2.2.3 for details). The default meteorological forcing dataset provided with CLM4 (Qian et al. 2006) is replaced with the 1901-2010 CRUNCEP forcing dataset (see Chapter 26) for CLM4.5, though users can also still use the Qian et al. (2006) dataset or other alternative forcing datasets.

CLM4.5 was released to the community in June 2013 along with the Community Earth System Model version 1.2 (CESM1.2).

1.2 Biogeophysical and Biogeochemical Processes

Biogeophysical and biogeochemical processes are simulated for each subgrid land unit, column, and plant functional type (PFT) independently and each subgrid unit maintains its own prognostic variables (see section 2.1.1 for definitions of subgrid units). The same atmospheric forcing is used to force all subgrid units within a grid cell. The surface variables and fluxes required by the atmosphere are obtained by averaging the subgrid quantities weighted by their fractional areas. The processes simulated include (Figure 1.1):

- Surface characterization including land type heterogeneity and ecosystem structure (Chapter 2)
- Absorption, reflection, and transmittance of solar radiation (Chapter 3, 4)
- Absorption and emission of longwave radiation (Chapter 4)

- Momentum, sensible heat (ground and canopy), and latent heat (ground evaporation, canopy evaporation, transpiration) fluxes (Chapter 5)
- Heat transfer in soil and snow including phase change (Chapter 6)
- Canopy hydrology (interception, throughfall, and drip) (Chapter 7)
- Snow hydrology (snow accumulation and melt, compaction, water transfer between snow layers) (Chapter 7)
- Soil hydrology (surface runoff, infiltration, redistribution of water within the column, sub-surface drainage, groundwater) (Chapter 7)
- Stomatal physiology and photosynthesis (Chapter 8)
- Lake temperatures and fluxes (Chapter 9)
- Glacier processes (Chapter 10)
- Routing of runoff from rivers to ocean (Chapter 11)
- Urban energy balance and climate (Chapter 12)
- Vegetation carbon and nitrogen allocation and respiration (Chapter 13)
- Vegetation phenology (Chapter 14)
- Soil and litter carbon decomposition (Chapter 15)
- Nitrogen cycling including deposition, biological fixation, denitrification, leaching, and losses due to fire (Chapter 16)
- Plant mortality (Chapter 17)
- Fire ignition and suppression, including natural, deforestation, and agricultural fire (Chapter 18)
- Methane production, oxidation, and emissions (Chapter 19)
- Crop dynamics and irrigation (Chapter 20)

- Land cover and land use change including wood harvest (Chapter 21)
- Dynamic global vegetation distribution (Chapter 22)
- Biogenic volatile organic compound emissions (Chapter 23)
- Dust mobilization and deposition (Chapter 24)
- Carbon isotope fractionation (Chapter 25)

Figure 1.1. Land biogeophysical, biogeochemical, and landscape processes simulated by CLM (adapted from Lawrence et al. (2011) for CLM4.5).

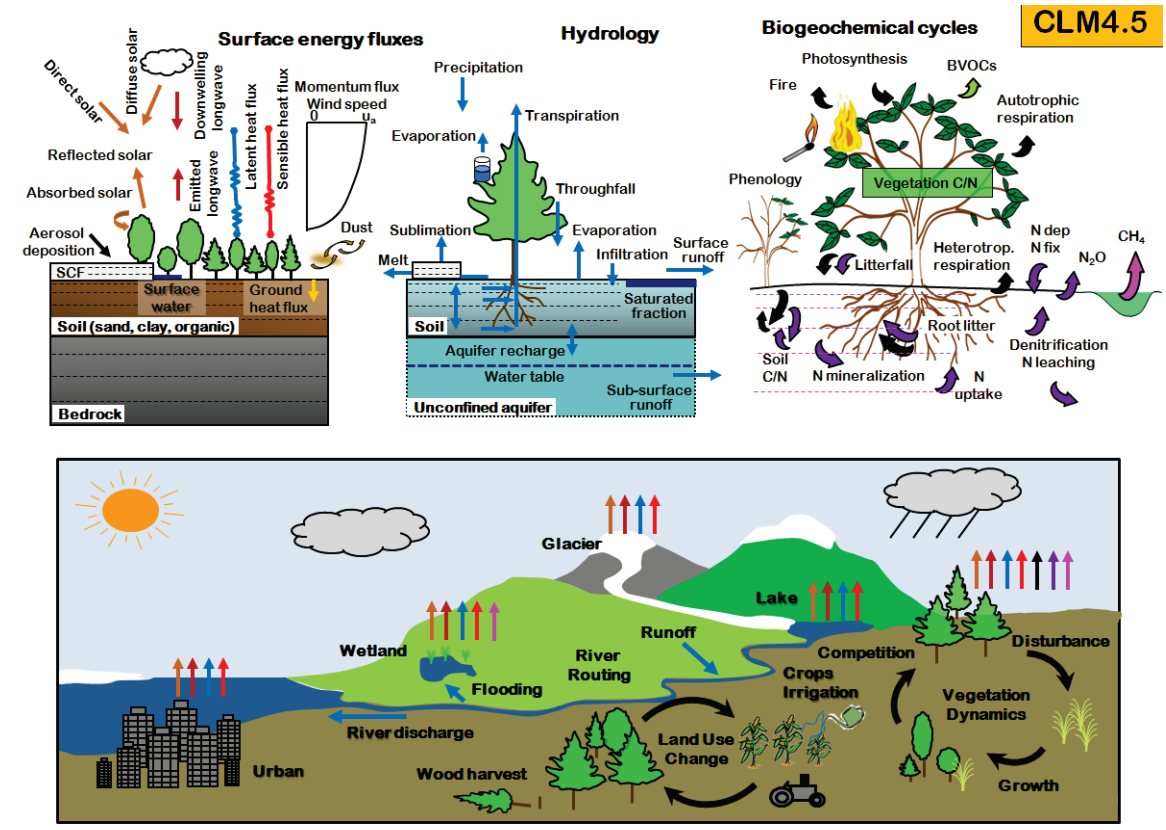

2. Surface Characterization and Model Input Requirements

2.1 Surface Characterization

2.1.1 Surface Heterogeneity and Data Structure

Spatial land surface heterogeneity in CLM is represented as a nested subgrid hierarchy in which grid cells are composed of multiple land units, snow/soil columns, and PFTs (Figure 2.1). Each grid cell can have a different number of land units, each land unit can have a different number of columns, and each column can have multiple PFTs. The first subgrid level, the land unit, is intended to capture the broadest spatial patterns of subgrid heterogeneity. The current land units are glacier, lake, urban, vegetated, and crop (when the crop model option is turned on). The land unit level can be used to further delineate these patterns. For example, the urban land unit is divided into density classes representing the tall building district, high density, and medium density urban areas.

The second subgrid level, the column, is intended to capture potential variability in the soil and snow state variables within a single land unit. For example, the vegetated land unit could contain several columns with independently evolving vertical profiles of soil water and temperature. Similarly, the managed vegetation land unit could be divided into two columns, irrigated and non-irrigated. The snow/soil column is represented by fifteen layers for soil and up to five layers for snow, depending on snow depth. The central characteristic of the column subgrid level is that this is where the state variables for water and energy in the soil and snow are defined, as well as the fluxes of these components within the soil and snow. Regardless of the number and type of PFTs occupying space on the column, the column physics operates with a single set of upper

boundary fluxes, as well as a single set of transpiration fluxes from multiple soil levels. These boundary fluxes are weighted averages over all PFTs. Currently, for glacier, lake, and vegetated land units, a single column is assigned to each land unit. The crop land unit is split into irrigated and unirrigated columns with a single crop occupying each column. The urban land units have five columns (roof, sunlit walls and shaded walls, and pervious and impervious canyon floor) (Oleson et al. 2010b).

Figure 2.1. Configuration of the CLM subgrid hierarchy.

Note that the Crop land unit is only used when the model is run with the crop model active. Abbreviations: TBD – Tall Building District; HD – High Density; MD – Medium Density, G – Glacier, L – Lake, U – Urban, C – Crop, V – Vegetated, PFT – Plant Functional Type, I – Irrigated, U – Unirrigated .

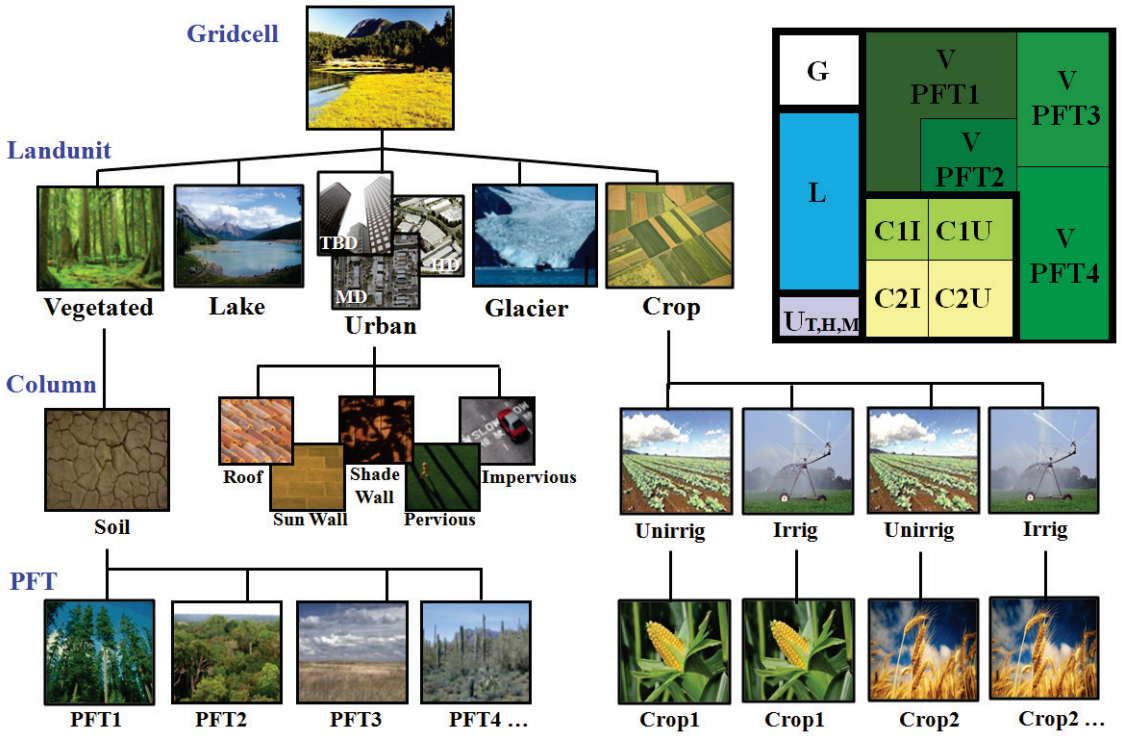

The third subgrid level is referred to as the PFT level, but it also includes the treatment for bare ground. It is intended to capture the biogeophysical and biogeochemical differences between broad categories of plants in terms of their functional characteristics. On the vegetated land unit, up to 16 possible PFTs that differ in physiology and structure may coexist on a single column. All fluxes to and from the surface are defined at the PFT level, as are the vegetation state variables (e.g. vegetation temperature and canopy water storage). On the crop land unit, several different crop types can be represented on each crop land unit column (see Chapter 20 for details).

In addition to state and flux variable data structures for conserved components at each subgrid level (e.g., energy, water, carbon), each subgrid level also has a physical state data structure for handling quantities that are not involved in conservation checks (diagnostic variables). For example, the urban canopy air temperature and humidity are defined through physical state variables at the land unit level, the number of snow layers and the soil roughness lengths are defined as physical state variables at the column level, and the leaf area index and the fraction of canopy that is wet are defined as physical state variables at the PFT level.

The standard configuration of the model subgrid hierarchy is illustrated in Figure 2.1. Here, only four PFTs are shown associated with the single column beneath the vegetated land unit but up to sixteen are possible. The crop land unit is present only when the crop model is active.

Note that the biogeophysical processes related to soil and snow require PFT level properties to be aggregated to the column level. For example, the net heat flux into the

ground is required as a boundary condition for the solution of snow/soil temperatures (Chapter 6). This column level property must be determined by aggregating the net heat flux from all PFTs sharing the column. This is generally accomplished in the model by computing a weighted sum of the desired quantity over all PFTs whose weighting depends on the PFT area relative to all PFTs, unless otherwise noted in the text.

2.1.2 Vegetation Composition

Vegetated surfaces are comprised of up to 15 possible plant functional types (PFTs) plus bare ground (Table 2.1). An additional PFT is added if the irrigation model is active and six additional PFTs are added if the crop model is active (Chapter 20). These plant types differ in leaf and stem optical properties that determine reflection, transmittance, and absorption of solar radiation (Table 3.1), root distribution parameters that control the uptake of water from the soil (Table 8.3), aerodynamic parameters that determine resistance to heat, moisture, and momentum transfer (Table 5.1), and photosynthetic parameters that determine stomatal resistance, photosynthesis, and transpiration (Tables 8.1, 8.2). The composition and abundance of PFTs within a grid cell can either be prescribed as time-invariant fields (e.g., using the present day dataset described in section 21.3.3) or can evolve with time if the model is run in transient landcover mode (Chapter 21).

Table 2.1. Plant functional types

Plant functional type	Acronym
Needleleaf evergreen tree – temperate	NET Temperate
Needleleaf evergreen tree - boreal	NET Boreal
Needleleaf deciduous tree – boreal	NDT Boreal
Broadleaf evergreen tree – tropical	BET Tropical
Broadleaf evergreen tree – temperate	BET Temperate
Broadleaf deciduous tree – tropical	BDT Tropical
Broadleaf deciduous tree – temperate	BDT Temperate
Broadleaf deciduous tree – boreal	BDT Boreal
Broadleaf evergreen shrub - temperate	BES Temperate
Broadleaf deciduous shrub – temperate	BDS Temperate
Broadleaf deciduous shrub – boreal	BDS Boreal
C_3 arctic grass	-
C_3 grass	-
C_4 grass	-
C_3 Unmanaged Rainfed Crop	Crop R
[1]C_3 Unmanaged Irrigated Crop	Crop I
[2]Rainfed Corn	Corn R
[2]Irrigated Corn	Corn I
[2]Rainfed Temperate Cereals	Temp Cereal R
[2]Irrigated Temperate Cereals	Temp Cereal I
[3]Rainfed Winter Cereals	Winter Cereal R
[3]Irrigated Winter Cereals	Winter Cereal I
[2]Rainfed Soybean	Soybean R
[2]Irrigated Soybean	Soybean I

[1]Only used if irrigation is active (Chapter 20). [2]Only used if crop model is active (Chapter 20). [3]Reserved for future implementations of crop model (Chapter 20).

2.1.3 Vegetation Structure

Vegetation structure is defined by leaf and stem area indices (L, S) and canopy top and bottom heights (z_{top}, z_{bot}) (Table 2.2). Separate leaf and stem area indices and canopy heights are prescribed or calculated for each PFT. Daily leaf and stem area indices are obtained from gridded datasets of monthly values (section 2.2.3). Canopy top and bottom heights are also obtained from gridded datasets. However, these are currently invariant in space and time and were obtained from PFT-specific values (Bonan et al. 2002a). When the biogeochemistry model is active, vegetation state (LAI, SAI, canopy top and bottom heights) are calculated prognostically (see Chapter 14).

Table 2.2. Prescribed plant functional type heights

Plant functional type	z_{top} (m)	z_{bot} (m)
NET Temperate	17	8.5
NET Boreal	17	8.5
NDT Boreal	14	7
BET Tropical	35	1
BET temperate	35	1
BDT tropical	18	10
BDT temperate	20	11.5
BDT boreal	20	11.5
BES temperate	0.5	0.1
BDS temperate	0.5	0.1
BDS boreal	0.5	0.1
C_3 arctic grass	0.5	0.01
C_3 grass	0.5	0.01
C_4 grass	0.5	0.01
Crop R	0.5	0.01
Crop I	0.5	0.01
[1]Corn R	-	-
[1]Corn I	-	-
[1]Temp Cereal R	-	-
[1]Temp Cereal I	-	-
[1]Winter Cereal R	-	-
[1]Winter Cereal I	-	-
[1]Soybean R	-	-
[1]Soybean I	-	-

[1]Determined by the crop model (Chapter 20)

2.1.4 Phenology and vegetation burial by snow

When the biogeochemistry model is inactive, leaf and stem area indices (m^2 leaf area m^{-2} ground area) are updated daily by linearly interpolating between monthly values. Monthly PFT leaf area index values are developed from the 1-km MODIS-derived monthly grid cell average leaf area index of Myneni et al. (2002), as described in Lawrence and Chase (2007). Stem area index is calculated from the monthly PFT leaf area index using the methods of Zeng et al. (2002). The leaf and stem area indices are adjusted for vertical burying by snow (Wang and Zeng 2009) as

$$A = A^* \left(1 - f_{veg}^{sno}\right) \tag{2.1}$$

where A^* is the leaf or stem area before adjustment for snow, A is the remaining exposed leaf or stem area, f_{veg}^{sno} is the vertical fraction of vegetation covered by snow

$$\begin{aligned} f_{veg}^{sno} &= \frac{z_{sno} - z_{bot}}{z_{top} - z_{bot}} && \text{for tree and shrub} \\ f_{veg}^{sno} &= \frac{\min\left(z_{sno}, z_c\right)}{z_c} && \text{for grass and crop} \end{aligned}, \tag{2.2}$$

where $z_{sno} - z_{bot} \geq 0,\ 0 \leq f_{veg}^{sno} \leq 1$, z_{sno} is the depth of snow (m) (section 7.2), and $z_c = 0.2$ is the snow depth when short vegetation is assumed to be completely buried by snow (m). For numerical reasons, exposed leaf and stem area are set to zero if less than 0.05. If the sum of exposed leaf and stem area is zero, then the surface is treated as snow-covered ground.

2.2 Model Input Requirements

2.2.1 Atmospheric Coupling

The current state of the atmosphere (Table 2.3) at a given time step is used to force the land model. This atmospheric state is provided by an atmospheric model in coupled

mode or from an observed dataset in offline mode (Chapter 26). The land model then initiates a full set of calculations for surface energy, constituent, momentum, and radiative fluxes. The land model calculations are implemented in two steps. The land model proceeds with the calculation of surface energy, constituent, momentum, and radiative fluxes using the snow and soil hydrologic states from the previous time step. The land model then updates the soil and snow hydrology calculations based on these fluxes. These fields are passed to the atmosphere (Table 2.4). The albedos sent to the atmosphere are for the solar zenith angle at the next time step but with surface conditions from the current time step.

Table 2.3. Atmospheric input to land model

[1]Reference height	z'_{atm}	m
Zonal wind at z_{atm}	u_{atm}	m s^{-1}
Meridional wind at z_{atm}	v_{atm}	m s^{-1}
Potential temperature	$\overline{\theta_{atm}}$	K
Specific humidity at z_{atm}	q_{atm}	kg kg^{-1}
Pressure at z_{atm}	P_{atm}	Pa
Temperature at z_{atm}	T_{atm}	K
Incident longwave radiation	$L_{atm}\downarrow$	W m^{-2}
[2]Liquid precipitation	q_{rain}	mm s^{-1}
[2]Solid precipitation	q_{sno}	mm s^{-1}
Incident direct beam visible solar radiation	$S_{atm}\downarrow^{\mu}_{vis}$	W m^{-2}
Incident direct beam near-infrared solar radiation	$S_{atm}\downarrow^{\mu}_{nir}$	W m^{-2}
Incident diffuse visible solar radiation	$S_{atm}\downarrow_{vis}$	W m^{-2}
Incident diffuse near-infrared solar radiation	$S_{atm}\downarrow_{nir}$	W m^{-2}
Carbon dioxide (CO_2) concentration	c_a	ppmv
[3]Aerosol deposition rate	D_{sp}	kg m^{-2} s^{-1}
[4]Nitrogen deposition rate	NF_{ndep_sminn}	g (N) m^{-2} yr^{-1}
[5]Lightning frequency	I_l	flash km^{-2} hr^{-1}

[1]The atmospheric reference height received from the atmospheric model z'_{atm} is assumed to be the height above the surface as defined by the roughness length z_0 plus displacement height d. Thus, the reference height used for flux computations (Chapter 5) is $z_{atm} = z'_{atm} + z_0 + d$. The reference heights for temperature, wind, and specific humidity ($z_{atm,h}$, $z_{atm,m}$, $z_{atm,w}$) are required. These are set equal to z_{atm}.

[2]The CAM provides convective and large-scale liquid and solid precipitation, which are added to yield total liquid precipitation q_{rain} and solid precipitation q_{sno}.

[3]There are 14 aerosol deposition rates required depending on species and affinity for bonding with water; 8 of these are dust deposition rates (dry and wet rates for 4 dust size bins, $D_{dst,dry1}, D_{dst,dry2}, D_{dst,dry3}, D_{dst,dry4}$, $D_{dst,wet1}, D_{dst,wet2}, D_{dst,wet3}, D_{dst,wet4}$), 3 are black carbon deposition rates (dry and wet hydrophilic and dry hydrophobic rates, $D_{bc,dryhphil}, D_{bc,wethphil}, D_{bc,dryhphob}$), and 3 are organic carbon deposition rates (dry and wet hydrophilic and dry hydrophobic rates, $D_{oc,dryhphil}, D_{oc,wethphil}, D_{oc,dryhphob}$). These fluxes are computed interactively by the atmospheric model (when prognostic aerosol representation is active) or are prescribed from a time-varying (annual cycle or transient), globally-gridded deposition file defined in the namelist (see the CLM4.5 User's Guide). Aerosol deposition rates were calculated in a transient 1850-2009 CAM simulation (at a resolution of 1.9x2.5x26L) with interactive chemistry (troposphere and stratosphere) driven by CCSM3 20th century sea-surface temperatures and emissions (Lamarque et al. 2010) for short-lived gases and aerosols; observed concentrations were specified for methane, N_2O, the ozone-depleting substances (CFCs) ,and CO_2. The fluxes are used by the snow-related parameterizations (Chapters 3 and 7).

[4]The nitrogen deposition rate is required by the biogeochemistry model when active and represents the total deposition of mineral nitrogen onto the land surface, combining deposition of NO_y and NH_x. The rate is supplied either as a time-invariant spatially-varying annual mean rate or time-varying for a transient simulation. Nitrogen deposition rates were calculated from the same CAM chemistry simulation that generated the aerosol deposition rates.

[5]Climatological 3-hourly lightning frequency at ~1.8^o resolution is provided, which was calculated via bilinear interpolation from 1995-2011 NASA LIS/OTD grid product v2.2

(http://ghrc.msfc.nasa.gov) 2-hourly, 2.5° lightning frequency data. In future versions of the model, lightning data may be obtained directly from the atmosphere model.

Density of air (ρ_{atm}) (kg m^{-3}) is also required but is calculated directly from $\rho_{atm} = \frac{P_{atm} - 0.378 e_{atm}}{R_{da} T_{atm}}$ where P_{atm} is atmospheric pressure (Pa), e_{atm} is atmospheric vapor pressure (Pa), R_{da} is the gas constant for dry air (J kg^{-1} K^{-1}) (Table 2.6), and T_{atm} is the atmospheric temperature (K). The atmospheric vapor pressure e_{atm} is derived from atmospheric specific humidity q_{atm} (kg kg^{-1}) as $e_{atm} = \frac{q_{atm} P_{atm}}{0.622 + 0.378 q_{atm}}$.

The O_2 partial pressure (Pa) is required but is calculated from molar ratio and the atmospheric pressure P_{atm} as $o_i = 0.209 P_{atm}$.

Table 2.4. Land model output to atmospheric model

[1]Latent heat flux	$\lambda_{vap} E_v + \lambda E_g$	W m^{-2}
Sensible heat flux	$H_v + H_g$	W m^{-2}
Water vapor flux	$E_v + E_g$	mm s^{-1}
Zonal momentum flux	τ_x	kg m^{-1} s^{-2}
Meridional momentum flux	τ_y	kg m^{-1} s^{-2}
Emitted longwave radiation	$L\uparrow$	W m^{-2}
Direct beam visible albedo	$I\uparrow^{\mu}_{vis}$	-
Direct beam near-infrared albedo	$I\uparrow^{\mu}_{nir}$	-
Diffuse visible albedo	$I\uparrow_{vis}$	-
Diffuse near-infrared albedo	$I\uparrow_{nir}$	-
Absorbed solar radiation	$\vec{S}$	W m^{-2}
Radiative temperature	T_{rad}	K
Temperature at 2 meter height	T_{2m}	K
Specific humidity at 2 meter height	q_{2m}	kg kg^{-1}
Snow water equivalent	W_{sno}	m
Aerodynamic resistance	r_{am}	s m^{-1}
Friction velocity	u_*	m s^{-1}
[2]Dust flux	F_j	kg m^{-2} s^{-1}
Net ecosystem exchange	NEE	kgCO_2 m^{-2} s^{-1}

[1] λ_{vap} is the latent heat of vaporization (J kg^{-1}) (Table 2.6) and λ is either the latent heat of vaporization λ_{vap} or latent heat of sublimation λ_{sub} (J kg^{-1}) (Table 2.6) depending on the liquid water and ice content of the top snow/soil layer (section 5.4).

[2]There are $j = 1,\ldots,4$ dust transport bins.

2.2.2 Initialization

Initialization of the land model (i.e., providing the model with initial temperature and moisture states) depends on the type of run (startup or restart) (see the CLM4.5 User's Guide). A startup run starts the model from either initial conditions that are set internally in the Fortran code (referred to as arbitrary initial conditions) or from an initial conditions dataset that enables the model to start from a spun up state (i.e., where the land is in equilibrium with the simulated climate). In restart runs, the model is continued from a previous simulation and initialized from a restart file that ensures that the output is bit-for-bit the same as if the previous simulation had not stopped. The fields that are required from the restart or initial conditions files can be obtained by examining the code. Arbitrary initial conditions are specified as follows.

Vegetated and glacier land units have fifteen vertical layers, while lakes have ten. For soil points, temperature calculations are done over all layers, $N_{levgrnd} = 15$, while hydrology calculations are done over the top ten layers, $N_{levsoi} = 10$, the bottom five layers being specified as bedrock. Soil points are initialized with surface ground temperature T_g and soil layer temperature T_i, for $i = 1, \ldots, N_{levgrnd}$, of 274 K, vegetation temperature T_v of 283 K, no snow or canopy water ($W_{sno} = 0$, $W_{can} = 0$), and volumetric soil water content $\theta_i = 0.15$ mm^3 mm^{-3} for layers $i = 1, \ldots, N_{levsoi}$ and $\theta_i = 0.0$ mm^3 mm^{-3} for layers $i = N_{levsoi} + 1, \ldots, N_{levgrnd}$. Lake temperatures ($T_g$ and T_i) are initialized at 277 K and $W_{sno} = 0$.

Glacier temperatures ($T_g = T_{snl+1}$ and T_i for $i = snl + 1, \ldots, N_{levgrnd}$ where snl is the negative of the number of snow layers, i.e., snl ranges from –5 to 0) are initialized to

250 K with a snow water equivalent $W_{sno} = 1000$ mm, snow depth $z_{sno} = \frac{W_{sno}}{\rho_{sno}}$ (m) where $\rho_{sno} = 250$ kg m^{-3} is an initial estimate for the bulk density of snow, and θ_i=1.0 for $i = 1, \ldots, N_{levgrnd}$. The snow layer structure (e.g., number of snow layers snl and layer thickness) is initialized based on the snow depth (section 6.1). The snow liquid water and ice contents (kg m^{-2}) are initialized as $w_{liq,i} = 0$ and $w_{ice,i} = \Delta z_i \rho_{sno}$, respectively, where $i = snl + 1, \ldots, 0$ are the snow layers, and Δz_i is the thickness of snow layer i (m). The soil liquid water and ice contents are initialized as $w_{liq,i} = 0$ and $w_{ice,i} = \Delta z_i \rho_{ice} \theta_i$ for $T_i \le T_f$, and $w_{liq,i} = \Delta z_i \rho_{liq} \theta_i$ and $w_{ice,i} = 0$ for $T_i > T_f$, where ρ_{ice} and ρ_{liq} are the densities of ice and liquid water (kg m^{-3}) (Table 2.6), and T_f is the freezing temperature of water (K) (Table 2.6). All vegetated and glacier land units are initialized with water stored in the unconfined aquifer and unsaturated soil $W_a = 4000$ mm and water table depth z_∇ at five meters below the soil column.

2.2.3 Surface Data

Required surface data for each land grid cell are listed in Table 2.5 and include the glacier, lake, and urban fractions of the grid cell (vegetated and crop occupy the remainder), the fractional cover of each plant functional type (PFT), monthly leaf and stem area index and canopy top and bottom heights for each PFT, soil color, soil texture, soil organic matter density, maximum fractional saturated area, slope, elevation, biogenic volatile organic compounds (BVOCs) emissions factors, population density, gross domestic production, peat area fraction, and peak month of agricultural burning. Optional surface data include crop irrigation and managed crops. All fields are

aggregated to the model's grid from high-resolution input datasets (Table 2.5) that are obtained from a variety of sources described below.

Table 2.5. Surface data required for CLM and their base spatial resolution

Surface Field	Resolution
Percent glacier	0.05°
Percent lake and lake depth	0.05°
Percent urban	0.05°
Percent plant functional types (PFTs)	0.05°
Monthly leaf and stem area index	0.5°
Canopy height (top, bottom)	0.5°
Soil color	0.5°
Percent sand, percent clay	0.083°
Soil organic matter density	0.083°
Maximum fractional saturated area	0.125°
Elevation	1km
Slope	1km
Biogenic Volatile Organic Compounds	0.5°
Crop Irrigation	0.083°
Managed crops	0.5°
Population density	0.5°
Gross domestic production	0.5°
Peat area fraction	0.5°
Peak month of agricultural waste burning	0.5°

At the base spatial resolution of 0.05°, the percentage of each PFT is defined with respect to the vegetated portion of the grid cell and the sum of the PFTs is 100%. The

percent lake, wetland, glacier, and urban at their base resolution are specified with respect to the entire grid cell. The surface dataset creation routines re-adjust the PFT percentages to ensure that the sum of all land cover types in the grid cell sum to 100%. A minimum threshold of 0.1% of the grid cell by area is required for urban areas.

The percentage glacier mask was derived from vector data of global glacier and ice sheet spatial coverage. Vector data for glaciers (ice caps, icefields and mountain glaciers) were taken from the first globally complete glacier inventory, the Randolph Glacier Inventory version 1.0 (RGIv1.0: Arendt et al. 2012). Vector data for the Greenland Ice Sheet were provided by Frank Paul and Tobias Bolch (University of Zurich: Rastner et al. 2012). Antarctic Ice Sheet data were provided by Andrew Bliss (University of Alaska) and were extracted from the Scientific Committee on Antarctic Research (SCAR) Antarctic Digital Database version 5.0. Floating ice is only provided for the Antarctic and does not include the small area of Arctic ice shelves. High spatial resolution vector data were then processed to determine the area of glacier, ice sheet and floating ice within 30-second grid cells globally. The 30-second glacier, ice sheet and Antarctic ice shelf masks were subsequently draped over equivalent-resolution GLOBE topography (Global Land One-km Base Elevation Project, Hastings et al. 1999) to extract approximate ice-covered elevations of ice-covered regions. Grid cells flagged as land-ice in the mask but ocean in GLOBE (typically, around ice sheets at high latitudes) were designated land-ice with an elevation of 0 meters. Finally, the high-resolution mask/topography datasets were aggregated and processed into three 3-minute datasets: 3-minute fractional areal land ice coverage (including both glaciers and ice sheets); 3-minute distributions of areal glacier fractional coverage by elevation and areal ice sheet fractional coverage by elevation. Ice

fractions were binned at 100 meter intervals, with bin edges defined from 0 to 6000 meters (plus one top bin encompassing all remaining high-elevation ice, primarily in the Himalaya). These distributions by elevation are needed when running CLM4 with multiple glacier elevation classes.

Percent lake and lake depth are area-averaged from the 90-second resolution data of Kourzeneva (2009, 2010) to the 0.05° resolution using the MODIS land-mask. Percent urban is derived from LandScan 2004, a population density dataset derived from census data, nighttime lights satellite observations, road proximity and slope (Dobson et al. 2000) as described by Jackson et al. (2010) at 1km resolution and aggregated to 0.05°. A number of urban radiative, thermal, and morphological fields are also required and are obtained from Jackson et al. (2010). Their description can be found in Table 3 of the Community Land Model Urban (CLMU) technical note (Oleson et al. 2010b).

Percent PFTs are derived from MODIS satellite data as described in Lawrence and Chase (2007) (section 21.3.3). Prescribed PFT leaf area index is derived from the MODIS satellite data of Myneni et al. (2002) using the de-aggregation methods described in Lawrence and Chase (2007) (section 2.2.3). Prescribed PFT stem area index is derived from PFT leaf area index phenology combined with the methods of Zeng et al. (2002). Prescribed canopy top and bottom heights are from Bonan (1996) as described in Bonan et al. (2002b). If the biogeochemistry model is active, it supplies the leaf and stem area index and canopy top and bottom heights dynamically, and the prescribed values are ignored.

Soil color determines dry and saturated soil albedo (section 3.2). Soil colors are from Lawrence and Chase (2007) (section 3.2).

The soil texture and organic matter content determine soil thermal and hydrologic properties (sections 6.3 and 7.4.1). The International Geosphere-Biosphere Programme (IGBP) soil dataset (Global Soil Data Task 2000) of 4931 soil mapping units and their sand and clay content for each soil layer were used to create a mineral soil texture dataset (Bonan et al. 2002b). Soil organic matter data is merged from two sources. The majority of the globe is from ISRIC-WISE (Batjes, 2006). The high latitudes come from the 0.25° version of the Northern Circumpolar Soil Carbon Database (Hugelius et al. 2012). Both datasets report carbon down to 1m depth. Carbon is partitioned across the top seven CLM4 layers (~1m depth) as in Lawrence and Slater (2008).

The maximum fractional saturated area ($f_{\max}$) is used in determining surface runoff and infiltration (section 7.3). Maximum fractional saturated area at 0.125^{o} resolution is calculated from 1-km compound topographic indices (CTIs) based on the USGS HYDRO1K dataset (Verdin and Greenlee 1996) following the algorithm in Niu et al. (2005). $f_{\max}$ is the ratio between the number of 1-km pixels with CTIs equal to or larger than the mean CTI and the total number of pixels in a 0.125° grid cell. See section 7.3.1 and Li et al. (2013b) for further details. Slope and elevation are also obtained from the USGS HYDRO1K 1-km dataset (Verdin and Greenlee 1996). Slope is used in the River Transport Model (Chapter 11) and in the surface water parameterization (section 7.3.2), and elevation is used to calculate the grid cell standard deviation of topography for the snow cover fraction parameterization (section 7.2.1).

Biogenic Volatile Organic Compounds emissions factors are from the Model of Emissions of Gases and Aerosols from Nature version 2.1 (MEGAN2.1; Guenther et al. 2012).

The default list of PFTs includes an unmanaged crop treated as a second C3 grass (Table 2.1). The unmanaged crop has grid cell fractional cover assigned from MODIS satellite data (Lawrence and Chase 2007). A managed crop option uses grid cell fractional cover from the present-day crop dataset of Ramankutty and Foley (1998) (CLM4CNcrop). Managed crops are assigned in the proportions given by Ramankutty and Foley (1998) without exceeding the area previously assigned to the unmanaged crop. The unmanaged crop continues to occupy any of its original area that remains and continues to be handled just by the CN part of CLM4CNcrop. The managed crop types (corn, soybean, and temperate cereals) were chosen based on the availability of corresponding algorithms in AgroIBIS (Kucharik et al. 2000; Kucharik and Brye 2003). Temperate cereals include wheat, barley, and rye here. All temperate cereals are treated as summer crops (like spring wheat, for example) at this time. Winter cereals (such as winter wheat) may be introduced in a future version of the model.

To allow crops to coexist with natural vegetation in a grid cell and be treated by separate models (i.e., CLM4.5BGCcrop versus the Dynamic Vegetation version (CLM4.5BGCDV)), we separate the vegetated land unit into a naturally vegetated land unit and a human managed land unit. PFTs in the naturally vegetated land unit share one soil column and compete for water (default CLM setting). PFTs in the human managed land unit do not share soil columns and thus permit for differences in land management between crops.

CLM includes the option to irrigate cropland areas that are equipped for irrigation. The application of irrigation responds dynamically to climate (see Chapter 20). In CLM, irrigation is implemented for the C3 generic crop only. When irrigation is enabled, the

cropland area of each grid cell is divided into an irrigated and unirrigated fraction according to a dataset of areas equipped for irrigation (Siebert et al. 2005). The area of irrigated cropland in each grid cell is given by the smaller of (1) the grid cell's total cropland area, according to the default CLM4 dataset, and (2) the grid cell's area equipped for irrigation. The remainder of the grid cell's cropland area (if any) is then assigned to unirrigated cropland. Irrigated and unirrigated crops are placed on separate soil columns, so that irrigation is only applied to the soil beneath irrigated crops.

Several input datasets are required for the fire model (Li et al. 2013a) including population density, gross domestic production, peat area fraction, and peak month of agricultural waste burning. Population density at 0.5^{o} resolution for 1850-2100 combines 5-min resolution decadal population density data for 1850–1980 from the Database of the Global Environment version 3.1 (HYDEv3.1) with 0.5^{o} resolution population density data for 1990, 1995, 2000, and 2005 from the Gridded Population of the World version 3 dataset (GPWv3) (CIESIN, 2005). Gross Domestic Production (GDP) per capita in 2000 at 0.5^{o} is from Van Vuuren et al. (2006), which is the base-year GDP data for IPCC-SRES and derived from country-level World Bank's World Development Indicators (WDI) measured in constant 1995 US$ (World Bank, 2004) and the UN Statistics Database (UNSTAT, 2005). The peatland area fraction at 0.5^{o} resolution is derived from three vector datasets: peatland data in Indonesia and Malaysian Borneo (Olson et al. 2001); peatland data in Canada (Tarnocai et al. 2011); and bog, fen and mire data in boreal regions (north of 45^{o}N) outside Canada provided by the Global Lakes and Wetlands Database (GLWD) (Lehner and Döll, 2004). The climatological peak month for agricultural waste burning is from van der Werf et al. (2010).

2.2.4 Adjustable Parameters and Physical Constants

Values of certain adjustable parameters inherent in the biogeophysical or biogeochemical parameterizations have either been obtained from the literature or calibrated based on comparisons with observations. These are described in the text. Physical constants, generally shared by all of the components in the coupled modeling system, are presented in Table 2.6.

Table 2.6. Physical constants

Pi	π	3.14159265358979323846	-
Acceleration of gravity	g	9.80616	m s^{-2}
Standard pressure	P_{std}	101325	Pa
Stefan-Boltzmann constant	σ	5.67×10^{-8}	W m^{-2} K^{-4}
Boltzmann constant	κ	1.38065×10^{-23}	J K^{-1} $molecule^{-1}$
Avogadro's number	N_A	6.02214×10^{26}	molecule $kmol^{-1}$
Universal gas constant	R_{gas}	$N_A\kappa$	J K^{-1} $kmol^{-1}$
Molecular weight of dry air	MW_{da}	28.966	kg $kmol^{-1}$
Dry air gas constant	R_{da}	R_{gas}/MW_{da}	J K^{-1} kg^{-1}
Molecular weight of water vapor	MW_{wv}	18.016	kg $kmol^{-1}$
Water vapor gas constant	R_{wv}	R_{gas}/MW_{wv}	J K^{-1} kg^{-1}
Von Karman constant	k	0.4	-
Freezing temperature of fresh water	T_f	273.15	K
Density of liquid water	ρ_{liq}	1000	kg m^{-3}
Density of ice	ρ_{ice}	917	kg m^{-3}
Specific heat capacity of dry air	C_p	1.00464×10^3	J kg^{-1} K^{-1}
Specific heat capacity of water	C_{liq}	4.188×10^3	J kg^{-1} K^{-1}
Specific heat capacity of ice	C_{ice}	2.11727×10^3	J kg^{-1} K^{-1}
Latent heat of vaporization	λ_{vap}	2.501×10^6	J kg^{-1}
Latent heat of fusion	L_f	3.337×10^5	J kg^{-1}
Latent heat of sublimation	λ_{sub}	$\lambda_{vap}+L_f$	J kg^{-1}
[1]Thermal conductivity of water	λ_{liq}	0.57	W m^{-1} K^{-1}
[1]Thermal conductivity of ice	λ_{ice}	2.29	W m^{-1} K^{-1}
[1]Thermal conductivity of air	λ_{air}	0.023	W m^{-1} K^{-1}
Radius of the earth	R_e	6.37122×10^6	m

[1]Not shared by other components of the coupled modeling system.

3. Surface Albedos

3.1 Canopy Radiative Transfer

Radiative transfer within vegetative canopies is calculated from the two-stream approximation of Dickinson (1983) and Sellers (1985) as described by Bonan (1996)

$$-\bar{\mu}\frac{dI\uparrow}{d\left(L+S\right)}+\left[1-\left(1-\beta\right)\omega\right]I\uparrow-\omega\beta I\downarrow=\omega\bar{\mu}K\beta_0 e^{-K(L+S)} \tag{3.1}$$

$$\bar{\mu}\frac{dI\downarrow}{d\left(L+S\right)}+\left[1-\left(1-\beta\right)\omega\right]I\downarrow-\omega\beta I\uparrow=\omega\bar{\mu}K\left(1-\beta_0\right)e^{-K(L+S)} \tag{3.2}$$

where $I\uparrow$ and $I\downarrow$ are the upward and downward diffuse radiative fluxes per unit incident flux, $K=G\left(\mu\right)/\mu$ is the optical depth of direct beam per unit leaf and stem area, μ is the cosine of the zenith angle of the incident beam, $G\left(\mu\right)$ is the relative projected area of leaf and stem elements in the direction $\cos^{-1}\mu$, $\bar{\mu}$ is the average inverse diffuse optical depth per unit leaf and stem area, ω is a scattering coefficient, β and β_0 are upscatter parameters for diffuse and direct beam radiation, respectively, L is the exposed leaf area index (section 2.1.4), and S is the exposed stem area index (section 2.1.4). Given the direct beam albedo $\alpha_{g,\Lambda}^{\mu}$ and diffuse albedo $\alpha_{g,\Lambda}$ of the ground (section 3.2), these equations are solved to calculate the fluxes, per unit incident flux, absorbed by the vegetation, reflected by the vegetation, and transmitted through the vegetation for direct and diffuse radiation and for visible ($< 0.7\ \mu$m) and near-infrared ($\geq 0.7\ \mu$m) wavebands. The absorbed radiation is partitioned to sunlit and shaded fractions

of the canopy. The optical parameters $G(\mu)$, $\bar{\mu}$, ω, β, and β_0 are calculated based on work in Sellers (1985) as follows.

The relative projected area of leaves and stems in the direction $\cos^{-1}\mu$ is

$$G(\mu) = \phi_1 + \phi_2\mu \tag{3.3}$$

where $\phi_1 = 0.5 - 0.633\chi_L - 0.33\chi_L^2$ and $\phi_2 = 0.877(1 - 2\phi_1)$ for $-0.4 \le \chi_L \le 0.6$. χ_L is the departure of leaf angles from a random distribution and equals +1 for horizontal leaves, 0 for random leaves, and –1 for vertical leaves.

The average inverse diffuse optical depth per unit leaf and stem area is

$$\bar{\mu} = \int_0^1 \frac{\mu'}{G(\mu')} d\mu' = \frac{1}{\phi_2}\left[1 - \frac{\phi_1}{\phi_2}\ln\left(\frac{\phi_1 + \phi_2}{\phi_1}\right)\right] \tag{3.4}$$

where μ' is the direction of the scattered flux.

The optical parameters ω, β, and β_0, which vary with wavelength (Λ), are weighted combinations of values for vegetation and snow. The model determines that snow is on the canopy if $T_v \le T_f$, where T_v is the vegetation temperature (K) (Chapter 5) and T_f is the freezing temperature of water (K) (Table 2.6). In this case, the optical parameters are

$$\omega_\Lambda = \omega_\Lambda^{veg}(1 - f_{wet}) + \omega_\Lambda^{sno} f_{wet} \tag{3.5}$$

$$\omega_\Lambda\beta_\Lambda = \omega_\Lambda^{veg}\beta_\Lambda^{veg}(1 - f_{wet}) + \omega_\Lambda^{sno}\beta_\Lambda^{sno} f_{wet} \tag{3.6}$$

$$\omega_\Lambda\beta_{0,\Lambda} = \omega_\Lambda^{veg}\beta_{0,\Lambda}^{veg}(1 - f_{wet}) + \omega_\Lambda^{sno}\beta_{0,\Lambda}^{sno} f_{wet} \tag{3.7}$$

where f_{wet} is the wetted fraction of the canopy (section 7.1). The snow and vegetation weights are applied to the products $\omega_\Lambda \beta_\Lambda$ and $\omega_\Lambda \beta_{0,\Lambda}$ because these products are used in the two-stream equations. If there is no snow on the canopy,

$$\omega_\Lambda = \omega_\Lambda^{veg} \tag{3.8}$$

$$\omega_\Lambda \beta_\Lambda = \omega_\Lambda^{veg} \beta_\Lambda^{veg} \tag{3.9}$$

$$\omega_\Lambda \beta_{0,\Lambda} = \omega_\Lambda^{veg} \beta_{0,\Lambda}^{veg}. \tag{3.10}$$

For vegetation, $\omega_\Lambda^{veg} = \alpha_\Lambda + \tau_\Lambda$. α_Λ is a weighted combination of the leaf and stem reflectances ($\alpha_\Lambda^{leaf}, \alpha_\Lambda^{stem}$)

$$\alpha_\Lambda = \alpha_\Lambda^{leaf} w_{leaf} + \alpha_\Lambda^{stem} w_{stem} \tag{3.11}$$

where $w_{leaf} = L/(L+S)$ and $w_{stem} = S/(L+S)$. τ_Λ is a weighted combination of the leaf and stem transmittances ($\tau_\Lambda^{leaf}, \tau_\Lambda^{stem}$)

$$\tau_\Lambda = \tau_\Lambda^{leaf} w_{leaf} + \tau_\Lambda^{stem} w_{stem}. \tag{3.12}$$

The upscatter for diffuse radiation is

$$\omega_\Lambda^{veg} \beta_\Lambda^{veg} = \frac{1}{2}\left[\alpha_\Lambda + \tau_\Lambda + (\alpha_\Lambda - \tau_\Lambda)\cos^2 \bar{\theta}\right] \tag{3.13}$$

where $\bar{\theta}$ is the mean leaf inclination angle relative to the horizontal plane (i.e., the angle between leaf normal and local vertical) (Sellers 1985). Here, $\cos\bar{\theta}$ is approximated by

$$\cos\bar{\theta} = \frac{1+\chi_L}{2} \tag{3.14}$$

Using this approximation, for vertical leaves ($\chi_L = -1$, $\bar{\theta} = 90^o$), $\omega_\Lambda^{veg} \beta_\Lambda^{veg} = 0.5(\alpha_\Lambda + \tau_\Lambda)$, and for horizontal leaves ($\chi_L = 1$, $\bar{\theta} = 0^o$), $\omega_\Lambda^{veg} \beta_\Lambda^{veg} = \alpha_\Lambda$,

which agree with both Dickinson (1983) and Sellers (1985). For random (spherically distributed) leaves ($\chi_L = 0$, $\bar{\theta} = 60^o$), the approximation yields $\omega_\Lambda^{veg}\beta_\Lambda^{veg} = 5/8\,\alpha_\Lambda + 3/8\,\tau_\Lambda$ whereas the approximate solution of Dickinson (1983) is $\omega_\Lambda^{veg}\beta_\Lambda^{veg} = 2/3\,\alpha_\Lambda + 1/3\,\tau_\Lambda$. This discrepancy arises from the fact that a spherical leaf angle distribution has a true mean leaf inclination $\bar{\theta} \approx 57$ (Campbell and Norman 1998) in equation (3.13), while $\bar{\theta} = 60$ in equation (3.14). The upscatter for direct beam radiation is

$$\omega_\Lambda^{veg}\beta_{0,\Lambda}^{veg} = \frac{1+\bar{\mu}K}{\bar{\mu}K}\,a_s(\mu)_\Lambda \tag{3.15}$$

where the single scattering albedo is

$$\begin{aligned} a_s(\mu)_\Lambda &= \frac{\omega_\Lambda^{veg}}{2}\int_0^1 \frac{\mu' G(\mu)}{\mu G(\mu') + \mu' G(\mu)}\,d\mu' \\ &= \frac{\omega_\Lambda^{veg}}{2}\,\frac{G(\mu)}{\mu\phi_2 + G(\mu)}\left[1 - \frac{\mu\phi_1}{\mu\phi_2 + G(\mu)}\ln\left(\frac{\mu\phi_1 + \mu\phi_2 + G(\mu)}{\mu\phi_1}\right)\right]. \end{aligned} \tag{3.16}$$

The upward diffuse fluxes per unit incident direct beam and diffuse flux (i.e., the surface albedos) are

$$I\uparrow_\Lambda^\mu = \frac{h_1}{\sigma} + h_2 + h_3 \tag{3.17}$$

$$I\uparrow_\Lambda = h_7 + h_8. \tag{3.18}$$

The downward diffuse fluxes per unit incident direct beam and diffuse radiation, respectively, are

$$I\downarrow_\Lambda^\mu = \frac{h_4}{\sigma}e^{-K(L+S)} + h_5 s_1 + \frac{h_6}{s_1} \tag{3.19}$$

$$I\downarrow_{\Lambda} = h_9 s_1 + \frac{h_{10}}{s_1}. \tag{3.20}$$

With reference to Figure 4.1, the direct beam flux transmitted through the canopy, per unit incident flux, is $e^{-K(L+S)}$, and the direct beam and diffuse fluxes absorbed by the vegetation, per unit incident flux, are

$$\vec{I}_{\Lambda}^{\mu} = 1 - I\uparrow_{\Lambda}^{\mu} - \left(1-\alpha_{g,\Lambda}\right) I\downarrow_{\Lambda}^{\mu} - \left(1-\alpha_{g,\Lambda}^{\mu}\right) e^{-K(L+S)} \tag{3.21}$$

$$\vec{I}_{\Lambda} = 1 - I\uparrow_{\Lambda} - \left(1-\alpha_{g,\Lambda}\right) I\downarrow_{\Lambda}. \tag{3.22}$$

These fluxes are partitioned to the sunlit and shaded canopy using an analytical solution to the two-stream approximation for sunlit and shaded leaves (Dai et al. 2004), as described by Bonan et al. (2011). The absorption of direct beam radiation by sunlit leaves is

$$\vec{I}_{sun,\Lambda}^{\mu} = \left(1-\omega_{\Lambda}\right)\left[1 - s_2 + \frac{1}{\bar{\mu}}\left(a_1 + a_2\right)\right] \tag{3.23}$$

and for shaded leaves is

$$\vec{I}_{sha,\Lambda}^{\mu} = \vec{I}_{\Lambda}^{\mu} - \vec{I}_{sun,\Lambda}^{\mu} \tag{3.24}$$

with

$$a_1 = \frac{h_1}{\sigma}\left[\frac{1-s_2^2}{2K}\right] + h_2\left[\frac{1-s_2 s_1}{K+h}\right] + h_3\left[\frac{1-s_2/s_1}{K-h}\right] \tag{3.25}$$

$$a_2 = \frac{h_4}{\sigma}\left[\frac{1-s_2^2}{2K}\right] + h_5\left[\frac{1-s_2 s_1}{K+h}\right] + h_6\left[\frac{1-s_2/s_1}{K-h}\right]. \tag{3.26}$$

For diffuse radiation, the absorbed radiation for sunlit leaves is

$$\vec{I}_{sun,\Lambda} = \left[\frac{1-\omega_{\Lambda}}{\bar{\mu}}\right]\left(a_1 + a_2\right) \tag{3.27}$$

and for shaded leaves is

$$\vec{I}_{sha,\Lambda} = \vec{I}_{\Lambda} - \vec{I}_{sun,\Lambda} \tag{3.28}$$

with

$$a_1 = h_7\left[\frac{1-s_2 s_1}{K+h}\right] + h_8\left[\frac{1-s_2/s_1}{K-h}\right] \tag{3.29}$$

$$a_2 = h_9\left[\frac{1-s_2 s_1}{K+h}\right] + h_{10}\left[\frac{1-s_2/s_1}{K-h}\right]. \tag{3.30}$$

The parameters $h_1 - h_{10}$, σ, h, s_1, and s_2 are from Sellers (1985) [note the error in h_4 in Sellers (1985)]:

$$b = 1 - \omega_{\Lambda} + \omega_{\Lambda}\beta_{\Lambda} \tag{3.31}$$

$$c = \omega_{\Lambda}\beta_{\Lambda} \tag{3.32}$$

$$d = \omega_{\Lambda}\bar{\mu}K\beta_{0,\Lambda} \tag{3.33}$$

$$f = \omega_{\Lambda}\bar{\mu}K\left(1-\beta_{0,\Lambda}\right) \tag{3.34}$$

$$h = \frac{\sqrt{b^2 - c^2}}{\bar{\mu}} \tag{3.35}$$

$$\sigma = \left(\bar{\mu}K\right)^2 + c^2 - b^2 \tag{3.36}$$

$$u_1 = b - c/\alpha^{\mu}_{g,\Lambda} \text{ or } u_1 = b - c/\alpha_{g,\Lambda} \tag{3.37}$$

$$u_2 = b - c\alpha^{\mu}_{g,\Lambda} \text{ or } u_2 = b - c\alpha_{g,\Lambda} \tag{3.38}$$

$$u_3 = f + c\alpha^{\mu}_{g,\Lambda} \text{ or } u_3 = f + c\alpha_{g,\Lambda} \tag{3.39}$$

$$s_1 = \exp\left\{-\min\left[h\left(L+S\right), 40\right]\right\} \tag{3.40}$$

$$s_2 = \exp\left\{-\min\left[K\left(L+S\right),40\right]\right\} \tag{3.41}$$

$$p_1 = b + \bar{\mu}h \tag{3.42}$$

$$p_2 = b - \bar{\mu}h \tag{3.43}$$

$$p_3 = b + \bar{\mu}K \tag{3.44}$$

$$p_4 = b - \bar{\mu}K \tag{3.45}$$

$$d_1 = \frac{p_1\left(u_1 - \bar{\mu}h\right)}{s_1} - p_2\left(u_1 + \bar{\mu}h\right)s_1 \tag{3.46}$$

$$d_2 = \frac{u_2 + \bar{\mu}h}{s_1} - \left(u_2 - \bar{\mu}h\right)s_1 \tag{3.47}$$

$$h_1 = -dp_4 - cf \tag{3.48}$$

$$h_2 = \frac{1}{d_1}\left[\left(d - \frac{h_1}{\sigma}p_3\right)\frac{\left(u_1 - \bar{\mu}h\right)}{s_1} - p_2\left(d - c - \frac{h_1}{\sigma}\left(u_1 + \bar{\mu}K\right)\right)s_2\right] \tag{3.49}$$

$$h_3 = \frac{-1}{d_1}\left[\left(d - \frac{h_1}{\sigma}p_3\right)\left(u_1 + \bar{\mu}h\right)s_1 - p_1\left(d - c - \frac{h_1}{\sigma}\left(u_1 + \bar{\mu}K\right)\right)s_2\right] \tag{3.50}$$

$$h_4 = -fp_3 - cd \tag{3.51}$$

$$h_5 = \frac{-1}{d_2}\left[\left(\frac{h_4\left(u_2 + \bar{\mu}h\right)}{\sigma s_1}\right) + \left(u_3 - \frac{h_4}{\sigma}\left(u_2 - \bar{\mu}K\right)\right)s_2\right] \tag{3.52}$$

$$h_6 = \frac{1}{d_2}\left[\frac{h_4}{\sigma}\left(u_2 - \bar{\mu}h\right)s_1 + \left(u_3 - \frac{h_4}{\sigma}\left(u_2 - \bar{\mu}K\right)\right)s_2\right] \tag{3.53}$$

$$h_7 = \frac{c\left(u_1 - \bar{\mu}h\right)}{d_1 s_1} \tag{3.54}$$

$$h_8 = \frac{-c\left(u_1 + \bar{\mu}h\right)s_1}{d_1} \tag{3.55}$$

$$h_9 = \frac{u_2 + \bar{\mu} h}{d_2 s_1} \tag{3.56}$$

$$h_{10} = \frac{-s_1 \left(u_2 - \bar{\mu} h \right)}{d_2}. \tag{3.57}$$

Plant functional type optical properties (Table 3.1) for trees and shrubs are from Dorman and Sellers (1989). Leaf and stem optical properties (VIS and NIR reflectance and transmittance) were derived for grasslands and crops from full optical range spectra of measured optical properties (Asner et al. 1998). Optical properties for intercepted snow (Table 3.2) are from Sellers et al. (1986).

Table 3.1. Plant functional type optical properties

Plant Functional Type	χ_L	α_{vis}^{leaf}	α_{nir}^{leaf}	α_{vis}^{stem}	α_{nir}^{stem}	τ_{vis}^{leaf}	τ_{nir}^{leaf}	τ_{vis}^{stem}	τ_{nir}^{stem}
NET Temperate	0.01	0.07	0.35	0.16	0.39	0.05	0.10	0.001	0.001
NET Boreal	0.01	0.07	0.35	0.16	0.39	0.05	0.10	0.001	0.001
NDT Boreal	0.01	0.07	0.35	0.16	0.39	0.05	0.10	0.001	0.001
BET Tropical	0.10	0.10	0.45	0.16	0.39	0.05	0.25	0.001	0.001
BET temperate	0.10	0.10	0.45	0.16	0.39	0.05	0.25	0.001	0.001
BDT tropical	0.01	0.10	0.45	0.16	0.39	0.05	0.25	0.001	0.001
BDT temperate	0.25	0.10	0.45	0.16	0.39	0.05	0.25	0.001	0.001
BDT boreal	0.25	0.10	0.45	0.16	0.39	0.05	0.25	0.001	0.001
BES temperate	0.01	0.07	0.35	0.16	0.39	0.05	0.10	0.001	0.001
BDS temperate	0.25	0.10	0.45	0.16	0.39	0.05	0.25	0.001	0.001
BDS boreal	0.25	0.10	0.45	0.16	0.39	0.05	0.25	0.001	0.001
C_3 arctic grass	-0.30	0.11	0.35	0.31	0.53	0.05	0.34	0.120	0.250
C_3 grass	-0.30	0.11	0.35	0.31	0.53	0.05	0.34	0.120	0.250
C_4 grass	-0.30	0.11	0.35	0.31	0.53	0.05	0.34	0.120	0.250
Crop R	-0.30	0.11	0.35	0.31	0.53	0.05	0.34	0.120	0.250
Crop I	-0.30	0.11	0.35	0.31	0.53	0.05	0.34	0.120	0.250
Corn R	-0.50	0.11	0.35	0.31	0.53	0.05	0.34	0.120	0.250
Corn I	-0.50	0.11	0.35	0.31	0.53	0.05	0.34	0.120	0.250
Temp Cereal R	0.65	0.11	0.35	0.31	0.53	0.05	0.34	0.120	0.250
Temp Cereal I	0.65	0.11	0.35	0.31	0.53	0.05	0.34	0.120	0.250
Winter Cereal R	0.65	0.11	0.35	0.31	0.53	0.05	0.34	0.120	0.250
Winter Cereal I	0.65	0.11	0.35	0.31	0.53	0.05	0.34	0.120	0.250
Soybean R	-0.5	0.11	0.35	0.31	0.53	0.05	0.34	0.120	0.250
Soybean I	-0.5	0.11	0.35	0.31	0.53	0.05	0.34	0.120	0.250

Table 3.2. Intercepted snow optical properties

	Waveband (Λ)	
Parameter	vis	nir
ω^{sno}	0.8	0.4
β^{sno}	0.5	0.5
β_0^{sno}	0.5	0.5

3.2 Ground Albedos

The overall direct beam $\alpha_{g,\Lambda}^{\mu}$ and diffuse $\alpha_{g,\Lambda}$ ground albedos are weighted combinations of "soil" and snow albedos

$$\alpha_{g,\Lambda}^{\mu} = \alpha_{soi,\Lambda}^{\mu}\left(1 - f_{sno}\right) + \alpha_{sno,\Lambda}^{\mu} f_{sno} \tag{3.58}$$

$$\alpha_{g,\Lambda} = \alpha_{soi,\Lambda}\left(1 - f_{sno}\right) + \alpha_{sno,\Lambda} f_{sno} \tag{3.59}$$

where f_{sno} is the fraction of the ground covered with snow (section 7.2.1).

$\alpha_{soi,\Lambda}^{\mu}$ and $\alpha_{soi,\Lambda}$ vary with glacier, lake, wetland, and soil surfaces. Glacier albedos are from Paterson (1994)

$$\alpha_{soi,vis}^{\mu} = \alpha_{soi,vis} = 0.6$$

$$\alpha_{soi,nir}^{\mu} = \alpha_{soi,nir} = 0.4\,.$$

Unfrozen lake and wetland albedos depend on the cosine of the solar zenith angle μ

$$\alpha_{soi,\Lambda}^{\mu} = \alpha_{soi,\Lambda} = 0.05\left(\mu + 0.15\right)^{-1}. \tag{3.60}$$

Frozen lake and wetland albedos are from NCAR LSM (Bonan 1996)

$$\alpha_{soi,vis}^{\mu} = \alpha_{soi,vis} = 0.60$$

$$\alpha^{\mu}_{soi,nir} = \alpha_{soi,nir} = 0.40 .$$

As in NCAR LSM (Bonan 1996), soil albedos vary with color class

$$\alpha^{\mu}_{soi,\Lambda} = \alpha_{soi,\Lambda} = \left(\alpha_{sat,\Lambda} + \Delta\right) \le \alpha_{dry,\Lambda} \tag{3.61}$$

where Δ depends on the volumetric water content of the first soil layer θ_1 (section 7.4) as $\Delta = 0.11 - 0.40\theta_1 > 0$, and $\alpha_{sat,\Lambda}$ and $\alpha_{dry,\Lambda}$ are albedos for saturated and dry soil color classes (Table 3.3).

CLM soil colors are prescribed so that they best reproduce observed MODIS local solar noon surface albedo values at the CLM grid cell following the methods of Lawrence and Chase (2007). The soil colors are fitted over the range of 20 soil classes shown in Table 3.3 and compared to the MODIS monthly local solar noon all-sky surface albedo as described in Strahler et al. (1999) and Schaaf et al. (2002). The CLM two-stream radiation model was used to calculate the model equivalent surface albedo using climatological monthly soil moisture along with the vegetation parameters of PFT fraction, LAI, and SAI. The soil color that produced the closest all-sky albedo in the two-stream radiation model was selected as the best fit for the month. The fitted monthly soil colors were averaged over all snow-free months to specify a representative soil color for the grid cell. In cases where there was no snow-free surface albedo for the year, the soil color derived from snow-affected albedo was used to give a representative soil color that included the effects of the minimum permanent snow cover.

Table 3.3. Dry and saturated soil albedos

	Dry		Saturated			Dry		Saturated	
Color Class	vis	nir	vis	nir	Color Class	vis	nir	vis	nir
1	0.36	0.61	0.25	0.50	11	0.24	0.37	0.13	0.26
2	0.34	0.57	0.23	0.46	12	0.23	0.35	0.12	0.24
3	0.32	0.53	0.21	0.42	13	0.22	0.33	0.11	0.22
4	0.31	0.51	0.20	0.40	14	0.20	0.31	0.10	0.20
5	0.30	0.49	0.19	0.38	15	0.18	0.29	0.09	0.18
6	0.29	0.48	0.18	0.36	16	0.16	0.27	0.08	0.16
7	0.28	0.45	0.17	0.34	17	0.14	0.25	0.07	0.14
8	0.27	0.43	0.16	0.32	18	0.12	0.23	0.06	0.12
9	0.26	0.41	0.15	0.30	19	0.10	0.21	0.05	0.10
10	0.25	0.39	0.14	0.28	20	0.08	0.16	0.04	0.08

3.2.1 *Snow Albedo*

Snow albedo and solar absorption within each snow layer are simulated with the Snow, Ice, and Aerosol Radiative Model (SNICAR), which incorporates a two-stream radiative transfer solution from Toon et al. (1989). Albedo and the vertical absorption profile depend on solar zenith angle, albedo of the substrate underlying snow, mass concentrations of atmospheric-deposited aerosols (black carbon, mineral dust, and organic carbon), and ice effective grain size (r_e), which is simulated with a snow aging routine described in section 3.2.3. Representation of impurity mass concentrations within the snowpack is described in section 7.2.4. Implementation of SNICAR in CLM is also described somewhat by Flanner and Zender (2005) and Flanner et al. (2007).

The two-stream solution requires the following bulk optical properties for each snow layer and spectral band: extinction optical depth (τ), single-scatter albedo (ω), and

scattering asymmetry parameter (g). The snow layers used for radiative calculations are identical to snow layers applied elsewhere in CLM, except for the case when snow mass is greater than zero but no snow layers exist. When this occurs, a single radiative layer is specified to have the column snow mass and an effective grain size of freshly-fallen snow (section 3.2.3). The bulk optical properties are weighted functions of each constituent k, computed for each snow layer and spectral band as

$$\tau = \sum_{1}^{k} \tau_k \tag{3.62}$$

$$\omega = \frac{\sum_{1}^{k} \omega_k \tau_k}{\sum_{1}^{k} \tau_k} \tag{3.63}$$

$$g = \frac{\sum_{1}^{k} g_k \omega_k \tau_k}{\sum_{1}^{k} \omega_k \tau_k} \tag{3.64}$$

For each constituent (ice, two black carbon species, two organic carbon species, and four dust species), ω, g, and the mass extinction cross-section ψ (m^2 kg^{-1}) are computed offline with Mie Theory, e.g., applying the computational technique from Bohren and Huffman (1983). The extinction optical depth for each constituent depends on its mass extinction cross-section and layer mass, w_k (kg m^{-2}) as

$$\tau_k = \psi_k w_k \tag{3.65}$$

The two-stream solution (Toon et al. 1989) applies a tri-diagonal matrix solution to produce upward and downward radiative fluxes at each layer interface, from which net radiation, layer absorption, and surface albedo are easily derived. Solar fluxes are computed in five spectral bands, listed in Table 3.4. Because snow albedo varies strongly

across the solar spectrum, it was determined that four bands were needed to accurately represent the near-infrared (NIR) characteristics of snow, whereas only one band was needed for the visible spectrum. Boundaries of the NIR bands were selected to capture broad radiative features and maximize accuracy and computational efficiency. We partition NIR (0.7-5.0μm) surface downwelling flux from CLM according to the weights listed in Table 3.4, which are unique for diffuse and direct incident flux. These fixed weights were determined with offline hyperspectral radiative transfer calculations for an atmosphere typical of mid-latitude winter (Flanner et al. 2007). The tri-diagonal solution includes intermediate terms that allow for easy interchange of two-stream techniques. We apply the Eddington solution for the visible band (following Wiscombe and Warren 1980) and the hemispheric mean solution (Toon et al. 1989) for NIR bands. These choices were made because the Eddington scheme works well for highly scattering media, but can produce negative albedo for absorptive NIR bands with diffuse incident flux. Delta scalings are applied to τ, ω, and g (Wiscombe and Warren 1980) in all spectral bands, producing effective values (denoted with *) that are applied in the two-stream solution

$$\tau^* = (1-\omega g^2)\tau \tag{3.66}$$

$$\omega^* = \frac{(1-g^2)\omega}{1-g^2\omega} \tag{3.67}$$

$$g^* = \frac{g}{1+g} \tag{3.68}$$

Table 3.4. Spectral bands and weights used for snow radiative transfer

Spectral band	Direct-beam weight	Diffuse weight
Band 1: 0.3-0.7μm (visible)	(1.0)	(1.0)
Band 2: 0.7-1.0μm (near-IR)	0.494	0.586
Band 3: 1.0-1.2μm (near-IR)	0.181	0.202
Band 4: 1.2-1.5μm (near-IR)	0.121	0.109
Band 5: 1.5-5.0μm (near-IR)	0.204	0.103

Under direct-beam conditions, singularities in the radiative approximation are occasionally approached in spectral bands 4 and 5 that produce unrealistic conditions (negative energy absorption in a layer, negative albedo, or total absorbed flux greater than incident flux). When any of these three conditions occur, the Eddington approximation is attempted instead, and if both approximations fail, the cosine of the solar zenith angle is adjusted by 0.02 (conserving incident flux) and a warning message is produced. This situation occurs in only about 1 in 10^6 computations of snow albedo. After looping over the five spectral bands, absorption fluxes and albedo are averaged back into the bulk NIR band used by the rest of CLM.

Soil albedo (or underlying substrate albedo), which is defined for visible and NIR bands, is a required boundary condition for the snow radiative transfer calculation. Currently, the bulk NIR soil albedo is applied to all four NIR snow bands. With ground albedo as a lower boundary condition, SNICAR simulates solar absorption in all snow layers as well as the underlying soil or ground. With a thin snowpack, penetrating solar radiation to the underlying soil can be quite large and heat cannot be released from the

soil to the atmosphere in this situation. Thus, solar radiation penetration is limited to snowpacks with total snow depth greater than or equal to 0.1 m ($z_{sno} \geq 0.1$) to prevent unrealistic soil warming within a single timestep.

The radiative transfer calculation is performed twice for each column containing a mass of snow greater than 1×10^{-30} kg m^{-2} (excluding lake and urban columns); once each for direct-beam and diffuse incident flux. Absorption in each layer i of pure snow is initially recorded as absorbed flux per unit incident flux on the ground ($S_{sno,i}$), as albedos must be calculated for the next timestep with unknown incident flux. The snow absorption fluxes that are used for column temperature calculations are

$$S_{g,i} = S_{sno,i}\left(1-\alpha_{sno}\right) \tag{3.69}$$

This weighting is performed for direct-beam and diffuse, visible and NIR fluxes. After the ground-incident fluxes (transmitted through the vegetation canopy) have been calculated for the current time step (sections 3.1 and 4.1), the layer absorption factors ($S_{g,i}$) are multiplied by the ground-incident fluxes to produce solar absorption (W m^{-2}) in each snow layer and the underlying ground.

3.2.2 *Snowpack Optical Properties*

Ice optical properties for the five spectral bands are derived offline and stored in a namelist-defined lookup table for online retrieval (see CLM4.5 User's Guide). Mie properties are first computed at fine spectral resolution (470 bands), and are then weighted into the five bands applied by CLM according to incident solar flux, $I^{\downarrow}(\lambda)$. For example, the broadband mass-extinction cross section ($\overline{\psi}$) over wavelength interval λ_1 to λ_2 is

$$\overline{\psi} = \frac{\int_{\lambda_1}^{\lambda_2} \psi(\lambda) I^{\downarrow}(\lambda) \mathrm{d}\lambda}{\int_{\lambda_1}^{\lambda_2} I^{\downarrow}(\lambda) \mathrm{d}\lambda} \tag{3.70}$$

Broadband single-scatter albedo ($\overline{\omega}$) is additionally weighted by the diffuse albedo for a semi-infinite snowpack (α_{sno})

$$\overline{\omega} = \frac{\int_{\lambda_1}^{\lambda_2} \omega(\lambda) I^{\downarrow}(\lambda) \alpha_{sno}(\lambda) \mathrm{d}\lambda}{\int_{\lambda_1}^{\lambda_2} I^{\downarrow}(\lambda) \alpha_{sno}(\lambda) \mathrm{d}\lambda} \tag{3.71}$$

Inclusion of this additional albedo weight was found to improve accuracy of the five-band albedo solutions (relative to 470-band solutions) because of the strong dependence of optically-thick snowpack albedo on ice grain single-scatter albedo (Flanner et al. 2007). The lookup tables contain optical properties for lognormal distributions of ice particles over the range of effective radii: 30μm < r_e < 1500μm, at 1μm resolution. Single-scatter albedos for the end-members of this size range are listed in Table 3.5.

Optical properties for black carbon are described in Flanner et al. (2007). Single-scatter albedo, mass extinction cross-section, and asymmetry parameter values for all snowpack species, in the five spectral bands used, are listed in Tables 3.5, 3.6, and 3.7. These properties were also derived with Mie Theory, using various published sources of indices of refraction and assumptions about particle size distribution. Weighting into the five CLM spectral bands was determined only with incident solar flux, as in equation (3.69).

Table 3.5. Single-scatter albedo values used for snowpack impurities and ice

Species	Band 1	Band 2	Band 3	Band 4	Band 5
Hydrophilic black carbon	0.516	0.434	0.346	0.276	0.139
Hydrophobic black carbon	0.288	0.187	0.123	0.089	0.040
Hydrophilic organic carbon	0.997	0.994	0.990	0.987	0.951
Hydrophobic organic carbon	0.963	0.921	0.860	0.814	0.744
Dust 1	0.979	0.994	0.993	0.993	0.953
Dust 2	0.944	0.984	0.989	0.992	0.983
Dust 3	0.904	0.965	0.969	0.973	0.978
Dust 4	0.850	0.940	0.948	0.953	0.955
Ice (r_e = 30μm)	0.9999	0.9999	0.9992	0.9938	0.9413
Ice (r_e = 1500μm)	0.9998	0.9960	0.9680	0.8730	0.5500

Table 3.6. Mass extinction values (m^2 kg^{-1}) used for snowpack impurities and ice.

Species	Band 1	Band 2	Band 3	Band 4	Band 5
Hydrophilic black carbon	25369	12520	7739	5744	3527
Hydrophobic black carbon	11398	5923	4040	3262	2224
Hydrophilic organic carbon	37774	22112	14719	10940	5441
Hydrophobic organic carbon	3289	1486	872	606	248
Dust 1	2687	2420	1628	1138	466
Dust 2	841	987	1184	1267	993
Dust 3	388	419	400	397	503
Dust 4	197	203	208	205	229
Ice (r_e = 30μm)	55.7	56.1	56.3	56.6	57.3
Ice (r_e = 1500μm)	1.09	1.09	1.09	1.09	1.1

Table 3.7. Asymmetry scattering parameters used for snowpack impurities and ice.

Species	Band 1	Band 2	Band 3	Band 4	Band 5
Hydrophilic black carbon	0.52	0.34	0.24	0.19	0.10
Hydrophobic black carbon	0.35	0.21	0.15	0.11	0.06
Hydrophilic organic carbon	0.77	0.75	0.72	0.70	0.64
Hydrophobic organic carbon	0.62	0.57	0.54	0.51	0.44
Dust 1	0.69	0.72	0.67	0.61	0.44
Dust 2	0.70	0.65	0.70	0.72	0.70
Dust 3	0.79	0.75	0.68	0.63	0.67
Dust 4	0.83	0.79	0.77	0.76	0.73
Ice (r_e = 30μm)	0.88	0.88	0.88	0.88	0.90
Ice (r_e = 1500μm)	0.89	0.90	0.90	0.92	0.97

3.2.3 *Snow Aging*

Snow aging is represented as evolution of the ice effective grain size (r_e). Previous studies have shown that use of spheres which conserve the surface area-to-volume ratio (or specific surface area) of ice media composed of more complex shapes produces relatively small errors in simulated hemispheric fluxes (e.g., Grenfell and Warren 1999). Effective radius is the surface area-weighted mean radius of an ensemble of spherical particles and is directly related to specific surface area (SSA) as $r_e = 3/(\rho_{ice} SSA)$, where ρ_{ice} is the density of ice. Hence, r_e is a simple and practical metric for relating the snowpack microphysical state to dry snow radiative characteristics.

Wet snow processes can also drive rapid changes in albedo. The presence of liquid water induces rapid coarsening of the surrounding ice grains (e.g., Brun 1989), and liquid water tends to refreeze into large ice clumps that darken the bulk snowpack. The presence of small liquid drops, by itself, does not significantly darken snowpack, as ice and water have very similar indices of refraction throughout the solar spectrum. Pooled or ponded water, however, can significantly darken snowpack by greatly reducing the number of refraction events per unit mass. This influence is not currently accounted for.

The net change in effective grain size occurring each time step is represented in each snow layer as a summation of changes caused by dry snow metamorphism ($dr_{e,dry}$), liquid water-induced metamorphism ($dr_{e,wet}$), refreezing of liquid water, and addition of freshly-fallen snow. The mass of each snow layer is partitioned into fractions of snow carrying over from the previous time step (f_{old}), freshly-fallen snow (f_{new}), and refrozen liquid water (f_{rfz}), such that snow r_e is updated each time step t as

$$r_e(t) = \left[r_e(t-1) + dr_{e,dry} + dr_{e,wet} \right] f_{\text{old}} + r_{e,0} f_{\text{new}} + r_{e,rfz} f_{\text{rfrz}} \tag{3.72}$$

Here, the effective radius of freshly-fallen snow ($r_{e,0}$) is fixed globally at 54.5μm (corresponding to a specific surface area of 60 m^2 kg^{-1}), and the effective radius of refrozen liquid water ($r_{e,rfz}$) is set to 1000μm.

Dry snow aging is based on a microphysical model described by Flanner and Zender (2006). This model simulates diffusive vapor flux amongst collections of ice crystals with various size and inter-particle spacing. Specific surface area and effective radius are prognosed for any combination of snow temperature, temperature gradient, density, and initial size distribution. The combination of warm snow, large temperature gradient, and low density produces the most rapid snow aging, whereas aging proceeds

slowly in cold snow, regardless of temperature gradient and density. Because this model is currently too computationally expensive for inclusion in climate models, we fit parametric curves to model output over a wide range of snow conditions and apply these parameters in CLM. The functional form of the parametric equation is

$$\frac{dr_{e,dry}}{dt} = \left(\frac{dr_e}{dt}\right)_0 \left(\frac{\eta}{(r_e - r_{e,0}) + \eta}\right)^{1/\kappa} \tag{3.73}$$

The parameters $(dr_e/dt)_0$, η, and κ are retrieved interactively from a lookup table with dimensions corresponding to snow temperature, temperature gradient, and density. The domain covered by this lookup table includes temperature ranging from 223 to 273 K, temperature gradient ranging from 0 to 300 K m^{-1}, and density ranging from 50 to 400 kg m^{-3}. Temperature gradient is calculated at the midpoint of each snow layer n, using mid-layer temperatures (T_n) and snow layer thicknesses (dz_n), as

$$\left(\frac{dT}{dz}\right)_n = \frac{1}{dz_n} \mathrm{abs}\left[\frac{T_{n-1}dz_n + T_n dz_{n-1}}{dz_n + dz_{n-1}} + \frac{T_{n+1}dz_n + T_n dz_{n+1}}{dz_n + dz_{n+1}}\right] \tag{3.74}$$

For the bottom snow layer ($n = 0$), T_{n+1} is taken as the temperature of the top soil layer, and for the top snow layer it is assumed that $T_{n-1} = T_n$.

The contribution of liquid water to enhanced metamorphism is based on parametric equations published by Brun (1989), who measured grain growth rates under different liquid water contents. This relationship, expressed in terms of r_e (μm) and subtracting an offset due to dry aging, depends on the mass liquid water fraction f_{liq} as

$$\frac{dr_e}{dt} = \frac{10^{18} C_1 f_{liq}^{\ 3}}{4\pi r_e^{\ 2}} \tag{3.75}$$

The constant C_1 is 4.22×10^{-13}, and: $f_{liq} = w_{liq} / (w_{liq} + w_{ice})$ (section 7.2).

In cases where snow mass is greater than zero, but a snow layer has not yet been defined, r_e is set to $r_{e,0}$. When snow layers are combined or divided, r_e is calculated as a mass-weighted mean of the two layers, following computations of other state variables (section 7.2.7). Finally, the allowable range of r_e, corresponding to the range over which Mie optical properties have been defined, is 30-1500μm.

3.3 Solar Zenith Angle

The CLM uses the same formulation for solar zenith angle as the Community Atmosphere Model. The cosine of the solar zenith angle μ is

$$\mu = \sin\phi \sin\delta - \cos\phi \cos\delta \cos h \tag{3.76}$$

where h is the solar hour angle (radians) (24 hour periodicity), δ is the solar declination angle (radians), and ϕ is latitude (radians) (positive in Northern Hemisphere). The solar hour angle h (radians) is

$$h = 2\pi d + \theta \tag{3.77}$$

where d is calendar day ($d = 0.0$ at 0Z on January 1), and θ is longitude (radians) (positive east of the Greenwich meridian).

The solar declination angle δ is calculated as in Berger (1978a,b) and is valid for one million years past or hence, relative to 1950 A.D. The orbital parameters may be specified directly or the orbital parameters are calculated for the desired year. The required orbital parameters to be input by the user are the obliquity of the Earth ε (degrees, $-90^\circ < \varepsilon < 90^\circ$), Earth's eccentricity e ($0.0 < e < 0.1$), and the longitude of the perihelion relative to the moving vernal equinox $\tilde{\omega}$ ($0^\circ < \tilde{\omega} < 360^\circ$) (unadjusted for the apparent orbit of the Sun around the Earth (Berger et al. 1993)). The solar declination δ (radians) is

$$\delta = \sin^{-1}\left[\sin(\varepsilon)\sin(\lambda)\right] \tag{3.78}$$

where ε is Earth's obliquity and λ is the true longitude of the Earth.

The obliquity of the Earth ε (degrees) is

$$\varepsilon = \varepsilon^* + \sum_{i=1}^{i=47} A_i \cos\left(f_i t + \delta_i\right) \tag{3.79}$$

where ε^* is a constant of integration (Table 3.8), A_i, f_i, and δ_i are amplitude, mean rate, and phase terms in the cosine series expansion (Berger 1978a,b), and $t = t_0 - 1950$ where t_0 is the year. The series expansion terms are not shown here but can be found in the source code file shr_orb_mod.F90.

The true longitude of the Earth λ (radians) is counted counterclockwise from the vernal equinox ($\lambda = 0$ at the vernal equinox)

$$\lambda = \lambda_m + \left(2e - \frac{1}{4}e^3\right)\sin\left(\lambda_m - \tilde{\omega}\right) + \frac{5}{4}e^2 \sin 2\left(\lambda_m - \tilde{\omega}\right) + \frac{13}{12}e^3 \sin 3\left(\lambda_m - \tilde{\omega}\right) \tag{3.80}$$

where λ_m is the mean longitude of the Earth at the vernal equinox, e is Earth's eccentricity, and $\tilde{\omega}$ is the longitude of the perihelion relative to the moving vernal equinox. The mean longitude λ_m is

$$\lambda_m = \lambda_{m0} + \frac{2\pi\left(d - d_{ve}\right)}{365} \tag{3.81}$$

where $d_{ve} = 80.5$ is the calendar day at vernal equinox (March 21 at noon), and

$$\lambda_{m0} = 2\left[\left(\frac{1}{2}e + \frac{1}{8}e^3\right)\left(1+\beta\right)\sin\tilde{\omega} - \frac{1}{4}e^2\left(\frac{1}{2}+\beta\right)\sin 2\tilde{\omega} + \frac{1}{8}e^3\left(\frac{1}{3}+\beta\right)\sin 3\tilde{\omega}\right] \tag{3.82}$$

where $\beta = \sqrt{1-e^2}$. Earth's eccentricity e is

$$e = \sqrt{\left(e^{\cos}\right)^2 + \left(e^{\sin}\right)^2} \qquad (3.83)$$

where

$$\begin{aligned} e^{\cos} &= \sum_{j=1}^{19} M_j \cos\left(g_j t + B_j\right), \\ e^{\sin} &= \sum_{j=1}^{19} M_j \sin\left(g_j t + B_j\right) \end{aligned} \qquad (3.84)$$

are the cosine and sine series expansions for e, and M_j, g_j, and B_j are amplitude, mean rate, and phase terms in the series expansions (Berger 1978a,b). The longitude of the perihelion relative to the moving vernal equinox $\tilde{\omega}$ (degrees) is

$$\tilde{\omega} = \Pi \frac{180}{\pi} + \psi \qquad (3.85)$$

where Π is the longitude of the perihelion measured from the reference vernal equinox (i.e., the vernal equinox at 1950 A.D.) and describes the absolute motion of the perihelion relative to the fixed stars, and ψ is the annual general precession in longitude and describes the absolute motion of the vernal equinox along Earth's orbit relative to the fixed stars. The general precession ψ (degrees) is

$$\psi = \frac{\tilde{\psi} t}{3600} + \zeta + \sum_{i=1}^{78} F_i \sin\left(f_i' t + \delta_i'\right) \qquad (3.86)$$

where $\tilde{\psi}$ (arcseconds) and ζ (degrees) are constants (Table 3.8), and F_i, f_i', and δ_i' are amplitude, mean rate, and phase terms in the sine series expansion (Berger 1978a,b). The longitude of the perihelion Π (radians) depends on the sine and cosine series expansions for the eccentricity e as follows:

$$\Pi = \begin{cases} 0 & \text{for } -1\times10^{-8} \le e^{\cos} \le 1\times10^{-8} \text{ and } e^{\sin} = 0 \\ 1.5\pi & \text{for } -1\times10^{-8} \le e^{\cos} \le 1\times10^{-8} \text{ and } e^{\sin} < 0 \\ 0.5\pi & \text{for } -1\times10^{-8} \le e^{\cos} \le 1\times10^{-8} \text{ and } e^{\sin} > 0 \\ \tan^{-1}\left[\dfrac{e^{\sin}}{e^{\cos}}\right] + \pi & \text{for } e^{\cos} < -1\times10^{-8} \\ \tan^{-1}\left[\dfrac{e^{\sin}}{e^{\cos}}\right] + 2\pi & \text{for } e^{\cos} > 1\times10^{-8} \text{ and } e^{\sin} < 0 \\ \tan^{-1}\left[\dfrac{e^{\sin}}{e^{\cos}}\right] & \text{for } e^{\cos} > 1\times10^{-8} \text{ and } e^{\sin} \ge 0 \end{cases}. \quad (3.87)$$

The numerical solution for the longitude of the perihelion $\tilde{\omega}$ is constrained to be between 0 and 360 degrees (measured from the autumn equinox). A constant 180 degrees is then added to $\tilde{\omega}$ because the Sun is considered as revolving around the Earth (geocentric coordinate system) (Berger et al. 1993).

Table 3.8. Orbital parameters

Parameter	
ε *	23.320556
$\tilde{\psi}$ (arcseconds)	50.439273
ζ (degrees)	3.392506

4. Radiative Fluxes

The net radiation at the surface is $\left(\vec{S}_v + \vec{S}_g\right) - \left(\vec{L}_v + \vec{L}_g\right)$, where $\vec{S}$ is the net solar flux absorbed by the vegetation ("v") and the ground ("g") and $\vec{L}$ is the net longwave flux (positive toward the atmosphere) (W m^{-2}).

4.1 Solar Fluxes

Figure 4.1 illustrates the direct beam and diffuse fluxes in the canopy. $I\uparrow_\Lambda^\mu$ and $I\uparrow_\Lambda$ are the upward diffuse fluxes, per unit incident direct beam and diffuse flux (section 3.1). $I\downarrow_\Lambda^\mu$ and $I\downarrow_\Lambda$ are the downward diffuse fluxes below the vegetation per unit incident direct beam and diffuse radiation (section 3.1). The direct beam flux transmitted through the canopy, per unit incident flux, is $e^{-K(L+S)}$. $\vec{I}_\Lambda^\mu$ and $\vec{I}_\Lambda$ are the fluxes absorbed by the vegetation, per unit incident direct beam and diffuse radiation (section 3.1). $\alpha_{g,\Lambda}^\mu$ and $\alpha_{g,\Lambda}$ are the direct beam and diffuse ground albedos (section 3.2). L and S are the exposed leaf area index and stem area index (section 2.1.4). K is the optical depth of direct beam per unit leaf and stem area (section 3.1).

Figure 4.1. Schematic diagram of (a) direct beam radiation, (b) diffuse solar radiation, and (c) longwave radiation absorbed, transmitted, and reflected by vegetation and ground. For clarity, terms involving $T^{n+1} - T^n$ are not shown in (c).

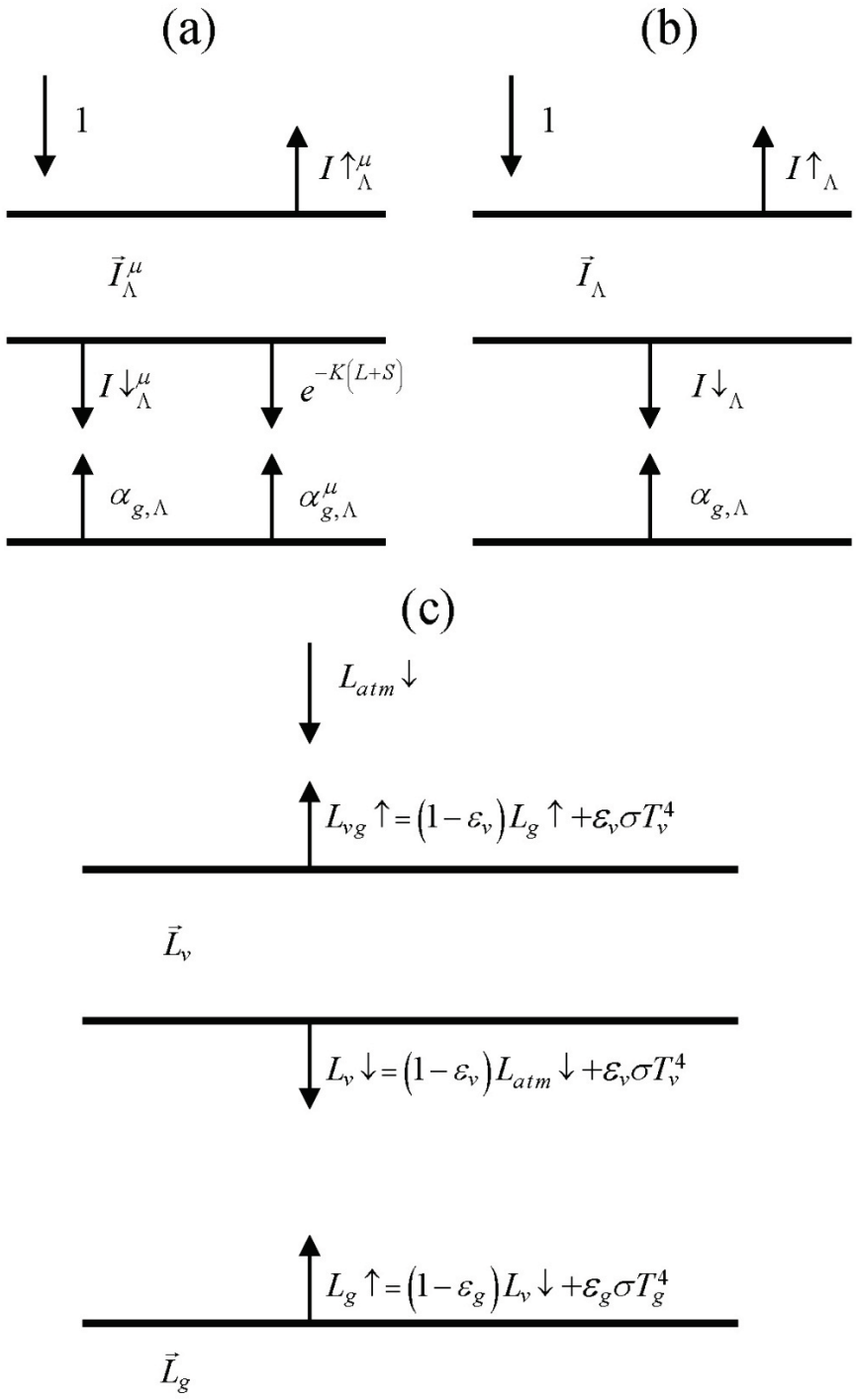

The total solar radiation absorbed by the vegetation and ground is

$$\vec{S}_v = \sum_{\Lambda} S_{atm}\downarrow^{\mu}_{\Lambda}\ \vec{I}^{\mu}_{\Lambda} + S_{atm}\downarrow_{\Lambda}\ \vec{I}_{\Lambda} \tag{4.1}$$

$$\begin{aligned}\vec{S}_g = &\sum_{\Lambda} S_{atm}\downarrow^{\mu}_{\Lambda}\ e^{-K(L+S)}\left(1-\alpha^{\mu}_{g,\Lambda}\right)+\\ &\left(S_{atm}\downarrow^{\mu}_{\Lambda}\ I\downarrow^{\mu}_{\Lambda} + S_{atm}\downarrow_{\Lambda}\ I\downarrow_{\Lambda}\right)\left(1-\alpha_{g,\Lambda}\right)\end{aligned} \tag{4.2}$$

where $S_{atm}\downarrow^{\mu}_{\Lambda}$ and $S_{atm}\downarrow_{\Lambda}$ are the incident direct beam and diffuse solar fluxes (W m^{-2}).

For non-vegetated surfaces, $e^{-K(L+S)} = 1$, $\vec{I}^{\mu}_{\Lambda} = \vec{I}_{\Lambda} = 0$, $I\downarrow^{\mu}_{\Lambda} = 0$, and $I\downarrow_{\Lambda} = 1$, so that

$$\begin{aligned}\vec{S}_g &= \sum_{\Lambda} S_{atm}\downarrow^{\mu}_{\Lambda}\left(1-\alpha^{\mu}_{g,\Lambda}\right) + S_{atm}\downarrow_{\Lambda}\left(1-\alpha_{g,\Lambda}\right)\\ \vec{S}_v &= 0\end{aligned}. \tag{4.3}$$

Solar radiation is conserved as

$$\sum_{\Lambda}\left(S_{atm}\downarrow^{\mu}_{\Lambda} + S_{atm}\downarrow_{\Lambda}\right) = \left(\vec{S}_v + \vec{S}_g\right) + \sum_{\Lambda}\left(S_{atm}\downarrow^{\mu}_{\Lambda}\ I\uparrow^{\mu}_{\Lambda} + S_{atm}\downarrow_{\Lambda}\ I\uparrow_{\Lambda}\right) \tag{4.4}$$

where the latter term in parentheses is reflected solar radiation.

Photosynthesis and transpiration depend non-linearly on solar radiation, via the light response of stomata. The canopy is treated as two leaves (sunlit and shaded) and the solar radiation in the visible waveband (< 0.7 μm) absorbed by the vegetation is apportioned to the sunlit and shaded leaves (section 3.1). The absorbed photosynthetically active (visible waveband) radiation averaged over the sunlit canopy (per unit plant area) is

$$\phi^{sun} = \left(\vec{I}^{\mu}_{sun,vis} S_{atm}\downarrow^{\mu}_{vis} + \vec{I}_{sun,vis} S_{atm}\downarrow_{vis}\right)\Big/ L^{sun} \tag{4.5}$$

and the absorbed radiation for the average shaded leaf (per unit plant area) is

$$\phi^{sha} = \left(\vec{I}^{\mu}_{sha,vis} S_{atm}\downarrow^{\mu}_{vis} + \vec{I}_{sha,vis} S_{atm}\downarrow_{vis}\right)\Big/ L^{sha} \tag{4.6}$$

with L^{sun} and L^{sha} the sunlit and shaded plant area index, respectively. The sunlit plant area index is

$$L^{sun} = \frac{1 - e^{-K(L+S)}}{K} \tag{4.7}$$

and the shaded leaf area index is $L^{sha} = (L+S) - L^{sun}$. In calculating L^{sun},

$$K = \frac{G(\mu)}{\mu} \tag{4.8}$$

where $G(\mu)$ and μ are parameters in the two-stream approximation (section 3.1).

The model uses the two-stream approximation to calculate radiative transfer of direct and diffuse radiation through a canopy that is differentiated into leaves that are sunlit and those that are shaded (section 3.1). The two-stream equations are integrated over all plant area (leaf and stem area) in the canopy. The model has an optional (though not supported) multi-layer canopy, as described by Bonan et al. (2012). The multi-layer model is only intended to address the non-linearity of light profiles, photosynthesis, and stomatal conductance in the plant canopy.

In the multi-layer canopy, canopy-integrated radiative fluxes are calculated from the two-stream approximation. The model additionally derives the light profile with depth in the canopy by taking the derivatives of the absorbed radiative fluxes with respect to plant area index ($L' = L + S$) and evaluating them incrementally through the canopy with cumulative plant area index (x). The terms $d\vec{I}^{\mu}_{sun,\Lambda}(x)/dL'$ and $d\vec{I}_{sun,\Lambda}(x)/dL'$ are the direct beam and diffuse solar radiation, respectively, absorbed by the sunlit fraction of the canopy (per unit plant area) at a depth defined by the cumulative plant area index x; $d\vec{I}^{\mu}_{sha,\Lambda}(x)/dL'$ and $d\vec{I}_{sha,\Lambda}(x)/dL'$ are the corresponding fluxes for the shaded fraction of

the canopy at depth x. These fluxes are normalized by the sunlit or shaded fraction at depth x, defined by $f_{sun} = \exp(-Kx)$, to give fluxes per unit sunlit or shaded plant area at depth x.

4.2 Longwave Fluxes

The net longwave radiation (W m^{-2}) (positive toward the atmosphere) at the surface is

$$\vec{L} = L\uparrow - L_{atm}\downarrow \tag{4.9}$$

where $L\uparrow$ is the upward longwave radiation from the surface and $L_{atm}\downarrow$ is the downward atmospheric longwave radiation (W m^{-2}). The radiative temperature T_{rad} (K) is defined from the upward longwave radiation as

$$T_{rad} = \left(\frac{L\uparrow}{\sigma}\right)^{1/4} \tag{4.10}$$

where σ is the Stefan-Boltzmann constant (W m^{-2} K^{-4}) (Table 2.6). With reference to Figure 4.1, the upward longwave radiation from the surface to the atmosphere is

$$\begin{aligned} L\uparrow = {} & \delta_{veg} L_{vg}\uparrow + \left(1-\delta_{veg}\right)\left(1-\varepsilon_g\right) L_{atm}\downarrow + \\ & \left(1-\delta_{veg}\right)\varepsilon_g \sigma \left(T_g^n\right)^4 + 4\varepsilon_g \sigma \left(T_g^n\right)^3 \left(T_g^{n+1} - T_g^n\right) \end{aligned} \tag{4.11}$$

where $L_{vg}\uparrow$ is the upward longwave radiation from the vegetation/soil system for exposed leaf and stem area $L + S \geq 0.05$, δ_{veg} is a step function and is zero for $L + S < 0.05$ and one otherwise, ε_g is the ground emissivity, and T_g^{n+1} and T_g^n are the snow/soil surface temperatures at the current and previous time steps, respectively (Chapter 6).

For non-vegetated surfaces, the above equation reduces to

$$L\uparrow = \left(1-\varepsilon_g\right)L_{atm}\downarrow + \varepsilon_g\sigma\left(T_g^n\right)^4 + 4\varepsilon_g\sigma\left(T_g^n\right)^3\left(T_g^{n+1}-T_g^n\right) \tag{4.12}$$

where the first term is the atmospheric longwave radiation reflected by the ground, the second term is the longwave radiation emitted by the ground, and the last term is the increase (decrease) in longwave radiation emitted by the ground due to an increase (decrease) in ground temperature.

For vegetated surfaces, the upward longwave radiation from the surface reduces to

$$L\uparrow = L_{vg}\uparrow + 4\varepsilon_g\sigma\left(T_g^n\right)^3\left(T_g^{n+1}-T_g^n\right) \tag{4.13}$$

where

$$\begin{aligned}
L_{vg}\uparrow = {} & \left(1-\varepsilon_g\right)\left(1-\varepsilon_v\right)\left(1-\varepsilon_v\right)L_{atm}\downarrow \\
& + \varepsilon_v\left[1+\left(1-\varepsilon_g\right)\left(1-\varepsilon_v\right)\right]\sigma\left(T_v^n\right)^3\left[T_v^n + 4\left(T_v^{n+1}-T_v^n\right)\right] \\
& + \varepsilon_g\left(1-\varepsilon_v\right)\sigma\left(T_g^n\right)^4 \\
= {} & \left(1-\varepsilon_g\right)\left(1-\varepsilon_v\right)\left(1-\varepsilon_v\right)L_{atm}\downarrow \\
& + \varepsilon_v\sigma\left(T_v^n\right)^4 \\
& + \varepsilon_v\left(1-\varepsilon_g\right)\left(1-\varepsilon_v\right)\sigma\left(T_v^n\right)^4 \\
& + 4\varepsilon_v\sigma\left(T_v^n\right)^3\left(T_v^{n+1}-T_v^n\right) \\
& + 4\varepsilon_v\left(1-\varepsilon_g\right)\left(1-\varepsilon_v\right)\sigma\left(T_v^n\right)^3\left(T_v^{n+1}-T_v^n\right) \\
& + \varepsilon_g\left(1-\varepsilon_v\right)\sigma\left(T_g^n\right)^4
\end{aligned} \tag{4.14}$$

where ε_v is the vegetation emissivity and T_v^{n+1} and T_v^n are the vegetation temperatures at the current and previous time steps, respectively (Chapter 5). The first term in the equation above is the atmospheric longwave radiation that is transmitted through the canopy, reflected by the ground, and transmitted through the canopy to the atmosphere. The second term is the longwave radiation emitted by the canopy directly to the atmosphere. The third term is the longwave radiation emitted downward from the

canopy, reflected by the ground, and transmitted through the canopy to the atmosphere. The fourth term is the increase (decrease) in longwave radiation due to an increase (decrease) in canopy temperature that is emitted by the canopy directly to the atmosphere. The fifth term is the increase (decrease) in longwave radiation due to an increase (decrease) in canopy temperature that is emitted downward from the canopy, reflected from the ground, and transmitted through the canopy to the atmosphere. The last term is the longwave radiation emitted by the ground and transmitted through the canopy to the atmosphere.

The upward longwave radiation from the ground is

$$L_g \uparrow = \left(1-\varepsilon_g\right) L_v \downarrow + \varepsilon_g \sigma \left(T_g^n\right)^4 \tag{4.15}$$

where $L_v \downarrow$ is the downward longwave radiation below the vegetation

$$L_v \downarrow = \left(1-\varepsilon_v\right) L_{atm} \downarrow + \varepsilon_v \sigma \left(T_v^n\right)^4 + 4\varepsilon_v \sigma \left(T_v^n\right)^3 \left(T_v^{n+1} - T_v^n\right). \tag{4.16}$$

The net longwave radiation flux for the ground is (positive toward the atmosphere)

$$\vec{L}_g = \varepsilon_g \sigma \left(T_g^n\right)^4 - \delta_{veg} \varepsilon_g L_v \downarrow - \left(1-\delta_{veg}\right) \varepsilon_g L_{atm} \downarrow . \tag{4.17}$$

The above expression for $\vec{L}_g$ is the net longwave radiation forcing that is used in the soil temperature calculation (Chapter 6). Once updated soil temperatures have been obtained, the term $4\varepsilon_g \sigma \left(T_g^n\right)^3 \left(T_g^{n+1} - T_g^n\right)$ is added to $\vec{L}_g$ to calculate the ground heat flux (section 5.4)

The net longwave radiation flux for vegetation is (positive toward the atmosphere)

$$\vec{L}_v = \left[2 - \varepsilon_v \left(1-\varepsilon_g\right)\right] \varepsilon_v \sigma \left(T_v\right)^4 - \varepsilon_v \varepsilon_g \sigma \left(T_g^n\right)^4 - \varepsilon_v \left[1 + \left(1-\varepsilon_g\right)\left(1-\varepsilon_v\right)\right] L_{atm} \downarrow . \tag{4.18}$$

These equations assume that absorptivity equals emissivity. The emissivity of the ground is

$$\varepsilon_g = \varepsilon_{soi}\left(1 - f_{sno}\right) + \varepsilon_{sno} f_{sno} \tag{4.19}$$

where $\varepsilon_{soi} = 0.96$ for soil, 0.97 for glacier, and 0.96 for wetland, $\varepsilon_{sno} = 0.97$, and f_{sno} is the fraction of ground covered by snow (section 7.2.1). The vegetation emissivity is

$$\varepsilon_v = 1 - e^{-(L+S)/\overline{\mu}} \tag{4.20}$$

where L and S are the leaf and stem area indices (section 2.1.4) and $\overline{\mu} = 1$ is the average inverse optical depth for longwave radiation.

5. Momentum, Sensible Heat, and Latent Heat Fluxes

The zonal τ_x and meridional τ_y momentum fluxes (kg m^{-1} s^{-2}), sensible heat flux H (W m^{-2}), and water vapor flux E (kg m^{-2} s^{-1}) between the atmosphere at reference height $z_{atm,x}$ (m) [where x is height for wind (momentum) (m), temperature (sensible heat) (h), and humidity (water vapor) (w); with zonal and meridional winds u_{atm} and v_{atm} (m s^{-1}), potential temperature θ_{atm} (K), and specific humidity q_{atm} (kg kg^{-1})] and the surface [with u_s, v_s, θ_s, and q_s] are

$$\tau_x = -\rho_{atm} \frac{\left(u_{atm} - u_s\right)}{r_{am}} \tag{5.1}$$

$$\tau_y = -\rho_{atm} \frac{\left(v_{atm} - v_s\right)}{r_{am}} \tag{5.2}$$

$$H = -\rho_{atm} C_p \frac{\left(\theta_{atm} - \theta_s\right)}{r_{ah}} \tag{5.3}$$

$$E = -\rho_{atm} \frac{\left(q_{atm} - q_s\right)}{r_{aw}}. \tag{5.4}$$

These fluxes are derived in the next section from Monin-Obukhov similarity theory developed for the surface layer (i.e., the nearly constant flux layer above the surface sublayer). In this derivation, u_s and v_s are defined to equal zero at height $z_{0m} + d$ (the apparent sink for momentum) so that r_{am} is the aerodynamic resistance (s m^{-1}) for momentum between the atmosphere at height $z_{atm,m}$ and the surface at height $z_{0m} + d$. Thus, the momentum fluxes become

$$\tau_x = -\rho_{atm} \frac{u_{atm}}{r_{am}} \tag{5.5}$$

$$\tau_y = -\rho_{atm} \frac{v_{atm}}{r_{am}}. \tag{5.6}$$

Likewise, θ_s and q_s are defined at heights $z_{0h} + d$ and $z_{0w} + d$ (the apparent sinks for heat and water vapor, respectively). Consequently, r_{ah} and r_{aw} are the aerodynamic resistances (s m^{-1}) to sensible heat and water vapor transfer between the atmosphere at heights $z_{atm,h}$ and $z_{atm,w}$ and the surface at heights $z_{0h} + d$ and $z_{0w} + d$, respectively. The specific heat capacity of air C_p (J kg^{-1} K^{-1}) is a constant (Table 2.6). The atmospheric potential temperature used here is

$$\theta_{atm} = T_{atm} + \Gamma_d z_{atm,h} \tag{5.7}$$

where T_{atm} is the air temperature (K) at height $z_{atm,h}$ and $\Gamma_d = 0.0098$ K m^{-1} is the negative of the dry adiabatic lapse rate [this expression is first-order equivalent to $\theta_{atm} = T_{atm}\left(P_{srf}/P_{atm}\right)^{R_{da}/C_p}$ (Stull 1988), where P_{srf} is the surface pressure (Pa), P_{atm} is the atmospheric pressure (Pa), and R_{da} is the gas constant for dry air (J kg^{-1} K^{-1}) (Table 2.6)]. By definition, $\theta_s = T_s$. The density of moist air (kg m^{-3}) is

$$\rho_{atm} = \frac{P_{atm} - 0.378 e_{atm}}{R_{da} T_{atm}} \tag{5.8}$$

where the atmospheric vapor pressure e_{atm} (Pa) is derived from the atmospheric specific humidity q_{atm}

$$e_{atm} = \frac{q_{atm} P_{atm}}{0.622 + 0.378 q_{atm}}. \tag{5.9}$$

5.1 Monin-Obukhov Similarity Theory

The surface vertical kinematic fluxes of momentum $\overline{u'w'}$ and $\overline{v'w'}$ (m^2 s^{-2}), sensible heat $\overline{\theta'w'}$ (K m s^{-1}), and latent heat $\overline{q'w'}$ (kg kg^{-1} m s^{-1}), where u', v', w', θ', and q' are zonal horizontal wind, meridional horizontal wind, vertical velocity, potential temperature, and specific humidity turbulent fluctuations about the mean, are defined from Monin-Obukhov similarity applied to the surface layer. This theory states that when scaled appropriately, the dimensionless mean horizontal wind speed, mean potential temperature, and mean specific humidity profile gradients depend on unique functions of $\zeta = \frac{z-d}{L}$ (Zeng et al. 1998) as

$$\frac{k(z-d)}{u_*}\frac{\partial|\boldsymbol{u}|}{\partial z} = \phi_m(\zeta) \tag{5.10}$$

$$\frac{k(z-d)}{\theta_*}\frac{\partial\theta}{\partial z} = \phi_h(\zeta) \tag{5.11}$$

$$\frac{k(z-d)}{q_*}\frac{\partial q}{\partial z} = \phi_w(\zeta) \tag{5.12}$$

where z is height in the surface layer (m), d is the displacement height (m), L is the Monin-Obukhov length scale (m) that accounts for buoyancy effects resulting from vertical density gradients (i.e., the atmospheric stability), k is the von Karman constant (Table 2.6), and $|\boldsymbol{u}|$ is the atmospheric wind speed (m s^{-1}). ϕ_m, ϕ_h, and ϕ_w are universal (over any surface) similarity functions of ζ that relate the constant fluxes of momentum, sensible heat, and latent heat to the mean profile gradients of $|\boldsymbol{u}|$, θ, and q in the surface

layer. In neutral conditions, $\phi_m = \phi_h = \phi_w = 1$. The velocity (i.e., friction velocity) u_* (m s^{-1}), temperature θ_* (K), and moisture q_* (kg kg^{-1}) scales are

$$u_*^2 = \sqrt{\left(\overline{u'w'}\right)^2 + \left(\overline{v'w'}\right)^2} = \frac{|\boldsymbol{\tau}|}{\rho_{atm}} \tag{5.13}$$

$$\theta_* u_* = -\overline{\theta' w'} = -\frac{H}{\rho_{atm} C_p} \tag{5.14}$$

$$q_* u_* = -\overline{q' w'} = -\frac{E}{\rho_{atm}} \tag{5.15}$$

where $|\boldsymbol{\tau}|$ is the shearing stress (kg m^{-1} s^{-2}), with zonal and meridional components $\overline{u'w'} = -\frac{\tau_x}{\rho_{atm}}$ and $\overline{v'w'} = -\frac{\tau_y}{\rho_{atm}}$, respectively, H is the sensible heat flux (W m^{-2}) and E is the water vapor flux (kg m^{-2} s^{-1}).

The dimensionless length scale L is the Monin-Obukhov length defined as

$$L = -\frac{u_*^3}{k\left(\frac{g}{\overline{\theta_{v,atm}}}\right)\theta_v' w'} = \frac{u_*^2 \overline{\theta_{v,atm}}}{kg\theta_{v*}} \tag{5.16}$$

where g is the acceleration of gravity (m s^{-2}) (Table 2.6), and $\overline{\theta_{v,atm}} = \overline{\theta_{atm}}\left(1 + 0.61 q_{atm}\right)$ is the reference virtual potential temperature. $L > 0$ indicates stable conditions. $L < 0$ indicates unstable conditions. $L = \infty$ for neutral conditions. The temperature scale θ_{v*} is defined as

$$\theta_{v*} u_* = \left[\theta_* \left(1 + 0.61 q_{atm}\right) + 0.61 \overline{\theta_{atm}} q_*\right] u_* \tag{5.17}$$

where $\overline{\theta_{atm}}$ is the atmospheric potential temperature.

Following Panofsky and Dutton (1984), the differential equations for $\phi_m(\zeta)$, $\phi_h(\zeta)$, and $\phi_w(\zeta)$ can be integrated formally without commitment to their exact forms. Integration between two arbitrary heights in the surface layer z_2 and z_1 ($z_2 > z_1$) with horizontal winds $|\boldsymbol{u}|_1$ and $|\boldsymbol{u}|_2$, potential temperatures θ_1 and θ_2, and specific humidities q_1 and q_2 results in

$$|\boldsymbol{u}|_2 - |\boldsymbol{u}|_1 = \frac{u_*}{k}\left[\ln\left(\frac{z_2-d}{z_1-d}\right) - \psi_m\left(\frac{z_2-d}{L}\right) + \psi_m\left(\frac{z_1-d}{L}\right)\right] \tag{5.18}$$

$$\theta_2 - \theta_1 = \frac{\theta_*}{k}\left[\ln\left(\frac{z_2-d}{z_1-d}\right) - \psi_h\left(\frac{z_2-d}{L}\right) + \psi_h\left(\frac{z_1-d}{L}\right)\right] \tag{5.19}$$

$$q_2 - q_1 = \frac{q_*}{k}\left[\ln\left(\frac{z_2-d}{z_1-d}\right) - \psi_w\left(\frac{z_2-d}{L}\right) + \psi_w\left(\frac{z_1-d}{L}\right)\right]. \tag{5.20}$$

The functions $\psi_m(\zeta)$, $\psi_h(\zeta)$, and $\psi_w(\zeta)$ are defined as

$$\psi_m(\zeta) = \int_{z_{0m}/L}^{\zeta} \frac{\left[1-\phi_m(x)\right]}{x}\,dx \tag{5.21}$$

$$\psi_h(\zeta) = \int_{z_{0h}/L}^{\zeta} \frac{\left[1-\phi_h(x)\right]}{x}\,dx \tag{5.22}$$

$$\psi_w(\zeta) = \int_{z_{0w}/L}^{\zeta} \frac{\left[1-\phi_w(x)\right]}{x}\,dx \tag{5.23}$$

where z_{0m}, z_{0h}, and z_{0w} are the roughness lengths (m) for momentum, sensible heat, and water vapor, respectively.

Defining the surface values

$$|\boldsymbol{u}|_1 = 0 \text{ at } z_1 = z_{0m} + d,$$

$\theta_1 = \theta_s$ at $z_1 = z_{0h} + d$, and

$q_1 = q_s$ at $z_1 = z_{0w} + d$,

and the atmospheric values at $z_2 = z_{atm,x}$

$$\left|\boldsymbol{u}\right|_2 = V_a = \sqrt{u_{atm}^2 + v_{atm}^2 + U_c^2} \geq 1, \tag{5.24}$$

$\theta_2 = \theta_{atm}$, and

$q_2 = q_{atm}$,

the integral forms of the flux-gradient relations are

$$V_a = \frac{u_*}{k}\left[\ln\left(\frac{z_{atm,m} - d}{z_{0m}}\right) - \psi_m\left(\frac{z_{atm,m} - d}{L}\right) + \psi_m\left(\frac{z_{0m}}{L}\right)\right] \tag{5.25}$$

$$\theta_{atm} - \theta_s = \frac{\theta_*}{k}\left[\ln\left(\frac{z_{atm,h} - d}{z_{0h}}\right) - \psi_h\left(\frac{z_{atm,h} - d}{L}\right) + \psi_h\left(\frac{z_{0h}}{L}\right)\right] \tag{5.26}$$

$$q_{atm} - q_s = \frac{q_*}{k}\left[\ln\left(\frac{z_{atm,w} - d}{z_{0w}}\right) - \psi_w\left(\frac{z_{atm,w} - d}{L}\right) + \psi_w\left(\frac{z_{0w}}{L}\right)\right]. \tag{5.27}$$

The constraint $V_a \geq 1$ is required simply for numerical reasons to prevent H and E from becoming small with small wind speeds. The convective velocity U_c accounts for the contribution of large eddies in the convective boundary layer to surface fluxes as follows

$$\begin{array}{lll} U_c = 0 & \zeta \geq 0 & \text{(stable)} \\ U_c = \beta w_* & \zeta < 0 & \text{(unstable)} \end{array} \tag{5.28}$$

where w_* is the convective velocity scale

$$w_* = \left(\frac{-g u_* \theta_{v*} z_i}{\overline{\theta}_{v,atm}}\right)^{1/3}, \tag{5.29}$$

$z_i = 1000$ is the convective boundary layer height (m), and $\beta = 1$.

The momentum flux gradient relations are (Zeng et al. 1998)

$$\begin{aligned}
&\phi_m(\zeta) = 0.7k^{2/3}(-\zeta)^{1/3} && \text{for } \zeta < -1.574 \text{ (very unstable)} \\
&\phi_m(\zeta) = (1-16\zeta)^{-1/4} && \text{for -1.574} \le \zeta < 0 \text{ (unstable)} \\
&\phi_m(\zeta) = 1+5\zeta && \text{for } 0 \le \zeta \le 1 \text{ (stable)} \\
&\phi_m(\zeta) = 5+\zeta && \text{for } \zeta > 1 \text{ (very stable).}
\end{aligned} \tag{5.30}$$

The sensible and latent heat flux gradient relations are (Zeng et al. 1998)

$$\begin{aligned}
&\phi_h(\zeta) = \phi_w(\zeta) = 0.9k^{4/3}(-\zeta)^{-1/3} && \text{for } \zeta < -0.465 \text{ (very unstable)} \\
&\phi_h(\zeta) = \phi_w(\zeta) = (1-16\zeta)^{-1/2} && \text{for -0.465} \le \zeta < 0 \text{ (unstable)} \\
&\phi_h(\zeta) = \phi_w(\zeta) = 1+5\zeta && \text{for } 0 \le \zeta \le 1 \text{ (stable)} \\
&\phi_h(\zeta) = \phi_w(\zeta) = 5+\zeta && \text{for } \zeta > 1 \text{ (very stable).}
\end{aligned} \tag{5.31}$$

To ensure continuous functions of $\phi_m(\zeta)$, $\phi_h(\zeta)$, and $\phi_w(\zeta)$, the simplest approach (i.e., without considering any transition regimes) is to match the relations for very unstable and unstable conditions at $\zeta_m = -1.574$ for $\phi_m(\zeta)$ and $\zeta_h = \zeta_w = -0.465$ for $\phi_h(\zeta) = \phi_w(\zeta)$ (Zeng et al. 1998). The flux gradient relations can be integrated to yield wind profiles for the following conditions:

Very unstable $(\zeta < -1.574)$

$$V_a = \frac{u_*}{k}\left\{\left[\ln\frac{\zeta_m L}{z_{0m}} - \psi_m(\zeta_m)\right] + 1.14\left[(-\zeta)^{1/3} - (-\zeta_m)^{1/3}\right] + \psi_m\left(\frac{z_{0m}}{L}\right)\right\} \tag{5.32}$$

Unstable $(-1.574 \le \zeta < 0)$

$$V_a = \frac{u_*}{k}\left\{\left[\ln\frac{z_{atm,m} - d}{z_{0m}} - \psi_m(\zeta)\right] + \psi_m\left(\frac{z_{0m}}{L}\right)\right\} \tag{5.33}$$

Stable $(0 \le \zeta \le 1)$

$$V_a = \frac{u_*}{k}\left\{\left[\ln\frac{z_{atm,m}-d}{z_{0m}} + 5\zeta\right] - 5\frac{z_{0m}}{L}\right\} \tag{5.34}$$

Very stable $(\zeta > 1)$

$$V_a = \frac{u_*}{k}\left\{\left[\ln\frac{L}{z_{0m}} + 5\right] + \left[5\ln\zeta + \zeta - 1\right] - 5\frac{z_{0m}}{L}\right\} \tag{5.35}$$

where

$$\psi_m(\zeta) = 2\ln\left(\frac{1+x}{2}\right) + \ln\left(\frac{1+x^2}{2}\right) - 2\tan^{-1}x + \frac{\pi}{2} \tag{5.36}$$

and $x = (1-16\zeta)^{1/4}$.

The potential temperature profiles are:

Very unstable $(\zeta < -0.465)$

$$\theta_{atm} - \theta_s = \frac{\theta_*}{k}\left\{\left[\ln\frac{\zeta_h L}{z_{0h}} - \psi_h(\zeta_h)\right] + 0.8\left[(-\zeta_h)^{-1/3} - (-\zeta)^{-1/3}\right] + \psi_h\left(\frac{z_{0h}}{L}\right)\right\} \tag{5.37}$$

Unstable $(-0.465 \le \zeta < 0)$

$$\theta_{atm} - \theta_s = \frac{\theta_*}{k}\left\{\left[\ln\frac{z_{atm,h}-d}{z_{0h}} - \psi_h(\zeta)\right] + \psi_h\left(\frac{z_{0h}}{L}\right)\right\} \tag{5.38}$$

Stable $(0 \le \zeta \le 1)$

$$\theta_{atm} - \theta_s = \frac{\theta_*}{k}\left\{\left[\ln\frac{z_{atm,h}-d}{z_{0h}} + 5\zeta\right] - 5\frac{z_{0h}}{L}\right\} \tag{5.39}$$

Very stable $(\zeta > 1)$

$$\theta_{atm} - \theta_s = \frac{\theta_*}{k}\left\{\left[\ln\frac{L}{z_{0h}} + 5\right] + \left[5\ln\zeta + \zeta - 1\right] - 5\frac{z_{0h}}{L}\right\}. \tag{5.40}$$

The specific humidity profiles are:

Very unstable $\left(\zeta < -0.465\right)$

$$q_{atm} - q_s = \frac{q_*}{k}\left\{\left[\ln\frac{\zeta_w L}{z_{0w}} - \psi_w\left(\zeta_w\right)\right] + 0.8\left[\left(-\zeta_w\right)^{-1/3} - \left(-\zeta\right)^{-1/3}\right] + \psi_w\left(\frac{z_{0w}}{L}\right)\right\} \tag{5.41}$$

Unstable $\left(-0.465 \le \zeta < 0\right)$

$$q_{atm} - q_s = \frac{q_*}{k}\left\{\left[\ln\frac{z_{atm,w} - d}{z_{0w}} - \psi_w\left(\zeta\right)\right] + \psi_w\left(\frac{z_{0w}}{L}\right)\right\} \tag{5.42}$$

Stable $\left(0 \le \zeta \le 1\right)$

$$q_{atm} - q_s = \frac{q_*}{k}\left\{\left[\ln\frac{z_{atm,w} - d}{z_{0w}} + 5\zeta\right] - 5\frac{z_{0w}}{L}\right\} \tag{5.43}$$

Very stable $\left(\zeta > 1\right)$

$$q_{atm} - q_s = \frac{q_*}{k}\left\{\left[\ln\frac{L}{z_{0w}} + 5\right] + \left[5\ln\zeta + \zeta - 1\right] - 5\frac{z_{0w}}{L}\right\} \tag{5.44}$$

where

$$\psi_h\left(\zeta\right) = \psi_w\left(\zeta\right) = 2\ln\left(\frac{1+x^2}{2}\right). \tag{5.45}$$

Using the definitions of u_*, θ_*, and q_*, an iterative solution of these equations can be used to calculate the surface momentum, sensible heat, and water vapor flux using atmospheric and surface values for $\left|\boldsymbol{u}\right|$, θ, and q except that L depends on u_*, θ_*, and q_*. However, the bulk Richardson number

$$R_{iB} = \frac{\theta_{v,atm} - \theta_{v,s}}{\overline{\theta_{v,atm}}} \frac{g\left(z_{atm,m} - d\right)}{V_a^2} \tag{5.46}$$

is related to ζ (Arya 2001) as

$$R_{iB} = \zeta \left[\ln\left(\frac{z_{atm,h} - d}{z_{0h}} \right) - \psi_h(\zeta) \right] \left[\ln\left(\frac{z_{atm,m} - d}{z_{0m}} \right) - \psi_m(\zeta) \right]^{-2}. \tag{5.47}$$

Using $\phi_h = \phi_m^2 = \left(1 - 16\zeta\right)^{-1/2}$ for unstable conditions and $\phi_h = \phi_m = 1 + 5\zeta$ for stable conditions to determine $\psi_m(\zeta)$ and $\psi_h(\zeta)$, the inverse relationship $\zeta = f\left(R_{iB}\right)$ can be solved to obtain a first guess for ζ and thus L from

$$\begin{aligned} \zeta &= \frac{R_{iB} \ln\left(\dfrac{z_{atm,m} - d}{z_{0m}} \right)}{1 - 5\min\left(R_{iB}, 0.19\right)} && 0.01 \le \zeta \le 2 && \text{for } R_{iB} \ge 0 \text{ (neutral or stable)} \\ \zeta &= R_{iB} \ln\left(\frac{z_{atm,m} - d}{z_{0m}} \right) && -100 \le \zeta \le -0.01 && \text{for } R_{iB} < 0 \text{ (unstable)} \end{aligned} . \tag{5.48}$$

Upon iteration (section 5.3.2), the following is used to determine ζ and thus L

$$\zeta = \frac{\left(z_{atm,m} - d\right) kg\theta_{v*}}{u_*^2 \overline{\theta_{v,atm}}} \tag{5.49}$$

where

$$\begin{aligned} &0.01 \le \zeta \le 2 && \text{for } \zeta \ge 0 \text{ (neutral or stable)} \\ &-100 \le \zeta \le -0.01 && \text{for } \zeta < 0 \text{ (unstable)} \end{aligned} .$$

The difference in virtual potential air temperature between the reference height and the surface is

$$\theta_{v,atm} - \theta_{v,s} = \left(\theta_{atm} - \theta_s\right)\left(1 + 0.61 q_{atm}\right) + 0.61 \overline{\theta_{atm}} \left(q_{atm} - q_s\right). \tag{5.50}$$

The momentum, sensible heat, and water vapor fluxes between the surface and the atmosphere can also be written in the form

$$\tau_x = -\rho_{atm} \frac{\left(u_{atm} - u_s\right)}{r_{am}} \tag{5.51}$$

$$\tau_y = -\rho_{atm} \frac{\left(v_{atm} - v_s\right)}{r_{am}} \tag{5.52}$$

$$H = -\rho_{atm} C_p \frac{\left(\theta_{atm} - \theta_s\right)}{r_{ah}} \tag{5.53}$$

$$E = -\rho_{atm} \frac{\left(q_{atm} - q_s\right)}{r_{aw}} \tag{5.54}$$

where the aerodynamic resistances (s m^{-1}) are

$$r_{am} = \frac{V_a}{u_*^2} = \frac{1}{k^2 V_a}\left[\ln\left(\frac{z_{atm,m} - d}{z_{0m}}\right) - \psi_m\left(\frac{z_{atm,m} - d}{L}\right) + \psi_m\left(\frac{z_{0m}}{L}\right)\right]^2 \tag{5.55}$$

$$r_{ah} = \frac{\theta_{atm} - \theta_s}{\theta_* u_*} = \frac{1}{k^2 V_a}\left[\ln\left(\frac{z_{atm,m} - d}{z_{0m}}\right) - \psi_m\left(\frac{z_{atm,m} - d}{L}\right) + \psi_m\left(\frac{z_{0m}}{L}\right)\right] \left[\ln\left(\frac{z_{atm,h} - d}{z_{0h}}\right) - \psi_h\left(\frac{z_{atm,h} - d}{L}\right) + \psi_h\left(\frac{z_{0h}}{L}\right)\right] \tag{5.56}$$

$$r_{aw} = \frac{q_{atm} - q_s}{q_* u_*} = \frac{1}{k^2 V_a}\left[\ln\left(\frac{z_{atm,m} - d}{z_{0m}}\right) - \psi_m\left(\frac{z_{atm,m} - d}{L}\right) + \psi_m\left(\frac{z_{0m}}{L}\right)\right] \left[\ln\left(\frac{z_{atm,w} - d}{z_{0w}}\right) - \psi_w\left(\frac{z_{atm,w} - d}{L}\right) + \psi_w\left(\frac{z_{0w}}{L}\right)\right]. \tag{5.57}$$

A 2-m height "screen" temperature is useful for comparison with observations

$$T_{2m} = \theta_s + \frac{\theta_*}{k}\left[\ln\left(\frac{2 + z_{0h}}{z_{0h}}\right) - \psi_h\left(\frac{2 + z_{0h}}{L}\right) + \psi_h\left(\frac{z_{0h}}{L}\right)\right] \tag{5.58}$$

where for convenience, "2-m" is defined as 2 m above the apparent sink for sensible heat ($z_{0h} + d$). Similarly, a 2-m height specific humidity is defined as

$$q_{2m} = q_s + \frac{q_*}{k}\left[\ln\left(\frac{2+z_{0w}}{z_{0w}}\right) - \psi_w\left(\frac{2+z_{0w}}{L}\right) + \psi_w\left(\frac{z_{0w}}{L}\right)\right]. \quad (5.59)$$

Relative humidity is

$$RH_{2m} = \min\left(100, \frac{q_{2m}}{q_{sat}^{T_{2m}}} \times 100\right) \quad (5.60)$$

where $q_{sat}^{T_{2m}}$ is the saturated specific humidity at the 2-m temperature T_{2m} (section 5.5).

A 10-m wind speed is calculated as (note that this is not consistent with the 10-m wind speed calculated for the dust model as described in Chapter 24)

$$u_{10m} = \begin{cases} V_a & z_{atm,m} \le 10 \\ V_a - \frac{u_*}{k}\left[\ln\left(\frac{z_{atm,m}-d}{10+z_{0m}}\right) - \psi_m\left(\frac{z_{atm,m}-d}{L}\right) + \psi_m\left(\frac{10+z_{0m}}{L}\right)\right] & z_{atm,m} > 10 \end{cases} \quad (5.61)$$

5.2 Sensible and Latent Heat Fluxes for Non-Vegetated Surfaces

Surfaces are considered non-vegetated for the surface flux calculations if leaf plus stem area index $L + S < 0.05$ (section 2.1.4). By definition, this includes bare soil, wetlands, and glaciers. The solution for lakes is described in Chapter 9. For these surfaces, the surface may be exposed to the atmosphere, snow covered, and/or surface water covered, so that the sensible heat flux H_g (W m^{-2}) is, with reference to Figure 5.1,

$$H_g = \left(1 - f_{sno} - f_{h2osfc}\right) H_{soil} + f_{sno} H_{snow} + f_{h2osfc} H_{h2osfc} \quad (5.62)$$

where $\left(1 - f_{sno} - f_{h2osfc}\right)$, f_{sno}, and f_{h2osfc} are the exposed, snow covered, and surface water covered fractions of the grid cell. The individual fluxes based on the temperatures of the soil T_1, snow T_{snl+1}, and surface water T_{h2osfc} are

$$H_{soil} = -\rho_{atm} C_p \frac{\left(\theta_{atm} - T_1\right)}{r_{ah}} \tag{5.63}$$

$$H_{sno} = -\rho_{atm} C_p \frac{\left(\theta_{atm} - T_{snl+1}\right)}{r_{ah}} \tag{5.64}$$

$$H_{h2osfc} = -\rho_{atm} C_p \frac{\left(\theta_{atm} - T_{h2osfc}\right)}{r_{ah}} \tag{5.65}$$

where ρ_{atm} is the density of atmospheric air (kg m^{-3}), C_p is the specific heat capacity of air (J kg^{-1} K^{-1}) (Table 2.6), θ_{atm} is the atmospheric potential temperature (K), and r_{ah} is the aerodynamic resistance to sensible heat transfer (s m^{-1}).

The water vapor flux E_g (kg m^{-2} s^{-1}) is, with reference to Figure 5.2,

$$E_g = \left(1 - f_{sno} - f_{h2osfc}\right) E_{soil} + f_{sno} E_{snow} + f_{h2osfc} E_{h2osfc} \tag{5.66}$$

$$E_{soil} = -\frac{\beta_{soi} \rho_{atm} \left(q_{atm} - q_{soil}\right)}{r_{aw}} \tag{5.67}$$

$$E_{sno} = -\frac{\rho_{atm} \left(q_{atm} - q_{sno}\right)}{r_{aw}} \tag{5.68}$$

$$E_{h2osfc} = -\frac{\rho_{atm} \left(q_{atm} - q_{h2osfc}\right)}{r_{aw}} \tag{5.69}$$

where β_{soi} is an empirical function of soil water (Sakaguchi and Zeng 2009), q_{atm} is the atmospheric specific humidity (kg kg^{-1}), q_{soil}, q_{sno}, and q_{h2osfc} are the specific humidities (kg kg^{-1}) of the soil, snow, and surface water, respectively, and r_{aw} is the aerodynamic resistance to water vapor transfer (s m^{-1}). The specific humidities of the snow q_{sno} and surface water q_{h2osfc} are assumed to be at the saturation specific humidity of their respective temperatures

$$q_{sno} = q_{sat}^{T_{snl+1}} \tag{5.70}$$

$$q_{h2osfc} = q_{sat}^{T_{h2osfc}} \tag{5.71}$$

The specific humidity of the soil surface q_{soil} is assumed to be proportional to the saturation specific humidity

$$q_{soil} = \alpha_{soil} q_{sat}^{T_1} \tag{5.72}$$

where $q_{sat}^{T_1}$ is the saturated specific humidity at the soil surface temperature T_1 (section 5.5). The factor α_{soil} is a function of the surface soil water matric potential ψ as in Philip (1957)

$$\alpha_{soil} = \exp\left(\frac{\psi_1 g}{1\times10^3 R_{wv} T_1}\right) \tag{5.73}$$

where R_{wv} is the gas constant for water vapor (J kg^{-1} K^{-1}) (Table 2.6), g is the gravitational acceleration (m s^{-2}) (Table 2.6), and ψ_1 is the soil water matric potential of the top soil layer (mm). The soil water matric potential ψ_1 is

$$\psi_1 = \psi_{sat,1} s_1^{-B_1} \geq -1\times10^8 \tag{5.74}$$

where $\psi_{sat,1}$ is the saturated matric potential (mm) (section 7.4.1), B_1 is the Clapp and Hornberger (1978) parameter (section 7.4.1), and s_1 is the wetness of the top soil layer with respect to saturation. The surface wetness s_1 is a function of the liquid water and ice content

$$s_1 = \frac{1}{\Delta z_1 \theta_{sat,1}}\left[\frac{w_{liq,1}}{\rho_{liq}} + \frac{w_{ice,1}}{\rho_{ice}}\right] \qquad 0.01 \leq s_1 \leq 1.0 \tag{5.75}$$

where Δz_1 is the thickness of the top soil layer (m), ρ_{liq} and ρ_{ice} are the density of liquid water and ice (kg m^{-3}) (Table 2.6), $w_{liq,1}$ and $w_{ice,1}$ are the mass of liquid water and ice of the top soil layer (kg m^{-2}) (Chapter 7), and $\theta_{sat,1}$ is the saturated volumetric water content (i.e., porosity) of the top soil layer (mm^3 mm^{-3}) (section 7.4.1). If $q_{sat}^{T_1} > q_{atm}$ and $q_{atm} > q_{soil}$, then $q_{soil} = q_{atm}$ and $\frac{dq_{soil}}{dT} = 0$. This prevents large increases (decreases) in q_{soil} for small increases (decreases) in soil moisture in very dry soils.

The function β_{soi} ranges from 0 to 1 and is intended to represent the molecular diffusion process from the soil pore to the surface within the dry part of the soil (Sakaguchi and Zeng 2009) as

$$\beta_{soi} = \begin{cases} 1 & \theta_1 \geq \theta_{fc,1} \text{ or } q_{atm} - q_{soil} > 0 \\ 0.25\left(1 - f_{sno} - f_{h2osfc}\right)\left[1 - \cos\left(\pi \frac{\theta_1}{\theta_{fc,1}}\right)\right]^2 + f_{sno} + f_{h2osfc} & \theta_1 < \theta_{fc,1} \end{cases}. \quad (5.76)$$

where $\theta_{fc,1}$ is the field capacity of the top soil layer and $0.01 \leq \theta_1 / \theta_{fc,1} \leq 1$. The volumetric water content of the top soil layer (mm^3 mm^{-3}) is

$$\theta_1 = \frac{1}{\Delta z_1}\left[\frac{w_{liq,1}}{\rho_{liq}} + \frac{w_{ice,1}}{\rho_{ice}}\right]. \quad (5.77)$$

The volumetric water content at field capacity is derived by assuming a hydraulic conductivity of 0.1 mm day^{-1} and inverting the hydraulic conductivity function (section 7.4.1) as

$$\theta_{fc,1} = \theta_{sat,1}\left[\frac{0.1}{86400 k_{sat,1}}\right]^{\frac{1}{2B_i+3}} \quad (5.78)$$

where $k_{sat,1}$ is the saturated hydraulic conductivity of the top soil layer (mm s^{-1}) (section 7.4.1) and the exponent B_1 is a function of soil texture (section 7.4.1).

The roughness lengths used to calculate r_{am}, r_{ah}, and r_{aw} are $z_{0m} = z_{0m,g}$, $z_{0h} = z_{0h,g}$, and $z_{0w} = z_{0w,g}$. The displacement height $d = 0$. The momentum roughness length is $z_{0m,g} = 0.01$ for soil, glaciers, and wetland, and $z_{0m,g} = 0.0024$ for snow-covered surfaces ($f_{sno} > 0$). In general, z_{0m} is different from z_{0h} because the transfer of momentum is affected by pressure fluctuations in the turbulent waves behind the roughness elements, while for heat and water vapor transfer no such dynamical mechanism exists. Rather, heat and water vapor must be transferred by molecular diffusion across the interfacial sublayer. The following relation from Zilitinkevich (1970) is adopted by Zeng and Dickinson (1998)

$$z_{0h,g} = z_{0w,g} = z_{0m,g} e^{-a\left(u_* z_{0m,g}/\upsilon\right)^{0.45}} \tag{5.79}$$

where the quantity $u_* z_{0m,g}/\upsilon$ is the roughness Reynolds number (and may be interpreted as the Reynolds number of the smallest turbulent eddy in the flow) with the kinematic viscosity of air $\upsilon = 1.5 \times 10^{-5}$ m^2 s^{-1} and $a = 0.13$.

The numerical solution for the fluxes of momentum, sensible heat, and water vapor flux from non-vegetated surfaces proceeds as follows:

1. An initial guess for the wind speed V_a is obtained from eq. (5.24) assuming an initial convective velocity $U_c = 0$ m s^{-1} for stable conditions ($\theta_{v,atm} - \theta_{v,s} \geq 0$ as evaluated from eq. (5.50)) and $U_c = 0.5$ for unstable conditions ($\theta_{v,atm} - \theta_{v,s} < 0$).

2. An initial guess for the Monin-Obukhov length L is obtained from the bulk Richardson number using eqs. (5.46) and (5.48).

3. The following system of equations is iterated three times:

   - Friction velocity u_* (eqs. (5.32), (5.33), (5.34), (5.35))
   - Potential temperature scale θ_* (eqs. (5.37), (5.38), (5.39), (5.40))
   - Humidity scale q_* (eqs. (5.41), (5.42), (5.43), (5.44))
   - Roughness lengths for sensible $z_{0h,g}$ and latent heat $z_{0w,g}$ (eq. (5.79))
   - Virtual potential temperature scale θ_{v*} (eq. (5.17))
   - Wind speed including the convective velocity, V_a (eq. (5.24))
   - Monin-Obukhov length L (eq. (5.49))

4. Aerodynamic resistances r_{am}, r_{ah}, and r_{aw} (eqs. (5.55), (5.56), (5.57))

5. Momentum fluxes τ_x, τ_y (eqs. (5.5), (5.6))

6. Sensible heat flux H_g (eq. (5.62))

7. Water vapor flux E_g (eq. (5.66))

8. 2-m height air temperature T_{2m} and specific humidity q_{2m} (eqs. (5.58), (5.59))

The partial derivatives of the soil surface fluxes with respect to ground temperature, which are needed for the soil temperature calculations (section 6.1) and to update the soil surface fluxes (section 5.4), are

$$\frac{\partial H_g}{\partial T_g} = \frac{\rho_{atm} C_p}{r_{ah}} \tag{5.80}$$

$$\frac{\partial E_g}{\partial T_g} = \frac{\beta_{soi} \rho_{atm}}{r_{aw}} \frac{dq_g}{dT_g} \tag{5.81}$$

where

$$\frac{dq_g}{dT_g} = \left(1 - f_{sno} - f_{h2osfc}\right)\alpha_{soil}\frac{dq_{sat}^{T_{soil}}}{dT_{soil}} + f_{sno}\frac{dq_{sat}^{T_{sno}}}{dT_{sno}} + f_{h2osfc}\frac{dq_{sat}^{T_{h2osfc}}}{dT_{h2osfc}}. \qquad (5.82)$$

The partial derivatives $\frac{\partial r_{ah}}{\partial T_g}$ and $\frac{\partial r_{aw}}{\partial T_g}$, which cannot be determined analytically, are ignored for $\frac{\partial H_g}{\partial T_g}$ and $\frac{\partial E_g}{\partial T_g}$.

5.3 Sensible and Latent Heat Fluxes and Temperature for Vegetated Surfaces

In the case of a vegetated surface, the sensible heat H and water vapor flux E are partitioned into vegetation and ground fluxes that depend on vegetation T_v and ground T_g temperatures in addition to surface temperature T_s and specific humidity q_s. Because of the coupling between vegetation temperature and fluxes, Newton-Raphson iteration is used to solve for the vegetation temperature and the sensible heat and water vapor fluxes from vegetation simultaneously using the ground temperature from the previous time step. In section 5.3.1, the equations used in the iteration scheme are derived. Details on the numerical scheme are provided in section 5.3.2.

5.3.1 Theory

The air within the canopy is assumed to have negligible capacity to store heat so that the sensible heat flux H between the surface at height $z_{0h} + d$ and the atmosphere at

height $z_{atm,h}$ must be balanced by the sum of the sensible heat from the vegetation H_v and the ground H_g

$$H = H_v + H_g \tag{5.83}$$

where, with reference to Figure 5.1,

$$H = -\rho_{atm} C_p \frac{\left(\theta_{atm} - T_s\right)}{r_{ah}} \tag{5.84}$$

$$H_v = -\rho_{atm} C_p \left(T_s - T_v\right) \frac{\left(L + S\right)}{r_b} \tag{5.85}$$

$$H_g = \left(1 - f_{sno} - f_{h2osfc}\right) H_{soil} + f_{sno} H_{snow} + f_{h2osfc} H_{h2osfc} \tag{5.86}$$

$$H_{soil} = -\rho_{atm} C_p \frac{\left(T_s - T_1\right)}{r_{ah}'} \tag{5.87}$$

$$H_{sno} = -\rho_{atm} C_p \frac{\left(T_s - T_{snl+1}\right)}{r_{ah}'} \tag{5.88}$$

$$H_{h2osfc} = -\rho_{atm} C_p \frac{\left(T_s - T_{h2osfc}\right)}{r_{ah}'} \tag{5.89}$$

where ρ_{atm} is the density of atmospheric air (kg m^{-3}), C_p is the specific heat capacity of air (J kg^{-1} K^{-1}) (Table 2.6), θ_{atm} is the atmospheric potential temperature (K), and r_{ah} is the aerodynamic resistance to sensible heat transfer (s m^{-1}).

Here, T_s is the surface temperature at height $z_{0h} + d$, also referred to as the canopy air temperature. L and S are the exposed leaf and stem area indices (section 2.1.4), r_b is the leaf boundary layer resistance (s m^{-1}), and r_{ah}' is the aerodynamic resistance (s m^{-1}) to heat transfer between the ground at height z_{0h}' and the canopy air at height $z_{0h} + d$.

Figure 5.1. Schematic diagram of sensible heat fluxes for (a) non-vegetated surfaces and (b) vegetated surfaces.

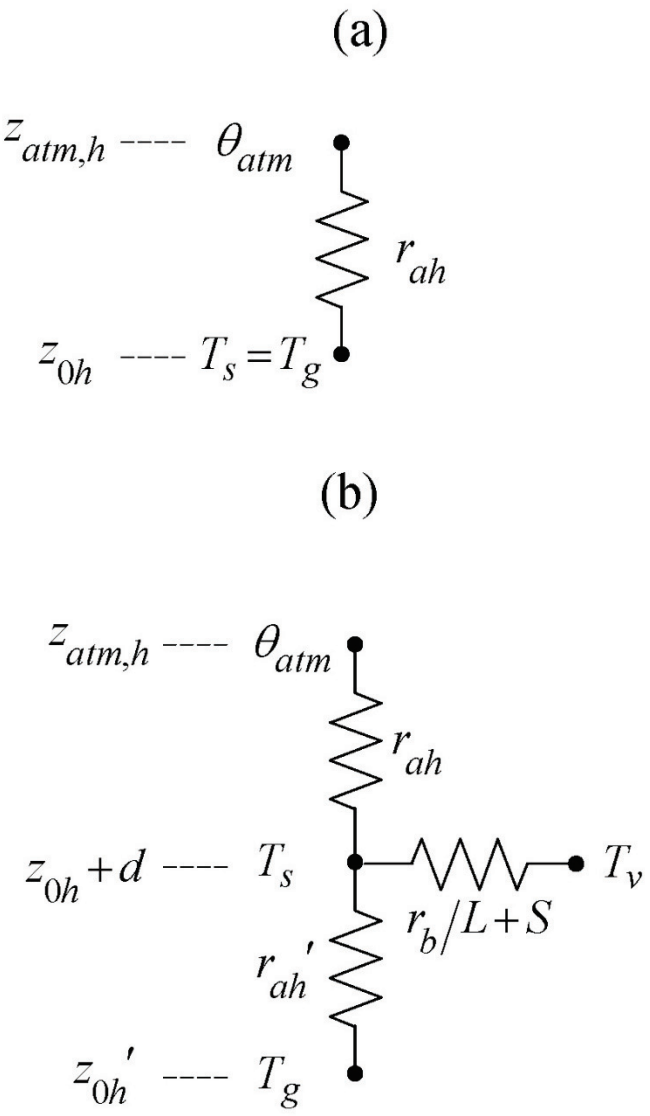

Figure 5.2. Schematic diagram of water vapor fluxes for (a) non-vegetated surfaces and (b) vegetated surfaces.

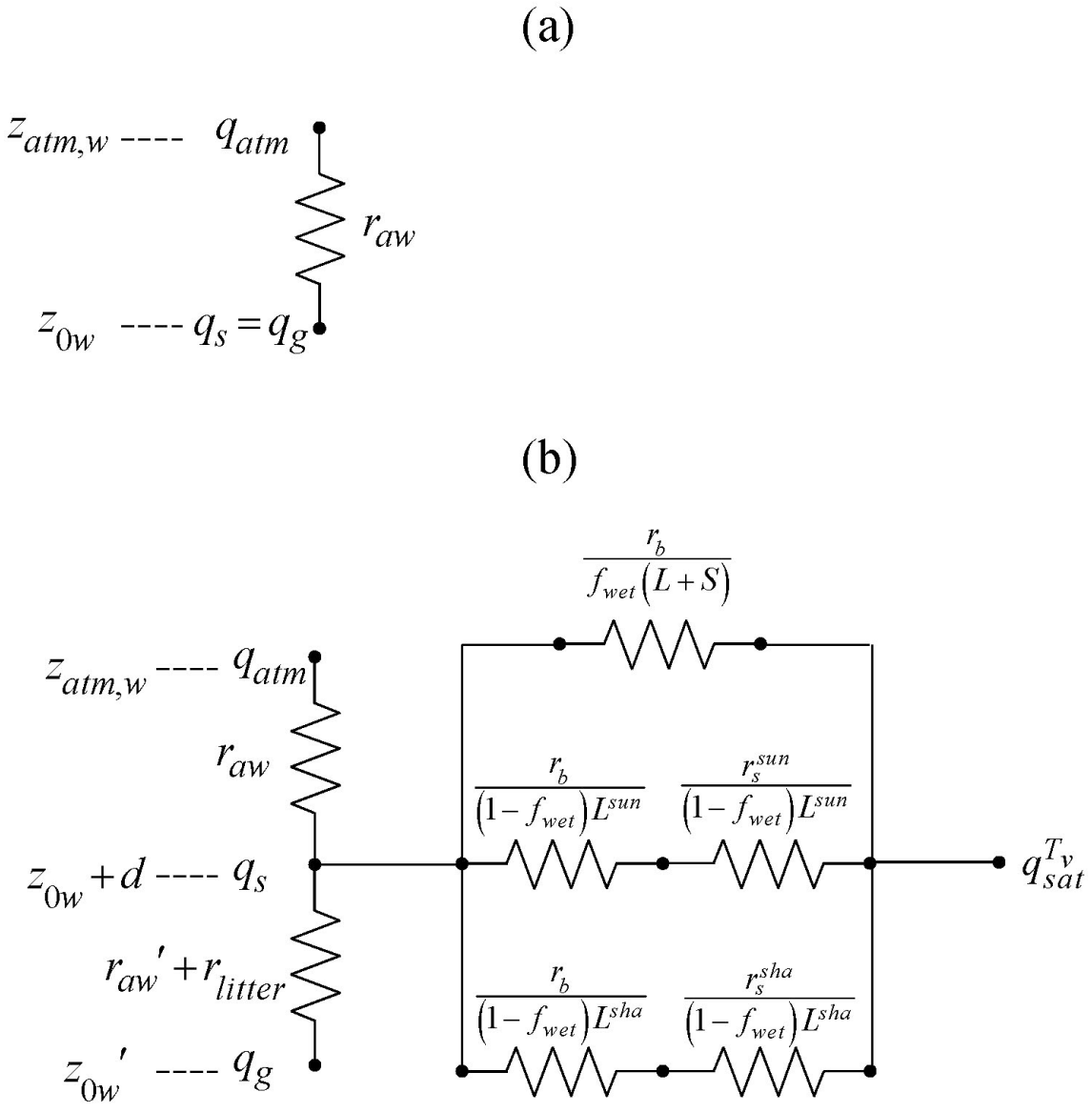

Equations (5.83)-(5.86) can be solved for the canopy air temperature T_s

$$T_s = \frac{c_a^h \theta_{atm} + c_g^h T_g + c_v^h T_v}{c_a^h + c_g^h + c_v^h} \tag{5.90}$$

where

$$c_a^h = \frac{1}{r_{ah}} \tag{5.91}$$

$$c_g^h = \frac{1}{r_{ah}'} \tag{5.92}$$

$$c_v^h = \frac{(L+S)}{r_b} \tag{5.93}$$

are the sensible heat conductances from the canopy air to the atmosphere, the ground to canopy air, and leaf surface to canopy air, respectively (m s^{-1}).

When the expression for T_s is substituted into equation (5.85), the sensible heat flux from vegetation H_v is a function of θ_{atm}, T_g, and T_v

$$H_v = -\rho_{atm} C_p \left[c_a^h \theta_{atm} + c_g^h T_g - \left(c_a^h + c_g^h \right) T_v \right] \frac{c_v^h}{c_a^h + c_v^h + c_g^h}. \tag{5.94}$$

Similarly, the expression for T_s can be substituted into equation (5.86) to obtain the sensible heat flux from ground H_g

$$H_g = -\rho_{atm} C_p \left[c_a^h \theta_{atm} + c_v^h T_v - \left(c_a^h + c_v^h \right) T_g \right] \frac{c_g^h}{c_a^h + c_v^h + c_g^h}. \tag{5.95}$$

The air within the canopy is assumed to have negligible capacity to store water vapor so that the water vapor flux E between the surface at height $z_{0w} + d$ and the

atmosphere at height $z_{atm,w}$ must be balanced by the sum of the water vapor flux from the vegetation E_v and the ground E_g

$$E = E_v + E_g \tag{5.96}$$

where, with reference to Figure 5.2,

$$E = -\rho_{atm} \frac{\left(q_{atm} - q_s\right)}{r_{aw}} \tag{5.97}$$

$$E_v = -\rho_{atm} \frac{\left(q_s - q_{sat}^{T_v}\right)}{r_{total}} \tag{5.98}$$

$$E_g = \left(1 - f_{sno} - f_{h2osfc}\right) E_{soil} + f_{sno} E_{snow} + f_{h2osfc} E_{h2osfc} \tag{5.99}$$

$$E_{soil} = -\rho_{atm} \frac{\beta_{soi}\left(q_s - q_{soil}\right)}{r_{aw}' + r_{litter}} \tag{5.100}$$

$$E_{sno} = -\rho_{atm} \frac{\left(q_s - q_{sno}\right)}{r_{aw}' + r_{litter}} \tag{5.101}$$

$$E_{h2osfc} = -\rho_{atm} \frac{\left(q_s - q_{h2osfc}\right)}{r_{aw}' + r_{litter}} \tag{5.102}$$

where q_{atm} is the atmospheric specific humidity (kg kg^{-1}), r_{aw} is the aerodynamic resistance to water vapor transfer (s m^{-1}), $q_{sat}^{T_v}$ (kg kg^{-1}) is the saturation water vapor specific humidity at the vegetation temperature (section 5.5), q_g , q_{sno} , and q_{h2osfc} are the specific humidities of the soil, snow, and surface water (section 5.2), r_{aw}' is the aerodynamic resistance (s m^{-1}) to water vapor transfer between the ground at height z_{0w}' and the canopy air at height $z_{0w} + d$, β_{soi} is an empirical function of soil water (section

5.2), and r_{litter} is a resistance for the plant litter layer (s m^{-1}). r_{total} is the total resistance to water vapor transfer from the canopy to the canopy air and includes contributions from leaf boundary layer and sunlit and shaded stomatal resistances r_b, r_s^{sun}, and r_s^{sha} (Figure 5.2). The water vapor flux from vegetation is the sum of water vapor flux from wetted leaf and stem area E_v^w (evaporation of water intercepted by the canopy) and transpiration from dry leaf surfaces E_v^t

$$E_v = E_v^w + E_v^t. \tag{5.103}$$

Equations (5.96)-(5.99) can be solved for the canopy specific humidity q_s

$$q_s = \frac{c_a^w q_{atm} + c_g^w q_g + c_v^w q_{sat}^{T_v}}{c_a^w + c_v^w + c_g^w} \tag{5.104}$$

where

$$c_a^w = \frac{1}{r_{aw}} \tag{5.105}$$

$$c_v^w = \frac{(L+S)}{r_b} r'' \tag{5.106}$$

$$c_g^w = \frac{\beta_{soi}}{r_{aw}' + r_{litter}} \tag{5.107}$$

are the water vapor conductances from the canopy air to the atmosphere, the leaf to canopy air, and ground to canopy air, respectively. The term r'' is determined from contributions by wet leaves and transpiration and limited by available water and potential evaporation as

$$r'' = \begin{cases} \min\left(f_{wet} + r_{dry}'', \dfrac{E_v^{w,pot} r_{dry}'' + \dfrac{W_{can}}{\Delta t}}{E_v^{w,pot}} \right) & E_v^{w,pot} > 0, \beta_t > 0 \\ \min\left(f_{wet}, \dfrac{E_v^{w,pot} r_{dry}'' + \dfrac{W_{can}}{\Delta t}}{E_v^{w,pot}} \right) & E_v^{w,pot} > 0, \beta_t \le 0 \\ 1 & E_v^{w,pot} \le 0 \end{cases} \tag{5.108}$$

where f_{wet} is the fraction of leaves and stems that are wet (section 7.1), W_{can} is canopy water (kg m^{-2}) (section 7.1), Δt is the time step (s), and β_t is a soil moisture function limiting transpiration (Chapter 8). The potential evaporation from wet foliage per unit wetted area is

$$E_v^{w,pot} = -\frac{\rho_{atm}\left(q_s - q_{sat}^{T_v}\right)}{r_b}. \tag{5.109}$$

The term r_{dry}'' is

$$r_{dry}'' = \frac{f_{dry} r_b}{L}\left(\frac{L^{sun}}{r_b + r_s^{sun}} + \frac{L^{sha}}{r_b + r_s^{sha}} \right) \tag{5.110}$$

where f_{dry} is the fraction of leaves that are dry (section 7.1), L^{sun} and L^{sha} are the sunlit and shaded leaf area indices (section 4.1), and r_s^{sun} and r_s^{sha} are the sunlit and shaded stomatal resistances (s m^{-1}) (Chapter 8).

When the expression for q_s is substituted into equation (5.98), the water vapor flux from vegetation E_v is a function of q_{atm}, q_g, and $q_{sat}^{T_v}$

$$E_v = -\rho_{atm}\left[c_a^w q_{atm} + c_g^w q_g - \left(c_a^w + c_g^w\right) q_{sat}^{T_v}\right]\frac{c_v^w}{c_a^w + c_v^w + c_g^w}. \quad (5.111)$$

Similarly, the expression for q_s can be substituted into equation (5.99) to obtain the water vapor flux from the ground beneath the canopy E_g

$$E_g = -\rho_{atm}\left[c_a^w q_{atm} + c_v^w q_{sat}^{T_v} - \left(c_a^w + c_v^w\right) q_g\right]\frac{c_g^w}{c_a^w + c_v^w + c_g^w}. \quad (5.112)$$

The aerodynamic resistances to heat (moisture) transfer between the ground at height z_{0h}' (z_{0w}') and the canopy air at height $z_{0h} + d$ ($z_{0w} + d$) are

$$r_{ah}' = r_{aw}' = \frac{1}{C_s U_{av}} \quad (5.113)$$

where

$$U_{av} = V_a\sqrt{\frac{1}{r_{am}V_a}} = u_* \quad (5.114)$$

is the magnitude of the wind velocity incident on the leaves (equivalent here to friction velocity) (m s^{-1}) and C_s is the turbulent transfer coefficient between the underlying soil and the canopy air. C_s is obtained by interpolation between values for dense canopy and bare soil (Zeng et al. 2005)

$$C_s = C_{s,bare}W + C_{s,dense}(1 - W) \quad (5.115)$$

where the weight W is

$$W = e^{-(L+S)}. \quad (5.116)$$

The dense canopy turbulent transfer coefficient in Zeng et al. (2005) is modified from its original value of 0.004 (Dickinson et al. 1993) by Sakaguchi and Zeng (2009) to account for stability as

$$C_{s,dense} = \begin{Bmatrix} 0.004 & T_s - T_g \le 0 \\ \dfrac{0.004}{1+\gamma \min(S,10)} & T_s - T_g > 0 \end{Bmatrix} \tag{5.117}$$

where $\gamma = 0.5$ and S is a stability parameter determined from

$$S = \frac{g z_{top}\left(T_s - T_g\right)}{T_s u_*^2} \tag{5.118}$$

where g is the gravitational acceleration (m s^{-2}) (Table 2.6), and z_{top} is canopy top height (m) (Table 2.2). The bare soil turbulent transfer coefficient is

$$C_{s,bare} = \frac{k}{a}\left(\frac{z_{0m,g} U_{av}}{\upsilon}\right)^{-0.45} \tag{5.119}$$

where the kinematic viscosity of air $\upsilon = 1.5 \times 10^{-5}$ m^2 s^{-1} and $a = 0.13$.

The litter resistance r_{litter} (Sakaguchi and Zeng 2009) (s m^{-1}) is

$$r_{litter} = \frac{1}{0.004 u_*}\left(1 - e^{-L_{litter}^{eff}}\right) \tag{5.120}$$

where the effective litter area index L_{litter}^{eff} (m^2 m^{-2}) is the fraction of plant litter area index L_{litter} (currently set to 0.5 m^2 m^{-2}) that is not covered by snow

$$L_{litter}^{eff} = L_{litter}\left[1 - \min\left(f_{litter}^{snow}, 1\right)\right]. \tag{5.121}$$

The effective snow cover of the litter layer is

$$f_{litter}^{snow} = \frac{z_{sno}}{\Delta z_{litter}} \tag{5.122}$$

where $\Delta z_{litter} = 0.05$ m is assumed as a typical depth for the litter layer, and z_{sno} is the depth of snow (section 7.2) (m).

The leaf boundary layer resistance r_b is

$$r_b = \frac{1}{C_v}\left(U_{av}/d_{leaf}\right)^{-1/2} \tag{5.123}$$

where $C_v = 0.01$ m s$^{-1/2}$ is the turbulent transfer coefficient between the canopy surface and canopy air, and d_{leaf} is the characteristic dimension of the leaves in the direction of wind flow (Table 5.1).

The partial derivatives of the fluxes from the soil beneath the canopy with respect to ground temperature, which are needed for the soil temperature calculations (section 6.1) and to update the soil surface fluxes (section 5.4), are

$$\frac{\partial H_g}{\partial T_g} = \frac{\rho_{atm} C_p}{r'_{ah}} \frac{c_a^h + c_v^h}{c_a^h + c_v^h + c_g^h} \tag{5.124}$$

$$\frac{\partial E_g}{\partial T_g} = \frac{\beta_{soi}\rho_{atm}}{r'_{aw} + r_{litter}} \frac{c_a^w + c_v^w}{c_a^w + c_v^w + c_g^w} \frac{dq_g}{dT_g}. \tag{5.125}$$

The partial derivatives $\frac{\partial r'_{ah}}{\partial T_g}$ and $\frac{\partial r'_{aw}}{\partial T_g}$, which cannot be determined analytically, are ignored for $\frac{\partial H_g}{\partial T_g}$ and $\frac{\partial E_g}{\partial T_g}$.

The roughness lengths used to calculate r_{am}, r_{ah}, and r_{aw} from equations (5.55), (5.56), and (5.57) are $z_{0m} = z_{0m,v}$, $z_{0h} = z_{0h,v}$, and $z_{0w} = z_{0w,v}$. The vegetation displacement height d and the roughness lengths are a function of plant height and adjusted for canopy density following Zeng and Wang (2007)

$$z_{0m,v} = z_{0h,v} = z_{0w,v} = \exp\left[V \ln\left(z_{top} R_{z0m}\right) + \left(1 - V\right)\ln\left(z_{0m,g}\right)\right] \tag{5.126}$$

$$d = z_{top} R_d V \tag{5.127}$$

where z_{top} is canopy top height (m) (Table 2.2), R_{z0m} and R_d are the ratio of momentum roughness length and displacement height to canopy top height, respectively (Table 5.1), and $z_{0m,g}$ is the ground momentum roughness length (m) (section 5.2). The fractional weight V is determined from

$$V = \frac{1 - \exp\left\{-\beta \min\left[L+S, (L+S)_{cr}\right]\right\}}{1 - \exp\left[-\beta (L+S)_{cr}\right]} \tag{5.128}$$

where $\beta = 1$ and $(L+S)_{cr} = 2$ (m^2 m^{-2}) is a critical value of exposed leaf plus stem area for which z_{0m} reaches its maximum.

Table 5.1. Plant functional type aerodynamic parameters

Plant functional type	R_{z0m}	R_d	d_{leaf} (m)
NET Temperate	0.055	0.67	0.04
NET Boreal	0.055	0.67	0.04
NDT Boreal	0.055	0.67	0.04
BET Tropical	0.075	0.67	0.04
BET temperate	0.075	0.67	0.04
BDT tropical	0.055	0.67	0.04
BDT temperate	0.055	0.67	0.04
BDT boreal	0.055	0.67	0.04
BES temperate	0.120	0.68	0.04
BDS temperate	0.120	0.68	0.04
BDS boreal	0.120	0.68	0.04
C_3 arctic grass	0.120	0.68	0.04
C_3 grass	0.120	0.68	0.04
C_4 grass	0.120	0.68	0.04
Crop R	0.120	0.68	0.04
Crop I	0.120	0.68	0.04
Corn R	0.120	0.68	0.04
Corn I	0.120	0.68	0.04
Temp Cereal R	0.120	0.68	0.04
Temp Cereal I	0.120	0.68	0.04
Winter Cereal R	0.120	0.68	0.04
Winter Cereal I	0.120	0.68	0.04
Soybean R	0.120	0.68	0.04
Soybean I	0.120	0.68	0.04

5.3.2 Numerical Implementation

Canopy energy conservation gives

$$-\vec{S}_v + \vec{L}_v\left(T_v\right) + H_v\left(T_v\right) + \lambda E_v\left(T_v\right) = 0 \tag{5.129}$$

where $\vec{S}_v$ is the solar radiation absorbed by the vegetation (section 4.1), $\vec{L}_v$ is the net longwave radiation absorbed by vegetation (section 4.2), and H_v and λE_v are the sensible and latent heat fluxes from vegetation, respectively. The term λ is taken to be the latent heat of vaporization λ_{vap} (Table 2.6).

$\vec{L}_v$, H_v, and λE_v depend on the vegetation temperature T_v. The Newton-Raphson method for finding roots of non-linear systems of equations can be applied to iteratively solve for T_v as

$$\Delta T_v = \frac{\vec{S}_v - \vec{L}_v - H_v - \lambda E_v}{\frac{\partial \vec{L}_v}{\partial T_v} + \frac{\partial H_v}{\partial T_v} + \frac{\partial \lambda E_v}{\partial T_v}} \tag{5.130}$$

where $\Delta T_v = T_v^{n+1} - T_v^n$ and the subscript "n" indicates the iteration.

The partial derivatives are

$$\frac{\partial \vec{L}_v}{\partial T_v} = 4\varepsilon_v \sigma \left[2 - \varepsilon_v\left(1 - \varepsilon_g\right)\right] T_v^3 \tag{5.131}$$

$$\frac{\partial H_v}{\partial T_v} = \rho_{atm} C_p \left(c_a^h + c_g^h\right) \frac{c_v^h}{c_a^h + c_v^h + c_g^h} \tag{5.132}$$

$$\frac{\partial \lambda E_v}{\partial T_v} = \lambda \rho_{atm} \left(c_a^w + c_g^w\right) \frac{c_v^w}{c_a^w + c_v^w + c_g^w} \frac{dq_{sat}^{T_v}}{dT_v}. \tag{5.133}$$

The partial derivatives $\frac{\partial r_{ah}}{\partial T_v}$ and $\frac{\partial r_{aw}}{\partial T_v}$, which cannot be determined analytically, are ignored for $\frac{\partial H_v}{\partial T_v}$ and $\frac{\partial \lambda E_v}{\partial T_v}$. However, if ζ changes sign more than four times during

the temperature iteration, $\zeta = -0.01$. This helps prevent "flip-flopping" between stable and unstable conditions. The total water vapor flux E_v, transpiration flux E_v^t, and sensible heat flux H_v are updated for changes in leaf temperature as

$$E_v = -\rho_{atm}\left[c_a^w q_{atm} + c_g^w q_g - \left(c_a^w + c_g^w\right)\left(q_{sat}^{T_v} + \frac{dq_{sat}^{T_v}}{dT_v}\Delta T_v\right)\right]\frac{c_v^w}{c_a^w + c_v^w + c_g^w} \quad (5.134)$$

$$E_v^t = -r_{dry}''\rho_{atm}\left[c_a^w q_{atm} + c_g^w q_g - \left(c_a^w + c_g^w\right)\left(q_{sat}^{T_v} + \frac{dq_{sat}^{T_v}}{dT_v}\Delta T_v\right)\right]\frac{c_v^h}{c_a^w + c_v^w + c_g^w} \quad (5.135)$$

$$H_v = -\rho_{atm}C_p\left[c_a^h\theta_{atm} + c_g^h T_g - \left(c_a^h + c_g^h\right)\left(T_v + \Delta T_v\right)\right]\frac{c_v^h}{c_a^h + c_v^h + c_g^h}. \quad (5.136)$$

The numerical solution for vegetation temperature and the fluxes of momentum, sensible heat, and water vapor flux from vegetated surfaces proceeds as follows:

1. Initial values for canopy air temperature and specific humidity are obtained from

$$T_s = \frac{T_g + \theta_{atm}}{2} \quad (5.137)$$

$$q_s = \frac{q_g + q_{atm}}{2}. \quad (5.138)$$

2. An initial guess for the wind speed V_a is obtained from eq. (5.24) assuming an initial convective velocity $U_c = 0$ m s^{-1} for stable conditions ($\theta_{v,atm} - \theta_{v,s} \geq 0$ as evaluated from eq. (5.50)) and $U_c = 0.5$ for unstable conditions ($\theta_{v,atm} - \theta_{v,s} < 0$).

3. An initial guess for the Monin-Obukhov length L is obtained from the bulk Richardson number using equation (5.46) and (5.48).

4. Iteration proceeds on the following system of equations:

   - Friction velocity u_* (eqs. (5.32), (5.33), (5.34), (5.35))

- Ratio $\frac{\theta_*}{\theta_{atm}-\theta_s}$ (eqs. (5.37), (5.38), (5.39), (5.40))
- Ratio $\frac{q_*}{q_{atm}-q_s}$ (eqs. (5.41), (5.42), (5.43), (5.44))
- Aerodynamic resistances r_{am}, r_{ah}, and r_{aw} (eqs. (5.55), (5.56), (5.57))
- Magnitude of the wind velocity incident on the leaves U_{av} (eq. (5.114))
- Leaf boundary layer resistance r_b (eq. (5.123))
- Aerodynamic resistances r_{ah}' and r_{aw}' (eq. (5.113))
- Sunlit and shaded stomatal resistances r_s^{sun} and r_s^{sha} (Chapter 8)
- Sensible heat conductances c_a^h, c_g^h, and c_v^h (eqs. (5.91), (5.92), (5.93))
- Latent heat conductances c_a^w, c_v^w, and c_g^w (eqs. (5.105), (5.106), (5.107))
- Sensible heat flux from vegetation H_v (eq. (5.94))
- Latent heat flux from vegetation λE_v (eq. (5.111))
- If the latent heat flux has changed sign from the latent heat flux computed at the previous iteration ($\lambda E_v^{n+1} \times \lambda E_v^{n} < 0$), the latent heat flux is constrained to be 10% of the computed value. The difference between the constrained and computed value ($\Delta_1 = 0.1\lambda E_v^{n+1} - \lambda E_v^{n+1}$) is added to the sensible heat flux later.
- Change in vegetation temperature ΔT_v (eq. (5.130)) and update the vegetation temperature as $T_v^{n+1} = T_v^n + \Delta T_v$. T_v is constrained to change by no more than 1ºK in one iteration. If this limit is exceeded, the energy error is

$$\Delta_2 = \vec{S}_v - \vec{L}_v - \frac{\partial \vec{L}_v}{\partial T_v}\Delta T_v - H_v - \frac{\partial H_v}{\partial T_v}\Delta T_v - \lambda E_v - \frac{\partial \lambda E_v}{\partial T_v}\Delta T_v \qquad (5.139)$$

where $\Delta T_v = 1$ or -1. The error Δ_2 is added to the sensible heat flux later.

- Water vapor flux E_v (eq. (5.134))
- Transpiration E_v^t (eq. (5.135) if $\beta_t > 0$, otherwise $E_v^t = 0$)
- The water vapor flux E_v is constrained to be less than or equal to the sum of transpiration E_v^t and the water available from wetted leaves and stems $W_{can}/\Delta t$. The energy error due to this constraint is

$$\Delta_3 = \max\left(0, E_v - E_v^t - \frac{W_{can}}{\Delta t}\right). \qquad (5.140)$$

  The error $\lambda\Delta_3$ is added to the sensible heat flux later.

- Sensible heat flux H_v (eq. (5.136)). The three energy error terms, Δ_1, Δ_2, and $\lambda\Delta_3$ are also added to the sensible heat flux.
- The saturated vapor pressure e_i (Chapter 8), saturated specific humidity $q_{sat}^{T_v}$ and its derivative $\frac{dq_{sat}^{T_v}}{dT_v}$ at the leaf surface (section 5.5), are re-evaluated based on the new T_v.
- Canopy air temperature T_s (eq. (5.90))
- Canopy air specific humidity q_s (eq. (5.104))
- Temperature difference $\theta_{atm} - \theta_s$
- Specific humidity difference $q_{atm} - q_s$

- Potential temperature scale $\theta_* = \frac{\theta_*}{\theta_{atm} - \theta_s}\left(\theta_{atm} - \theta_s\right)$ where $\frac{\theta_*}{\theta_{atm} - \theta_s}$ was calculated earlier in the iteration
- Humidity scale $q_* = \frac{q_*}{q_{atm} - q_s}\left(q_{atm} - q_s\right)$ where $\frac{q_*}{q_{atm} - q_s}$ was calculated earlier in the iteration
- Virtual potential temperature scale θ_{v*} (eq. (5.17))
- Wind speed including the convective velocity, V_a (eq. (5.24))
- Monin-Obukhov length L (eq. (5.49))
- The iteration is stopped after two or more steps if $\tilde{\Delta} T_v < 0.01$ and $\left|\lambda E_v^{n+1} - \lambda E_v^n\right| < 0.1$ where $\tilde{\Delta} T_v = \max\left(\left|T_v^{n+1} - T_v^n\right|, \left|T_v^n - T_v^{n-1}\right|\right)$, or after forty iterations have been carried out.

5. Momentum fluxes τ_x, τ_y (eqs. (5.5), (5.6))
6. Sensible heat flux from ground H_g (eq. (5.95))
7. Water vapor flux from ground E_g (eq. (5.112))
8. 2-m height air temperature T_{2m}, specific humidity q_{2m}, relative humidity RH_{2m} (eqs. (5.58), (5.59), (5.60))

5.4 Update of Ground Sensible and Latent Heat Fluxes

The sensible and water vapor heat fluxes derived above for bare soil and soil beneath canopy are based on the ground surface temperature from the previous time step T_g^n and are used as the surface forcing for the solution of the soil temperature equations

(section 6.1). This solution yields a new ground surface temperature T_g^{n+1}. The ground sensible and water vapor fluxes are then updated for T_g^{n+1} as

$$H_g' = H_g + \left(T_g^{n+1} - T_g^n\right)\frac{\partial H_g}{\partial T_g} \tag{5.141}$$

$$E_g' = E_g + \left(T_g^{n+1} - T_g^n\right)\frac{\partial E_g}{\partial T_g} \tag{5.142}$$

where H_g and E_g are the sensible heat and water vapor fluxes derived from equations (5.80) and (5.81) for non-vegetated surfaces and equations (5.124) and (5.125) for vegetated surfaces using T_g^n. One further adjustment is made to H_g' and E_g'. If the soil moisture in the top snow/soil layer is not sufficient to support the updated ground evaporation, i.e., if $E_g' > 0$ and $f_{evap} < 1$ where

$$f_{evap} = \frac{\left(w_{ice,\,snl+1} + w_{liq,snl+1}\right)/\Delta t}{\sum_{j=1}^{npft}\left(E_g'\right)_j \left(wt\right)_j} \le 1, \tag{5.143}$$

an adjustment is made to reduce the ground evaporation accordingly as

$$E_g'' = f_{evap} E_g'. \tag{5.144}$$

The term $\sum_{j=1}^{npft}\left(E_g'\right)_j \left(wt\right)_j$ is the sum of E_g' over all evaporating PFTs where $\left(E_g'\right)_j$ is the ground evaporation from the j^{th} PFT on the column, $\left(wt\right)_j$ is the relative area of the j^{th} PFT with respect to the column, and $npft$ is the number of PFTs on the column. $w_{ice,snl+1}$ and $w_{liq,snl+1}$ are the ice and liquid water contents (kg m^{-2}) of the top snow/soil layer (Chapter 7). Any resulting energy deficit is assigned to sensible heat as

$$H_g'' = H_g + \lambda\left(E_g' - E_g''\right). \tag{5.145}$$

The ground water vapor flux E_g'' is partitioned into evaporation of liquid water from snow/soil q_{seva} (kg m^{-2} s^{-1}), sublimation from snow/soil ice q_{subl} (kg m^{-2} s^{-1}), liquid dew on snow/soil q_{sdew} (kg m^{-2} s^{-1}), or frost on snow/soil q_{frost} (kg m^{-2} s^{-1}) as

$$q_{seva} = \max\left(E_{sno}'' \frac{w_{liq,snl+1}}{w_{ice,snl+1} + w_{liq,snl+1}}, 0\right) \quad E_{sno}'' \geq 0, w_{ice,snl+1} + w_{liq,snl+1} > 0 \tag{5.146}$$

$$q_{subl} = E_{sno}'' - q_{seva} \quad E_{sno}'' \geq 0 \tag{5.147}$$

$$q_{sdew} = \left|E_{sno}''\right| \quad E_{sno}'' < 0 \text{ and } T_g \geq T_f \tag{5.148}$$

$$q_{frost} = \left|E_{sno}''\right| \quad E_{sno}'' < 0 \text{ and } T_g < T_f. \tag{5.149}$$

The loss or gain in snow mass due to q_{seva}, q_{subl}, q_{sdew}, and q_{frost} on a snow surface are accounted for during the snow hydrology calculations (section 7.2). The loss of soil and surface water due to q_{seva} is accounted for in the calculation of infiltration (section 7.3), while losses or gains due to q_{subl}, q_{sdew}, and q_{frost} on a soil surface are accounted for following the sub-surface drainage calculations (section 7.6).

The ground heat flux G is calculated as

$$G = \vec{S}_g - \vec{L}_g - H_g - \lambda E_g \tag{5.150}$$

where $\vec{S}_g$ is the solar radiation absorbed by the ground (section 4.1), $\vec{L}_g$ is the net longwave radiation absorbed by the ground (section 4.2)

$$\vec{L}_g = L_g \uparrow - \delta_{veg}\varepsilon_g L_v \downarrow - \left(1 - \delta_{veg}\right)\varepsilon_g L_{atm} \downarrow + 4\varepsilon_g \sigma \left(T_g^n\right)^3 \left(T_g^{n+1} - T_g^n\right), \tag{5.151}$$

where

$$L_g \uparrow = \varepsilon_g \sigma \left[\left(1 - f_{sno} - f_{h2osfc}\right) \left(T_1^n\right)^4 + f_{sno} \left(T_{sno}^n\right)^4 + f_{h2osfc} \left(T_{h2osfc}^n\right)^4 \right] \quad (5.152)$$

and H_g and λE_g are the sensible and latent heat fluxes after the adjustments described above.

When converting ground water vapor flux to an energy flux, the term λ is arbitrarily assumed to be

$$\lambda = \begin{cases} \lambda_{sub} & \text{if } w_{liq,snl+1} = 0 \text{ and } w_{ice,snl+1} > 0 \\ \lambda_{vap} & \text{otherwise} \end{cases} \quad (5.153)$$

where λ_{sub} and λ_{vap} are the latent heat of sublimation and vaporization, respectively (J kg^{-1}) (Table 2.6). When converting vegetation water vapor flux to an energy flux, λ_{vap} is used.

The system balances energy as

$$\vec{S}_g + \vec{S}_v + L_{atm} \downarrow - L \uparrow - H_v - H_g - \lambda_{vap} E_v - \lambda E_g - G = 0 . \quad (5.154)$$

5.5 Saturation Vapor Pressure

Saturation vapor pressure e_{sat}^T (Pa) and its derivative $\frac{de_{sat}^T}{dT}$, as a function of temperature T (ºC), are calculated from the eighth-order polynomial fits of Flatau et al. (1992)

$$e_{sat}^T = 100 \left[a_0 + a_1 T + \cdots + a_n T^n \right] \quad (5.155)$$

$$\frac{de_{sat}^T}{dT} = 100 \left[b_0 + b_1 T + \cdots + b_n T^n \right] \quad (5.156)$$

where the coefficients for ice are valid for $-75\,^{\circ}\mathrm{C} \le T < 0\,^{\circ}\mathrm{C}$ and the coefficients for water are valid for $0\,^{\circ}\mathrm{C} \le T \le 100\,^{\circ}\mathrm{C}$ (Table 5.2 and 5.3). The saturated water vapor specific humidity q_{sat}^{T} and its derivative $\frac{dq_{sat}^{T}}{dT}$ are

$$q_{sat}^{T} = \frac{0.622 e_{sat}^{T}}{P_{atm} - 0.378 e_{sat}^{T}} \tag{5.157}$$

$$\frac{dq_{sat}^{T}}{dT} = \frac{0.622 P_{atm}}{\left(P_{atm} - 0.378 e_{sat}^{T}\right)^{2}} \frac{de_{sat}^{T}}{dT}\,. \tag{5.158}$$

Table 5.2. Coefficients for e_{sat}^{T}

	water	ice
a_0	6.11213476	6.11123516
a_1	4.44007856×10^{-1}	5.03109514×10^{-1}
a_2	1.43064234×10^{-2}	1.88369801×10^{-2}
a_3	2.64461437×10^{-4}	4.20547422×10^{-4}
a_4	3.05903558×10^{-6}	6.14396778×10^{-6}
a_5	1.96237241×10^{-8}	6.02780717×10^{-8}
a_6	8.92344772×10^{-11}	3.87940929×10^{-10}
a_7	$-3.73208410\times10^{-13}$	1.49436277×10^{-12}
a_8	2.09339997×10^{-16}	2.62655803×10^{-15}

Table 5.3. Coefficients for $\frac{de_{sat}^{T}}{dT}$

	water	ice
b_0	4.44017302×10^{-1}	5.03277922×10^{-1}
b_1	2.86064092×10^{-2}	3.77289173×10^{-2}
b_2	7.94683137×10^{-4}	1.26801703×10^{-3}
b_3	1.21211669×10^{-5}	2.49468427×10^{-5}
b_4	1.03354611×10^{-7}	3.13703411×10^{-7}
b_5	4.04125005×10^{-10}	2.57180651×10^{-9}
b_6	$-7.88037859\times10^{-13}$	1.33268878×10^{-11}
b_7	$-1.14596802\times10^{-14}$	3.94116744×10^{-14}
b_8	3.81294516×10^{-17}	4.98070196×10^{-17}

6. Soil and Snow Temperatures

The first law of heat conduction is

$$F = -\lambda \nabla T \tag{6.1}$$

where F is the amount of heat conducted across a unit cross-sectional area in unit time (W m^{-2}), λ is thermal conductivity (W m^{-1} K^{-1}), and ∇T is the spatial gradient of temperature (K m^{-1}). In one-dimensional form

$$F_z = -\lambda \frac{\partial T}{\partial z} \tag{6.2}$$

where z is in the vertical direction (m) and is positive downward and F_z is positive upward. To account for non-steady or transient conditions, the principle of energy conservation in the form of the continuity equation is invoked as

$$c \frac{\partial T}{\partial t} = -\frac{\partial F_z}{\partial z} \tag{6.3}$$

where c is the volumetric snow/soil heat capacity (J m^{-3} K^{-1}) and t is time (s). Combining equations (6.2) and (6.3) yields the second law of heat conduction in one-dimensional form

$$c \frac{\partial T}{\partial t} = \frac{\partial}{\partial z}\left[\lambda \frac{\partial T}{\partial z} \right]. \tag{6.4}$$

This equation is solved numerically to calculate the soil, snow, and surface water temperatures for a fifteen-layer soil column with up to five overlying layers of snow and a single surface water layer with the boundary conditions of h as the heat flux into the top soil, snow, and surface water layers from the overlying atmosphere (section 6.1) and

zero heat flux at the bottom of the soil column. The temperature profile is calculated first without phase change and then readjusted for phase change (section 6.2).

6.1 Numerical Solution

The soil column is discretized into fifteen layers (Table 6.1) where the depth of soil layer i, or node depth, z_i (m), is

$$z_i = f_s \left\{ \exp\left[0.5\left(i - 0.5\right)\right] - 1 \right\} \tag{6.5}$$

where $f_s = 0.025$ is a scaling factor. The thickness of each layer Δz_i (m) is

$$\Delta z_i = \begin{Bmatrix} 0.5\left(z_1 + z_2\right) & i = 1 \\ 0.5\left(z_{i+1} - z_{i-1}\right) & i = 2, 3, \ldots, N_{levgrnd} - 1 \\ z_N - z_{N-1} & i = N_{levgrnd} \end{Bmatrix} \tag{6.6}$$

where $N_{levgrnd} = 15$ is the number of soil layers. The depths at the layer interfaces $z_{h,i}$ (m) are

$$z_{h,i} = \begin{Bmatrix} 0.5\left(z_i + z_{i+1}\right) & i = 1, 2, \ldots, N_{levgrnd} - 1 \\ z_{N_{levgrnd}} + 0.5\Delta z_{N_{levgrnd}} & i = N_{levgrnd} \end{Bmatrix}. \tag{6.7}$$

The exponential form of equation (6.5) is to obtain more soil layers near the soil surface where the soil water gradient is generally strong (section 7.4).

Table 6.1. Soil layer structure.

Layer node depth (z_i), thickness (Δz_i), and depth at layer interface ($z_{h,i}$) for fifteen-layer soil column. All in meters.

Layer	z_i	Δz_i	$z_{h,i}$
1 (top)	0.0071	0.0175	0.0175
2	0.0279	0.0276	0.0451
3	0.0623	0.0455	0.0906
4	0.1189	0.0750	0.1655
5	0.2122	0.1236	0.2891
6	0.3661	0.2038	0.4929
7	0.6198	0.3360	0.8289
8	1.0380	0.5539	1.3828
9	1.7276	0.9133	2.2961
10	2.8646	1.5058	3.8019
11	4.7392	2.4826	6.2845
12	7.8298	4.0931	10.3775
13	12.9253	6.7484	17.1259
14	21.3265	11.1262	28.2520
15 (bottom)	35.1776	13.8512	42.1032

The overlying snow pack is modeled with up to five layers depending on the total snow depth. The layers from top to bottom are indexed in the Fortran code as $i = -4, -3, -2, -1, 0$, which permits the accumulation or ablation of snow at the top of the snow pack without renumbering the layers. Layer $i = 0$ is the snow layer next to the soil surface and layer $i = snl + 1$ is the top layer, where the variable snl is the negative of the number of snow layers. The number of snow layers and the thickness of each layer is a function of snow depth z_{sno} (m) as follows.

$$\left\{\begin{array}{ll} snl = -1 & \\ \Delta z_0 = z_{sno} & \text{for } 0.01 \le z_{sno} \le 0.03 \end{array}\right\},$$

$$\left\{\begin{array}{ll} snl = -2 & \\ \Delta z_{-1} = z_{sno}/2 & \\ \Delta z_0 = \Delta z_{-1} & \text{for } 0.03 < z_{sno} \le 0.04 \end{array}\right\},$$

$$\left\{\begin{array}{ll} snl = -2 & \\ \Delta z_{-1} = 0.02 & \\ \Delta z_0 = z_{sno} - \Delta z_{-1} & \text{for } 0.04 < z_{sno} \le 0.07 \end{array}\right\},$$

$$\left\{\begin{array}{ll} snl = -3 & \\ \Delta z_{-2} = 0.02 & \\ \Delta z_{-1} = (z_{sno} - 0.02)/2 & \\ \Delta z_0 = \Delta z_{-1} & \text{for } 0.07 < z_{sno} \le 0.12 \end{array}\right\},$$

$$\left\{\begin{array}{ll} snl = -3 & \\ \Delta z_{-2} = 0.02 & \\ \Delta z_{-1} = 0.05 & \\ \Delta z_0 = z_{sno} - \Delta z_{-2} - \Delta z_{-1} & \text{for } 0.12 < z_{sno} \le 0.18 \end{array}\right\},$$

$$\left\{\begin{array}{ll} snl = -4 & \\ \Delta z_{-3} = 0.02 & \\ \Delta z_{-2} = 0.05 & \text{for } 0.18 < z_{sno} \le 0.29 \\ \Delta z_{-1} = \left(z_{sno} - \Delta z_{-3} - \Delta z_{-2}\right)/2 & \\ \Delta z_0 = \Delta z_{-1} & \end{array}\right\},$$

$$\left\{\begin{array}{ll} snl = -4 & \\ \Delta z_{-3} = 0.02 & \\ \Delta z_{-2} = 0.05 & \text{for } 0.29 < z_{sno} \le 0.41 \\ \Delta z_{-1} = 0.11 & \\ \Delta z_0 = z_{sno} - \Delta z_{-3} - \Delta z_{-2} - \Delta z_{-1} & \end{array}\right\},$$

$$\left\{\begin{array}{ll} snl = -5 & \\ \Delta z_{-4} = 0.02 & \\ \Delta z_{-3} = 0.05 & \text{for } 0.41 < z_{sno} \le 0.64 \\ \Delta z_{-2} = 0.11 & \\ \Delta z_{-1} = \left(z_{sno} - \Delta z_{-4} - \Delta z_{-3} - \Delta z_{-2}\right)/2 & \\ \Delta z_0 = \Delta z_{-1} & \end{array}\right\},$$

$$\left\{\begin{array}{ll} snl = -5 & \\ \Delta z_{-4} = 0.02 & \\ \Delta z_{-3} = 0.05 & \text{for } 0.64 < z_{sno} \\ \Delta z_{-2} = 0.11 & \\ \Delta z_{-1} = 0.23 & \\ \Delta z_0 = z_{sno} - \Delta z_{-4} - \Delta z_{-3} - \Delta z_{-2} - \Delta z_{-1} & \end{array}\right\}.$$

The node depths, which are located at the midpoint of the snow layers, and the layer interfaces are both referenced from the soil surface and are defined as negative values

$$z_i = z_{h,i} - 0.5\Delta z_i \qquad i = snl + 1, \ldots, 0 \tag{6.8}$$

$$z_{h,i} = z_{h,i+1} - \Delta z_{i+1} \qquad i = snl, \ldots, -1. \tag{6.9}$$

Note that $z_{h,0}$, the interface between the bottom snow layer and the top soil layer, is zero. Thermal properties (i.e., temperature T_i [K]; thermal conductivity λ_i [W m^{-1} K^{-1}];

volumetric heat capacity c_i [J m^{-3} K^{-1}]) are defined for soil layers at the node depths (Figure 6.1) and for snow layers at the layer midpoints. When present, snow occupies a fraction of a grid cell's area, therefore snow depth represents the thickness of the snowpack averaged over only the snow covered area. The grid cell average snow depth is related to the depth of the snow covered area as $\overline{z}_{sno} = f_{sno} z_{sno}$. By default, the grid cell average snow depth is written to the history file.

The heat flux F_i (W m^{-2}) from layer i to layer $i+1$ is

$$F_i = -\lambda\left[z_{h,i}\right]\left(\frac{T_i - T_{i+1}}{z_{i+1} - z_i}\right) \tag{6.10}$$

where the thermal conductivity at the interface $\lambda\left[z_{h,i}\right]$ is

$$\lambda\left[z_{h,i}\right] = \left\{\begin{array}{ll} \dfrac{\lambda_i \lambda_{i+1}\left(z_{i+1} - z_i\right)}{\lambda_i\left(z_{i+1} - z_{h,i}\right) + \lambda_{i+1}\left(z_{h,i} - z_i\right)} & i = snl+1, \ldots, N_{levgrnd} - 1 \\ 0 & i = N_{levgrnd} \end{array}\right\}. \tag{6.11}$$

These equations are derived, with reference to Figure 6.1, assuming that the heat flux from i (depth z_i) to the interface between i and $i+1$ (depth $z_{h,i}$) equals the heat flux from the interface to $i+1$ (depth z_{i+1}), i.e.,

$$-\lambda_i \frac{T_i - T_m}{z_{h,i} - z_i} = -\lambda_{i+1} \frac{T_m - T_{i+1}}{z_{i+1} - z_{h,i}} \tag{6.12}$$

where T_m is the temperature at the interface of layers i and $i+1$.

Figure 6.1. Schematic diagram of numerical scheme used to solve for soil temperature. Shown are three soil layers, $i-1$, i, and $i+1$. The thermal conductivity λ, specific heat capacity c, and temperature T are defined at the layer node depth z. T_m is the interface temperature. The thermal conductivity $\lambda\left[z_h\right]$ is defined at the interface of two layers z_h. The layer thickness is Δz. The heat fluxes F_{i-1} and F_i are defined as positive upwards.

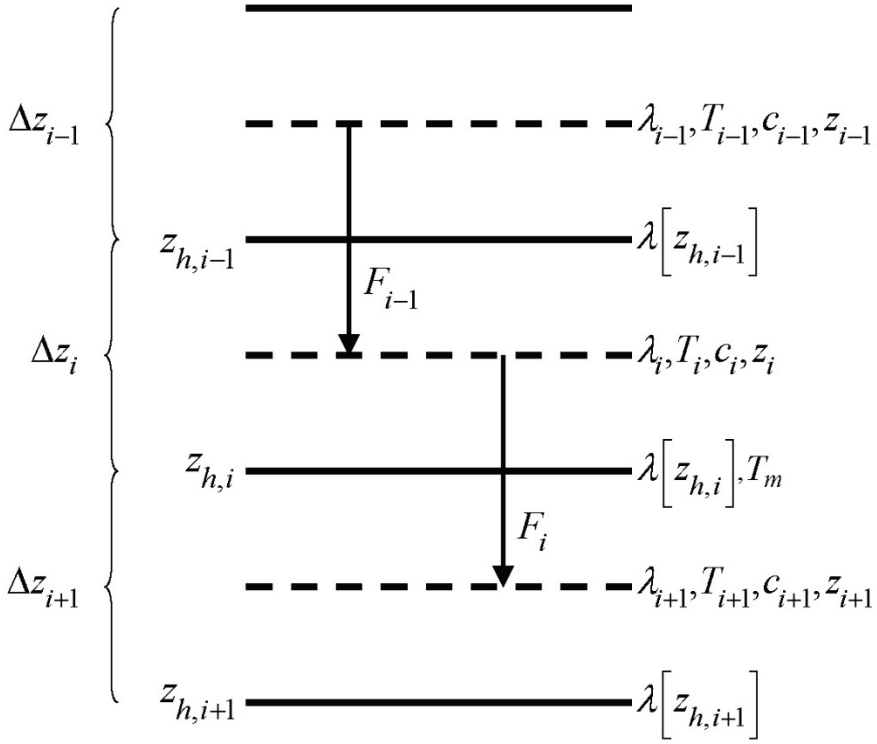

The energy balance for the i^{th} layer is

$$\frac{c_i \Delta z_i}{\Delta t}\left(T_i^{n+1} - T_i^n\right) = -F_{i-1} + F_i \tag{6.13}$$

where the superscripts n and $n+1$ indicate values at the beginning and end of the time step, respectively, and Δt is the time step (s). This equation is solved using the Crank-Nicholson method, which combines the explicit method with fluxes evaluated at n (F_{i-1}^{n}, F_{i}^{n}) and the implicit method with fluxes evaluated at $n+1$ ($F_{i-1}^{n+1}, F_{i}^{n+1}$)

$$\frac{c_i \Delta z_i}{\Delta t}\left(T_i^{n+1} - T_i^{n}\right) = \alpha\left(-F_{i-1}^{n} + F_i^{n}\right) + \left(1-\alpha\right)\left(-F_{i-1}^{n+1} + F_i^{n+1}\right) \tag{6.14}$$

where $\alpha = 0.5$, resulting in a tridiagonal system of equations

$$r_i = a_i T_{i-1}^{n+1} + b_i T_i^{n+1} + c_i T_{i+1}^{n+1} \tag{6.15}$$

where a_i, b_i, and c_i are the subdiagonal, diagonal, and superdiagonal elements in the tridiagonal matrix and r_i is a column vector of constants. When surface water is present, the equation for the top soil layer has an additional term representing the surface water temperature; this results in a four element band-diagonal system of equations.

For the top soil layer $i = 1$, top snow layer $i = snl + 1$, or surface water layer, the heat flux from the overlying atmosphere h (W m^{-2}, defined as positive into the surface) is

$$h^{n+1} = -\alpha F_{i-1}^{n} - \left(1-\alpha\right) F_{i-1}^{n+1}. \tag{6.16}$$

The energy balance for these layers is then

$$\frac{c_i \Delta z_i}{\Delta t}\left(T_i^{n+1} - T_i^{n}\right) = h^{n+1} + \alpha F_i^{n} + \left(1-\alpha\right) F_i^{n+1}. \tag{6.17}$$

The heat flux h at $n+1$ may be approximated as follows

$$h^{n+1} = h^{n} + \frac{\partial h}{\partial T_i}\left(T_i^{n+1} - T_i^{n}\right). \tag{6.18}$$

The resulting equations are then

$$\frac{c_i \Delta z_i}{\Delta t}\left(T_i^{n+1} - T_i^n\right) = h^n + \frac{\partial h}{\partial T_i}\left(T_i^{n+1} - T_i\right) - \alpha \frac{\lambda\left[z_{h,i}\right]\left(T_i^n - T_{i+1}^n\right)}{z_{i+1} - z_i} - \left(1-\alpha\right)\frac{\lambda\left[z_{h,i}\right]\left(T_i^{n+1} - T_{i+1}^{n+1}\right)}{z_{i+1} - z_i} \tag{6.19}$$

For the top snow layer, $i = snl + 1$, the coefficients are

$$a_i = 0 \tag{6.20}$$

$$b_i = 1 + \frac{\Delta t}{c_i \Delta z_i}\left[\left(1-\alpha\right)\frac{\lambda\left[z_{h,i}\right]}{z_{i+1} - z_i} - \frac{\partial h}{\partial T_i}\right] \tag{6.21}$$

$$c_i = -\left(1-\alpha\right)\frac{\Delta t}{c_i \Delta z_i}\frac{\lambda\left[z_{h,i}\right]}{z_{i+1} - z_i} \tag{6.22}$$

$$r_i = T_i^n + \frac{\Delta t}{c_i \Delta z_i}\left[{h_{sno}}^n - \frac{\partial h}{\partial T_i}T_i^n + \alpha F_i\right] \tag{6.23}$$

where

$$F_i = -\lambda\left[z_{h,i}\right]\left(\frac{T_i^n - T_{i+1}^n}{z_{i+1} - z_i}\right). \tag{6.24}$$

The heat flux into the snow surface from the overlying atmosphere h is

$$h = \vec{S}_{sno} - \vec{L}_{sno} - H_{sno} - \lambda E_{sno} \tag{6.25}$$

where $\vec{S}_{sno}$ is the solar radiation absorbed by the top snow layer (section 3.2.1), $\vec{L}_{sno}$ is the longwave radiation absorbed by the snow (positive toward the atmosphere) (section 4.2), H_{sno} is the sensible heat flux from the snow (Chapter 5), and λE_{sno} is the latent heat flux from the snow (Chapter 5). The partial derivative of the heat flux h with respect to temperature is

$$\frac{\partial h}{\partial T} = -\frac{\partial \vec{L}}{\partial T} - \frac{\partial H}{\partial T} - \frac{\partial \lambda E}{\partial T} \tag{6.26}$$

where the partial derivative of the net longwave radiation is

$$\frac{\partial \vec{L}}{\partial T} = 4\varepsilon_g \sigma \left(T^n\right)^3 \tag{6.27}$$

and the partial derivatives of the sensible and latent heat fluxes are given by equations (5.80) and (5.81) for non-vegetated surfaces, and by equations (5.124) and (5.125) for vegetated surfaces. σ is the Stefan-Boltzmann constant (W m^{-2} K^{-4}) (Table 2.6) and ε_g is the ground emissivity (section 4.2). For purposes of computing h and $\frac{\partial h}{\partial T_g}$, the term λ is arbitrarily assumed to be

$$\lambda = \begin{cases} \lambda_{sub} & \text{if } w_{liq,snl+1} = 0 \text{ and } w_{ice,snl+1} > 0 \\ \lambda_{vap} & \text{otherwise} \end{cases} \tag{6.28}$$

where λ_{sub} and λ_{vap} are the latent heat of sublimation and vaporization, respectively (J kg^{-1}) (Table 2.6), and $w_{liq,snl+1}$ and $w_{ice,snl+1}$ are the liquid water and ice contents of the top snow/soil layer, respectively (kg m^{-2}) (Chapter 7).

For the top soil layer, $i = 1$, the coefficients are

$$a_i = -f_{sno}\left(1-\alpha\right)\frac{\Delta t}{c_i \Delta z_i}\frac{\lambda\left[z_{h,i-1}\right]}{z_i - z_{i-1}} \tag{6.29}$$

$$b_i = 1 + \left(1-\alpha\right)\frac{\Delta t}{c_i \Delta z_i}\left[f_{sno}\frac{\lambda\left[z_{h,i-1}\right]}{z_i - z_{i-1}} + \frac{\lambda\left[z_{h,i}\right]}{z_{i+1} - z_i}\right] - \left(1 - f_{sno}\right)\frac{\Delta t}{c_i \Delta z_i}\frac{\partial h}{\partial T} \tag{6.30}$$

$$c_i = -\left(1-\alpha\right)\frac{\Delta t}{c_i \Delta z_i}\frac{\lambda\left[z_{h,i}\right]}{z_{i+1} - z_i} \tag{6.31}$$

$$r_i = T_i^n + \frac{\Delta t}{c_i \Delta z_i}\left[\left(1 - f_{sno}\right)\left({h_{soil}}^n - \frac{\partial h}{\partial T}T_i^n\right) + \alpha\left(F_i - f_{sno}F_{i-1}\right)\right] \tag{6.32}$$

The heat flux into the soil surface from the overlying atmosphere h is

$$h = \vec{S}_{soil} - \vec{L}_{soil} - H_{soil} - \lambda E_{soil} \tag{6.33}$$

It can be seen that when no snow is present ($f_{sno} = 0$), the expressions for the coefficients of the top soil layer have the same form as those for the top snow layer.

The surface snow/soil layer temperature computed in this way is the layer-averaged temperature and hence has somewhat reduced diurnal amplitude compared with surface temperature. An accurate surface temperature is provided that compensates for this effect and numerical error by tuning the heat capacity of the top layer (through adjustment of the layer thickness) to give an exact match to the analytic solution for diurnal heating. The top layer thickness for $i = snl + 1$ is given by

$$\Delta z_{i*} = 0.5\left[z_i - z_{h,i-1} + c_a \left(z_{i+1} - z_{h,i-1} \right) \right] \tag{6.34}$$

where c_a is a tunable parameter, varying from 0 to 1, and is taken as 0.34 by comparing the numerical solution with the analytic solution (Z.-L. Yang 1998, unpublished manuscript). Δz_{i*} is used in place of Δz_i for $i = snl + 1$ in equations (6.19)-(6.24). The top snow/soil layer temperature computed in this way is the ground surface temperature T_g^{n+1}.

The boundary condition at the bottom of the snow/soil column is zero heat flux, $F_i = 0$, resulting in, for $i = N_{levgrnd}$,

$$\frac{c_i \Delta z_i}{\Delta t}\left(T_i^{n+1} - T_i^n \right) = \alpha \frac{\lambda\left[z_{h,i-1} \right]\left(T_{i-1}^n - T_i^n \right)}{z_i - z_{i-1}} + \left(1 - \alpha \right) \frac{\lambda\left[z_{h,i-1} \right]\left(T_{i-1}^{n+1} - T_i^{n+1} \right)}{z_i - z_{i-1}} \tag{6.35}$$

$$a_i = -\left(1 - \alpha \right) \frac{\Delta t}{c_i \Delta z_i} \frac{\lambda\left[z_{h,i-1} \right]}{z_i - z_{i-1}} \tag{6.36}$$

$$b_i = 1 + (1-\alpha)\frac{\Delta t}{c_i \Delta z_i}\frac{\lambda\left[z_{h,i-1}\right]}{z_i - z_{i-1}} \tag{6.37}$$

$$c_i = 0 \tag{6.38}$$

$$r_i = T_i^n - \alpha \frac{\Delta t}{c_i \Delta z_i} F_{i-1} \tag{6.39}$$

where

$$F_{i-1} = -\frac{\lambda\left[z_{h,i-1}\right]}{z_i - z_{i-1}}\left(T_{i-1}^n - T_i^n\right). \tag{6.40}$$

For the interior snow/soil layers, $snl + 1 < i < N_{levgrnd}$, excluding the top soil layer,

$$\begin{aligned}\frac{c_i \Delta z_i}{\Delta t}\left(T_i^{n+1} - T_i^n\right) = &-\alpha \frac{\lambda\left[z_{h,i}\right]\left(T_i^n - T_{i+1}^n\right)}{z_{i+1} - z_i} + \alpha \frac{\lambda\left[z_{h,i-1}\right]\left(T_{i-1}^n - T_i^n\right)}{z_i - z_{i-1}} \\ &-(1-\alpha)\frac{\lambda\left[z_{h,i}\right]\left(T_i^{n+1} - T_{i+1}^{n+1}\right)}{z_{i+1} - z_i} + (1-\alpha)\frac{\lambda\left[z_{h,i-1}\right]\left(T_{i-1}^{n+1} - T_i^{n+1}\right)}{z_i - z_{i-1}}\end{aligned} \tag{6.41}$$

$$a_i = -(1-\alpha)\frac{\Delta t}{c_i \Delta z_i}\frac{\lambda\left[z_{h,i-1}\right]}{z_i - z_{i-1}} \tag{6.42}$$

$$b_i = 1 + (1-\alpha)\frac{\Delta t}{c_i \Delta z_i}\left[\frac{\lambda\left[z_{h,i-1}\right]}{z_i - z_{i-1}} + \frac{\lambda\left[z_{h,i}\right]}{z_{i+1} - z_i}\right] \tag{6.43}$$

$$c_i = -(1-\alpha)\frac{\Delta t}{c_i \Delta z_i}\frac{\lambda\left[z_{h,i}\right]}{z_{i+1} - z_i} \tag{6.44}$$

$$r_i = T_i^n + \alpha \frac{\Delta t}{c_i \Delta z_i}\left(F_i - F_{i-1}\right) + \frac{\Delta t}{c_i \Delta z_i}\vec{S}_{g,i}. \tag{6.45}$$

where $\vec{S}_{g,i}$ is the absorbed solar flux in layer i (section 3.2.1).

When surface water exists, the following top soil layer coefficients are modified

$$b_i = 1 + (1-\alpha)\frac{\Delta t}{c_i \Delta z_i}\left[f_{h2osfc}\frac{\lambda_{h2osfc}}{z_i - z_{h2osfc}} + f_{sno}\frac{\lambda\left[z_{h,i-1}\right]}{z_i - z_{i-1}} + \frac{\lambda\left[z_{h,i}\right]}{z_{i+1} - z_i}\right] - \left(1 - f_{sno} - f_{h2osfc}\right)\frac{\Delta t}{c_i \Delta z_i}\frac{\partial h}{\partial T} \tag{6.46}$$

$$r_i = T_i^n + \frac{\Delta t}{c_i \Delta z_i}\left[\begin{array}{l}\left(1 - f_{sno} - f_{h2osfc}\right)\left({h_{soil}}^n - \frac{\partial h}{\partial T} T_i^n \right) \\ +\alpha\left(F_i - f_{sno} F_{i-1} + f_{h2osfc}\frac{\lambda_{h2osfc}}{z_1 - z_{h2osfc}}\left(T_1 - T_{h2osfc}\right)\right)\end{array}\right] \tag{6.47}$$

$$d_i = -f_{h2osfc}(1-\alpha)\frac{\Delta t}{c_i \Delta z_i}\left[\frac{\lambda_{h2osfc}}{z_i - z_{h2osfc}}\right] \tag{6.48}$$

where d_i is an additional coefficient representing the heat flux from the surface water layer. The surface water layer coefficients are

$$a_{h2osfc} = 0 \tag{6.49}$$

$$b_{h2osfc} = 1 + \frac{\Delta t}{c_{h2osfc}\Delta z_{h2osfc}}\left[(1-\alpha)\frac{\lambda_{h2osfc}}{z_1 - z_{h2osfc}} - \frac{\partial h}{\partial T}\right] \tag{6.50}$$

$$c_{h2osfc} = -(1-\alpha)\frac{\Delta t}{c_{h2osfc}\Delta z_{h2osfc}}\frac{\lambda_{h2osfc}}{z_1 - z_{h2osfc}} \tag{6.51}$$

$$r_{h2osfc} = T_{h2osfc}^n + \frac{\Delta t}{c_i \Delta z_i}\left[{h_{h2osfc}}^n - \frac{\partial h}{\partial T} T_{h2osfc}^n + \alpha\frac{\lambda_{h2osfc}}{z_1 - z_{h2osfc}}\left(T_1 - T_{h2osfc}\right)\right] \tag{6.52}$$

6.2 Phase Change

6.2.1 Soil and Snow Layers

Upon update, the snow/soil temperatures are evaluated to determine if phase change will take place as

$$
\begin{array}{lll}
T_i^{n+1} > T_f \text{ and } w_{ice,i} > 0 & i = snl+1,\ldots,N_{levgrnd} & \text{melting} \\
T_i^{n+1} < T_f \text{ and } w_{liq,i} > 0 & i = snl+1,\ldots,0 & \text{freezing} \\
T_i^{n+1} < T_f \text{ and } w_{liq,i} > w_{liq,\max,i} & i = 1,\ldots,N_{levgrnd} & \text{freezing}
\end{array} \tag{6.53}
$$

where T_i^{n+1} is the soil layer temperature after solution of the tridiagonal equation set, $w_{ice,i}$ and $w_{liq,i}$ are the mass of ice and liquid water (kg m^{-2}) in each snow/soil layer, respectively, and T_f is the freezing temperature of water (K) (Table 2.6). For the freezing process in soil layers, the concept of supercooled soil water from Niu and Yang (2006) is adopted. The supercooled soil water is the liquid water that coexists with ice over a wide range of temperatures below freezing and is implemented through a freezing point depression equation

$$
w_{liq,\max,i} = \Delta z_i \theta_{sat,i} \left[\frac{10^3 L_f \left(T_f - T_i \right)}{g T_i \psi_{sat,i}} \right]^{-1/B_i} \quad T_i < T_f \tag{6.54}
$$

where $w_{liq,\max,i}$ is the maximum liquid water in layer i (kg m^{-2}) when the soil temperature T_i is below the freezing temperature T_f, L_f is the latent heat of fusion (J kg^{-1}) (Table 2.6), g is the gravitational acceleration (m s^{-2}) (Table 2.6), and $\psi_{sat,i}$ and B_i are the soil texture-dependent saturated matric potential (mm) and Clapp and Hornberger (1978) exponent (section 7.4.1).

For the special case when snow is present (snow mass $W_{sno} > 0$) but there are no explicit snow layers ($snl = 0$) (i.e., there is not enough snow present to meet the minimum snow depth requirement of 0.01 m), snow melt will take place for soil layer $i = 1$ if the soil layer temperature is greater than the freezing temperature ($T_1^{n+1} > T_f$).

The rate of phase change is assessed from the energy excess (or deficit) needed to change T_i to freezing temperature, T_f. The excess or deficit of energy H_i (W m^{-2}) is determined as follows

$$H_i = \left\{ \begin{array}{ll} \frac{\partial h}{\partial T}\left(T_f - T_i^n\right) - \frac{c_i \Delta z_i}{\Delta t}\left(T_f - T_i^n\right) & i = snl + 1 \\ \left(1 - f_{sno} - f_{h2osfc}\right)\frac{\partial h}{\partial T}\left(T_f - T_i^n\right) - \frac{c_i \Delta z_i}{\Delta t}\left(T_f - T_i^n\right) & i = 1 \\ -\frac{c_i \Delta z_i}{\Delta t}\left(T_f - T_i^n\right) & i \neq \{1, snl + 1\} \end{array} \right\}. \quad (6.55)$$

If the melting criteria is met (equation (6.53)) and $H_m = \frac{H_i \Delta t}{L_f} > 0$, then the ice mass is readjusted as

$$w_{ice,i}^{n+1} = w_{ice,i}^n - H_m \geq 0 \qquad i = snl + 1, \ldots, N_{levgrnd}. \quad (6.56)$$

If the freezing criteria is met (equation (6.53)) and $H_m < 0$, then the ice mass is readjusted for $i = snl + 1, \ldots, 0$ as

$$w_{ice,i}^{n+1} = \min\left(w_{liq,i}^n + w_{ice,i}^n, w_{ice,i}^n - H_m\right) \quad (6.57)$$

and for $i = 1, \ldots, N_{levgrnd}$ as

$$w_{ice,i}^{n+1} = \left\{ \begin{array}{ll} \min\left(w_{liq,i}^n + w_{ice,i}^n - w_{liq,\max,i}^n, w_{ice,i}^n - H_m\right) & w_{liq,i}^n + w_{ice,i}^n \geq w_{liq,\max,i}^n \\ 0 & w_{liq,i}^n + w_{ice,i}^n < w_{liq,\max,i}^n \end{array} \right\}. \quad (6.58)$$

Liquid water mass is readjusted as

$$w_{liq,i}^{n+1} = w_{liq,i}^n + w_{ice,i}^n - w_{ice,i}^{n+1} \geq 0. \quad (6.59)$$

Because part of the energy H_i may not be consumed in melting or released in freezing, the energy is recalculated as

$$H_{i*} = H_i - \frac{L_f \left(w_{ice,i}^n - w_{ice,i}^{n+1} \right)}{\Delta t} \tag{6.60}$$

and this energy is used to cool or warm the snow/soil layer (if $\left| H_{i*} \right| > 0$) as

$$T_i^{n+1} = \begin{Bmatrix} T_f + \dfrac{\Delta t}{c_i \Delta z_i} H_{i*} \Big/ \left(1 - \dfrac{\Delta t}{c_i \Delta z_i} \dfrac{\partial h}{\partial T} \right) & i = snl + 1 \\ T_f + \dfrac{\Delta t}{c_i \Delta z_i} H_{i*} \Big/ \left(1 - \left(1 - f_{sno} - f_{h2osfc} \right) \dfrac{\Delta t}{c_i \Delta z_i} \dfrac{\partial h}{\partial T} \right) & i = 1 \\ T_f + \dfrac{\Delta t}{c_i \Delta z_i} H_{i*} & i \neq \{1, snl + 1\} \end{Bmatrix}. \tag{6.61}$$

For the special case when snow is present ($W_{sno} > 0$), there are no explicit snow layers ($snl = 0$), and $\dfrac{H_1 \Delta t}{L_f} > 0$ (melting), the snow mass W_{sno} (kg m^{-2}) is reduced according to

$$W_{sno}^{n+1} = W_{sno}^n - \frac{H_1 \Delta t}{L_f} \geq 0 . \tag{6.62}$$

The snow depth is reduced proportionally

$$z_{sno}^{n+1} = \frac{W_{sno}^{n+1}}{W_{sno}^n} z_{sno}^n . \tag{6.63}$$

Again, because part of the energy may not be consumed in melting, the energy for the surface soil layer $i = 1$ is recalculated as

$$H_{1*} = H_1 - \frac{L_f \left(W_{sno}^n - W_{sno}^{n+1} \right)}{\Delta t} . \tag{6.64}$$

If there is excess energy ($H_{1*} > 0$), this energy becomes available to the top soil layer as

$$H_1 = H_{1*} . \tag{6.65}$$

The ice mass, liquid water content, and temperature of the top soil layer are then determined from equations (6.56), (6.59), and (6.61) using the recalculated energy from

equation (6.65). Snow melt M_{1S} (kg m^{-2} s^{-1}) and phase change energy $E_{p,1S}$ (W m^{-2}) for this special case are

$$M_{1S} = \frac{W_{sno}^{n} - W_{sno}^{n+1}}{\Delta t} \geq 0 \tag{6.66}$$

$$E_{p,1S} = L_f M_{1S}\,. \tag{6.67}$$

The total energy of phase change E_p (W m^{-2}) for the snow/soil column is

$$E_p = E_{p,1S} + \sum_{i=snl+1}^{N_{levgrnd}} E_{p,i} \tag{6.68}$$

where

$$E_{p,i} = L_f \frac{\left(w_{ice,i}^{n} - w_{ice,i}^{n+1}\right)}{\Delta t}\,. \tag{6.69}$$

The total snow melt M (kg m^{-2} s^{-1}) is

$$M = M_{1S} + \sum_{i=snl+1}^{i=0} M_i \tag{6.70}$$

where

$$M_i = \frac{\left(w_{ice,i}^{n} - w_{ice,i}^{n+1}\right)}{\Delta t} \geq 0\,. \tag{6.71}$$

The solution for snow/soil temperatures conserves energy as

$$G - E_p - \sum_{i=snl+1}^{i=N_{levgrnd}} \frac{c_i \Delta z_i}{\Delta t}\left(T_i^{n+1} - T_i^{n}\right) = 0 \tag{6.72}$$

where G is the ground heat flux (section 5.4).

6.2.2 Surface Water

Phase change of surface water takes place when the surface water temperature, T_{h2osfc}, becomes less than T_f . The energy available for freezing is

$$H_{h2osfc} = \frac{\partial h}{\partial T}\left(T_f - T^n_{h2osfc}\right) - \frac{c_{h2osfc}\Delta z_{h2osfc}}{\Delta t}\left(T_f - T^n_{h2osfc}\right) \tag{6.73}$$

where c_{h2osfc} is the volumetric heat capacity of water, and Δz_{h2osfc} is the depth of the surface water layer. If $H_m = \frac{H_{h2osfc}\Delta t}{L_f} > 0$ then H_m is removed from surface water and added to the snow column as ice

$$H^{n+1}{}_{h2osfc} = H^n{}_{h2osfc} - H_m \tag{6.74}$$

$$w^{n+1}_{ice,0} = w^n_{ice,0} + H_m \tag{6.75}$$

The snow depth is adjusted to account for the additional ice mass

$$\Delta z_{sno} = \frac{H_m}{\rho_{ice}} \tag{6.76}$$

If H_m is greater than W_{sfc}, the excess heat $\frac{L_f\left(H_m - W_{sfc}\right)}{\Delta t}$ is used to cool the snow layer.

6.3 Soil and Snow Thermal Properties

The thermal and hydraulic (section 6.3 and 7.4.1) properties of the soil are assumed to be a weighted combination of the mineral and organic properties of the soil (Lawrence and Slater 2008). The soil layer organic matter fraction $f_{om,i}$ is

$$f_{om,i} = \rho_{om,i} / \rho_{om,\max}\,. \tag{6.77}$$

Soil thermal conductivity λ_i (W m^{-1} K^{-1}) is from Farouki (1981)

$$\begin{aligned} \lambda_i &= \left\{ \begin{array}{ll} K_{e,i}\lambda_{sat,i} + \left(1 - K_{e,i}\right)\lambda_{dry,i} & S_{r,i} > 1\times10^{-7} \\ \lambda_{dry,i} & S_{r,i} \le 1\times10^{-7} \end{array} \right\} \quad i = 1,\ldots,N_{levsoi} \\ \lambda_i &= \lambda_{bedrock} \qquad\qquad\qquad\qquad\qquad\quad i = N_{levsoi}+1,\ldots N_{levgrnd} \end{aligned} \tag{6.78}$$

where $\lambda_{sat,i}$ is the saturated thermal conductivity, $\lambda_{dry,i}$ is the dry thermal conductivity, $K_{e,i}$ is the Kersten number, $S_{r,i}$ is the wetness of the soil with respect to saturation, and $\lambda_{bedrock} = 3$ W m^{-1} K^{-1} is the thermal conductivity assumed for the deep ground layers (typical of saturated granitic rock; Clauser and Huenges, 1995). For glaciers and wetlands,

$$\lambda_i = \begin{cases} \lambda_{liq,i} & T_i \geq T_f \\ \lambda_{ice,i} & T_i < T_f \end{cases} \tag{6.79}$$

where λ_{liq} and λ_{ice} are the thermal conductivities of liquid water and ice, respectively (Table 2.6). The saturated thermal conductivity $\lambda_{sat,i}$ (W m^{-1} K^{-1}) depends on the thermal conductivities of the soil solid, liquid water, and ice constituents

$$\lambda_{sat} = \lambda_s^{1-\theta_{sat}} \lambda_{liq}^{\frac{\theta_{liq}}{\theta_{liq}+\theta_{ice}}\theta_{sat}} \lambda_{ice}^{\theta_{sat}\left(1-\frac{\theta_{liq}}{\theta_{liq}+\theta_{ice}}\right)} \tag{6.80}$$

where the thermal conductivity of soil solids $\lambda_{s,i}$ varies with the sand, clay, and organic matter content

$$\lambda_{s,i} = (1 - f_{om,i})\lambda_{s,\min,i} + f_{om,i}\lambda_{s,om} \tag{6.81}$$

where the mineral soil solid thermal conductivity $\lambda_{s,\min,i}$ is

$$\lambda_{s,\min,i} = \frac{8.80\ (\%sand)_i + 2.92\ (\%clay)_i}{(\%sand)_i + (\%clay)_i}, \tag{6.82}$$

and $\lambda_{s,om} = 0.25$ W m^{-1} K^{-1} (Farouki, 1981). $\theta_{sat,i}$ is the volumetric water content at saturation (porosity) (section 7.4.1).

The thermal conductivity of dry soil is

$$\lambda_{dry,i} = (1 - f_{om,i})\lambda_{dry,\min,i} + f_{om,i}\lambda_{dry,om} \tag{6.83}$$

where the thermal conductivity of dry mineral soil $\lambda_{dry,\min,i}$ (W m^{-1} K^{-1}) depends on the bulk density $\rho_{d,i} = 2700\left(1-\theta_{sat,i}\right)$ (kg m^{-3}) as

$$\lambda_{dry,\min,i} = \frac{0.135\rho_{d,i} + 64.7}{2700 - 0.947\rho_{d,i}} \tag{6.84}$$

and $\lambda_{dry,om} = 0.05$ W m^{-1} K^{-1} (Farouki, 1981) is the dry thermal conductivity of organic matter. The Kersten number $K_{e,i}$ is a function of the degree of saturation S_r and phase of water

$$K_{e,i} = \begin{cases} \log\left(S_{r,i}\right) + 1 \geq 0 & T_i \geq T_f \\ S_{r,i} & T_i < T_f \end{cases} \tag{6.85}$$

where

$$S_{r,i} = \left(\frac{w_{liq,i}}{\rho_{liq}\Delta z_i} + \frac{w_{ice,i}}{\rho_{ice}\Delta z_i}\right)\frac{1}{\theta_{sat,i}} = \frac{\theta_{liq,i} + \theta_{ice,i}}{\theta_{sat,i}} \leq 1. \tag{6.86}$$

Thermal conductivity λ_i (W m^{-1} K^{-1}) for snow is from Jordan (1991)

$$\lambda_i = \lambda_{air} + \left(7.75\times10^{-5}\rho_{sno,i} + 1.105\times10^{-6}\rho_{sno,i}^2\right)\left(\lambda_{ice} - \lambda_{air}\right) \tag{6.87}$$

where λ_{air} is the thermal conductivity of air (Table 2.6) and $\rho_{sno,i}$ is the bulk density of snow (kg m^{-3})

$$\rho_{sno,i} = \frac{w_{ice,i} + w_{liq,i}}{\Delta z_i}. \tag{6.88}$$

The volumetric heat capacity c_i (J m^{-3} K^{-1}) for soil is from de Vries (1963) and depends on the heat capacities of the soil solid, liquid water, and ice constituents

$$c_i = c_{s,i}\left(1-\theta_{sat,i}\right) + \frac{w_{ice,i}}{\Delta z_i}C_{ice} + \frac{w_{liq,i}}{\Delta z_i}C_{liq} \tag{6.89}$$

where C_{liq} and C_{ice} are the specific heat capacities (J kg^{-1} K^{-1}) of liquid water and ice, respectively (Table 2.6). The heat capacity of soil solids $c_{s,i}$ (J m^{-3} K^{-1}) is

$$c_{s,i} = (1 - f_{om,i}) c_{s,\min,i} + f_{om,i} c_{s,om} \tag{6.90}$$

where the heat capacity of mineral soil solids $c_{s,\min,i}$ (J m^{-3} K^{-1}) is

$$\begin{aligned} c_{s,\min,i} &= \left(\frac{2.128\ (\%sand)_i + 2.385\ (\%clay)_i}{(\%sand)_i + (\%clay)_i} \right) \times 10^6 \quad && i = 1, \ldots, N_{levsoi} \\ c_{s,\min,i} &= c_{s,bedrock} && i = N_{levsoi} + 1, \ldots, N_{levgrnd} \end{aligned} \tag{6.91}$$

where $c_{s,bedrock} = 2 \times 10^6$ J m^{-3} K^{-1} is the heat capacity of bedrock and $c_{s,om} = 2.5 \times 10^6$ J m^{-3} K^{-1} (Farouki, 1981) is the heat capacity of organic matter. For glaciers, wetlands, and snow

$$c_i = \frac{w_{ice,i}}{\Delta z_i} C_{ice} + \frac{w_{liq,i}}{\Delta z_i} C_{liq} . \tag{6.92}$$

For the special case when snow is present ($W_{sno} > 0$) but there are no explicit snow layers ($snl = 0$), the heat capacity of the top layer is a blend of ice and soil heat capacity

$$c_1 = c_1^* + \frac{C_{ice} W_{sno}}{\Delta z_1} \tag{6.93}$$

where c_1^* is calculated from equation (6.89) or (6.92).

7. Hydrology

The model parameterizes interception, throughfall, canopy drip, snow accumulation and melt, water transfer between snow layers, infiltration, evaporation, surface runoff, sub-surface drainage, redistribution within the soil column, and groundwater discharge and recharge to simulate changes in canopy water ΔW_{can}, surface water ΔW_{sfc}, snow water ΔW_{sno}, soil water $\Delta w_{liq,i}$, and soil ice $\Delta w_{ice,i}$, and water in the unconfined aquifer ΔW_a (all in kg m^{-2} or mm of H_2O) (Figure 7.1).

The total water balance of the system is

$$\Delta W_{can} + \Delta W_{sfc} + \Delta W_{sno} + \sum_{i=1}^{N_{levsoi}} \left(\Delta w_{liq,i} + \Delta w_{ice,i} \right) + \Delta W_a = \begin{pmatrix} q_{rain} + q_{sno} - E_v - E_g - q_{over} \\ -q_{h2osfc} - q_{drai} - q_{rgwl} - q_{snwcp,ice} \end{pmatrix} \Delta t \quad (7.1)$$

where q_{rain} is the liquid part of precipitation, q_{sno} is the solid part of precipitation, E_v is ET from vegetation (Chapter 5), E_g is ground evaporation (Chapter 5), q_{over} is surface runoff (section 7.3), q_{h2osfc} is runoff from surface water storage (section 7.3), q_{drai} is sub-surface drainage (section 7.6), q_{rgwl} and $q_{snwcp,ice}$ are liquid and solid runoff from glaciers, wetlands, and lakes, and runoff from other surface types due to snow capping (section 7.7) (all in kg m^{-2} s^{-1}), N_{levsoi} is the number of soil layers (note that hydrology calculations are only done over soil layers 1 to N_{levsoi}; ground levels $N_{levsoi}+1$ to $N_{levgrnd}$ are currently hydrologically inactive; Lawrence et al. 2008) and Δt is the time step (s).

Figure 7.1. Hydrologic processes represented in CLM.

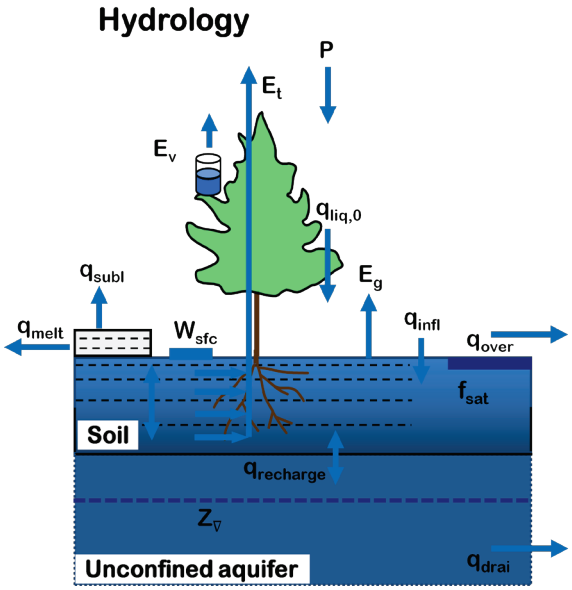

7.1 Canopy Water

Precipitation is either intercepted by the canopy, falls directly to the snow/soil surface (throughfall), or drips off the vegetation (canopy drip). Interception by vegetation q_{intr} (kg m^{-2} s^{-1}) does not distinguish between liquid and solid phases

$$q_{intr} = \alpha\left(q_{rain} + q_{sno}\right)\left\{1 - \exp\left[-0.5\left(L + S\right)\right]\right\} \tag{7.2}$$

where L and S are the exposed leaf and stem area index, respectively (section 2.1.4), and $\alpha = 0.25$ scales interception from point to grid cell (Lawrence et al. 2007). Throughfall (kg m^{-2} s^{-1}), however, is divided into liquid and solid phases reaching the ground (soil or snow surface) as

$$q_{thru,liq} = q_{rain}\left[1 - \alpha\left\{1 - \exp\left[-0.5\left(L + S\right)\right]\right\}\right] \tag{7.3}$$

$$q_{thru,ice} = q_{sno}\left[1 - \alpha\left\{1 - \exp\left[-0.5\left(L + S\right)\right]\right\}\right]. \tag{7.4}$$

Similarly, the canopy drip is

$$q_{drip,liq} = \frac{W_{can}^{intr} - W_{can,\max}}{\Delta t} \frac{q_{rain}}{q_{rain} + q_{sno}} \geq 0 \tag{7.5}$$

$$q_{drip,ice} = \frac{W_{can}^{intr} - W_{can,\max}}{\Delta t} \frac{q_{sno}}{q_{rain} + q_{sno}} \geq 0 \tag{7.6}$$

where

$$W_{can}^{intr} = W_{can}^{n} + q_{intr}\Delta t \geq 0 \tag{7.7}$$

is the canopy water after accounting for interception, W_{can}^{n} is the canopy water from the previous time step, and $W_{can,\max}$ (kg m^{-2}) is the maximum amount of water the canopy can hold

$$W_{can,\max} = p\left(L + S\right). \tag{7.8}$$

The maximum storage of solid water is assumed to be the same as that of liquid water, $p = 0.1$ kg m^{-2} (Dickinson et al. 1993). The canopy water is updated as

$$W_{can}^{n+1} = W_{can}^{n} + q_{intr}\Delta t - \left(q_{drip,liq} + q_{drip,ice}\right)\Delta t - E_v^w \Delta t \geq 0\,. \tag{7.9}$$

where E_v^w is the flux of water vapor from stem and leaf surfaces (Chapter 5). The total rate of liquid and solid precipitation reaching the ground is then

$$q_{grnd,liq} = q_{thru,liq} + q_{drip,liq} \tag{7.10}$$

$$q_{grnd,ice} = q_{thru,ice} + q_{drip,ice}\,. \tag{7.11}$$

Solid precipitation reaching the soil or snow surface, $q_{grnd,ice}\Delta t$, is added immediately to the snow pack (section 7.2). The liquid part, $q_{grnd,liq}\Delta t$ is added after surface fluxes (Chapter 5) and snow/soil temperatures (Chapter 6) have been determined.

The wetted fraction of the canopy (stems plus leaves), which is required for the surface albedo (section 3.1) and surface flux (Chapter 5) calculations is (Dickinson et al. 1993)

$$f_{wet} = \begin{cases} \left[\frac{W_{can}}{p(L+S)} \right]^{2/3} \le 1 & L+S>0 \\ 0 & L+S=0 \end{cases} \tag{7.12}$$

while the fraction of the canopy that is dry and transpiring is

$$f_{dry} = \begin{cases} \frac{(1-f_{wet})L}{L+S} & L+S>0 \\ 0 & L+S=0 \end{cases}. \tag{7.13}$$

7.2 Snow

The parameterizations for snow are based primarily on Anderson (1976), Jordan (1991), and Dai and Zeng (1997). The snowpack can have up to five layers. These layers are indexed in the Fortran code as $i = -4,-3,-2,-1,0$ where layer $i = 0$ is the snow layer next to the top soil layer and layer $i = -4$ is the top layer of a five-layer snow pack. Since the number of snow layers varies according to the snow depth, we use the notation $snl+1$ to describe the top layer of snow for the variable layer snow pack, where snl is the negative of the number of snow layers. Refer to Figure 7.2 for an example of the snow layer structure for a three layer snow pack.

Figure 7.2. Example of three layer snow pack ($snl = -3$).

Shown are three snow layers, $i = -2$, $i = -1$, and $i = 0$. The layer node depth is z, the layer interface is z_h, and the layer thickness is Δz.

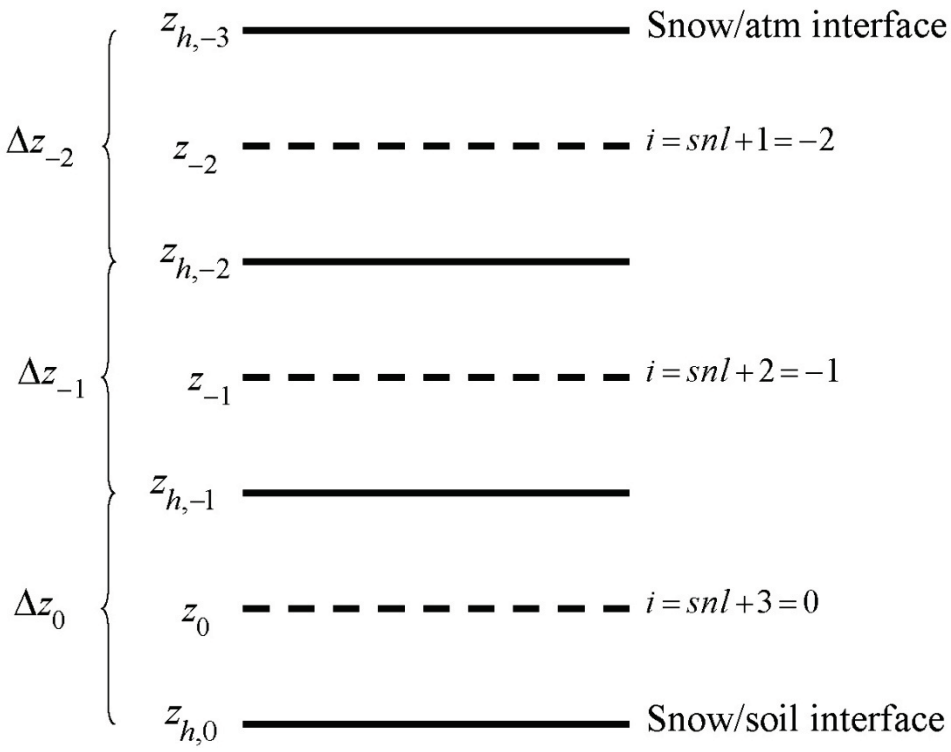

The state variables for snow are the mass of water $w_{liq,i}$ (kg m^{-2}), mass of ice $w_{ice,i}$ (kg m^{-2}), layer thickness Δz_i (m), and temperature T_i (Chapter 6). The water vapor phase is neglected. Snow can also exist in the model without being represented by explicit snow layers. This occurs when the snowpack is less than a specified minimum snow depth ($z_{sno} < 0.01$ m). In this case, the state variable is the mass of snow W_{sno} (kg m^{-2}).

Section 7.2.1 describes the calculation of fractional snow covered area, which is used in the surface albedo calculation (Chapter 3) and the surface flux calculations (Chapter 5). The following two sections (7.2.2 and 7.2.3) describe the ice and water content of the snow pack assuming that at least one snow layer exists. Section 7.2.4 describes how black and organic carbon and mineral dust particles are represented within snow, including meltwater flushing. See section 7.2.5 for a description of how a snow layer is initialized.

7.2.1 Snow Covered Area Fraction

The fraction of the ground covered by snow, f_{sno}, is based on the method of Swenson and Lawrence (2012). Because the processes governing snowfall and snowmelt differ, changes in f_{sno} are calculated separately for accumulation and depletion. When snowfall occurs, f_{sno} is updated as

$$f^{n+1}{}_{sno} = 1 - \left(\left(1 - \tanh(k_{accum} q_{sno} \Delta t) \right) \left(1 - f^{n}{}_{sno} \right) \right) \tag{7.14}$$

where k_{accum} is a constant whose default value is 0.1, $q_{sno}\Delta t$ is the amount of new snow, $f^{n+1}{}_{sno}$ is the updated snow covered fraction (SCF), and $f^{n}{}_{sno}$ is the SCF from the previous time step.

When snow melt occurs, f_{sno} is calculated from the depletion curve

$$f_{sno} = 1 - \left(\frac{\cos^{-1}\left(2R_{sno} - 1 \right)}{\pi} \right)^{N_{melt}} \tag{7.15}$$

where R_{sno} is the ratio of W_{sno} to the maximum accumulated snow $W_{\max}$, and N_{melt} is a parameter that depends on the topographic variability within the grid cell. Whenever

W_{sno} reaches zero, $W_{\max}$ is reset to zero. The depletion curve shape parameter is defined as

$$N_{melt} = \frac{200}{\min\left(10, \sigma_{topo}\right)} \tag{7.16}$$

The standard deviation of the elevation within a grid cell, σ_{topo} , is calculated from a high resolution DEM (a 1km DEM is used for CLM).

7.2.2 Ice Content

The conservation equation for mass of ice in snow layers is

$$\frac{\partial w_{ice,i}}{\partial t} = \begin{Bmatrix} f_{sno} q_{ice,i-1} - \dfrac{\left(\Delta w_{ice,i}\right)_p}{\Delta t} & i = snl+1 \\ -\dfrac{\left(\Delta w_{ice,i}\right)_p}{\Delta t} & i = snl+2,\ldots,0 \end{Bmatrix} \tag{7.17}$$

where $q_{ice,i-1}$ is the rate of ice accumulation from precipitation or frost or the rate of ice loss from sublimation (kg m^{-2} s^{-1}) in the top layer and $\left(\Delta w_{ice,i}\right)_p \Big/ \Delta t$ is the change in ice due to phase change (melting rate) (section 6.2). The term $q_{ice,i-1}$ is computed in two steps as

$$q_{ice,i-1} = q_{grnd,ice} + \left(q_{frost} - q_{subl}\right) \tag{7.18}$$

where $q_{grnd,ice}$ is the rate of solid precipitation reaching the ground (section 7.1) and q_{frost} and q_{subl} are gains due to frost and losses due to sublimation, respectively (section 5.4). In the first step, immediately after $q_{grnd,ice}$ has been determined after accounting for interception (section 7.1), a new snow depth z_{sno} (m) is calculated from

$$z_{sno}^{n+1} = z_{sno}^{n} + \Delta z_{sno} \tag{7.19}$$

where

$$\Delta z_{sno} = \frac{q_{grnd,ice}\Delta t}{f_{sno}\rho_{sno}} \tag{7.20}$$

and ρ_{sno} is the bulk density of newly fallen snow (kg m^{-3}) (Anderson 1976)

$$\rho_{sno} = \begin{cases} 50+1.7(17)^{1.5} & T_{atm} > T_f + 2 \\ 50+1.7(T_{atm} - T_f + 15)^{1.5} & T_f - 15 < T_{atm} \le T_f + 2 \\ 50 & T_{atm} \le T_f - 15 \end{cases} \tag{7.21}$$

where T_{atm} is the atmospheric temperature (K), and T_f is the freezing temperature of water (K) (Table 2.6). The mass of snow W_{sno} is

$$W_{sno}^{n+1} = W_{sno}^{n} + q_{grnd,ice}\Delta t\,. \tag{7.22}$$

The ice content of the top layer and the layer thickness are updated as

$$w_{ice,snl+1}^{n+1} = w_{ice,snl+1}^{n} + q_{grnd,ice}\Delta t \tag{7.23}$$

$$\Delta z_{snl+1}^{n+1} = \Delta z_{snl+1}^{n} + \Delta z_{sno}\,. \tag{7.24}$$

Since wetlands are modeled as columns of water (no soil), snow is not allowed to accumulate if the surface temperature is above freezing ($T_g > T_f$). In this case, the incoming solid precipitation is assigned to the runoff term q_{rgwl} (section 7.7).

In the second step, after surface fluxes and snow/soil temperatures have been determined (Chapters 5 and 6), $w_{ice,snl+1}$ is updated for frost or sublimation as

$$w_{ice,snl+1}^{n+1} = w_{ice,snl+1}^{n} + f_{sno}\left(q_{frost} - q_{subl}\right)\Delta t\,. \tag{7.25}$$

If $w_{ice,snl+1}^{n+1} < 0$ upon solution of equation (7.25), the ice content is reset to zero and the liquid water content $w_{liq,snl+1}$ is reduced by the amount required to bring $w_{ice,snl+1}^{n+1}$ up to zero.

The snow water equivalent W_{sno} is capped to not exceed 1000 kg m^{-2}. If the addition of q_{frost} were to result in $W_{sno} > 1000$ kg m^{-2}, the frost term q_{frost} is instead added to the ice runoff term $q_{snwcp,ice}$ (section 7.7).

7.2.3 Water Content

The conservation equation for mass of water in snow layers is

$$\frac{\partial w_{liq,i}}{\partial t} = \left(q_{liq,i-1} - q_{liq,i}\right) + \frac{\left(\Delta w_{liq,i}\right)_p}{\Delta t} \tag{7.26}$$

where $q_{liq,i-1}$ is the flow of liquid water into layer i from the layer above, $q_{liq,i}$ is the flow of water out of layer i to the layer below, $\left(\Delta w_{liq,i}\right)_p / \Delta t$ is the change in liquid water due to phase change (melting rate) (section 6.2). For the top snow layer only,

$$q_{liq,i-1} = f_{sno}\left(q_{grnd,liq} + \left(q_{sdew} - q_{seva}\right)\right) \tag{7.27}$$

where $q_{grnd,liq}$ is the rate of liquid precipitation reaching the snow (section 7.1), q_{seva} is the evaporation of liquid water and q_{sdew} is the liquid dew (section 5.4). After surface fluxes and snow/soil temperatures have been determined (Chapters 5 and 6), $w_{liq,snl+1}$ is updated for the liquid precipitation reaching the ground and dew or evaporation as

$$w_{liq,snl+1}^{n+1} = w_{liq,snl+1}^{n} + f_{sno}\left(q_{grnd,liq} + q_{sdew} - q_{seva}\right)\Delta t\,. \tag{7.28}$$

When the liquid water within a snow layer exceeds the layer's holding capacity, the excess water is added to the underlying layer, limited by the effective porosity $(1-\theta_{ice})$ of the layer. The flow of water is assumed to be zero ($q_{liq,i} = 0$) if the effective porosity of either of the two layers ($1-\theta_{ice,i}$ and $1-\theta_{ice,i+1}$) is less than $\theta_{imp} = 0.05$, the water

impermeable volumetric water content. Thus, water flow between layers, $q_{liq,i}$, for layers $i = snl+1,\ldots,0$, is initially calculated as

$$q_{liq,i} = \frac{\rho_{liq}\left[\theta_{liq,i} - S_r\left(1-\theta_{ice,i}\right)\right] f_{sno}\Delta z_i}{\Delta t} \geq 0 \tag{7.29}$$

where the volumetric liquid water $\theta_{liq,i}$ and ice $\theta_{ice,i}$ contents are

$$\theta_{ice,i} = \frac{w_{ice,i}}{f_{sno}\Delta z_i \rho_{ice}} \leq 1 \tag{7.30}$$

$$\theta_{liq,i} = \frac{w_{liq,i}}{f_{sno}\Delta z_i \rho_{liq}} \leq 1-\theta_{ice,i}\,, \tag{7.31}$$

and $S_r = 0.033$ is the irreducible water saturation (snow holds a certain amount of liquid water due to capillary retention after drainage has ceased (Anderson 1976)). The water holding capacity of the underlying layer limits the flow of water $q_{liq,i}$ calculated in equation (7.29), unless the underlying layer is the surface soil layer, as

$$q_{liq,i} \leq \frac{\rho_{liq}\left[1-\theta_{ice,i+1}-\theta_{liq,i+1}\right]\Delta z_{i+1}}{\Delta t} \quad i = snl+1,\ldots,-1\,. \tag{7.32}$$

The liquid water content $w_{liq,i}$ is updated as

$$w_{liq,i}^{n+1} = w_{liq,i}^{n} + \left(q_{i-1} - q_i\right)\Delta t\,. \tag{7.33}$$

Equations (7.29)-(7.33) are solved sequentially from top ($i = snl+1$) to bottom ($i = 0$) snow layer in each time step. The total flow of liquid water reaching the soil surface is then $q_{liq,0}$ which is used in the calculation of surface runoff and infiltration (section 7.3).

7.2.4 Black and organic carbon and mineral dust within snow

Particles within snow originate from atmospheric aerosol deposition (D_{sp} in Table 2.3 (kg m^{-2} s^{-1}) and influence snow radiative transfer (sections 3.2.1, 3.2.2, and 3.3.3). Particle masses and mixing ratios are represented with a simple mass-conserving scheme.

The model maintains masses of the following eight particle species within each snow layer: hydrophilic black carbon, hydrophobic black carbon, hydrophilic organic carbon, hydrophobic organic carbon, and four species of mineral dust with the following particle sizes: 0.1-1.0, 1.0-2.5, 2.5-5.0, and 5.0-10.0 μm. Each of these species has unique optical properties (Table 3.5) and meltwater removal efficiencies (Table 7.1).

The black carbon and organic carbon deposition rates described in Table 2.3 are combined into four categories as follows

$$D_{bc,hphil} = D_{bc,dryhphil} + D_{bc,wethphil} \tag{7.34}$$

$$D_{bc,hphob} = D_{bc,dryhphob} \tag{7.35}$$

$$D_{oc,hphil} = D_{oc,dryhphil} + D_{oc,wethphil} \tag{7.36}$$

$$D_{oc,hphob} = D_{oc,dryhphob} \tag{7.37}$$

Deposited particles are assumed to be instantly mixed (homogeneously) within the surface snow layer and are added after the inter-layer water fluxes are computed (section 7.2.3) so that some aerosol is in the top layer after deposition and is not immediately washed out before radiative calculations are done. Particle masses are then redistributed each time step based on meltwater drainage through the snow column (section 7.2.3) and snow layer combination and subdivision (section 7.2.7). The change in mass of each of the particle species $\Delta m_{sp,i}$ (kg m^{-2}) is

$$\Delta m_{sp,i} = \left[k_{sp} \left(q_{liq,i-1} c_{sp,i-1} - q_{liq,i} c_i \right) + D_{sp} \right] \Delta t \tag{7.38}$$

where k_{sp} is the meltwater scavenging efficiency that is unique for each species (Table 7.1), $q_{liq,i-1}$ is the flow of liquid water into layer i from the layer above, $q_{liq,i}$ is the flow of water out of layer i into the layer below (kg m^{-2} s^{-1}) (section 7.2.3), $c_{sp,i-1}$ and $c_{sp,i}$ are

the particle mass mixing ratios in layers $i-1$ and i (kg kg^{-1}), D_{sp} is the atmospheric deposition rate (zero for all layers except layer $snl+1$), and Δt is the model time step (s). The particle mass mixing ratio is

$$c_i = \frac{m_{sp,i}}{w_{liq,i} + w_{ice,i}}. \tag{7.39}$$

Values of k_{sp} are partially derived from experiments published by Conway et al. (1996). Particles masses are re-distributed proportionately with snow mass when layers are combined or divided, thus conserving particle mass within the snow column. The mass of particles carried out with meltwater through the bottom snow layer is assumed to be permanently lost from the snowpack, and is not maintained within the model.

Table 7.1. Meltwater scavenging efficiency for particles within snow

Species	k_{sp}
Hydrophilic black carbon	0.20
Hydrophobic black carbon	0.03
Hydrophilic organic carbon	0.20
Hydrophobic organic carbon	0.03
Dust species 1 (0.1-1.0 μm)	0.02
Dust species 2 (1.0-2.5 μm)	0.02
Dust species 3 (2.5-5.0 μm)	0.01
Dust species 4 (5.0-10.0 μm)	0.01

7.2.5 Initialization of snow layer

If there are no existing snow layers ($snl+1=1$) but $z_{sno} \geq 0.01$ m after accounting for solid precipitation q_{sno}, then a snow layer is initialized ($snl=-1$) as follows

$$\begin{aligned} \Delta z_0 &= z_{sno} \\ z_o &= -0.5\Delta z_0 \\ z_{h,-1} &= -\Delta z_0 \\ T_0 &= \min\left(T_f, T_{atm}\right) \\ w_{ice,0} &= W_{sno} \\ w_{liq,0} &= 0 \end{aligned} . \tag{7.40}$$

7.2.6 Snow Compaction

Snow compaction is initiated after the soil hydrology calculations [surface runoff (section 7.3), infiltration (section 7.3), soil water (section 7.4), groundwater-soilwater interactions (section 7.6)] are complete. Compaction of snow includes three types of processes: destructive metamorphism of new snow (crystal breakdown due to wind or

thermodynamic stress); snow load or overburden (pressure); and melting (changes in snow structure due to melt-freeze cycles plus changes in crystals due to liquid water). The total fractional compaction rate for each snow layer $C_{R,i}$ (s^{-1}) is the sum of the three compaction processes

$$C_{R,i} = \frac{1}{\Delta z_i}\frac{\partial \Delta z_i}{\partial t} = C_{R1,i} + C_{R2,i} + C_{R3,i}\,. \tag{7.41}$$

Compaction is not allowed if the layer is saturated

$$1 - \left(\frac{w_{ice,i}}{f_{sno}\Delta z_i \rho_{ice}} + \frac{w_{liq,i}}{f_{sno}\Delta z_i \rho_{liq}} \right) \le 0.001 \tag{7.42}$$

or if the ice content is below a minimum value ($w_{ice,i} \le 0.1$).

Compaction as a result of destructive metamorphism $C_{R1,i}$ (s^{-1}) is temperature dependent (Anderson 1976)

$$C_{R1,i} = \left[\frac{1}{\Delta z_i}\frac{\partial \Delta z_i}{\partial t} \right]_{metamorphism} = -c_3 c_1 c_2 \exp\left[-c_4 \left(T_f - T_i \right) \right] \tag{7.43}$$

where $c_3 = 2.777 \times 10^{-6}$ (s^{-1}) is the fractional compaction rate for $T_i = T_f$, $c_4 = 0.04$ K^{-1}, and

$$\begin{aligned}
c_1 &= 1 && \frac{w_{ice,i}}{f_{sno}\Delta z_i} \le 100 \text{ kg m}^{-3} \\
c_1 &= \exp\left[-0.046 \left(\frac{w_{ice,i}}{f_{sno}\Delta z_i} - 100 \right) \right] && \frac{w_{ice,i}}{f_{sno}\Delta z_i} > 100 \text{ kg m}^{-3} \\
c_2 &= 2 && \frac{w_{liq,i}}{f_{sno}\Delta z_i} > 0.01 \\
c_2 &= 1 && \frac{w_{liq,i}}{f_{sno}\Delta z_i} \le 0.01
\end{aligned} \tag{7.44}$$

where $w_{ice,i}/\left(f_{sno}\Delta z_i\right)$ and $w_{liq,i}/\left(f_{sno}\Delta z_i\right)$ are the bulk densities of liquid water and ice (kg m^{-3}).

The compaction rate as a result of overburden $C_{R2,i}$ (s^{-1}) is a linear function of the snow load pressure $P_{s,i}$ (kg m^{-2}) (Anderson 1976)

$$C_{R2,i} = \left[\frac{1}{\Delta z_i}\frac{\partial \Delta z_i}{\partial t}\right]_{overburden} = -\frac{P_{s,i}}{\eta} \tag{7.45}$$

where η is a viscosity coefficient (kg s m^{-2}) that varies with density and temperature as

$$\eta = \eta_0 \exp\left[c_5\left(T_f - T_i\right) + c_6\frac{w_{ice,i}}{f_{sno}\Delta z_i}\right] \tag{7.46}$$

where $\eta_0 = 9\times10^5$ kg s m^{-2}, and $c_5 = 0.08$ K^{-1}, $c_6 = 0.023$ m^3 kg^{-1} are constants. The snow load pressure $P_{s,i}$ is calculated for each layer as the sum of the ice $w_{ice,i}$ and liquid water contents $w_{liq,i}$ of the layers above plus half the ice and liquid water contents of the layer being compacted

$$P_{s,i} = \frac{\left(w_{ice,i} + w_{liq,i}\right)}{2} + \sum_{j=snl+1}^{j=i-1}\left(w_{ice,j} + w_{liq,j}\right). \tag{7.47}$$

The compaction rate due to melting $C_{R3,i}$ (s^{-1}) is taken to be the ratio of the change in snow ice mass after the melting to the mass before melting

$$C_{R3,i} = \left[\frac{1}{\Delta z_i}\frac{\partial \Delta z_i}{\partial t}\right]_{melt} = -\frac{1}{\Delta t}\max\left(0, \frac{W_{sno,i}^n - W_{sno,i}^{n+1}}{W_{sno,i}^n}\right) \tag{7.48}$$

and melting is identified during the phase change calculations (section 6.2). Because snow depth is defined as the average depth of the snow covered area, the snow depth must also be updated for changes in f_{sno}.

$$C_{R4,i} = \left[\frac{1}{\Delta z_i} \frac{\partial \Delta z_i}{\partial t} \right]_{fsno} = -\frac{1}{\Delta t} \max\left(0, \frac{f_{sno,i}^{n} - f_{sno,i}^{n+1}}{f_{sno,i}^{n}} \right) \tag{7.49}$$

The snow layer thickness after compaction is then

$$\Delta z_i^{n+1} = \Delta z_i^{n} \left(1 + C_{R,i} \Delta t \right). \tag{7.50}$$

7.2.7 Snow Layer Combination and Subdivision

After the determination of snow temperature including phase change (Chapter 6), snow hydrology (sections 7.2.2, 7.2.3, and 7.2.4), and the compaction calculations (7.2.6), the number of snow layers is adjusted by either combining or subdividing layers. The combination and subdivision of snow layers is based on Jordan (1991).

7.2.7.1 Combination

If a snow layer has nearly melted or if its thickness Δz_i is less than the prescribed minimum thickness $\Delta z_{\min}$ (Table 7.2), the layer is combined with a neighboring layer. The overlying or underlying layer is selected as the neighboring layer according to the following rules

- If the top layer is being removed, it is combined with the underlying layer
- If the underlying layer is not snow (i.e., it is the top soil layer), the layer is combined with the overlying layer
- If the layer is nearly completely melted, the layer is combined with the underlying layer
- If none of the above rules apply, the layer is combined with the thinnest neighboring layer.

A first pass is made through all snow layers to determine if any layer is nearly melted ($w_{ice,i} \le 0.1$). If so, the remaining liquid water and ice content of layer i is combined with the underlying neighbor $i+1$ as

$$w_{liq,i+1} = w_{liq,i+1} + w_{liq,i} \tag{7.51}$$

$$w_{ice,i+1} = w_{ice,i+1} + w_{ice,i}\,. \tag{7.52}$$

This includes the snow layer directly above the top soil layer. In this case, the liquid water and ice content of the melted snow layer is added to the contents of the top soil layer. The layer properties, T_i, $w_{ice,i}$, $w_{liq,i}$, Δz_i, are then re-indexed so that the layers above the eliminated layer are shifted down by one and the number of snow layers is decremented accordingly.

At this point, if there are no explicit snow layers remaining ($snl = 0$), the snow water equivalent W_{sno} and snow depth z_{sno} are set to zero, otherwise, W_{sno} and z_{sno} are re-calculated as

$$W_{sno} = \sum_{i=snl+1}^{i=0} \left(w_{ice,i} + w_{liq,i} \right) \tag{7.53}$$

$$z_{sno} = \sum_{i=snl+1}^{i=0} \Delta z_i\,. \tag{7.54}$$

If the snow depth $0 < z_{sno} < 0.01$ m or the snow density $\dfrac{W_{sno}}{f_{sno} z_{sno}} < 50$ kg/m3, the number of snow layers is set to zero, the total ice content of the snowpack $\sum_{i=snl+1}^{i=0} w_{ice,i}$ is assigned to W_{sno}, and the total liquid water $\sum_{i=snl+1}^{i=0} w_{liq,i}$ is assigned to the top soil layer. Otherwise, the layers are combined according to the rules above.

When two snow layers are combined (denoted here as 1 and 2), their thickness combination (c) is

$$\Delta z_c = \Delta z_1 + \Delta z_2 , \tag{7.55}$$

their mass combination is

$$w_{liq,c} = w_{liq,1} + w_{liq,2} \tag{7.56}$$

$$w_{ice,c} = w_{ice,1} + w_{ice,2} , \tag{7.57}$$

and their temperatures are combined as

$$T_c = T_f + \frac{h_c - L_f w_{liq,c}}{C_{ice} w_{ice,c} + C_{liq} w_{liq,c}} \tag{7.58}$$

where $h_c = h_1 + h_2$ is the combined enthalpy h_i of the two layers where

$$h_i = \left(C_{ice} w_{ice,i} + C_{liq} w_{liq,i} \right) \left(T_i - T_f \right) + L_f w_{liq,i} . \tag{7.59}$$

In these equations, L_f is the latent heat of fusion (J kg^{-1}) and C_{liq} and C_{ice} are the specific heat capacities (J kg^{-1} K^{-1}) of liquid water and ice, respectively (Table 2.6). After layer combination, the node depths and layer interfaces (Figure 7.2) are recalculated from

$$z_i = z_{h,i} - 0.5 \Delta z_i \qquad i = 0, \ldots, snl + 1 \tag{7.60}$$

$$z_{h,i-1} = z_{h,i} - \Delta z_i \qquad i = 0, \ldots, snl + 1 \tag{7.61}$$

where Δz_i is the layer thickness.

Table 7.2. Minimum and maximum thickness of snow layers (m)

Layer	$\Delta z_{\min}$	N_l	N_u	$(\Delta z_{\max})_l$	$(\Delta z_{\max})_u$
1 (top)	0.010	1	>1	0.03	0.02
2	0.015	2	>2	0.07	0.05
3	0.025	3	>3	0.18	0.11
4	0.055	4	>4	0.41	0.23
5 (bottom)	0.115	5	-	-	-

The maximum snow layer thickness, $\Delta z_{\max}$, depends on the number of layers, N_l and N_u (section 7.2.7.2).

7.2.7.2 Subdivision

The snow layers are subdivided when the layer thickness exceeds the prescribed maximum thickness $\Delta z_{\max}$ with lower and upper bounds that depend on the number of snow layers (Table 7.2). For example, if there is only one layer, then the maximum thickness of that layer is 0.03 m, however, if there is more than one layer, then the maximum thickness of the top layer is 0.02 m. Layers are checked sequentially from top to bottom for this limit. If there is only one snow layer and its thickness is greater than 0.03 m (Table 7.2), the layer is subdivided into two layers of equal thickness, liquid water and ice contents, and temperature. If there is an existing layer below the layer to be subdivided, the thickness Δz_i, liquid water and ice contents, $w_{liq,i}$ and $w_{ice,i}$, and temperature T_i of the excess snow are combined with the underlying layer according to equations (7.55)-(7.58). If there is no underlying layer after adjusting the layer for the excess snow, the layer is subdivided into two layers of equal thickness, liquid water and

ice contents. The vertical snow temperature profile is maintained by calculating the slope between the layer above the splitting layer (T_1) and the splitting layer (T_2) and constraining the new temperatures (T_2^{n+1}, T_3^{n+1}) to lie along this slope. The temperature of the lower layer is first evaluated from

$$T_3' = T_2^n - \left(\frac{T_1^n - T_2^n}{\left(\Delta z_1^n + \Delta z_2^n\right)/2} \right) \left(\frac{\Delta z_2^{n+1}}{2} \right), \tag{7.62}$$

then adjusted as,

$$\begin{aligned} T_3^{n+1} &= T_2^n && T_3' \geq T_f \\ T_2^{n+1} &= T_2^n + \left(\frac{T_1^n - T_2^n}{\left(\Delta z_1 + \Delta z_2^n\right)/2} \right) \left(\frac{\Delta z_2^{n+1}}{2} \right) && T_3' < T_f \end{aligned} \tag{7.63}$$

where here the subscripts 1, 2, and 3 denote three layers numbered from top to bottom. After layer subdivision, the node depths and layer interfaces are recalculated from equations (7.60) and (7.61).

7.3 Surface Runoff, Surface Water Storage, and Infiltration

The moisture input at the grid cell surface , $q_{liq,0}$, is the sum of liquid precipitation reaching the ground and melt water from snow (kg m^{-2} s^{-1}). The moisture flux is then partitioned between surface runoff, surface water storage, and infiltration into the soil.

7.3.1 Surface Runoff

The simple TOPMODEL-based (Beven and Kirkby 1979) runoff model (SIMTOP) described by Niu et al. (2005) is implemented to parameterize runoff. A key concept underlying this approach is that of fractional saturated area f_{sat}, which is determined by the topographic characteristics and soil moisture state of a grid cell. The saturated

portion of a grid cell contributes to surface runoff, q_{over}, by the saturation excess mechanism (Dunne runoff)

$$q_{over} = f_{sat} q_{liq,0} \tag{7.64}$$

The fractional saturated area is a function of soil moisture

$$f_{sat} = f_{\max} \exp\left(-0.5 f_{over} z_{\nabla}\right) \tag{7.65}$$

where $f_{\max}$ is the potential or maximum value of f_{sat}, f_{over} is a decay factor (m^{-1}), and z_{∇} is the water table depth (m) (section 7.6). The maximum saturated fraction, $f_{\max}$, is defined as the value of the discrete cumulative distribution function (CDF) of the topographic index when the grid cell mean water table depth is zero. Thus, $f_{\max}$ is the percent of pixels in a grid cell whose topographic index is larger than or equal to the grid cell mean topographic index. It should be calculated explicitly from the CDF at each grid cell at the resolution that the model is run. However, because this is a computationally intensive task for global applications, $f_{\max}$ is calculated once at 0.125° resolution using the 1-km compound topographic indices (CTIs) based on the HYDRO1K dataset (Verdin and Greenlee 1996) from USGS following the algorithm in Niu et al. (2005) and then area-averaged to the desired model resolution (section 2.2.3). Pixels with CTIs exceeding the 95 percentile threshold in each 0.125° grid cell are excluded from the calculation to eliminate biased estimation of statistics due to large CTI values at pixels on stream networks. For grid cells over regions without CTIs such as Australia, the global mean $f_{\max}$ is used to fill the gaps. See Li et al. (2013b) for additional details. The decay factor f_{over} for global simulations was determined through sensitivity analysis and comparison with observed runoff to be 0.5 m^{-1}.

7.3.2 Surface Water Storage

A surface water store has been added to the model to represent wetlands and small, sub-grid scale water bodies. As a result, the wetland land unit has been removed. The state variables for surface water are the mass of water W_{sfc} (kg m^{-2}) and temperature T_{h2osfc} (Chapter 6). Surface water storage and outflow are functions of fine spatial scale elevation variations called microtopography. The microtopography is assumed to be distributed normally around the grid cell mean elevation. Given the standard deviation of the microtopographic distribution, σ_{micro} (m), the fractional area of the grid cell that is inundated can be calculated. Surface water storage, W_{sfc}, is related to the height (relative to the grid cell mean elevation) of the surface water, d, by

$$W_{sfc} = \frac{d}{2}\left(1 + erf\left(\frac{d}{\sigma_{micro}\sqrt{2}}\right)\right) + \frac{\sigma_{micro}}{\sqrt{2\pi}} e^{\frac{-d^2}{2\sigma_{micro}^2}} \tag{7.66}$$

where erf is the error function. For a given value of W_{sfc}, equation (7.66) can be solved for d using the Newton-Raphson method. Once d is known, one can determine the fraction of the area that is inundated as

$$f_{h2osfc} = \frac{1}{2}\left(1 + erf\left(\frac{d}{\sigma_{micro}\sqrt{2}}\right)\right) \tag{7.67}$$

No global datasets exist for microtopography, so the default parameterization is a simple function of slope

$$\sigma_{micro} = \left(\beta + \beta_0\right)^{\eta} \tag{7.68}$$

where β is the topographic slope, $\beta_0 = (\sigma_{\max})^{\frac{1}{\eta}}$ determines the maximum value of σ, and η is an adjustable parameter. Default values in the model are $\sigma_{\max} = 0.4$ and $\eta = -3$.

If the spatial scale of the microtopography is small relative to that of the grid cell, one can assume that the inundated areas are distributed randomly within the grid cell. With this assumption, a result from percolation theory can be used to quantify the fraction of the inundated portion of the grid cell that is interconnected

$$\begin{aligned} f_{connected} &= \left(f_{h2osfc} - f_c\right)^{\mu} \qquad for\ f_{h2osfc} > f_c \\ f_{connected} &= 0 \qquad\qquad\qquad\quad for\ f_{h2osfc} \le f_c \end{aligned} \tag{7.69}$$

where f_c is a threshold below which no single connected inundated area spans the grid cell and μ is a scaling exponent. Default values of f_c and μ are 0.4 and 0.14, respectively. When the inundated fraction of the grid cell surpasses f_c, the surface water store acts as a linear reservoir

$$q_{out,\,h2osfc} = k_{h2osfc} f_{connected} (W_{sfc} - W_c) \frac{1}{\Delta t} \tag{7.70}$$

where $q_{out,\,h2osfc}$ is the surface water runoff, k_{h2osfc} is a constant, W_c is the amount of surface water present when $f_{h2osfc} = f_c$, and Δt is the model time step. The linear storage coefficent $k_{h2osfc} = \sin(\beta)$ is a function of grid cell mean topographic slope where β is the slope in radians.

7.3.3 Infiltration

The surface moisture flux remaining after surface runoff has been removed,

$$q_{\text{in},\,surface} = (1 - f_{sat}) q_{liq,0} \tag{7.71}$$

is divided into inputs to surface water ($q_{in,h2osfc}$) and the soil $q_{in,soil}$. If $q_{in,soil}$ exceeds the maximum soil infiltration capacity (kg m^{-2} s^{-1}),

$$q_{infl,\max} = (1 - f_{sat})\Theta_{ice} k_{sat} \tag{7.72}$$

where Θ_{ice} is an ice impedance factor (section 7.4), infiltration excess (Hortonian) runoff is generated

$$q_{infl,excess} = \max\left(q_{in,soil} - \left(1 - f_{h2osfc}\right) q_{\mathrm{inf}\,l,\max}, 0\right) \tag{7.73}$$

and transferred from $q_{in,soil}$ to $q_{in,h2osfc}$. After evaporative losses have been removed, these moisture fluxes are

$$q_{in,h2osfc} = f_{h2osfc} q_{in,surface} + q_{infl,excess} - q_{evap,h2osfc} \tag{7.74}$$

and

$$q_{\mathrm{in},\,soil} = (1 - f_{h2osfc}) q_{in,surface} - q_{\mathrm{inf}\,l,excess} - (1 - f_{sno} - f_{h2osfc}) q_{evap,\,soil} \tag{7.75}$$

The balance of surface water is then calculated as

$$\Delta W_{sfc} = \left(q_{in,\,h2osfc} - q_{out,\,h2osfc} - q_{drain,\,h2osfc}\right)\Delta t \tag{7.76}$$

Bottom drainage from the surface water store

$$q_{drain,\,h2osfc} = \min\left(f_{h2osfc} q_{\mathrm{inf}\,l,\max}, \frac{W_{sfc}}{\Delta t}\right) \tag{7.77}$$

is then added to $q_{in,soil}$ giving the total infiltration into the surface soil layer

$$q_{infl} = q_{in,soil} + q_{drain,h2osfc} \tag{7.78}$$

Infiltration q_{infl} and explicit surface runoff q_{over} are not allowed for glaciers.

7.4 Soil Water

Soil water is predicted from a multi-layer model, in which the vertical soil moisture transport is governed by infiltration, surface and sub-surface runoff, gradient diffusion, gravity, canopy transpiration through root extraction, and interactions with groundwater (Figure 7.1). The following derivation generally follows that of Z.-L. Yang (1998, unpublished manuscript) with modifications by Zeng and Decker (2009).

For one-dimensional vertical water flow in soils, the conservation of mass is stated as

$$\frac{\partial \theta}{\partial t} = -\frac{\partial q}{\partial z} - Q \tag{7.79}$$

where θ is the volumetric soil water content (mm^3 of water mm^{-3} of soil), t is time (s), z is height above some datum in the soil column (mm) (positive upwards), q is soil water flux (kg m^{-2} s^{-1} or mm s^{-1}) (positive upwards), and Q is a soil moisture sink term (mm of water mm^{-1} of soil s^{-1}) (ET loss). This equation is solved numerically by dividing the soil column into multiple layers in the vertical and integrating downward over each layer with an upper boundary condition of the infiltration flux into the top soil layer q_{infl} and a lower boundary condition that depends on the depth of the water table.

The soil water flux q in equation (7.79) can be described by Darcy's law

$$q = -k \frac{\partial \psi_h}{\partial z} \tag{7.80}$$

where k is the hydraulic conductivity (mm s^{-1}), and ψ_h is the hydraulic potential (mm). The hydraulic potential is

$$\psi_h = \psi_m + \psi_z \tag{7.81}$$

where ψ_m is the soil matric potential (mm) (which is related to the adsorptive and capillary forces within the soil matrix), and ψ_z is the gravitational potential (mm) (the vertical distance from an arbitrary reference elevation to a point in the soil). If the reference elevation is the soil surface, then $\psi_z = z$. Letting $\psi = \psi_m$, Darcy's law becomes

$$q = -k\left[\frac{\partial(\psi + z)}{\partial z}\right]. \tag{7.82}$$

Darcy's equation can be further manipulated to yield

$$q = -k\left[\frac{\partial(\psi + z)}{\partial z}\right] = -k\left(\frac{\partial \psi}{\partial z} + 1\right) = -k\left(\frac{\partial \theta}{\partial z}\frac{\partial \psi}{\partial \theta} + 1\right). \tag{7.83}$$

Substitution of this equation into equation (7.79), with $Q = 0$, yields the Richards equation

$$\frac{\partial \theta}{\partial t} = \frac{\partial}{\partial z}\left[k\left(\frac{\partial \theta}{\partial z}\frac{\partial \psi}{\partial \theta}\right) + 1\right]. \tag{7.84}$$

Zeng and Decker (2009) note that this θ-based form of the Richards equation cannot maintain the hydrostatic equilibrium soil moisture distribution because of the truncation errors of the finite-difference numerical scheme. They show that this deficiency can be overcome by subtracting the equilibrium state from equation (7.82) as

$$q = -k\left[\frac{\partial(\psi + z - C)}{\partial z}\right] \tag{7.85}$$

where C is a constant hydraulic potential above the water table z_∇

$$C = \psi_E + z = \psi_{sat}\left[\frac{\theta_E(z)}{\theta_{sat}}\right]^{-B} + z = \psi_{sat} + z_\nabla \tag{7.86}$$

so that

$$q = -k\left[\frac{\partial(\psi - \psi_E)}{\partial z}\right] \tag{7.87}$$

where ψ_E is the equilibrium soil matric potential (mm). Substitution of equations (7.86) and (7.85) into equation (7.84) yields Zeng and Decker's (2009) modified Richards equation

$$\frac{\partial \theta}{\partial t} = \frac{\partial}{\partial z}\left[k\left(\frac{\partial(\psi - \psi_E)}{\partial z}\right)\right] - Q \tag{7.88}$$

where the soil moisture sink term Q is now included.

7.4.1 Hydraulic Properties

The hydraulic conductivity k_i (mm s^{-1}) and the soil matric potential ψ_i (mm) for layer i vary with volumetric soil water θ_i and soil texture. As with the soil thermal properties (section 6.3) the hydraulic properties of the soil are assumed to be a weighted combination of the mineral properties, which are determined according to sand and clay contents based on work by Clapp and Hornberger (1978) and Cosby et al. (1984), and organic properties of the soil (Lawrence and Slater 2008).

The hydraulic conductivity is defined at the depth of the interface of two adjacent layers $z_{h,i}$ (Figure 7.3) and is a function of the saturated hydraulic conductivity $k_{sat}\left[z_{h,i}\right]$, the liquid volumetric soil moisture of the two layers θ_i and θ_{i+1} and an ice impedance factor Θ_{ice}

$$k\left[z_{h,i}\right]=\left\{\begin{array}{ll}\Theta_{ice}k_{sat}\left[z_{h,i}\right]\left[\dfrac{0.5\left(\theta_i+\theta_{i+1}\right)}{0.5\left(\theta_{sat,i}+\theta_{sat,i+1}\right)}\right]^{2B_i+3} & 1\le i\le N_{levsoi}-1 \\ \Theta_{ice}k_{sat}\left[z_{h,i}\right]\left(\dfrac{\theta_i}{\theta_{sat,i}}\right)^{2B_i+3} & i=N_{levsoi}\end{array}\right\}. \quad (7.89)$$

The ice impedance factor is a function of ice content, and is meant to quantify the increased tortuosity of the water flow when part of the pore space is filled with ice. Swenson et al. (2012) used a power law form $\Theta_{ice}=10^{-\Omega F_{ice}}$ where $\Omega=6$ and $F_{ice}=\dfrac{\theta_{ice}}{\theta_{sat}}$ is the ice-filled fraction of the pore space.

Because the hydraulic properties of mineral and organic soil may differ significantly, the bulk hydraulic properties of each soil layer are computed as weighted averages of the properties of the mineral and organic components. The water content at saturation (i.e. porosity) is

$$\theta_{sat,i}=(1-f_{om,i})\theta_{sat,\min,i}+f_{om,i}\theta_{sat,om} \quad (7.90)$$

where $f_{om,i}$ is the soil organic matter fraction, $\theta_{sat,om}=0.9$ (Farouki 1981; Letts et al. 2000) is the porosity of organic matter and the porosity of the mineral soil $\theta_{sat,\min,i}$ is

$$\theta_{sai,\min,i}=0.489-0.00126(\%sand)_i. \quad (7.91)$$

The exponent "B" is

$$B_i=(1-f_{om,i})B_{\min,i}+f_{om,i}B_{om} \quad (7.92)$$

where $B_{om}=2.7$ (Letts et al. 2000) and

$$B_{\min,i}=2.91+0.159(\%clay)_i. \quad (7.93)$$

The soil matric potential (mm) is defined at the node depth z_i of each layer i (Figure 7.3)

$$\psi_i = \psi_{sat,i}\left(\frac{\theta_i}{\theta_{sat,i}}\right)^{-B_i} \geq -1\times10^8 \qquad 0.01 \leq \frac{\theta_i}{\theta_{sat,i}} \leq 1 \tag{7.94}$$

where the saturated soil matric potential (mm) is

$$\psi_{sat,i} = (1 - f_{om,i})\psi_{sat,\min,i} + f_{om,i}\psi_{sat,om} \tag{7.95}$$

where $\psi_{sat,om} = -10.3\,\text{mm}$ (Letts et al. 2000) is the saturated organic matter matric potential and the saturated mineral soil matric potential $\psi_{sat,\min,i}$ is

$$\psi_{sat,\min,i} = -10.0\times10^{1.88-0.0131(\%sand)_i}\,. \tag{7.96}$$

The saturated hydraulic conductivity, $k_{sat}\left[z_{h,i}\right]$ (mm s^{-1}), for organic soils ($k_{sat,om}$) may be two to three orders of magnitude larger than that of mineral soils ($k_{sat,\min}$). Bulk soil layer values of k_{sat} calculated as weighted averages based on f_{om} may therefore be determined primarily by the organic soil properties even for values of f_{om} as low as 1 %. To better represent the influence of organic soil material on the grid cell average saturated hydraulic conductivity, the soil organic matter fraction is further subdivided into "connected" and "unconnected" fractions using a result from percolation theory (Stauffer and Aharony 1994, Berkowitz and Balberg 1992). Assuming that the organic and mineral fractions are randomly distributed throughout a soil layer, percolation theory predicts that above a threshold value $f_{om} = f_{threshold}$, connected flow pathways consisting of organic material only exist and span the soil space. Flow through these pathways

interacts only with organic material, and thus can be described by $k_{sat,om}$. This fraction of the grid cell is given by

$$\begin{aligned} f_{perc} &= N_{perc}\left(f_{om} - f_{threshold}\right)^{\beta_{perc}} f_{om} \qquad f_{om} \geq f_{threshold} \\ f_{perc} &= 0 \qquad\qquad\qquad\qquad\qquad\quad f_{om} < f_{threshold} \end{aligned} \tag{7.97}$$

where $\beta^{perc} = 0.139$, $f_{threshold} = 0.5$, and $N_{perc} = \left(1 - f_{threshold}\right)^{-\beta_{perc}}$. In the unconnected portion of the grid cell, $f_{uncon} = \left(1 - f_{perc}\right)$, the saturated hydraulic conductivity is assumed to correspond to flow pathways that pass through the mineral and organic components in series

$$k_{sat,uncon} = f_{uncon}\left(\frac{\left(1 - f_{om}\right)}{k_{sat,\min}} + \frac{\left(f_{om} - f_{perc}\right)}{k_{sat,om}}\right)^{-1}. \tag{7.98}$$

where saturated hydraulic conductivity for mineral soil depends on soil texture (Cosby et al. 1984) as

$$k_{sat,\min}\left[z_{h,i}\right] = 0.0070556 \times 10^{-0.884 + 0.0153\left(\%sand\right)_i}. \tag{7.99}$$

The bulk soil layer saturated hydraulic conductivity is then computed as

$$k_{sat}\left[z_{h,i}\right] = f_{uncon,i} k_{sat,uncon}\left[z_{h,i}\right] + (1 - f_{uncon,i}) k_{sat,om}\left[z_{h,i}\right]. \tag{7.100}$$

7.4.2 Numerical Solution

With reference to Figure 7.3, the equation for conservation of mass (equation (7.79)) can be integrated over each layer as

$$\int_{-z_{h,i}}^{-z_{h,i-1}} \frac{\partial \theta}{\partial t} dz = -\int_{-z_{h,i}}^{-z_{h,i-1}} \frac{\partial q}{\partial z} dz - \int_{-z_{h,i}}^{-z_{h,i-1}} Q\, dz. \tag{7.101}$$

Note that the integration limits are negative since z is defined as positive upward from the soil surface. This equation can be written as

$$\Delta z_i \frac{\partial \theta_{liq,i}}{\partial t} = -q_{i-1} + q_i - e_i \tag{7.102}$$

where q_i is the flux of water across interface $z_{h,i}$, q_{i-1} is the flux of water across interface $z_{h,i-1}$, and e_i is a layer-averaged soil moisture sink term (ET loss) defined as positive for flow out of the layer (mm s^{-1}). Taking the finite difference with time and evaluating the fluxes implicitly at time $n+1$ yields

$$\frac{\Delta z_i \Delta \theta_{liq,i}}{\Delta t} = -q_{i-1}^{n+1} + q_i^{n+1} - e_i \tag{7.103}$$

where $\Delta \theta_{liq,i} = \theta_{liq,i}^{n+1} - \theta_{liq,i}^{n}$ is the change in volumetric soil liquid water of layer i in time Δt and Δz_i is the thickness of layer i (mm).

The water removed by transpiration in each layer e_i is a function of the total transpiration E_v^t (Chapter 5) and the effective root fraction $r_{e,i}$

$$e_i = r_{e,i} E_v^t . \tag{7.104}$$

Figure 7.3. Schematic diagram of numerical scheme used to solve for soil water fluxes. Shown are three soil layers, $i-1$, i, and $i+1$. The soil matric potential ψ and volumetric soil water θ_{liq} are defined at the layer node depth z. The hydraulic conductivity $k\left[z_h\right]$ is defined at the interface of two layers z_h. The layer thickness is Δz. The soil water fluxes q_{i-1} and q_i are defined as positive upwards. The soil moisture sink term e (ET loss) is defined as positive for flow out of the layer.

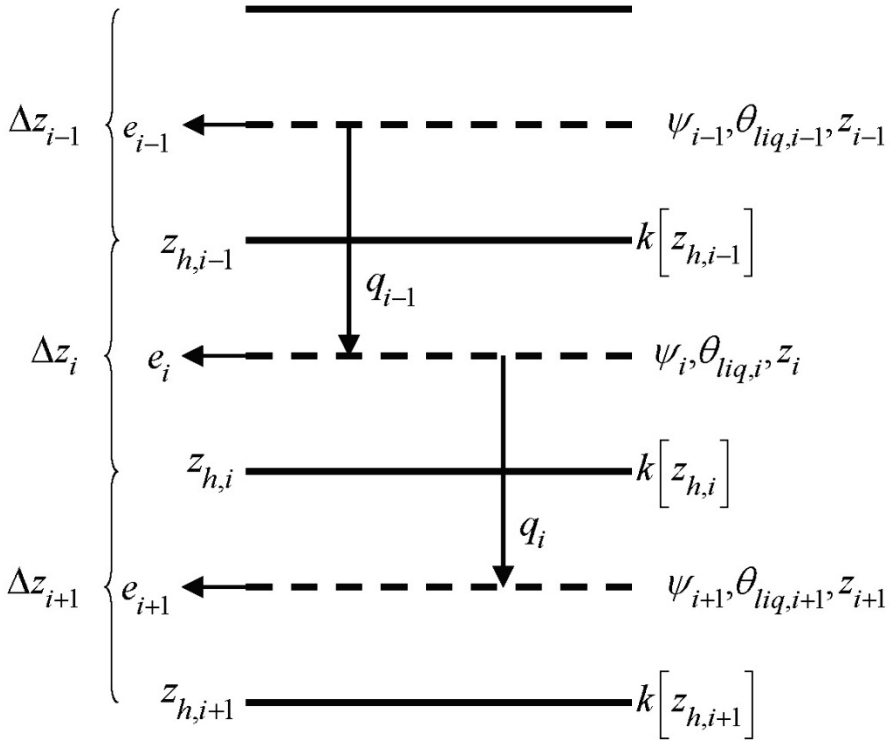

Note that because more than one plant functional type (PFT) may share a soil column, the transpiration E_v^t is a weighted sum of transpiration from all PFTs whose weighting depends on PFT area as

$$E_v^t = \sum_{j=1}^{npft} \left(E_v^t\right)_j \left(wt\right)_j \tag{7.105}$$

where $npft$ is the number of PFTs sharing a soil column, $\left(E_v^t\right)_j$ is the transpiration from the j^{th} PFT on the column, and $\left(wt\right)_j$ is the relative area of the j^{th} PFT with respect to the column. The effective root fraction $r_{e,i}$ is also a column-level quantity that is a weighted sum over all PFTs. The weighting depends on the per unit area transpiration of each PFT and its relative area as

$$r_{e,i} = \frac{\sum_{j=1}^{npft} \left(r_{e,i}\right)_j \left(E_v^t\right)_j \left(wt\right)_j}{\sum_{j=1}^{npft} \left(E_v^t\right)_j \left(wt\right)_j} \tag{7.106}$$

where $\left(r_{e,i}\right)_j$ is the effective root fraction for the j^{th} PFT

$$\begin{aligned} \left(r_{e,i}\right)_j &= \frac{\left(r_i\right)_j \left(w_i\right)_j}{\left(\beta_t\right)_j} \quad && \left(\beta_t\right)_j > 0 \\ \left(r_{e,i}\right)_j &= 0 && \left(\beta_t\right)_j = 0 \end{aligned} \tag{7.107}$$

and $\left(r_i\right)_j$ is the fraction of roots in layer i (Chapter 8), $\left(w_i\right)_j$ is a soil dryness or plant wilting factor for layer i (Chapter 8), and $\left(\beta_t\right)_j$ is a wetness factor for the total soil column for the j^{th} PFT (Chapter 8).

The soil water fluxes in equation (7.103), which are a function of $\theta_{liq,i}$ and $\theta_{liq,i+1}$ because of their dependence on hydraulic conductivity and soil matric potential, can be linearized about θ using a Taylor series expansion as

$$q_i^{n+1} = q_i^n + \frac{\partial q_i}{\partial \theta_{liq,i}} \Delta\theta_{liq,i} + \frac{\partial q_i}{\partial \theta_{liq,i+1}} \Delta\theta_{liq,i+1} \tag{7.108}$$

$$q_{i-1}^{n+1} = q_{i-1}^n + \frac{\partial q_{i-1}}{\partial \theta_{liq,i-1}} \Delta\theta_{liq,i-1} + \frac{\partial q_{i-1}}{\partial \theta_{liq,i}} \Delta\theta_{liq,i} \,. \tag{7.109}$$

Substitution of these expressions for q_i^{n+1} and q_{i-1}^{n+1} into equation (7.103) results in a general tridiagonal equation set of the form

$$r_i = a_i \Delta\theta_{liq,i-1} + b_i \Delta\theta_{liq,i} + c_i \Delta\theta_{liq,i+1} \tag{7.110}$$

where

$$a_i = -\frac{\partial q_{i-1}}{\partial \theta_{liq,i-1}} \tag{7.111}$$

$$b_i = \frac{\partial q_i}{\partial \theta_{liq,i}} - \frac{\partial q_{i-1}}{\partial \theta_{liq,i}} - \frac{\Delta z_i}{\Delta t} \tag{7.112}$$

$$c_i = \frac{\partial q_i}{\partial \theta_{liq,i+1}} \tag{7.113}$$

$$r_i = q_{i-1}^n - q_i^n + e_i \,. \tag{7.114}$$

The tridiagonal equation set is solved over $i = 1, \ldots, N_{levsoi} + 1$ where the layer $i = N_{levsoi} + 1$ is a virtual layer representing the aquifer.

The finite-difference forms of the fluxes and partial derivatives in equations (7.111) -(7.114) can be obtained from equation (7.87) as

$$q_{i-1}^{n} = -k\left[z_{h,i-1}\right]\left[\frac{\left(\psi_{i-1}-\psi_{i}\right)+\left(\psi_{E,i}-\psi_{E,i-1}\right)}{z_{i}-z_{i-1}}\right] \tag{7.115}$$

$$q_{i}^{n} = -k\left[z_{h,i}\right]\left[\frac{\left(\psi_{i}-\psi_{i+1}\right)+\left(\psi_{E,i+1}-\psi_{E,i}\right)}{z_{i+1}-z_{i}}\right] \tag{7.116}$$

$$\frac{\partial q_{i-1}}{\partial \theta_{liq,i-1}} = -\left[\frac{k\left[z_{h,i-1}\right]}{z_{i}-z_{i-1}}\frac{\partial \psi_{i-1}}{\partial \theta_{liq,i-1}}\right]-\frac{\partial k\left[z_{h,i-1}\right]}{\partial \theta_{liq,i-1}}\left[\frac{\left(\psi_{i-1}-\psi_{i}\right)+\left(\psi_{E,i}-\psi_{E,i-1}\right)}{z_{i}-z_{i-1}}\right] \tag{7.117}$$

$$\frac{\partial q_{i-1}}{\partial \theta_{liq,i}} = \left[\frac{k\left[z_{h,i-1}\right]}{z_{i}-z_{i-1}}\frac{\partial \psi_{i}}{\partial \theta_{liq,i}}\right]-\frac{\partial k\left[z_{h,i-1}\right]}{\partial \theta_{liq,i}}\left[\frac{\left(\psi_{i-1}-\psi_{i}\right)+\left(\psi_{E,i}-\psi_{E,i-1}\right)}{z_{i}-z_{i-1}}\right] \tag{7.118}$$

$$\frac{\partial q_{i}}{\partial \theta_{liq,i}} = -\left[\frac{k\left[z_{h,i}\right]}{z_{i+1}-z_{i}}\frac{\partial \psi_{i}}{\partial \theta_{liq,i}}\right]-\frac{\partial k\left[z_{h,i}\right]}{\partial \theta_{liq,i}}\left[\frac{\left(\psi_{i}-\psi_{i+1}\right)+\left(\psi_{E,i+1}-\psi_{E,i}\right)}{z_{i+1}-z_{i}}\right] \tag{7.119}$$

$$\frac{\partial q_{i}}{\partial \theta_{liq,i+1}} = \left[\frac{k\left[z_{h,i}\right]}{z_{i+1}-z_{i}}\frac{\partial \psi_{i+1}}{\partial \theta_{liq,i+1}}\right]-\frac{\partial k\left[z_{h,i}\right]}{\partial \theta_{liq,i+1}}\left[\frac{\left(\psi_{i}-\psi_{i+1}\right)+\left(\psi_{E,i+1}-\psi_{E,i}\right)}{z_{i+1}-z_{i}}\right]. \tag{7.120}$$

The derivatives of the soil matric potential at the node depth are derived from equation (7.94)

$$\frac{\partial \psi_{i-1}}{\partial \theta_{liq,\,i-1}} = -B_{i-1}\frac{\psi_{i-1}}{\theta_{i-1}} \tag{7.121}$$

$$\frac{\partial \psi_{i}}{\partial \theta_{liq,i}} = -B_{i}\frac{\psi_{i}}{\theta_{i}} \tag{7.122}$$

$$\frac{\partial \psi_{i+1}}{\partial \theta_{liq,i+1}} = -B_{i+1}\frac{\psi_{i+1}}{\theta_{i+1}} \tag{7.123}$$

with the constraint $0.01\theta_{sat,i} \le \theta_{i} \le \theta_{sat,i}$.

The derivatives of the hydraulic conductivity at the layer interface are derived from equation (7.89)

$$\frac{\partial k\left[z_{h,i-1}\right]}{\partial \theta_{liq,i-1}} = \frac{\partial k\left[z_{h,i-1}\right]}{\partial \theta_{liq,i}} = \left(1 - \frac{f_{frz,i-1} + f_{frz,i}}{2}\right)\left(2B_{i-1} + 3\right) k_{sat}\left[z_{h,i-1}\right] \times \left[\frac{0.5\left(\theta_{i-1} + \theta_i\right)}{0.5\left(\theta_{sat,i-1} + \theta_{sat,i}\right)}\right]^{2B_{i-1}+2} \left(\frac{0.5}{0.5\left(\theta_{sat,i-1} + \theta_{sat,i}\right)}\right) \quad (7.124)$$

$$\frac{\partial k\left[z_{h,i}\right]}{\partial \theta_{liq,i}} = \frac{\partial k\left[z_{h,i}\right]}{\partial \theta_{liq,i+1}} = \left(1 - \frac{f_{frz,i} + f_{frz,i+1}}{2}\right)\left(2B_i + 3\right) k_{sat}\left[z_{h,i}\right] \times \left[\frac{0.5\left(\theta_i + \theta_{i+1}\right)}{0.5\left(\theta_{sat,i} + \theta_{sat,i+1}\right)}\right]^{2B_i+2} \left(\frac{0.5}{0.5\left(\theta_{sat,i} + \theta_{sat,i+1}\right)}\right). \quad (7.125)$$

7.4.2.1 Equilibrium soil matric potential and volumetric moisture

The equilibrium soil matric potential ψ_E can be derived from equation (7.86) as

$$\psi_E = \psi_{sat}\left(\frac{\theta_E(z)}{\theta_{sat}}\right)^{-B} \quad (7.126)$$

and the equilibrium volumetric water content $\theta_E(z)$ at depth z can also be derived as

$$\theta_E(z) = \theta_{sat}\left(\frac{\psi_{sat} + z_\nabla - z}{\psi_{sat}}\right)^{-\frac{1}{B}}. \quad (7.127)$$

Here, the soil matric potentials, the water table depth z_∇ and the soil depths have units of mm. For the finite-difference scheme, a layer-average equilibrium volumetric water content is used in equation (7.126) and can be obtained from

$$\overline{\theta_{E,i}} = \int_{z_{h,i-1}}^{z_{h,i}} \frac{\theta_E(z)}{z_{h,i} - z_{h,i-1}} dz \quad (7.128)$$

which when integrated yields

$$\overline{\theta_{E,i}} = \frac{\theta_{sat,i}\psi_{sat,i}}{\left(z_{h,i} - z_{h,i-1}\right)\left(1 - \frac{1}{B_i}\right)}\left[\left(\frac{\psi_{sat,i} - z_\nabla + z_{h,i}}{\psi_{sat,i}}\right)^{1-\frac{1}{B_i}} - \left(\frac{\psi_{sat,i} - z_\nabla + z_{h,i-1}}{\psi_{sat,i}}\right)^{1-\frac{1}{B_i}}\right]. \quad (7.129)$$

Equation (7.129) is valid when the water table z_{∇} is deeper than both interface depths $z_{h,i-1}$ and $z_{h,i}$. Since the water table can be within the soil column, the equation is modified if the water table is within soil layer i ($z_{h,i-1} < z_{\nabla} < z_{h,i}$) as a weighted average of the saturated part and the unsaturated part

$$\overline{\theta_{E,i}} = \overline{\theta_{E,sat,i}} \left(\frac{z_{h,i} - z_{\nabla}}{z_{h,i} - z_{h,i-1}} \right) + \overline{\theta_{E,unsat,i}} \left(\frac{z_{\nabla} - z_{h,i-1}}{z_{h,i} - z_{h,i-1}} \right) \tag{7.130}$$

where $\overline{\theta_{E,sat,i}} = \theta_{sat,i}$ and the unsaturated part $\overline{\theta_{E,unsat,i}}$ is

$$\overline{\theta_{E,unsat,i}} = \frac{\theta_{sat,i} \psi_{sat,i}}{\left(z_{\nabla} - z_{h,i-1} \right) \left(1 - \frac{1}{B_i} \right)} \left[1 - \left(\frac{\psi_{sat,i} - z_{\nabla} + z_{h,i-1}}{\psi_{sat,i}} \right)^{1 - \frac{1}{B_i}} \right]. \tag{7.131}$$

If $z_{\nabla} < z_{h,i-1}$, then $\overline{\theta_{E,i}} = \overline{\theta_{E,sat,i}} = \theta_{sat,i}$. If the water table is below the soil column ($z_{\nabla} > z_{h,N_{levsoi}}$), an equilibrium volumetric soil moisture is calculated for a virtual layer $i = N_{levsoi} + 1$ as

$$\overline{\theta_{E,i=N_{levsoi+1}}} = \frac{\theta_{sat,i-1} \psi_{sat,i-1}}{\left(z_{\nabla} - z_{h,i-1} \right) \left(1 - \frac{1}{B_{i-1}} \right)} \left[1 - \left(\frac{\psi_{sat,i-1} - z_{\nabla} + z_{h,i-1}}{\psi_{sat,i-1}} \right)^{1 - \frac{1}{B_{i-1}}} \right] \tag{7.132}$$

The equilibrium volumetric soil moisture is constrained by

$$0 \le \overline{\theta_{E,i}} \le \theta_{sat,i} \tag{7.133}$$

The equilibrium soil matric potential is then

$$\psi_{E,i} = \psi_{sat,i} \left(\frac{\overline{\theta_{E,i}}}{\theta_{sat,i}} \right)^{-B_i} \ge -1 \times 10^8 \qquad \frac{\overline{\theta_{E,i}}}{\theta_{sat,i}} \ge 0.01 \tag{7.134}$$

7.4.2.2 Equation set for layer $i = 1$

For the top soil layer ($i = 1$), the boundary condition is the infiltration rate (section 7.3), $q_{i-1}^{n+1} = -q_{infl}^{n+1}$, and the water balance equation is

$$\frac{\Delta z_i \Delta \theta_{liq,i}}{\Delta t} = q_{infl}^{n+1} + q_i^{n+1} - e_i \,. \tag{7.135}$$

After grouping like terms, the coefficients of the tridiagonal set of equations for $i = 1$ are

$$a_i = 0 \tag{7.136}$$

$$b_i = \frac{\partial q_i}{\partial \theta_{liq,i}} - \frac{\Delta z_i}{\Delta t} \tag{7.137}$$

$$c_i = \frac{\partial q_i}{\partial \theta_{liq,i+1}} \tag{7.138}$$

$$r_i = q_{infl}^{n+1} - q_i^n + e_i \,. \tag{7.139}$$

7.4.2.3 Equation set for layers $i = 2, \ldots, N_{levsoi} - 1$

The coefficients of the tridiagonal set of equations for $i = 2, \ldots, N_{levsoi} - 1$ are

$$a_i = -\frac{\partial q_{i-1}}{\partial \theta_{liq,i-1}} \tag{7.140}$$

$$b_i = \frac{\partial q_i}{\partial \theta_{liq,i}} - \frac{\partial q_{i-1}}{\partial \theta_{liq,i}} - \frac{\Delta z_i}{\Delta t} \tag{7.141}$$

$$c_i = \frac{\partial q_i}{\partial \theta_{liq,i+1}} \tag{7.142}$$

$$r_i = q_{i-1}^n - q_i^n + e_i \,. \tag{7.143}$$

7.4.2.4 Equation set for layers $i = N_{levsoi}, \ldots N_{levsoi}+1$

For the lowest soil layer ($i = N_{levsoi}$), the bottom boundary condition depends on the depth of the water table. If the water table is within the soil column ($z_{\nabla} \le z_{h,N_{levsoi}}$), a zero-flux bottom boundary condition is applied ($q_i^n = 0$) and the coefficients of the tridiagonal set of equations for $i = N_{levsoi}$ are

$$a_i = -\frac{\partial q_{i-1}}{\partial \theta_{liq,i-1}} \tag{7.144}$$

$$b_i = -\frac{\partial q_{i-1}}{\partial \theta_{liq,i}} - \frac{\Delta z_i}{\Delta t} \tag{7.145}$$

$$c_i = 0 \tag{7.146}$$

$$r_i = q_{i-1}^n + e_i \,. \tag{7.147}$$

The coefficients for the aquifer layer $i = N_{levsoi}+1$ are then

$$a_i = 0 \tag{7.148}$$

$$b_i = -\frac{\Delta z_i}{\Delta t} \tag{7.149}$$

$$c_i = 0 \tag{7.150}$$

$$r_i = 0 \,. \tag{7.151}$$

If the water table is below the soil column ($z_{\nabla} > z_{h,N_{levsoi}}$), the coefficients for $i = N_{levsoi}$ are

$$a_i = -\frac{\partial q_{i-1}}{\partial \theta_{liq,i-1}} \tag{7.152}$$

$$b_i = \frac{\partial q_i}{\partial \theta_{liq,i}} - \frac{\partial q_{i-1}}{\partial \theta_{liq,i}} - \frac{\Delta z_i}{\Delta t} \tag{7.153}$$

$$c_i = \frac{\partial q_i}{\partial \theta_{liq,i+1}} \tag{7.154}$$

$$r_i = q_{i-1}^n - q_i^n + e_i \,. \tag{7.155}$$

The $i = N_{levsoi} + 1$ terms are evaluated using

$$\psi_{N_{levsoi}+1} = \psi_{sat,N_{levsoi}} \left[s_{N_{levsoi}+1} \right]^{-B_{N_{levsoi}}} \geq -1 \times 10^8 \tag{7.156}$$

$$z_{N_{levsoi}+1} = 0.5\left(z_\nabla + z_{N_{levsoi}} \right) \tag{7.157}$$

where

$$s_{N_{levsoi}+1} = 0.5\left(\frac{\theta_{sat,N_{levsoi}} + \theta_{N_{levsoi}}}{\theta_{sat,N_{levsoi}}} \right) \qquad 0.01 \leq s_{N_{levsoi}+1} \leq 1 \,, \tag{7.158}$$

$\psi_{E,N_{levsoi}+1}$ is evaluated from equations (7.132) and (7.134), and

$$\frac{\partial \psi_{N_{levsoi}+1}}{\partial \theta_{liq,N_{levsoi}+1}} = -B_{N_{levsoi}} \frac{\psi_{N_{levsoi}+1}}{s_{N_{levsoi}} \theta_{sat,N_{levsoi}}} \,. \tag{7.159}$$

The coefficients for the aquifer layer $i = N_{levsoi} + 1$ are then

$$a_i = -\frac{\partial q_{i-1}}{\partial \theta_{liq,i-1}} \tag{7.160}$$

$$b_i = -\frac{\partial q_{i-1}}{\partial \theta_{liq,i}} - \frac{\Delta z_i}{\Delta t} \tag{7.161}$$

$$c_i = 0 \tag{7.162}$$

$$r_i = q_{i-1}^n \,. \tag{7.163}$$

Upon solution of the tridiagonal equation set (Press et al. 1992), the liquid water contents are updated as follows

$$w_{liq,i}^{n+1} = w_{liq,i}^n + \Delta \theta_{liq,i} \Delta z_i \qquad i = 1, \ldots, N_{levsoi} \,. \tag{7.164}$$

The volumetric water content is

$$\theta_i = \frac{w_{liq,i}}{\Delta z_i \rho_{liq}} + \frac{w_{ice,i}}{\Delta z_i \rho_{ice}}. \tag{7.165}$$

7.5 Frozen Soils and Perched Water Table

When soils freeze, the power-law form of the ice impedance factor (section 7.4.1) can greatly decrease the hydraulic conductivity of the soil, leading to nearly impermeable soil layers. When unfrozen soil layers are present above relatively ice-rich frozen layers, the possibility exists for perched saturated zones. Lateral drainage from perched saturated regions is parameterized as a function of the thickness of the saturated zone

$$q_{drai,perch} = k_{drai,perch}\left(z_{frost} - z_{\nabla,perch}\right) \tag{7.166}$$

where $k_{drai,perch}$ depends on topographic slope and soil hydraulic conductivity,

$$k_{drai,perch} = 10^{-5}\sin(\beta)\left(\frac{\sum_{i=N_{perch}}^{i=N_{frost}} \Theta_{ice,i} k_{sat}\left[z_i\right]\Delta z_i}{\sum_{i=N_{perch}}^{i=N_{frost}} \Delta z_i}\right) \tag{7.167}$$

where Θ_{ice} is an ice impedance factor determined from the ice content of the soil layers interacting with the water table (section 7.6), β is the mean grid cell topographic slope in radians, z_{frost} is the depth to the frost table, and $z_{\nabla,perch}$ is the depth to the perched saturated zone. The frost table z_{frost} is defined as the shallowest frozen layer having an unfrozen layer above it, while the perched water table $z_{\nabla,perch}$ is defined as the depth at which the volumetric water content drops below a specified threshold. The default threshold is set to 0.9. Drainage from the perched saturated zone $q_{drai,perch}$ is removed from layers N_{perch} through N_{frost}, which are the layers containing $z_{\nabla,perch}$ and, z_{frost} respectively.

7.6 Groundwater-Soil Water Interactions

Drainage or sub-surface runoff is based on the SIMTOP scheme (Niu et al. 2005) with a modification to account for reduced drainage in frozen soils. In the work of Niu et al. (2005), the drainage q_{drai} (kg m^{-2} s^{-1}) was formulated as

$$q_{drai} = q_{drai,\max} \exp\left(-f_{drai} z_{\nabla}\right). \tag{7.168}$$

Here, the water table depth z_{∇} has units of meters. To restrict drainage in frozen soils, Niu et al. (2005) added the following condition

$$q_{drai} = 0 \qquad \text{for } w_{ice,N_{levsoi}} > w_{liq,N_{levsoi}}. \tag{7.169}$$

In preliminary testing it was found that a more gradual restriction of drainage was required so that the water table depth remained dynamic under partially frozen conditions. The following modification is made to equation (7.168)

$$q_{drai} = \Theta_{ice} q_{drai,\max} \exp\left(-f_{drai} z_{\nabla}\right) \tag{7.170}$$

where Θ_{ice} is an ice impedance factor determined from the ice content of the soil layers interacting with the water table

$$\Theta_{ice} = 10^{-\Omega\left(\frac{\sum_{i=jwt}^{i=N_{levsoi}} F_{ice,i}\Delta z_i}{\sum_{i=jwt}^{i=N_{levsoi}} \Delta z_i}\right)} \tag{7.171}$$

where $\Omega = 6$ is an adjustable parameter, jwt is the index of the layer directly above the water table, $F_{ice} = \dfrac{\theta_{ice}}{\theta_{sat}}$ is the ice-filled fraction of the pore space of soil layer i (kg m^{-2}), and Δz_i is the layer thickness (mm). This expression is functionally the same as that used to determine the ice impedance factor in section 7.4. In equation (7.170), the decay factor $f_{drai} = 2.5$ m^{-1} and the maximum drainage when the water table depth is at the

surface $q_{drai,\max} = 10\sin(\beta)$ kg m^{-2} s^{-1} , where β is the mean grid cell topographic slope in radians, were determined for global simulations through sensitivity analysis and comparison with observed runoff.

Determination of water table depth z_∇ is based on work by Niu et al. (2007). In this approach, a groundwater component is added in the form of an unconfined aquifer lying below the soil column (Figure 7.1). The groundwater solution is dependent on whether the water table is within or below the soil column. The water stored in the unconfined aquifer W_a has a prescribed maximum value (5000 mm). When the water table is within the soil column, W_a is constant because there is no water exchange between the soil column and the underlying aquifer. In this case, recharge to the water table is diagnosed by applying Darcy's law across the water table

$$q_{recharge} = -k_{aq}\frac{\left(\Psi_\nabla - \Psi_{jwt}\right)}{\left(z_\nabla - z_{jwt}\right)} \tag{7.172}$$

where $\Psi_\nabla = 0$ is the matric potential at the water table and $k_{aq} = \Theta_{ice,jwt+1}k\left[z_{jwt+1}\right]$ is the hydraulic conductivity of the layer containing the water table. Change in the water table is then calculated as the difference between recharge and drainage, scaled by the specific yield of the layer containing the water table

$$\Delta z_\nabla = \frac{\left(q_{recharge} - q_{drai}\right)}{S_y}\Delta t \,. \tag{7.173}$$

The specific yield, S_y, which depends on the soil properties and the water table location, is derived by taking the difference between two equilibrium soil moisture profiles whose water tables differ by an infinitesimal amount

$$S_y = \theta_{sat}\left(1-\left(1+\frac{z_\nabla}{\Psi_{sat}}\right)^{\frac{-1}{B}}\right) \tag{7.174}$$

where B is the Clapp-Hornberger exponent. Because S_y is a function of the soil properties, it results in water table dynamics that are consistent with the soil water fluxes described in section 7.4.

For the case when the water table is below the soil column, the change in water stored in the unconfined aquifer W_a (mm) is updated as

$$\Delta W_a = \left(q_{recharge} - q_{drai}\right)\Delta t \tag{7.174}$$

and the water table is updated using equation (7.173) with the specific yield of layer N_{levsoi}.

The recharge rate is defined as positive when water enters the aquifer

$$q_{recharge} = \frac{\Delta\theta_{liq,N_{levsoi}+1}\Delta z_{N_{levsoi}+1}}{\Delta t} \tag{7.174}$$

where $\Delta\theta_{liq,N_{levsoi}+1} = \theta^{n+1}_{liq,N_{levsoi}+1} - \theta^{n}_{liq,N_{levsoi}+1}$ is the change in liquid water content for layer $i = N_{levsoi}+1$ calculated from the solution of the soil water equations (section 7.4), and $\Delta z_{N_{levsoi}+1}$ (mm) is

$$\Delta z_{N_{levsoi}+1} = z^n_\nabla - z_{h,N_{levsoi}}\,. \tag{7.174}$$

After the above calculations, two numerical adjustments are implemented to keep the liquid water content of each soil layer ($w_{liq,i}$) within physical constraints of $w^{\min}_{liq} \le w_{liq,i} \le \left(\theta_{sat,i} - \theta_{ice,i}\right)\Delta z_i$ where $w^{\min}_{liq} = 0.01$ (mm). First, beginning with the bottom soil layer $i = N_{levsoi}$, any excess liquid water in each soil layer

($w_{liq,i}^{excess} = w_{liq,i} - \left(\theta_{sat,i} - \theta_{ice,i}\right)\Delta z_i \geq 0$) is successively added to the layer above. Any excess liquid water that remains after saturating the entire soil column (plus a maximum surface ponding depth $w_{liq}^{pond} = 10$ kg m^{-2}), is added to drainage q_{drai}. Second, to prevent negative $w_{liq,i}$, each layer is successively brought up to $w_{liq,i} = w_{liq}^{\min}$ by taking the required amount of water from the layer below. If this results in $w_{liq,N_{levsoi}} < w_{liq}^{\min}$, then the layers above are searched in succession for the required amount of water ($w_{liq}^{\min} - w_{liq,N_{levsoi}}$) and removed from those layers subject to the constraint $w_{liq,i} \geq w_{liq}^{\min}$. If sufficient water is not found, then the water is removed from W_t and q_{drai}.

The soil surface layer liquid water and ice contents are then updated for dew q_{sdew}, frost q_{frost}, or sublimation q_{subl} (section 5.4) as

$$w_{liq,1}^{n+1} = w_{liq,1}^{n} + q_{sdew}\Delta t \tag{7.175}$$

$$w_{ice,1}^{n+1} = w_{ice,1}^{n} + q_{frost}\Delta t \tag{7.176}$$

$$w_{ice,1}^{n+1} = w_{ice,1}^{n} - q_{subl}\Delta t \,. \tag{7.177}$$

Sublimation of ice is limited to the amount of ice available.

7.7 Runoff from glaciers and snow-capped surfaces

All surfaces are constrained to have a snow water equivalent $W_{sno} \leq 1000$ kg m^{-2}. For snow-capped surfaces, the solid and liquid precipitation reaching the snow surface and dew in solid or liquid form, is separated into solid $q_{snwcp,ice}$ and liquid $q_{snwcp,liq}$ runoff terms

$$q_{snwcp,ice} = q_{grnd,ice} + q_{frost} \tag{7.178}$$

$$q_{snwcp,liq} = q_{grnd,liq} + q_{dew} \tag{7.179}$$

and snow pack properties are unchanged. The $q_{snwcp,ice}$ runoff is sent to the River Transport Model (RTM) (Chapter 11) where it is routed to the ocean as an ice stream and, if applicable, the ice is melted there.

For snow-capped surfaces other than glaciers and lakes the $q_{snwcp,liq}$ runoff is assigned to the glaciers and lakes runoff term q_{rgwl} (e.g. $q_{rgwl} = q_{snwcp,liq}$). For glacier surfaces the runoff term q_{rgwl} is calculated from the residual of the water balance

$$q_{rgwl} = q_{grnd,ice} + q_{grnd,liq} - E_g - E_v - \frac{\left(W_b^{n+1} - W_b^n\right)}{\Delta t} - q_{snwcp,ice} \tag{7.180}$$

where W_b^n and W_b^{n+1} are the water balances at the beginning and ending of the time step defined as

$$W_b = W_{can} + W_{sno} + \sum_{i=1}^{N}\left(w_{ice,i} + w_{liq,i}\right). \tag{7.181}$$

Currently, glaciers are non-vegetated and $E_v = W_{can} = 0$. The contribution of lake runoff to q_{rgwl} is described in section 9.6.3. The runoff term q_{rgwl} may be negative for glaciers and lakes, which reduces the total amount of runoff available to the RTM.

7.8 The Variable Infiltration Capacity parameterizations as a hydrologic option

The hydrologic parameterizations from the Variable Infiltration Capacity (VIC) land surface model (Liang et al. 1994) have been implemented as a hydrologic option. VIC includes two different time scales of runoff generation. To capture such dynamics, the soil column in the original VIC model (http://www.hydro.washington.edu/Lettenmaier/Models/VIC/Overview/ModelOverview.

shtml) is typically divided into three layers with variable soil depths. The upper two layers are designed to represent the dynamic responses of the soil to rainfall events for surface runoff generation, and the lower layer is used to characterize the seasonal soil moisture behavior and subsurface runoff generation. The implementation of the VIC parameterizations are as described in Li et al. (2011) except where updated for consistency with modifications to CLM hydrology in CLM4.5. Note that unless explicitly mentioned in this section, any descriptions from sections 7.1-7.7 are intact and remain valid when the VIC hydrology option is turned on.

Three VIC soil layers are defined by aggregating multiple layers in the CLM soil column with thicknesses of $\sum_{i=1}^{3}\Delta z_i$, $\sum_{i=4}^{6}\Delta z_i$, $\sum_{i=7}^{N_{levsoi}}\Delta z_i$, respectively. At each time step, the soil moisture profile is determined following the algorithms detailed in section 7.4, and aggregated to the three VIC layers for runoff generation calculations. The surface runoff generated by the saturation excess runoff mechanism, q_{over}, is calculated using equation (7.64), but with the fractional saturated area defined as

$$f_{sat} = 1 - \left(1 - w_{top} / w_{m,top}\right)^{1/\left(1+b_{inf}\right)} \tag{7.182}$$

where w_{top} and $w_{m,top}$ are calculated as $\sum_{i=1}^{6}\theta_i\Delta z_i$ and $\sum_{i=1}^{6}\theta_{s,i}\Delta z_i$, respectively, and represent the soil moisture (kg m^{-2}) and maximum soil moisture (kg m^{-2}) in the top two VIC layers combined.

In equation (7.182), it is hypothesized that the spatial heterogeneity of soil moisture holding capacity in the top VIC layers can be represented by a soil moisture holding capacity curve as defined in equation (7.183), in which b_{inf} is a parameter that controls the shape of the curve. That is, if one assumes that a grid cell (or soil column in this case)

is composed of many pixels (or points) with varying soil moisture capacity, this variation across the grid cell can be represented conceptually as

$$i = i_m\left(1-(1-A)^{1/b_{inf}}\right) \tag{7.183}$$

where i and i_m are the point and maximum point soil moisture holding capacities (kg m^{-2}), respectively; A is the fraction of a grid cell for which the soil moisture holding capacity is less than or equal to i; and $i_m = w_{m,top}\left(1+b_{inf}\right)$. When A is equal to f_{sat}, the corresponding point soil moisture holding capacity is denoted as i_0. The maximum soil infiltration capacity (kg m^{-2} s^{-1}) in equation (7.72) becomes

$$q_{inf,max} = \begin{Bmatrix} \left(1-f_{sat}\right)\theta_{ice,top}\left(\dfrac{w_{m,top}-w_{top}}{\Delta t}\right) & i_o + q_{in,soil}\Delta t \geq i_m \\ \left(1-f_{sat}\right)\dfrac{\theta_{ice,top}}{\Delta t}\left\{\left(w_{m,top}-w_{top}\right)-w_{m,top}\times\left[1-\max\left(1,\dfrac{\left(i_o+q_{in,soil}\Delta t\right)}{i_m}\right)^{1+b_{inf}}\right]\right\} & i_o + q_{in,soil}\Delta t < i_m \end{Bmatrix} \tag{7.184}$$

where $\theta_{ice,top}$ is an ice impedance factor determined from the ice content of the top two VIC layers combined, similar to the one used in equation (7.72). Interested readers are referred to Wood et al. (1992) for a schematic representation of equation (7.183) and derivations associated with equations (7.182), (7.183), and (7.184).

The subsurface runoff in equation (7.170) is parameterized as

$$q_{drai} = \Theta_{ice,bot}\left[\begin{matrix}\frac{D_s D_{smax}}{W_s w_{m,bot}} w_{bot} + \\ max\left(0,\frac{w_{bot}-W_s w_{m,bot}}{w_{m,bot}-W_s w_{m,bot}}\right)\left(D_{smax}-\frac{D_s D_{smax}}{W_s}\right)\end{matrix}\right]/\Delta t \tag{7.185}$$

where w_{bot} and $w_{m,bot}$ are the soil moisture (kg m^{-2}) and maximum soil moisture (kg m^{-2}) in the bottom VIC layer, respectively, D_{smax} is the maximum subsurface flow rate (kg m^{-2} s^{-1}), D_s is a fraction of D_{smax}, W_s is a fraction of $w_{m,bot}$, and $\Theta_{ice,bot}$ is an ice

impedance factor determined from the ice content of the bottom VIC layer, similar to the ones in equations (7.72) and (7.184).

As the VIC parameterizations are based on conceptual models, Huang and Liang (2006) recommended calibrating the VIC parameters, including b_{inf} , D_{smax} , D_s , W_s , and the second and third layer soil thicknesses using observations. In this implementation, the thicknesses of the VIC soil layers are fixed to maintain consistency with the soil water algorithms in section 7.4. The other four parameters, b_{inf} , D_{smax} , D_s , and W_s are prescribed and are included in the CLM surface dataset. Users can provide calibrated parameter values determined manually or automatically by modifying the surface dataset. Note that the units of D_{smax} on the surface dataset are mm d^{-1} (the traditional units for other standard VIC applications) which are then converted to kg m^{-2} s^{-1} for use in CLM. A preliminary calibration was performed by perturbing the three parameters b_{inf} , D_{smax} , and W_s, and fixing $D_s = 0.1$ globally. The parameter space for b_{inf} , D_{smax} , and W_s was sampled using the global sensitivity analysis framework described by Hou et al. (2012) to produce 64 combinations of parameter values based on *a priori* information about the parameters. For each set of parameter values, a global simulation was performed using the compset I_2000 (i.e., driven by satellite phenology) at a resolution of 0.9°x1.25° on the basis of the development tag betr_m_sci10_clm45sci13_clm4_0_54. At each model grid cell, the set of b_{inf} , D_{smax} , and W_s values corresponding to the simulation that produced the lowest absolute bias compared to the climatological mean annual total runoff from the Global Runoff Data Center (GRDC) was selected as the calibrated values. These values are provided only as a reference due to the preliminary nature of the calibration. Interested users of the VIC

hydrology option are encouraged to calibrate the parameters for their applications for improved performance.

8. Stomatal Resistance and Photosynthesis

Leaf stomatal resistance, which is needed for the water vapor flux (Chapter 5), is coupled to leaf photosynthesis similar to Collatz et al. (1991, 1992). These equations are solved separately for sunlit and shaded leaves using average absorbed photosynthetically active radiation for sunlit and shaded leaves [ϕ^{sun}, ϕ^{sha} W m^{-2} (section 4.1)] to give sunlit and shaded stomatal resistance (r_s^{sun}, r_s^{sha} s m^{-1}) and photosynthesis (A^{sun}, A^{sha} μmol CO_2 m^{-2} s^{-1}). Canopy photosynthesis is $A^{sun}L^{sun} + A^{sha}L^{sha}$, where L^{sun} and L^{sha} are the sunlit and shaded leaf area indices (section 4.1). Canopy conductance is $\frac{1}{r_b + r_s^{sun}} L^{sun} + \frac{1}{r_b + r_s^{sha}} L^{sha}$, where r_b is the leaf boundary layer resistance (section 5.3). The equation set is described by Bonan et al. (2011).

8.1 Stomatal resistance

Leaf stomatal resistance is calculated from the Ball-Berry conductance model as described by Collatz et al. (1991) and implemented in global climate models (Sellers et al. 1996). The model relates stomatal conductance (i.e., the inverse of resistance) to net leaf photosynthesis, scaled by the relative humidity at the leaf surface and the CO_2 concentration at the leaf surface. Leaf stomatal resistance is

$$\frac{1}{r_s} = g_s = m \frac{A_n}{c_s / P_{atm}} h_s + b\,\beta_t \tag{8.1}$$

where r_s is leaf stomatal resistance (s m^2 μmol^{-1}), m is a plant functional type dependent parameter (Table 8.1), A_n is leaf net photosynthesis (μmol CO_2 m^{-2} s^{-1}), c_s is the CO_2 partial pressure at the leaf surface (Pa), P_{atm} is the atmospheric pressure (Pa),

$h_s = e_s / e_i$ is the leaf surface humidity with e_s the vapor pressure at the leaf surface (Pa) and e_i the saturation vapor pressure (Pa) inside the leaf at the vegetation temperature T_v, and b is the minimum stomatal conductance (μmol m^{-2} s^{-1}). Parameter values are $m = 9$ for C_3 plants and $m = 4$ for C_4 plants (Collatz et al. 1991, 1992, Sellers et al. 1996). Sellers et al. (1996) used $b = 10000$ for C_3 plants and $b = 40000$ for C_4 plants, also used here. Photosynthesis is calculated for sunlit (A^{sun}) and shaded (A^{sha}) leaves to give r_s^{sun} and r_s^{sha}. Additionally, soil water influences stomatal resistance directly by multiplying the minimum conductance by a soil water stress function β_t (which ranges from 0 to 1) and also indirectly through A_n, as in (Sellers et al. 1996).

Resistance is converted from units of s m^2 μmol^{-1} to s m^{-1} as: 1 s m^{-1} = $1 \times 10^{-9} R_{gas} \frac{\theta_{atm}}{P_{atm}}$ μmol^{-1} m^2 s, where R_{gas} is the universal gas constant (J K^{-1} kmol^{-1}) (Table 2.6) and θ_{atm} is the atmospheric potential temperature (K).

Table 8.1. Plant functional type (PFT) photosynthetic parameters.

PFT	m	α	CN_L	F_{LNR}	SLA_0	ψ_o	ψ_c	V_{cmax25}
NET Temperate	9	–	35	0.0509	0.010	-66000	-255000	62.5
NET Boreal	9	–	40	0.0466	0.008	-66000	-255000	62.6
NDT Boreal	9	–	25	0.0546	0.024	-66000	-255000	39.1
BET Tropical	9	–	30	0.0461	0.012	-66000	-255000	55.0
BET temperate	9	–	30	0.0515	0.012	-66000	-255000	61.5
BDT tropical	9	–	25	0.0716	0.030	-35000	-224000	41.0
BDT temperate	9	–	25	0.1007	0.030	-35000	-224000	57.7
BDT boreal	9	–	25	0.1007	0.030	-35000	-224000	57.7
BES temperate	9	–	30	0.0517	0.012	-83000	-428000	61.7
BDS temperate	9	–	25	0.0943	0.030	-83000	-428000	54.0
BDS boreal	9	–	25	0.0943	0.030	-83000	-428000	54.0
C_3 arctic grass	9	–	25	0.1365	0.030	-74000	-275000	78.2
C_3 grass	9	–	25	0.1365	0.030	-74000	-275000	78.2
C_4 grass	4	0.05	25	0.0900	0.030	-74000	-275000	51.6
Crop R	9	–	25	0.1758	0.030	-74000	-275000	100.7
Crop I	9	–	25	0.1758	0.030	-74000	-275000	100.7
Corn R	4	0.05	25	0.2930	0.050	-74000	-275000	100.7
Corn I	4	0.05	25	0.2930	0.050	-74000	-275000	100.7
Temp Cereal R	9	–	25	0.4102	0.070	-74000	-275000	100.7
Temp Cereal I	9	–	25	0.4102	0.070	-74000	-275000	100.7
Winter Cereal R	9	–	25	0.4102	0.070	-74000	-275000	100.7
Winter Cereal I	9	–	25	0.4102	0.070	-74000	-275000	100.7
Soybean R	9	–	25	0.4102	0.070	-74000	-275000	100.7
Soybean I	9	–	25	0.4102	0.070	-74000	-275000	100.7

α (mol CO_2 mol^{-1} photon); CN_L (g C g^{-1} N); F_{LNR} (g N Rubisco g^{-1} N); SLA_0 (m^2 g^{-1} C); ψ_o and ψ_c (mm); V_{cmax25} (μmol m^{-2} s^{-1}, calculated from equation (8.17) for canopy top).

8.2 Photosynthesis

Photosynthesis in C_3 plants is based on the model of Farquhar et al. (1980). Photosynthesis in C_4 plants is based on the model of Collatz et al. (1992). Bonan et al. (2011) describe the implementation, modified here. In its simplest form, leaf net photosynthesis after accounting for respiration (R_d) is

$$A_n = \min\left(A_c, A_j, A_p\right) - R_d \,. \tag{8.2}$$

The RuBP carboxylase (Rubisco) limited rate of carboxylation A_c (μmol CO_2 m^{-2} s^{-1}) is

$$A_c = \begin{Bmatrix} \dfrac{V_{c\max}\left(c_i - \Gamma_*\right)}{c_i + K_c\left(1 + o_i / K_o\right)} & \text{for } C_3 \text{ plants} \\ V_{c\max} & \text{for } C_4 \text{ plants} \end{Bmatrix} \qquad c_i - \Gamma_* \geq 0 \,. \tag{8.3}$$

The maximum rate of carboxylation allowed by the capacity to regenerate RuBP (i.e., the light-limited rate) A_j (μmol CO_2 m^{-2} s^{-1}) is

$$A_j = \begin{Bmatrix} \dfrac{J\left(c_i - \Gamma_*\right)}{4c_i + 8\Gamma_*} & \text{for } C_3 \text{ plants} \\ \alpha(4.6\phi) & \text{for } C_4 \text{ plants} \end{Bmatrix} \qquad c_i - \Gamma_* \geq 0 \,. \tag{8.4}$$

The product-limited rate of carboxylation for C_3 plants and the PEP carboxylase-limited rate of carboxylation for C_4 plants A_p (μmol CO_2 m^{-2} s^{-1}) is

$$A_p = \begin{Bmatrix} 3T_p & \text{for } C_3 \text{ plants} \\ k_p \dfrac{c_i}{P_{atm}} & \text{for } C_4 \text{ plants} \end{Bmatrix} . \tag{8.5}$$

In these equations, c_i is the internal leaf CO_2 partial pressure (Pa) and $o_i = 0.209 P_{atm}$ is the O_2 partial pressure (Pa). K_c and K_o are the Michaelis-Menten constants (Pa) for CO_2 and O_2. Γ_* (Pa) is the CO_2 compensation point. $V_{c\max}$ is the maximum rate of

carboxylation (μmol m^{-2} s^{-1}) and J is the electron transport rate (μmol m^{-2} s^{-1}). T_p is the triose phosphate utilization rate (μmol m^{-2} s^{-1}), taken as $T_p = 0.167V_{c\max}$ so that $A_p = 0.5V_{c\max}$ for C_3 plants (as in Collatz et al. 1991). For C_4 plants, the light-limited rate A_j varies with ϕ in relation to the quantum efficiency ($\alpha = 0.05$ mol CO_2 mol^{-1} photon). ϕ is the absorbed photosynthetically active radiation (W m^{-2}) (section 4.1), which is converted to photosynthetic photon flux assuming 4.6 μmol photons per joule. k_p is the initial slope of C_4 CO_2 response curve.

For C_3 plants, the electron transport rate depends on the photosynthetically active radiation absorbed by the leaf. A common expression is the smaller of the two roots of the equation

$$\Theta_{PSII} J^2 - \left(I_{PSII} + J_{\max}\right) J + I_{PSII} J_{\max} = 0 \tag{8.6}$$

where $J_{\max}$ is the maximum potential rate of electron transport (μmol m^{-2} s^{-1}), I_{PSII} is the light utilized in electron transport by photosystem II (μmol m^{-2} s^{-1}), and Θ_{PSII} is a curvature parameter. For a given amount of photosynthetically active radiation absorbed by a leaf ϕ (W m^{-2}), converted to photosynthetic photon flux density with 4.6 μmol J^{-1}, the light utilized in electron transport is

$$I_{PSII} = 0.5\Phi_{PSII}(4.6\phi) \tag{8.7}$$

where Φ_{PSII} is the quantum yield of photosystem II, and the term 0.5 arises because one photon is absorbed by each of the two photosystems to move one electron. Parameter values are Θ_{PSII} = 0.7 and Φ_{PSII} = 0.85. In calculating A_j (for both C_3 and C_4 plants), $\phi = \phi^{sun}$ for sunlit leaves and $\phi = \phi^{sha}$ for shaded leaves.

The model uses co-limitation as described by Collatz et al. (1991, 1992). The actual gross photosynthesis rate, A, is given by the smaller root of the equations

$$\begin{aligned} \Theta_{cj} A_i^2 - \left(A_c + A_j\right) A_i + A_c A_j = 0 \\ \Theta_{ip} A^2 - \left(A_i + A_p\right) A + A_i A_p = 0 \end{aligned} . \tag{8.8}$$

Values are $\Theta_{cj} = 0.98$ and $\Theta_{ip} = 0.95$ for C_3 plants; and $\Theta_{cj} = 0.80$ and $\Theta_{ip} = 0.95$ for C_4 plants. $A_n = A - R_d$.

The parameters K_c, K_o, and Γ_* depend on temperature. Values at 25 °C are $K_{c25} = 404.9 \times 10^{-6} P_{atm}$, $K_{o25} = 278.4 \times 10^{-3} P_{atm}$, and Γ_{*25}=$42.75 \times 10^{-6} P_{atm}$. $V_{c\max}$, $J_{\max}$, T_p, k_p, and R_d also vary with temperature. Parameter values at 25 °C are calculated from $V_{c\max}$ at 25 °C: $J_{\max 25} = 1.97 V_{c\max 25}$, $T_{p25} = 0.167 V_{c\max 25}$, and $R_{d25} = 0.015 V_{c\max 25}$ (C_3) and $R_{d25} = 0.025 V_{c\max 25}$ (C_4). For C_4 plants, $k_{p25} = 20000\, V_{c\max 25}$. However, when the biogeochemistry is active, R_{d25} is calculated from leaf nitrogen as $R_{d25} = 0.2577 N_a$, where N_a is the area-based leaf nitrogen concentration (g N m^{-2} leaf area, equation (8.18)) and 0.2577 μmol CO_2 g^{-1} N s^{-1} the base respiration rate. The parameters $V_{c\max 25}$, $J_{\max 25}$, T_{p25}, k_{p25}, and R_{d25} are scaled over the canopy for sunlit and shaded leaves (section 8.3). In C3 plants, these are adjusted for leaf temperature T_v (K) as:

$$\begin{aligned} V_{c\max} &= V_{c\max 25}\, f\left(T_v\right) f_H\left(T_v\right) \\ J_{\max} &= J_{\max 25}\, f\left(T_v\right) f_H\left(T_v\right) \\ T_p &= T_{p25}\, f\left(T_v\right) f_H\left(T_v\right) \\ R_d &= R_{d25}\, f\left(T_v\right) f_H\left(T_v\right) \\ K_c &= K_{c25}\, f\left(T_v\right) \\ K_o &= K_{o25}\, f\left(T_v\right) \\ \Gamma_* &= \Gamma_{*25}\, f\left(T_v\right) \end{aligned} \tag{8.9}$$

with

$$f\left(T_v\right)=\exp\left[\frac{\Delta H_a}{298.15\times 0.001R_{gas}}\left(1-\frac{298.15}{T_v}\right)\right] \tag{8.10}$$

and

$$f_H\left(T_v\right)=\frac{1+\exp\left(\frac{298.15\Delta S-\Delta H_d}{298.15\times 0.001R_{gas}}\right)}{1+\exp\left(\frac{\Delta ST_v-\Delta H_d}{0.001R_{gas}T_v}\right)}\ . \tag{8.11}$$

Table 8.2 list parameter values for ΔH_a, ΔH_d, and ΔS, from Bonan et al. (2011). Because T_p as implemented here varies with $V_{c\max}$, the same temperature parameters are used for T_p. For C_4 plants,

$$\begin{aligned} V_{c\max} &= V_{c\max 25}\left[\frac{Q_{10}^{(T_v-298.15)/10}}{f_H\left(T_v\right)f_L\left(T_v\right)}\right] \\ f_H\left(T_v\right) &= 1+\exp\left[s_1\left(T_v-s_2\right)\right] \\ f_L\left(T_v\right) &= 1+\exp\left[s_3\left(s_4-T_v\right)\right] \end{aligned} \tag{8.12}$$

with $Q_{10}=2$, $s_1=0.3\ \mathrm{K}^{-1}$, $s_2=313.15$ K, $s_3=0.2\ \mathrm{K}^{-1}$, and $s_4=288.15$ K. Additionally,

$$R_d=R_{d25}\left\{\frac{Q_{10}^{(T_v-298.15)/10}}{1+\exp\left[s_5\left(T_v-s_6\right)\right]}\right\} \tag{8.13}$$

with $Q_{10}=2$, $s_5=1.3\ \mathrm{K}^{-1}$, and $s_6=328.15$ K, and

$$k_p=k_{p25}\,Q_{10}^{(T_v-298.15)/10} \tag{8.14}$$

with $Q_{10}=2$.

Table 8.2. Temperature dependence parameters for C3 photosynthesis.

Parameter	ΔH_a (J mol^{-1})	ΔH_d (J mol^{-1})	ΔS (J mol^{-1} K^{-1})
$V_{c\max}$	65330	149250	485
$J_{\max}$	43540	152040	495
T_p	65330	149250	485
R_d	46390	150650	490
K_c	79430	–	–
K_o	36380	–	–
Γ_*	37830	–	–

The parameters in Table 8.2 do not allow for temperature acclimation of photosynthesis. In the model, acclimation is implemented as in Kattge and Knorr (2007). In this parameterization, $V_{c\max}$ and $J_{\max}$ vary with the plant growth temperature. This is achieved by allowing ΔS to vary with growth temperature according to

$$\begin{aligned} \Delta S &= 668.39 - 1.07(T_{10} - T_f) \qquad \text{for } V_{c\max} \\ \Delta S &= 659.70 - 0.75(T_{10} - T_f) \qquad \text{for } J_{\max} \end{aligned} \tag{8.15}$$

The effect is to cause the temperature optimum of $V_{c\max}$ and $J_{\max}$ to increase with warmer temperature. In this parameterization, ΔH_d = 200000, ΔH_a = 72000 for $V_{c\max}$, and ΔH_a = 50000 for $J_{\max}$. Additionally, the ratio $J_{\max 25} / V_{c\max 25}$ at 25 °C decreases with growth temperature as

$$J_{\max 25} / V_{c\max 25} = 2.59 - 0.035(T_{10} - T_f)\,. \tag{8.16}$$

In these acclimation functions, T_{10} is the 10-day mean air temperature (K) and T_f is the freezing point of water (K). For lack of data, T_p acclimates similar to $V_{c\max}$. Acclimation is restricted over the temperature range $T_{10} - T_f \geq 11\,°\text{C}$ and $T_{10} - T_f \leq 35\,°\text{C}$.

8.3 V_{cmax25} and canopy scaling

The maximum rate of carboxylation at 25 °C varies with foliage nitrogen concentration and specific leaf area and is calculated as in Thornton and Zimmermann (2007). At 25ºC,

$$V_{c\max 25} = N_a F_{LNR} F_{NR} a_{R25} \tag{8.17}$$

where N_a is the area-based leaf nitrogen concentration (g N m^{-2} leaf area), F_{LNR} is the fraction of leaf nitrogen in Rubisco (g N in Rubisco g^{-1} N), $F_{NR} = 7.16$ is the mass ratio of total Rubisco molecular mass to nitrogen in Rubisco (g Rubisco g^{-1} N in Rubisco), and $a_{R25} = 60$ is the specific activity of Rubisco (μmol CO_2 g^{-1} Rubisco s^{-1}). N_a is calculated from mass-based leaf N concentration and specific leaf area

$$N_a = \frac{1}{CN_L\ SLA_0} \tag{8.18}$$

where CN_L is the leaf carbon-to-nitrogen ratio (g C g^{-1} N) and SLA_0 is specific leaf area at the canopy top (m^2 leaf area g^{-1} C). Table 8.1 lists values of F_{LNR}, CN_L, and SLA_0 for each plant functional type. F_{LNR} was chosen to give $V_{c\max 25}$ consistent with Kattge et al. (2009), as discussed by Bonan et al. (2011, 2012). Table 8.1 lists derived values for $V_{c\max 25}$ at the top of the canopy using SLA_0. Tropical broadleaf evergreen trees are an exception, and a higher $V_{c\max 25}$ is used to alleviate model biases (Bonan et al. 2012).

$V_{c\max 25}$ is calculated separately for sunlit and shaded leaves using an exponential profile to area-based leaf nitrogen (N_a), as in Bonan et al. (2011). $V_{c\max 25}$ at cumulative leaf area index x from the canopy top scales directly with N_a, which decreases exponentially with greater cumulative leaf area, so that

$$V_{c\max 25}(x) = V_{c\max 25}(0) e^{-K_n x} \tag{8.19}$$

where $V_{c\max 25}(0)$ is defined at the top of the canopy using SLA_0, and K_n is the decay coefficient for nitrogen. The canopy integrated value for sunlit and shaded leaves is

$$\begin{aligned} V_{c\max 25}^{sun} &= \int_0^L V_{c\max 25}(x) f_{sun}(x) dx \\ &= V_{c\max 25}(0)\left[1 - e^{-(K_n+K)L}\right]\frac{1}{K_n + K} \end{aligned} \tag{8.20}$$

$$\begin{aligned} V_{c\max 25}^{sha} &= \int_0^L V_{c\max 25}(x)\left[1 - f_{sun}(x)\right] dx \\ &= V_{c\max 25}(0)\left\{\left[1 - e^{-K_n L}\right]\frac{1}{K_n} - \left[1 - e^{-(K_n+K)L}\right]\frac{1}{K_n + K}\right\} \end{aligned} \tag{8.21}$$

and the average value for the sunlit and shaded leaves is

$$\overline{V}_{c\max 25}^{sun} = V_{c\max 25}^{sun} \Big/ L^{sun} \tag{8.22}$$

$$\overline{V}_{c\max 25}^{sha} = V_{c\max 25}^{sha} \Big/ L^{sha} \ . \tag{8.23}$$

This integration is over all leaf area (L) with $f_{sun}(x) = \exp(-Kx)$ and K the direct beam extinction coefficient (equation 4.9). Photosynthetic parameters $J_{\max 25}$, T_{p25}, k_{p25}, and R_{d25} scale similarly.

The value $K_n = 0.11$ chosen by Bonan et al. (2011) is consistent with observationally-derived estimates for forests, mostly tropical, and provides a gradient in

V_{cmax} similar to the original CLM4 specific leaf area scaling. However, Bonan et al. (2012) showed that the sunlit/shaded canopy parameterization does not match an explicit multi-layer canopy parameterization. The discrepancy arises from absorption of scattered radiation by shaded leaves and can be tuned out with higher K_n. The model uses $K_n = 0.30$ to match an explicit multi-layer canopy.

$V_{c\max 25}$ additionally varies with daylength (DYL) using the function $f(DYL)$, which introduces seasonal variation to $V_{c\max}$

$$f\left(DYL\right) = \frac{\left(DYL\right)^2}{\left(DYL_{\max}\right)^2} \tag{8.24}$$

with $0.01 \le f\left(DYL\right) \le 1$. Daylength (seconds) is given by

$$DYL = 2 \times 13750.9871 \cos^{-1}\left[\frac{-\sin\left(lat\right)\sin\left(decl\right)}{\cos\left(lat\right)\cos\left(decl\right)}\right] \tag{8.25}$$

where *lat* (latitude) and *decl* (declination angle) are from section 3.3. Maximum daylength ($DYL_{\max}$) is calculated similarly but using the maximum declination angle for present-day orbital geometry (±23.4667º [±0.409571 radians], positive for Northern Hemisphere latitudes and negative for Southern Hemisphere).

8.4 Soil water stress

Soil water influences stomatal conductance directly by multiplying the minimum conductance by a soil water stress function β_t and also indirectly through A_n in the C_3 and C_4 photosynthesis models, as in Sellers et al. (1996). The latter effect is achieved by multiplying $V_{c\max}$ and R_d by β_t.

The function β_t ranges from one when the soil is wet to near zero when the soil is dry and depends on the soil water potential of each soil layer, the root distribution of the plant functional type, and a plant-dependent response to soil water stress

$$\beta_t = \sum_i w_i r_i \tag{8.26}$$

where w_i is a plant wilting factor for layer i and r_i is the fraction of roots in layer i. The plant wilting factor w_i is

$$w_i = \begin{cases} \dfrac{\psi_c - \psi_i}{\psi_c - \psi_o}\left[\dfrac{\theta_{sat,i} - \theta_{ice,i}}{\theta_{sat,i}}\right] \le 1 & \text{for } T_i > T_f - 2 \text{ and } \theta_{liq,i} > 0 \\ 0 & \text{for } T_i \le T_f - 2 \text{ or } \theta_{liq,i} \le 0 \end{cases} \tag{8.27}$$

where ψ_i is the soil water matric potential (mm) and ψ_c and ψ_o are the soil water potential (mm) when stomata are fully closed or fully open (respectively) (Table 8.1). The term in brackets scales w_i by the ratio of the effective porosity (accounting for the ice fraction; $\theta_{sat} - \theta_{ice}$) relative to the total porosity.

Here, the soil water matric potential ψ_i is defined as

$$\psi_i = \psi_{sat,i}\, s_i^{-B_i} \ge \psi_c \tag{8.28}$$

where s_i is the soil wetness for layer i with respect to the effective porosity and $\psi_{sat,i}$ and B_i are the saturated soil matric potential (mm) and the Clapp and Hornberger (1978) parameter (section 7.4.1). The soil wetness s_i is

$$s_i = \frac{\theta_{liq,i}}{\theta_{sat,i} - \theta_{ice,i}} \ge 0.01 \tag{8.29}$$

where $\theta_{ice,i} = w_{ice,i} / \left(\rho_{ice} \Delta z_i \right) \le \theta_{sat,i}$ and $\theta_{liq,i} = w_{liq,i} / \left(\rho_{liq} \Delta z_i \right) \le \theta_{sat,i} - \theta_{ice,i}$. $w_{ice,i}$ and $w_{liq,i}$ are the ice and liquid water contents (kg m^{-2}) (Chapter 7), $\theta_{sat,i}$ is the saturated volumetric water content (section 7.4.1), ρ_{ice} and ρ_{liq} are the densities of ice and liquid water (kg m^{-3}) (Table 2.6), and Δz_i is the soil layer thickness (m) (section 6.1).

The root fraction r_i in each soil layer depends on the plant functional type

$$r_i = \begin{cases} 0.5 \left[\begin{array}{l} \exp\left(-r_a z_{h,i-1}\right) + \exp\left(-r_b z_{h,i-1}\right) - \\ \exp\left(-r_a z_{h,i}\right) - \exp\left(-r_b z_{h,i}\right) \end{array} \right] & \text{for } 1 \le i < N_{levsoi} \\ 0.5 \left[\exp\left(-r_a z_{h,i-1}\right) + \exp\left(-r_b z_{h,i-1}\right) \right] & \text{for } i = N_{levsoi} \end{cases} \quad (8.30)$$

where $z_{h,i}$ (m) is the depth from the soil surface to the interface between layers i and $i+1$ ($z_{h,0} = 0$, the soil surface) (section 6.1), and r_a and r_b are plant-dependent root distribution parameters adopted from Zeng (2001) (Table 8.3).

Table 8.3. Plant functional type root distribution parameters.

Plant Functional Type	r_a	r_b
NET Temperate	7.0	2.0
NET Boreal	7.0	2.0
NDT Boreal	7.0	2.0
BET Tropical	7.0	1.0
BET temperate	7.0	1.0
BDT tropical	6.0	2.0
BDT temperate	6.0	2.0
BDT boreal	6.0	2.0
BES temperate	7.0	1.5
BDS temperate	7.0	1.5
BDS boreal	7.0	1.5
C_3 grass arctic	11.0	2.0
C_3 grass	11.0	2.0
C_4 grass	11.0	2.0
Crop R	6.0	3.0
Crop I	6.0	3.0
Corn R	6.0	3.0
Corn I	6.0	3.0
Temp Cereal R	6.0	3.0
Temp Cereal I	6.0	3.0
Winter Cereal R	6.0	3.0
Winter Cereal I	6.0	3.0
Soybean R	6.0	3.0
Soybean I	6.0	3.0

8.5 Numerical implementation

The CO_2 partial pressure at the leaf surface c_s (Pa) and the vapor pressure at the leaf surface e_s (Pa), needed for the stomatal resistance model in equation (8.1), and the internal leaf CO_2 partial pressure c_i (Pa), needed for the photosynthesis model in equations (8.3)-(8.5), are calculated assuming there is negligible capacity to store CO_2 and water vapor at the leaf surface so that

$$A_n = \frac{c_a - c_i}{\left(1.4r_b + 1.6r_s\right)P_{atm}} = \frac{c_a - c_s}{1.4r_b P_{atm}} = \frac{c_s - c_i}{1.6r_s P_{atm}} \tag{8.31}$$

and the transpiration fluxes are related as

$$\frac{e_a - e_i}{r_b + r_s} = \frac{e_a - e_s}{r_b} = \frac{e_s - e_i}{r_s} \tag{8.32}$$

where r_b is leaf boundary layer resistance (s m^2 μ mol^{-1}) (section 5.3), the terms 1.4 and 1.6 are the ratios of diffusivity of CO_2 to H_2O for the leaf boundary layer resistance and stomatal resistance, $c_a = \mathrm{CO}_2\left(\mathrm{mol\ mol}^{-1}\right)P_{atm}$ is the atmospheric CO_2 partial pressure (Pa) calculated from CO_2 concentration (ppmv), e_i is the saturation vapor pressure (Pa) evaluated at the leaf temperature T_v, and e_a is the vapor pressure of air (Pa). The vapor pressure of air in the plant canopy e_a (Pa) is determined from

$$e_a = \frac{P_{atm} q_s}{0.622} \tag{8.33}$$

where q_s is the specific humidity of canopy air (kg kg^{-1}) (section 5.3). Equations (8.31) and (8.32) are solved for c_s and e_s

$$c_s = c_a - 1.4 r_b P_{atm} A_n \tag{8.34}$$

$$e_s = \frac{e_a r_s + e_i r_b}{r_b + r_s} \tag{8.35}$$

Substitution of equation (8.35) into equation (8.1) gives an expression for stomatal resistance (r_s) as a function of photosynthesis (A_n), given here in terms of conductance with $g_s = 1/r_s$ and $g_b = 1/r_b$

$$c_s g_s^2 + \left[c_s \left(g_b - b \right) - m A_n P_{atm} \right] g_s - g_b \left[c_s b + m A_n P_{atm} \, e_a / e_* \left(T_v \right) \right] = 0 . \tag{8.36}$$

Stomatal conductance is the larger of the two roots that satisfy the quadratic equation. Values for c_i are given by

$$c_i = c_a - \left(1.4 r_b + 1.6 r_s \right) P_{atm} A_n \tag{8.37}$$

The equations for c_i , c_s , r_s , and A_n are solved iteratively until c_i converges. Sun et al. (2012) pointed out that the CLM4 numerical approach does not always converge. Therefore, the model uses a hybrid algorithm that combines the secant method and Brent's method to solve for c_i . The equation set is solved separately for sunlit (A_n^{sun} , r_s^{sun}) and shaded (A_n^{sha} , r_s^{sha}) leaves.

The model has an optional (though not supported) multi-layer canopy, as described by Bonan et al. (2012). The multi-layer model is only intended to address the non-linearity of light profiles, photosynthesis, and stomatal conductance in the plant canopy. In the multi-layer canopy, sunlit (A_n^{sun} , r_s^{sun}) and shaded (A_n^{sha} , r_s^{sha}) leaves are explicitly resolved at depths in the canopy using a light profile (Chapter 4). In this case, $V_{c\max 25}$ is not integrated over the canopy, but is instead given explicitly for each canopy layer using equation (8.19). This also uses the Lloyd et al. (2010) relationship whereby K_n scales with V_{cmax} as

$$K_n = \exp\left(0.00963 V_{c\max} - 2.43\right) \tag{8.38}$$

such that higher values of V_{cmax} imply steeper declines in photosynthetic capacity through the canopy with respect to cumulative leaf area.

9. Lake Model

The lake model, denoted the *Lake, Ice, Snow, and Sediment Simulator* (LISSS), is from Subin et al. (2012a). It includes extensive modifications to the lake code of Zeng et al. (2002) used in CLM versions 2 through 4, which utilized concepts from the lake models of Bonan (1996), Henderson-Sellers (1985, 1986), Hostetler and Bartlein (1990) and the coupled lake-atmosphere model of Hostetler et al. (1993, 1994). Lakes have spatially variable depth prescribed in the surface data (section 9.2); the surface data optionally includes lake optical extinction coeffient and horizontal fetch, currently only used for site simulations. Lake physics includes freezing and thawing in the lake body, resolved snow layers, and "soil" and bedrock layers below the lake body. Temperatures and ice fractions are simulated for $N_{levlak} = 10$ layers (for global simulations) or $N_{levlak} = 25$ (for site simulations) with discretization described in section 9.1. Lake albedo is described in section 9.3. Lake surface fluxes (section 9.4) generally follow the formulations for non-vegetated surfaces, including the calculations of aerodynamic resistances (section 5.2); however, the lake surface temperature T_g (representing an infinitesimal interface layer between the top resolved lake layer and the atmosphere) is solved for simultaneously with the surface fluxes. After surface fluxes are evaluated, temperatures are solved simultaneously in the resolved snow layers (if present), the lake body, and the soil and bedrock, using the ground heat flux *G* as a top boundary condition. Snow, soil, and bedrock models generally follow the formulations for non-vegetated surfaces (Chapter 6), with modifications described below.

9.1 Vertical Discretization

Currently, there is one lake modeled in each grid cell (with prescribed or assumed depth d, extinction coefficient η, and fetch f), although this could be modified with changes to the CLM subgrid decomposition algorithm in future model versions. As currently implemented, the lake consists of 0-5 snow layers; water and ice layers (10 for global simulations and 25 for site simulations) comprising the "lake body;" 10 "soil" layers; and 5 bedrock layers. Each lake body layer has a fixed water mass (set by the nominal layer thickness and the liquid density), with frozen mass-fraction I a state variable. Resolved snow layers are present if the snow thickness $z_{sno} \geq s_{\min}$, where $s_{\min}$ = 4 cm by default, and is adjusted for model timesteps other than 1800 s in order to maintain numerical stability (section 9.6.5). For global simulations with 10 body layers, the default (50 m lake) body layer thicknesses are given by: Δz_i of 0.1, 1, 2, 3, 4, 5, 7, 7, 10.45, and 10.45 m, with node depths z_i located at the center of each layer (i.e., 0.05, 0.6, 2.1, 4.6, 8.1, 12.6, 18.6, 25.6, 34.325, 44.775 m). For site simulations with 25 layers, the default thicknesses are (m): 0.1 for layer 1; 0.25 for layers 2-5; 0.5 for layers 6-9; 0.75 for layers 10-13; 2 for layers 14-15; 2.5 for layers 16-17; 3.5 for layers 18-21; and 5.225 for layers 22-25. For lakes with depth $d \neq 50$ m and $d \geq 1$ m, the top layer is kept at 10 cm and the other 9 layer thicknesses are adjusted to maintain fixed proportions. For lakes with $d < 1$ m, all layers have equal thickness. Thicknesses of snow, soil, and bedrock layers follow the scheme used over non-vegetated surfaces (Chapter 6), with modifications to the snow layer thickness rules to keep snow layers at least as thick as $s_{\min}$ (section 9.6.5).

9.2 External Data

As discussed in Subin et al (2012a, b), the Global Lake and Wetland Database (Lehner and Doll 2004) is currently used to prescribe lake fraction in each land model grid cell, for a total of 2.3 million km^{-2}. As in Subin et al. (2012a, b), the Kourzeneva (2012) global gridded dataset is currently used to estimate a mean lake depth in each grid cell, based on interpolated compilations of geographic information.

9.3 Surface Albedo

For direct radiation, the albedo a for lakes with ground temperature T_g (K) above freezing is given by (Pivovarov, 1972)

$$a = \frac{0.5}{\cos z + 0.15} \tag{9.1}$$

where z is the zenith angle. For diffuse radiation, the expression in eq. (9.1) is integrated over the full sky to yield $a = 0.10$.

For frozen lakes without resolved snow layers, the albedo at cold temperatures a_0 is 0.60 for visible and 0.40 for near infrared radiation. As the temperature at the ice surface, T_g, approaches freezing [T_f (K) (Table 2.6)], the albedo is relaxed towards 0.10 based on Mironov et al. (2010):

$$a = a_0\left(1-x\right) + 0.10x, x = \exp\left(-95\frac{T_f - T_g}{T_f}\right) \tag{9.2}$$

where a is restricted to be no less than that given in eq. (9.1).

For frozen lakes with resolved snow layers, the reflectance of the ice surface is fixed at a_0, and the snow reflectance is calculated as over non-vegetated surfaces (Chapter 3). These two reflectances are combined to obtain the snow-fraction-weighted albedo as in over non-vegetated surfaces (Chapter 3).

9.4 Surface Fluxes and Surface Temperature

9.4.1 Overview of Changes from CLM4

i. The surface roughnesses, and surface absorption fraction β, are diagnostic rather than constants. As the surface roughnesses depend (weakly) on the friction velocity u_* (which itself depends weakly on the surface roughnesses), their calculation has been incorporated into the iteration solution for T_g, and the maximum number of iterations has been increased to 4. Convergence of the modified solution was tested during development.

ii. A coefficient of β has been added to S_g in eq. (9.17), correcting a previous error.

iii. The top layer thickness Δz_T used in eq. (9.13) has been appended with a coefficient of ½, correcting a previous error.

iv. The thermal conductivity λ_T used in eq. (9.13) depends on the properties of the top model layer (e.g., snow, ice, or water). When this layer is unfrozen, λ_T includes the eddy conductivity calculated in the previous timestep.

v. Several conditions are imposed on the ground temperature T_g to maintain a stable density profile at the lake surface eq. (9.24).

9.4.2 Surface Properties

The fraction of shortwave radiation absorbed at the surface, β, depends on the lake state. If resolved snow layers are present, then β is set equal to the absorption fraction predicted by the snow-optics submodel (Chapter 3) for the top snow layer. Otherwise, β is set equal to the near infrared fraction of the shortwave radiation reaching the surface simulated by the atmospheric model or atmospheric data model used for offline simulations (Chapter 26). The remainder of the shortwave radiation fraction ($1-\beta$) is

absorbed in the lake body or soil as described in section 9.5.5.

The surface roughnesses are functions of the lake state and atmospheric forcing. For frozen lakes ($T_g \le T_f$) with resolved snow layers, the momentum roughness length $z_{0m} = 2.4 \times 10^{-3}$ m (as over non-vegetated surfaces; Chapter 5), and the scalar roughness lengths (z_{0q}, for latent heat; and z_{0h}, for sensible heat) are given by (Zilitinkevich 1970)

$$\begin{aligned} R_0 &= \frac{z_{0m} u_*}{\nu}, \\ z_{0h} &= z_{0q} = z_{0m} \exp\left\{-0.13 R_0^{0.45}\right\} \end{aligned} \tag{9.3}$$

where R_0 is the near-surface atmospheric roughness Reynolds number, z_{0h} is the roughness length for sensible heat, z_{0q} is the roughness length for latent heat, ν ($m^2\ s^{-1}$) is the kinematic viscosity of air, and u_* ($m\ s^{-1}$) is the friction velocity in the atmospheric surface layer. For frozen lakes without resolved snow layers, $z_{0m} = 1 \times 10^{-3}$ m (Subin et al. 2012a), and the scalar roughness lengths are given by (9.3).

For unfrozen lakes, z_{0m} is given by (Subin et al. 2012a)

$$z_{0m} = \max\left(\frac{\alpha \nu}{u_*}, C\frac{{u_*}^2}{g}\right) \tag{9.4}$$

where $\alpha = 0.1$, ν is the kinematic viscosity of air given below, C is the effective Charnock coefficient given below, and g is the acceleration of gravity (Table 2.6). The kinematic viscosity is given by

$$\nu = \nu_0 \left(\frac{T_g}{T_0}\right)^{1.5} \frac{P_0}{P_{ref}} \tag{9.5}$$

where $\nu_0 = 1.51\times10^{-5}\ \frac{\text{m}^2}{\text{s}}$, $T_0 = 293.15$ K , $P_0 = 1.013\times10^5$ Pa , and P_{ref} is the pressure at the atmospheric reference height. The Charnock coefficient C is a function of the lake fetch F (m), given in the surface data or set to 25 times the lake depth d by default:

$$\begin{aligned} C &= C_{\min} + (C_{\max} - C_{\min}) \exp\left\{-\min\left(A, B\right)\right\} \\ A &= \left(\frac{Fg}{u_*^{\,2}}\right)^{1/3} \Big/ f_c \\ B &= \varepsilon \frac{\sqrt{dg}}{u} \end{aligned} \qquad (9.6)$$

where A and B define the fetch- and depth-limitation, respectively; $C_{\min} = 0.01$, $C_{\max} = 0.01$, $\varepsilon = 1$, $f_c = 100$, and u (m s^{-1}) is the atmospheric forcing wind.

9.4.3 Surface Flux Solution

Conservation of energy at the lake surface requires

$$\beta\vec{S}_g - \vec{L}_g - H_g - \lambda E_g - G = 0 \qquad (9.7)$$

where $\vec{S}_g$ is the absorbed solar radiation in the lake, β is the fraction absorbed at the surface, $\vec{L}_g$ is the net emitted longwave radiation (+ upwards), H_g is the sensible heat flux (+ upwards), E_g is the water vapor flux (+ upwards), and G is the ground heat flux (+ downwards). All of these fluxes depend implicitly on the temperature at the lake surface T_g. λ converts E_g to an energy flux based on

$$\lambda = \begin{cases} \lambda_{sub} & T_g \le T_f \\ \lambda_{vap} & T_g > T_f \end{cases}. \qquad (9.8)$$

The sensible heat flux (W m^{-2}) is

$$H_g = -\rho_{atm} C_p \frac{\left(\theta_{atm} - T_g\right)}{r_{ah}} \qquad (9.9)$$

where ρ_{atm} is the density of moist air (kg m^{-3}) (Chapter 5), C_p is the specific heat capacity of air (J kg^{-1} K^{-1}) (Table 2.6), θ_{atm} is the atmospheric potential temperature (K) (Chapter 5), T_g is the lake surface temperature (K) (at an infinitesimal interface just above the top resolved model layer: snow, ice, or water), and r_{ah} is the aerodynamic resistance to sensible heat transfer (s m^{-1}) (section 5.1).

The water vapor flux (kg m^{-2} s^{-1}) is

$$E_g = -\frac{\rho_{atm}\left(q_{atm} - q_{sat}^{T_g}\right)}{r_{aw}} \tag{9.10}$$

where q_{atm} is the atmospheric specific humidity (kg kg^{-1}) (section 2.2.1), $q_{sat}^{T_g}$ is the saturated specific humidity (kg kg^{-1}) (section 5.5) at the lake surface temperature T_g, and r_{aw} is the aerodynamic resistance to water vapor transfer (s m^{-1}) (section 5.1).

The zonal and meridional momentum fluxes are

$$\tau_x = -\rho_{atm}\frac{u_{atm}}{r_{atm}} \tag{9.11}$$

$$\tau_y = -\rho_{atm}\frac{v_{atm}}{r_{atm}} \tag{9.12}$$

where u_{atm} and v_{atm} are the zonal and meridional atmospheric winds (m s^{-1}) (section 2.2.1), and r_{am} is the aerodynamic resistance for momentum (s m^{-1}) (section 5.1).

The heat flux into the lake surface G (W m^{-2}) is

$$G = \frac{2\lambda_T}{\Delta z_T}\left(T_g - T_T\right) \tag{9.13}$$

where λ_T is the thermal conductivity (W m^{-1} K^{-1}), Δz_T is the thickness (m), and T_T is the temperature (K) of the top resolved lake layer (snow, ice, or water). The top thermal

conductivity λ_T of unfrozen lakes ($T_g > T_f$) includes conductivities due to molecular (λ_{liq}) and eddy (λ_K) diffusivities (section 9.5.4), as evaluated in the top lake layer at the previous timestep, where λ_{liq} is the thermal conductivity of water (Table 2.6). For frozen lakes without resolved snow layers, $\lambda_T = \lambda_{ice}$. When resolved snow layers are present, λ_T is calculated based on the water content, ice content, and thickness of the top snow layer, as for non-vegetated surfaces.

The absorbed solar radiation $\vec{S}_g$ is

$$\vec{S}_g = \sum_{\Lambda} S_{atm}\downarrow_{\Lambda}^{\mu} \left(1 - \alpha_{g,\Lambda}^{\mu}\right) + S_{atm}\downarrow_{\Lambda} \left(1 - \alpha_{g,\Lambda}\right) \tag{9.14}$$

where $S_{atm}\downarrow_{\Lambda}^{\mu}$ and $S_{atm}\downarrow_{\Lambda}$ are the incident direct beam and diffuse solar fluxes (W m^{-2}) and Λ denotes the visible (< 0.7 μm) and near-infrared ($\geq$ 0.7 μm) wavebands (section 2.2.1), and $\alpha_{g,\Lambda}^{\mu}$ and $\alpha_{g,\mu}$ are the direct beam and diffuse lake albedos (section 9.3).

The net emitted longwave radiation is

$$\vec{L}_g = L_g\uparrow - L_{atm}\downarrow \tag{9.15}$$

where $L_g\uparrow$ is the upward longwave radiation from the surface, $L_{atm}\downarrow$ is the downward atmospheric longwave radiation (section 2.2.1). The upward longwave radiation from the surface is

$$L\uparrow = \left(1 - \varepsilon_g\right) L_{atm}\downarrow + \varepsilon_g \sigma \left(T_g^n\right)^4 + 4\varepsilon_g \sigma \left(T_g^n\right)^3 \left(T_g^{n+1} - T_g^n\right) \tag{9.16}$$

where $\varepsilon_g = 0.97$ is the lake surface emissivity, σ is the Stefan-Boltzmann constant (W m^{-2} K^{-4}) (Table 2.6), and $T_g^{n+1} - T_g^n$ is the difference in lake surface temperature between Newton-Raphson iterations (see below).

The sensible heat H_g, the water vapor flux E_g through its dependence on the saturated specific humidity, the net longwave radiation $\vec{L}_g$, and the ground heat flux G, all depend on the lake surface temperature T_g. Newton-Raphson iteration is applied to solve for T_g and the surface fluxes as

$$\Delta T_g = \frac{\beta \vec{S}_g - \vec{L}_g - H_g - \lambda E_g - G}{\frac{\partial \vec{L}_g}{\partial T_g} + \frac{\partial H_g}{\partial T_g} + \frac{\partial \lambda E_g}{\partial T_g} + \frac{\partial G}{\partial T_g}} \tag{9.17}$$

where $\Delta T_g = T_g^{n+1} - T_g^n$ and the subscript "n" indicates the iteration. Therefore, the surface temperature T_g^{n+1} can be written as

$$T_g^{n+1} = \frac{\beta \vec{S}_g - \vec{L}_g - H_g - \lambda E_g - G + T_g^n \left(\frac{\partial \vec{L}_g}{\partial T_g} + \frac{\partial H_g}{\partial T_g} + \frac{\partial \lambda E_g}{\partial T_g} + \frac{\partial G}{\partial T_g} \right)}{\frac{\partial \vec{L}_g}{\partial T_g} + \frac{\partial H_g}{\partial T_g} + \frac{\partial \lambda E_g}{\partial T_g} + \frac{\partial G}{\partial T_g}} \tag{9.18}$$

where the partial derivatives are

$$\frac{\partial \vec{L}_g}{\partial T_g} = 4\varepsilon_g \sigma \left(T_g^n \right)^3, \tag{9.19}$$

$$\frac{\partial H_g}{\partial T_g} = \frac{\rho_{atm} C_p}{r_{ah}}, \tag{9.20}$$

$$\frac{\partial \lambda E_g}{\partial T_g} = \frac{\lambda \rho_{atm}}{r_{aw}} \frac{dq_{sat}^{T_g}}{dT_g}, \tag{9.21}$$

$$\frac{\partial G}{\partial T_g} = \frac{2\lambda_T}{\Delta z_T}. \tag{9.22}$$

The fluxes of momentum, sensible heat, and water vapor are solved for simultaneously with lake surface temperature as follows. The stability-related equations

are the same as for non-vegetated surfaces (section 5.2), except that the surface roughnesses are here (weakly varying) functions of the friction velocity u_*. To begin, z_{0m} is set based on the value calculated for the last timestep (for $T_g > T_f$) or based on the values in section 9.4.2 (otherwise), and the scalar roughness lengths are set based on the relationships in section 9.4.2.

1. An initial guess for the wind speed V_a including the convective velocity U_c is obtained from eq. (5.24) assuming an initial convective velocity $U_c = 0$ m s^{-1} for stable conditions ($\theta_{v,atm} - \theta_{v,s} \geq 0$ as evaluated from eq. (5.50)) and $U_c = 0.5$ for unstable conditions ($\theta_{v,atm} - \theta_{v,s} < 0$).
2. An initial guess for the Monin-Obukhov length L is obtained from the bulk Richardson number using equations (5.46) and (5.48).
3. The following system of equations is iterated four times:
    - Heat of vaporization / sublimation λ (eq. (9.8))
    - Thermal conductivity λ_T (above)
    - Friction velocity u_* (eqs. (5.32), (5.33), (5.34), (5.35))
    - Potential temperature scale θ_* (eqs. (5.37), (5.38), (5.39), (5.40))
    - Humidity scale q_* (eqs. (5.41), (5.42), (5.43), (5.44))
    - Aerodynamic resistances r_{am}, r_{ah}, and r_{aw} (eqs. (5.55), (5.56), (5.57))
    - Lake surface temperature T_g^{n+1} (eq.(9.18))
    - Heat of vaporization / sublimation λ (eq. (9.8))
    - Sensible heat flux H_g is updated for T_g^{n+1} (eq.(9.9))

- Water vapor flux E_g is updated for T_g^{n+1} as

$$E_g = -\frac{\rho_{atm}}{r_{aw}}\left[q_{atm} - q_{sat}^{T_g} - \frac{\partial q_{sat}^{T_g}}{\partial T_g}\left(T_g^{n+1} - T_g^{n}\right)\right] \tag{9.23}$$

  where the last term on the right side of equation (9.23) is the change in saturated specific humidity due to the change in T_g between iterations.

- Saturated specific humidity $q_{sat}^{T_g}$ and its derivative $\frac{dq_{sat}^{T_g}}{dT_g}$ are updated for T_g^{n+1} (section 5.1).
- Virtual potential temperature scale θ_{v*} (eq. (5.17))
- Wind speed including the convective velocity, V_a (eq. (5.24))
- Monin-Obukhov length L (eq. (5.49)).
- Roughness lengths (eq. (9.3), (9.4)).

Once the four iterations for lake surface temperature have been yielded a tentative solution T_g', several restrictions are imposed in order to maintain consistency with the top lake model layer temperature T_T (Subin et al. 2012a).

$$\begin{aligned} &1)\ T_T \le T_f < T_g' \Rightarrow T_g = T_f, \\ &2)\ T_T > T_g' > T_m \Rightarrow T_g = T_T, \\ &3)\ T_m > T_g' > T_T > T_f \Rightarrow T_g = T_T \end{aligned} \tag{9.24}$$

where T_m is the temperature of maximum liquid water density, 3.85°C (Hostetler and Bartlein 1990). The first condition requires that, if there is any snow or ice present, the surface temperature is restricted to be less than or equal to freezing. The second and third conditions maintain convective stability in the top lake layer.

If eq. (9.24) is applied, the turbulent fluxes H_g and E_g are re-evaluated. The emitted longwave radiation and the momentum fluxes are re-evaluated in any case. The final ground heat flux G is calculated from the residual of the energy balance eq. (9.7) in order to precisely conserve energy. This ground heat flux is taken as a prescribed flux boundary condition for the lake temperature solution (section 9.5.3). An energy balance check is included at each timestep to insure that eq. (9.7) is obeyed to within 0.1 W m^{-2}.

9.5 Lake Temperature

9.5.1 Introduction

The (optional-) snow, lake body (water and/or ice), soil, and bedrock system is unified for the lake temperature solution. The governing equation, similar to that for the snow-soil-bedrock system for vegetated land units (Chapter 6), is

$$\tilde{c}_v \frac{\partial T}{\partial t} = \frac{\partial}{\partial z}\left(\tau \frac{\partial T}{\partial z} \right) - \frac{d\phi}{dz} \tag{9.25}$$

where $\tilde{c}_v$ is the volumetric heat capacity (J m^{-3} K^{-1}), t is time (s), T is the temperature (K), τ is the thermal conductivity (W m^{-1} K^{-1}), and ϕ is the solar radiation (W m^{-2}) penetrating to depth z (m). The system is discretized into N layers, where

$$N = n_{sno} + N_{levlak} + N_{levgrnd} \ , \tag{9.26}$$

n_{sno} is the number of actively modeled snow layers at the current timestep (section 7.2), and $N_{levgrnd}$ is as for vegetated land units (Chapter 6). Energy is conserved as

$$\frac{d}{dt}\sum_{j=1}^{N}\left[\tilde{c}_{v,j}(t)\left(T_j - T_f\right) + L_j(t) \right]\Delta z_j = G + \left(1-\beta\right)\vec{S}_g \tag{9.27}$$

where $\tilde{c}_{v,j}(t)$ is the volumetric heat capacity of the jth layer (section 9.5.5), $L_j(t)$ is the latent heat of fusion per unit volume of the jth layer (proportional to the mass of liquid

water present), and the right-hand side represents the net influx of energy to the lake system. Note that $\tilde{c}_{v,j}(t)$ can only change due to phase change (except for changing snow layer mass, which, apart from energy required to melt snow, represents an untracked energy flux in the land model, along with advected energy associated with water flows in general), and this is restricted to occur at $T_j = T_f$ in the snow-lake-soil system, allowing eq. (9.27) to be precisely enforced and justifying the exclusion of $c_{v,j}$ from the time derivative in eq. (9.25).

9.5.2 Overview of Changes from CLM4

Thermal conductivities include additional eddy diffusivity, beyond the Hostetler and Bartlein (1990) formulation, due to unresolved processes (Fang and Stefan 1996; Subin et al. 2012a). Lake water is now allowed to freeze by an arbitrary fraction for each layer, which releases latent heat and changes thermal properties. Convective mixing occurs for all lakes, even if frozen. Soil and bedrock are included beneath the lake. The full snow model is used if the snow thickness exceeds a threshold; if there are resolved snow layers, radiation transfer is predicted by the snow-optics submodel (Chapter 3), and the remaining radiation penetrating the bottom snow layer is absorbed in the top layer of lake ice; conversely, if there are no snow layers, the solar radiation penetrating the bottom lake layer is absorbed in the top soil layer. The lakes have variable depth, and all physics is assumed valid for arbitrary depth, except for a depth-dependent enhanced mixing (section 9.5.4). Finally, a previous sign error in the calculation of eddy diffusivity (specifically, the Brunt-Väisälä frequency term; eq. (9.33)) was corrected.

9.5.3 Boundary Conditions

The top boundary condition, imposed at the top modeled layer $i = j_{top}$, where $j_{top} = -n_{sno} + 1$, is the downwards surface flux G defined by the energy flux residual during the surface temperature solution (section 9.4.3). The bottom boundary condition, imposed at $i = N_{levlak} + N_{levgrnd}$, is zero flux. The 2-m windspeed u_2 (m s^{-1}) is used in the calculation of eddy diffusivity:

$$u_2 = \frac{u_*}{k} \ln\left(\frac{2}{z_{0m}}\right) \geq 0.1. \tag{9.28}$$

where u_* is the friction velocity calculated in section 9.4.3 and k is the von Karman constant (Table 2.6).

9.5.4 Eddy Diffusivity and Thermal Conductivities

The total eddy diffusivity K_W (m^2 s^{-1}) for liquid water in the lake body is given by (Subin et al. 2012a)

$$K_W = m_d \left(\kappa_e + K_{ed} + \kappa_m\right) \tag{9.29}$$

where κ_e is due to wind-driven eddies (Hostetler and Bartlein 1990), K_{ed} is a modest enhanced diffusivity intended to represent unresolved mixing processes (Fang and Stefan 1996), $\kappa_m = \frac{\lambda_{liq}}{c_{liq}\rho_{liq}}$ is the molecular diffusivity of water (given by the ratio of its thermal conductivity (W m^{-1} K^{-1}) to the product of its heat capacity (J kg^{-1} K^{-1}) and density (kg m^{-3}), values given in Table 2.6), and m_d (unitless) is a factor which increases the overall diffusivity for large lakes, intended to represent 3-dimensional mixing processes such as caused by horizontal temperature gradients. As currently implemented,

$$m_d = \begin{cases} 1, & d < 25\text{m} \\ 10, & d \geq 25\text{m} \end{cases} \tag{9.30}$$

where d is the lake depth.

The wind-driven eddy diffusion coefficient $\kappa_{e,i}$ (m^2 s^{-1}) for layers $1 \leq i \leq N_{levlak}$ is

$$\kappa_{e,i} = \begin{cases} \dfrac{kw^* z_i}{P_0\left(1+37Ri^2\right)} \exp\left(-k^* z_i\right) & T_g > T_f \\ 0 & T_g \leq T_f \end{cases} \tag{9.31}$$

where $P_0 = 1$ is the neutral value of the turbulent Prandtl number, z_i is the node depth (m), the surface friction velocity (m s^{-1}) is $w^* = 0.0012u_2$, and k^* varies with latitude ϕ as $k^* = 6.6u_2^{-1.84}\sqrt{|\sin\phi|}$. For the bottom layer, $\kappa_{e,N_{levlak}} = \kappa_{e,N_{levlak}-1}$. As in Hostetler and Bartlein (1990), the 2-m wind speed u_2 (m s^{-1}) (eq. (9.28)) is used to evaluate w^* and k^* rather than the 10-m wind used by Henderson-Sellers (1985).

The Richardson number is

$$R_i = \frac{-1 + \sqrt{1 + \dfrac{40N^2k^2z_i^2}{w^{*^2}\exp\left(-2k^* z_i\right)}}}{20} \tag{9.32}$$

where

$$N^2 = \frac{g}{\rho_i}\frac{\partial\rho}{\partial z} \tag{9.33}$$

and g is the acceleration due to gravity (m s^{-2}) (Table 2.6), ρ_i is the density of water (kg m^{-3}), and $\dfrac{\partial\rho}{\partial z}$ is approximated as $\dfrac{\rho_{i+1} - \rho_i}{z_{i+1} - z_i}$. Note that because here, z is increasing downwards (unlike in Hostetler and Bartlein (1990)), eq. (9.33) contains no negative

sign; this is a correction from CLM4. The density of water is (Hostetler and Bartlein 1990)

$$\rho_i = 1000\left(1 - 1.9549\times10^{-5}\left|T_i - 277\right|^{1.68}\right). \tag{9.34}$$

The enhanced diffusivity K_{ed} is given by (Fang and Stefan 1996)

$$K_{ed} = 1.04\times10^{-8}\left(N^2\right)^{-0.43}, N^2 \geq 7.5\times10^{-5}\text{s}^2 \tag{9.35}$$

where N^2 is calculated as in eq. (9.33) except for the minimum value imposed in (9.35).

The thermal conductivity for the liquid water portion of lake body layer *i*, $\tau_{liq,i}$ (W m^{-1} K^{-1}) is given by

$$\tau_{liq,i} = K_W c_{liq} \rho_{liq} \ . \tag{9.36}$$

The thermal conductivity of the ice portion of lake body layer *i*, $\tau_{ice,eff}$ (W m^{-1} K^{-1}), is constant among layers, and is given by

$$\tau_{ice,eff} = \tau_{ice} \frac{\rho_{ice}}{\rho_{liq}} \tag{9.37}$$

where τ_{ice} (Table 2.6) is the nominal thermal conductivity of ice: $\tau_{ice,eff}$ is adjusted for the fact that the nominal model layer thicknesses remain constant even while the physical ice thickness exceeds the water thickness.

The overall thermal conductivity τ_i for layer *i* with ice mass-fraction I_i is the harmonic mean of the liquid and water fractions, assuming that they will be physically vertically stacked, and is given by

$$\tau_i = \frac{\tau_{ice,eff}\tau_{liq,i}}{\tau_{liq,i}I_i + \tau_{ice}\left(1 - I_i\right)} \ . \tag{9.38}$$

The thermal conductivity of snow, soil, and bedrock layers above and below the lake, respectively, are computed identically to those for vegetated land units (Chapter 6), except for the adjustment of thermal conductivity for frost heave or excess ice (Subin et al., 2012a, Supporting Information).

9.5.5 Radiation Penetration

If there are no resolved snow layers, the surface absorption fraction β is set according to the near-infrared fraction simulated by the atmospheric model. This is apportioned to the surface energy budget (section 9.4.2), and thus no additional radiation is absorbed in the top z_a (currently 0.6 m) of unfrozen lakes, for which the light extinction coefficient η (m^{-1}) varies between lake columns (eq. (9.41)). For frozen lakes ($T_g \le T_f$), the remaining $(1-\beta)\vec{S}_g$ fraction of surface absorbed radiation that is not apportioned to the surface energy budget is absorbed in the top lake body layer. This is a simplification, as lake ice is partially transparent. If there are resolved snow layers, then the snow optics submodel (Chapter 3) is used to calculate the snow layer absorption (except for the absorption predicted for the top layer by the snow optics submodel, which is assigned to the surface energy budget), with the remainder penetrating snow layers absorbed in the top lake body ice layer.

For unfrozen lakes, the solar radiation remaining at depth $z > z_a$ in the lake body is given by

$$\phi = \left(1-\beta\vec{S}_g\right)\exp\left\{-\eta\left(z-z_a\right)\right\} . \tag{9.39}$$

For all lake body layers, the flux absorbed by the layer *i*, ϕ_i , is

$$\phi_i = \left(1 - \beta \vec{S}_g\right)\left[\exp\left\{-\eta\left(z_i - \frac{\Delta z_i}{2} - z_a\right)\right\} - \exp\left\{-\eta\left(z_i + \frac{\Delta z_i}{2} - z_a\right)\right\}\right] . \quad (9.40)$$

The argument of each exponent is constrained to be non-negative (so $\phi_i = 0$ for layers contained within z_a). The remaining flux exiting the bottom of layer $i = N_{levlak}$ is absorbed in the top soil layer.

The light extinction coefficient η (m^{-1}), if not provided as external data, is a function of depth d (m) (Subin et al. 2012a):

$$\eta = 1.1925 d^{-0.424} . \quad (9.41)$$

9.5.6 Heat Capacities

The vertically-integrated heat capacity for each lake layer, $c_{v,i}$ (J m^{-2}) is determined by the mass-weighted average over the heat capacities for the water and ice fractions:

$$c_{v,i} = \Delta z_i \rho_{liq}\left[c_{liq}\left(1 - I_i\right) + c_{ice} I_i\right] . \quad (9.42)$$

Note that the density of water is used for both ice and water fractions, as the thickness of the layer is fixed.

The total heat capacity $c_{v,i}$ for each soil, snow, and bedrock layer (J m^{-2}) is determined as for vegetated land units (Chapter 6), as the sum of the heat capacities for the water, ice, and mineral constituents.

9.5.7 Crank-Nicholson Solution

The solution method for thermal diffusion is similar to that used for soil (Chapter 6), except that the lake body layers are sandwiched between the snow and soil layers (section 9.5.1), and radiation flux is absorbed throughout the lake layers. Before solution, layer temperatures T_i (K), thermal conductivities τ_i (W m^{-1} K^{-1}), heat capacities $c_{v,i}$ (J

m^{-2}), and layer and interface depths from all components are transformed into a uniform set of vectors with length $N = n_{sno} + N_{levlak} + N_{levgrnd}$ and consistent units to simplify the solution. Thermal conductivities at layer interfaces are calculated as the harmonic mean of the conductivities of the neighboring layers:

$$\lambda_i = \frac{\tau_i \tau_{i+1} \left(z_{i+1} - z_i \right)}{\tau_i \left(z_{i+1} - \hat{z}_i \right) + \tau_{i+1} \left(\hat{z}_i - z_i \right)} \ , \tag{9.43}$$

where λ_i is the conductivity at the interface between layer *i* and layer *i* + 1, z_i is the depth of the node of layer *i*, and $\hat{z}_i$ is the depth of the interface below layer *i*. Care is taken at the boundaries between snow and lake and between lake and soil. The governing equation (9.25) is discretized for each layer as

$$\frac{c_{v,i}}{\Delta t} \left(T_i^{n+1} - T_i^n \right) = F_{i-1} - F_i + \phi_i \tag{9.44}$$

where superscripts *n* + 1 and *n* denote values at the end and beginning of the timestep Δt, respectively, F_i (W m^{-2}) is the downward heat flux at the bottom of layer *i*, and ϕ_i is the solar radiation absorbed in layer *i*.

Eq. (9.44) is solved using the semi-implicit Crank-Nicholson Method, resulting in a tridiagonal system of equations:

$$\begin{aligned}
r_i &= a_i T_{i-1}^{n+1} + b_i T_i^{n+1} + c T_{i+1}^{n+1}, \\
a_i &= -0.5 \frac{\Delta t}{c_{v,i}} \frac{\partial F_{i-1}}{\partial T_{i-1}^n}, \\
b_i &= 1 + 0.5 \frac{\Delta t}{c_{v,i}} \left(\frac{\partial F_{i-1}}{\partial T_{i-1}^n} + \frac{\partial F_i}{\partial T_i^n} \right), \\
c_i &= -0.5 \frac{\Delta t}{c_{v,i}} \frac{\partial F_i}{\partial T_i^n}, \\
r_i &= T_i^n + 0.5 \frac{\Delta t}{c_{v,i}} \left(F_{i-1} - F_i \right) + \frac{\Delta t}{c_{v,i}} \phi_i .
\end{aligned} \tag{9.45}$$

The fluxes F_i are defined as follows: for the top layer, $F_{j_{top}-1} = 2G; a_{j_{top}} = 0$, where G is defined as in section 9.4.3 (the factor of 2 merely cancels out the Crank-Nicholson 0.5 in the equation for $r_{j_{top}}$). For the bottom layer, $F_{N_{levlak}+N_{levgrnd}} = 0$. For all other layers:

$$F_i = \lambda_i \frac{T_i^n - T_{i+1}^n}{z_{n+1} - z_n} \ . \tag{9.46}$$

9.5.8 Phase Change

Phase change in the lake, snow, and soil is done similarly to that done for the soil and snow for vegetated land units (Chapter 6), except without the allowance for freezing point depression in soil underlying lakes. After the heat diffusion is calculated, phase change occurs in a given layer if the temperature is below freezing and liquid water remains, or if the temperature is above freezing and ice remains.

If melting occurs, the available energy for melting, Q_{avail} (J m^{-2}), is computed as

$$Q_{avail} = \left(T_i - T_f\right) c_{v,i} \tag{9.47}$$

where T_i is the temperature of the layer after thermal diffusion (section 9.5.7), and $c_{v,i}$ is as calculated in section 9.5.6. The mass of melt in the layer M (kg m^{-2}) is given by

$$M = \min\left\{M_{ice}, \frac{Q_{avail}}{H_{fus}}\right\} \tag{9.48}$$

where H_{fus} (J kg^{-1}) is the latent heat of fusion of water (Table 2.6), and M_{ice} is the mass of ice in the layer: $I_i \rho_{liq} \Delta z_i$ for a lake body layer, or simply the soil / snow ice content state variable (w_{ice}) for a soil / snow layer. The heat remainder, Q_{rem} is given by

$$Q_{rem} = Q_{avail} - M H_{fus} \ . \tag{9.49}$$

Finally, the mass of ice in the layer M_{ice} is adjusted downwards by M, and the temperature T_i of the layer is adjusted to

$$T_i = T_f + \frac{Q_{rem}}{c'_{v,i}} \tag{9.50}$$

where $c'_{v,i} = c_{v,i} + M\left(c_{liq} - c_{ice}\right)$.

If freezing occurs, Q_{avail} is again given by (9.47) but will be negative. The melt M, also negative, is given by

$$M = \max\left\{-M_{liq}, \frac{Q_{avail}}{H_{fus}}\right\} \tag{9.51}$$

where M_{liq} is the mass of water in the layer: $\left(1 - I_i\right)\rho_{liq}\Delta z_i$ for a lake body layer, or the soil / snow water content state variable (w_{liq}). The heat remainder Q_{rem} is given by eq. (9.49) and will be negative or zero. Finally, M_{liq} is adjusted downwards by $-M$ and the temperature is reset according to eq. (9.50).

In the presence of nonzero snow water W_{sno} without resolved snow layers over an unfrozen top lake layer, the available energy in the top lake layer $\left(T_1 - T_f\right)c_{v,1}$ is used to melt the snow. Similar to above, W_{sno} is either completely melted and the remainder of heat returned to the top lake layer, or the available heat is exhausted and the top lake layer is set to freezing. The snow thickness is adjusted downwards in proportion to the amount of melt, maintaining constant density.

9.5.9 Convection

Convective mixing is based on Hostetler et al.'s (1993, 1994) coupled lake-atmosphere model, adjusting the lake temperature after diffusion and phase change to

maintain a stable density profile. Unfrozen lakes overturn when $\rho_i > \rho_{i+1}$, in which case the layer thickness weighted average temperature for layers 1 to $i+1$ is applied to layers 1 to $i+1$ and the densities are updated. This scheme is applied iteratively to layers $1 \le i < N_{levlak} - 1$. Unstable profiles occurring at the bottom of the lake (i.e., between layers $i = N_{levlak} - 1$ and $i = N_{levlak}$) are treated separately (Subin et al. 2012a), as occasionally these can be induced by heat expelled from the sediments (not present in the original Hostetler et al. (1994) model). Mixing proceeds from the bottom upward in this case (i.e., first mixing layers $i = N_{levlak} - 1$ and $i = N_{levlak}$, then checking $i = N_{levlak} - 2$ and $i = N_{levlak} - 1$ and mixing down to $i = N_{levlak}$ if needed, and on to the top), so as not to mix in with warmer over-lying layers.

For frozen lakes, this algorithm is generalized to conserve total enthalpy and ice content, and to maintain ice contiguous at the top of the lake. Thus, an additional mixing criterion is added: the presence of ice in a layer that is below a layer which is not completely frozen. When this occurs, these two lake layers and all those above mix. Total enthalpy Q is conserved as

$$Q = \sum_{j=1}^{i+1} \Delta z_j \rho_{liq} \left(T_j - T_f \right) \left[\left(1 - I_j \right) c_{liq} + I_j c_{ice} \right] . \tag{9.52}$$

Once the average ice fraction I_{av} is calculated from

$$\begin{aligned} I_{av} &= \frac{\sum_{j=1}^{i+1} I_j \Delta z_j}{Z_{i+1}}, \\ Z_{i+1} &= \sum_{j=1}^{i+1} \Delta z_j, \end{aligned} \tag{9.53}$$

the temperatures are calculated. A separate temperature is calculated for the frozen (T_{froz}) and unfrozen (T_{unfr}) fractions of the mixed layers. If the total heat content Q is positive (e.g. some layers will be above freezing), then the extra heat is all assigned to the unfrozen layers, while the fully frozen layers are kept at freezing. Conversely, if $Q < 0$, the heat deficit will all be assigned to the ice, and the liquid layers will be kept at freezing. For the layer that contains both ice and liquid (if present), a weighted average temperature will have to be calculated.

If $Q > 0$, then $T_{froz} = T_f$, and T_{unfr} is given by

$$T_{unfr} = \frac{Q}{\rho_{liq} Z_{i+1} \left[\left(1 - I_{av}\right) c_{liq} \right]} + T_f \ . \tag{9.54}$$

If $Q < 0$, then $T_{unfr} = T_f$, and T_{froz} is given by

$$T_{froz} = \frac{Q}{\rho_{liq} Z_{i+1} \left[I_{av} c_{ice} \right]} + T_f \ . \tag{9.55}$$

The ice is lumped together at the top. For each lake layer j from 1 to $i + 1$, the ice fraction and temperature are set as follows, where $Z_j = \sum_{m=1}^{j} \Delta z_m$:

1. If $Z_j \le Z_{i+1} I_{av}$, then $I_j = 1$ and $T_j = T_{froz}$.
2. Otherwise, if $Z_{j-1} < Z_{i+1} I_{av}$, then the layer will contain both ice and water. The ice fraction is given by $I_j = \frac{Z_{i+1} I_{av} - Z_{j-1}}{\Delta z_j}$. The temperature is set to conserve the desired heat content that would be present if the layer could have two temperatures, and then dividing by the heat capacity of the layer to yield

$$T_j = \frac{T_{froz} I_j c_{ice} + T_{unfr}\left(1 - I_j\right) c_{liq}}{I_j c_{ice} + \left(1 - I_j\right) c_{liq}} \quad . \tag{9.56}$$

3. Otherwise, $I_j = 0$ and $T_j = T_{unfr}$.

9.5.10 Energy Conservation

To check energy conservation, the left-hand side of eq. (9.27) is re-written to yield the total enthalpy of the lake system (J m^{-2}) H_{tot}:

$$H_{tot} = \sum_{i=j_{top}}^{N_{levlak}+N_{levgrnd}} \left[c_{v,i}\left(T_i - T_f\right) + M_{liq,i} H_{fus} \right] - W_{sno,bulk} H_{fus} \tag{9.57}$$

where $M_{liq,i}$ is the water mass of the *i*th layer (similar to section 9.5.8), and $W_{sno,bulk}$ is the mass of snow-ice not present in resolved snow layers. This expression is evaluated once at the beginning and once at the end of the timestep (re-evaluating each $c_{v,i}$), and the change is compared with the net surface energy flux to yield the error flux E_{soi} (W m^{-2}):

$$E_{soi} = \frac{\Delta H_{tot}}{\Delta t} - G - \sum_{i=j_{top}}^{N_{levlak}+N_{levgrnd}} \phi_i \tag{9.58}$$

If $\left|E_{soi}\right| < 0.1$ W m^{-2}, it is subtracted from the sensible heat flux and added to *G*. Otherwise, the model is aborted.

9.6 Lake Hydrology

9.6.1 Overview

Hydrology is done similarly to other impervious non-vegetated columns (e.g., glaciers) where snow layers may be resolved but infiltration into the permanent ground is not allowed. The water mass of lake columns is currently maintained constant, aside

from overlying snow. The water budget is balanced with q_{rgwl} (eq. (9.59); kg m^{-2} s^{-1}), a generalized runoff term for impervious land units that may be negative.

There are some modifications to the soil and snow parameterizations as compared with the soil in vegetated land units, or the snow overlying other impervious columns. The soil can freeze or thaw, with the allowance for frost heave (or the initialization of excess ice) (sections 9.5.4 and 9.5.8), but no air-filled pore space is allowed in the soil. To preserve numerical stability in the lake model (which uses a slightly different surface flux algorithm than over other non-vegetated land units), two changes are made to the snow model. First, dew or frost is not allowed to be absorbed by a top snow layer which has become completely melted during the timestep. Second, because occasional instabilities occurred during model testing when the Courant–Friedrichs–Lewy (CFL) condition was violated, due to the explicit time-stepping integration of the surface flux solution, resolved snow layers must be a minimum of $s_{\min}$ = 4 cm thick rather than 1 cm when the default timestep of 1800 s is used.

9.6.2 Water Balance

The total water balance of the system is given by

$$\Delta W_{sno} + \sum_{i=1}^{n_{levsoi}} \left(\Delta w_{liq,i} + \Delta w_{ice,i} \right) = \left(q_{rain} + q_{sno} - E_g - q_{rgwl} - q_{snwcp,ice} \right) \Delta t \qquad (9.59)$$

where W_{sno} (kg m^{-2}) is the total mass of snow (both liquid and ice, in resolved snow layers or bulk snow), $w_{liq,i}$ and $w_{ice,i}$ are the masses of water phases (kg m^{-2}) in soil layer i, q_{rain} and q_{sno} are the precipitation forcing from the atmosphere (kg m^{-2} s^{-1}), $q_{snwcp,ice}$ is the ice runoff associated with snow-capping (below), E_g is the ground evaporation

(section 9.4.3), and n_{levsoi} is the number of hydrologically active soil layers (as opposed to dry bedrock layers).

9.6.3 Precipitation, Evaporation, and Runoff

All precipitation reaches the ground, as there is no vegetated fraction. As for other land types, incident snowfall accumulates (with ice mass W_{sno} and thickness z_{sno}) until its thickness exceeds a minimum thickness $s_{\min}$, at which point a resolved snow layer is initiated, with water, ice, dissolved aerosol, snow-grain radius, etc., state variables tracked by the Snow Hydrology submodel (section 7.2). The density of fresh snow is assigned as for other land types (section 7.2). Solid precipitation is added immediately to the snow, while liquid precipitation is added to snow layers, if they exist, after accounting for dew, frost, and sublimation (below). If z_{sno} exceeds $s_{\min}$ after solid precipitation is added but no snow layers are present, a new snow layer is initiated immediately, and then dew, frost, and sublimation are accounted for. Snow-capping is invoked if the snow depth $z_{sno} > 1000\text{m}$, in which case additional precipitation and frost deposition is added to $q_{snwcp,ice}$.

If there are resolved snow layers, the generalized "evaporation" E_g (i.e., evaporation, dew, frost, and sublimation) is treated as over other land units, except that the allowed evaporation from the ground is unlimited (though the top snow layer cannot lose more water mass than it contains). If there are no resolved snow layers but $W_{sno} > 0$ and $E_g > 0$, sublimation $q_{sub,sno}$ (kg m^{-2} s^{-1}) will be given by

$$q_{sub,sno} = \min\left\{E_g, \frac{W_{sno}}{\Delta t}\right\} . \tag{9.60}$$

If $E_g < 0, T_g \le T_f$, and there are no resolved snow layers or the top snow layer is not unfrozen, then the rate of frost production $q_{frost} = \left| E_g \right|$. If $E_g < 0$ but the top snow layer has completely thawed during the Phase Change step of the Lake Temperature solution (section 9.5.8), then frost (or dew) is not allowed to accumulate ($q_{frost} = 0$), to insure that the layer is eliminated by the Snow Hydrology (section 7.2) code. (If $T_g > T_f$, then no snow is present (section 9.4.3), and evaporation or dew deposition is balanced by q_{rgwl}.) The snowpack is updated for frost and sublimation:

$$W_{sno} = W_{sno} + \Delta t \left(q_{frost} - q_{sub,sno} \right) . \tag{9.61}$$

If there are resolved snow layers, then this update occurs using the Snow Hydrology submodel (section 7.2). Otherwise, the snow ice mass is updated directly, and z_{sno} is adjusted by the same proportion as the snow ice (i.e., maintaining the same density), unless there was no snow before adding the frost, in which case the density is assumed to be 250 kg m^{-3}.

9.6.4 Soil Hydrology

The combined water and ice soil volume fraction in a soil layer θ_i is given by

$$\theta_i = \frac{1}{\Delta z_i} \left(\frac{w_{ice,i}}{\rho_{ice}} + \frac{w_{liq,i}}{\rho_{liq}} \right) . \tag{9.62}$$

If $\theta_i < \theta_{sat,i}$, the pore volume fraction at saturation (as may occur when ice melts), then the liquid water mass is adjusted to

$$w_{liq,i} = \left(\theta_{sat,i} \Delta z_i - \frac{w_{ice,i}}{\rho_{ice}} \right) \rho_{liq} . \tag{9.63}$$

Otherwise, if excess ice is melting and $w_{liq,i} > \theta_{sat,i}\rho_{liq}\Delta z_i$, then the water in the layer is reset to

$$w_{liq,i} = \theta_{sat,i}\rho_{liq}\Delta z_i \tag{9.64}$$

This allows excess ice to be initialized (and begin to be lost only after the pore ice is melted, which is realistic if the excess ice is found in heterogeneous chunks) but irreversibly lost when melt occurs.

9.6.5 Modifications to Snow Layer Logic

A thickness difference $z_{lsa} = s_{\min} - \tilde{s}_{\min}$ adjusts the minimum resolved snow layer thickness for lake columns as compared to non-lake columns. The value of z_{lsa} is chosen to satisfy the CFL condition for the model timestep. By default, $\tilde{s}_{\min}$ = 1 cm and $s_{\min}$ = 4 cm. See Subin et al. (2012a; including Supporting Information) for further discussion.

The rules for combining and sub-dividing snow layers (section 7.2.7) are adjusted for lakes to maintain minimum thicknesses of $s_{\min}$ and to increase all target layer thicknesses by z_{lsa}. The rules for combining layers are modified by simply increasing layer thickness thresholds by z_{lsa}. The rules for dividing snow layers are contained in a separate subroutine that is modified for lakes, and is a function of the number of layers and the layer thicknesses. There are two types of operations: (a) subdividing layers in half, and (b) shifting some volume from higher layers to lower layers (without increasing the layer number). For subdivisions of type (a), the thickness thresholds triggering subdivision are increased by $2z_{lsa}$ for lakes. For shifts of type (b), the thickness thresholds triggering the shifts are increased by z_{lsa}. At the end of the modified subroutine, a snow ice and liquid balance check are performed.

In rare instances, resolved snow layers may be present over an unfrozen top lake body layer. In this case, the snow layers may be eliminated if enough heat is present in the top layer to melt the snow: see Subin et al. (2012a, Supporting Information).

10. Glaciers

This chapter describes features of CLM that are specific to coupling to an ice sheet model (in the CESM context, this is the Glimmer-CISM model; Lipscomb and Sacks (2012) provide documentation and user's guide for Glimmer-CISM). General information about glacier land units can be found elsewhere in this document (see Chapter 2 for an overview).

10.1 Overview

CLM is responsible for computing three quantities that are passed to the ice sheet model:

1. Surface mass balance (SMB) – the net annual accumulation/ablation of mass at the upper surface (section 10.3)
2. Ground surface temperature, which serves as an upper boundary condition for Glimmer-CISM's temperature calculation
3. Surface topography, which currently is fixed in time, and is provided on CLM's surface dataset

The ice sheet model is typically run at much higher resolution than CLM (e.g., ~5 km rather than ~100 km). To improve the downscaling from CLM's grid to the ice sheet grid, the glaciated portion of each grid cell is divided into multiple elevation classes (section 10.2). The above quantities are computed separately in each elevation class. Glimmer-CISM then computes high-resolution quantities via horizontal and vertical interpolation.

There are several reasons for computing the SMB in CLM rather than in Glimmer-CISM:

1. It is much cheaper to compute the SMB in CLM for ~10 elevation classes than in Glimmer-CISM. For example, suppose we are running CLM at a resolution of ~50 km and Glimmer at ~5 km. Greenland has dimensions of about 1000 x 2000 km. For CLM we would have 20 x 40 x 10 = 8,000 columns, whereas for Glimmer we would have 200 x 400 = 80,000 columns.
2. We can use the sophisticated snow physics parameterization already in CLM instead of implementing a separate scheme for Glimmer-CISM. Any improvements to the CLM are applied to ice sheets automatically.
3. The atmosphere model can respond during runtime to ice-sheet surface changes. As shown by Pritchard et al. (2008), runtime albedo feedback from the ice sheet is critical for simulating ice-sheet retreat on paleoclimate time scales. Without this feedback the atmosphere warms much less, and the retreat is delayed.
4. Mass is more nearly conserved, given that the rate of surface ice growth or melting computed in CLM is equal to the rate seen by the dynamic ice sheet model. (Mass conservation is not exact, however, because of approximations made in interpolating from the CLM grid to the ice-sheet grid.)
5. The improved SMB is available in CLM for all glaciated grid cells (e.g., in the Alps, Rockies, Andes, and Himalayas), not just those which are part of ice sheets.

The current coupling between CLM and Glimmer-CISM is one-way only. That is, CLM sends the SMB and surface temperature to Glimmer-CISM but does not do anything with the fields that are returned. The CLM glacier fraction and surface topography are therefore fixed in time. One-way coupling is reasonable for runs of ~100 years or less, in which ice-sheet elevation changes are modest. For longer runs with larger elevation changes, two-way coupling is highly desirable. A two-way coupling scheme is under development.

10.2 Multiple elevation class scheme

In the typical operation of CLM, the glacier land unit contains a single column (section 2.1.1). However, when running CESM with an active ice sheet model, the glacier land unit is replaced by a glacier_mec land unit, where "mec" denotes "multiple elevation classes". In most ways, glacier_mec land units behave the same as standard glacier land units. However, each glacier_mec land unit is divided into a user-defined set of columns based on surface elevation. The default is 10 elevation classes whose lower limits are 0, 200, 400, 700, 1000, 1300, 1600, 2000, 2500, and 3000 m. Each column is characterized by a fractional area and surface elevation that are read in during model initialization. Each glacier_mec column within a grid cell has distinct ice and snow temperatures, snow water content, surface fluxes, and SMB.

Glacier_mec columns, like glacier columns, are initialized with a temperature of 250 K. While glacier columns are initialized with a snow liquid water equivalent (LWE) equal to the maximum allowed value of 1 m, glacier_mec columns begin with a snow LWE of 0.5 m so that they will reach their equilibrium mean snow depth sooner.

Glacier_mec columns typically require several decades of spin-up to equilibrate with a given climate.

The atmospheric surface temperature, potential temperature, specific humidity, density, and pressure are downscaled from the mean grid cell elevation to the glacier_mec column elevation using a specified lapse rate (typically 6.0 deg/km) and an assumption of uniform relative humidity. At a given time, lower-elevation columns can undergo surface melting while columns at higher elevations remain frozen. This gives a more accurate simulation of summer melting, which is a highly nonlinear function of air temperature. The precipitation rate and radiative fluxes are not currently downscaled, but could be in the future if care were taken to preserve the cell-integrated values.

In contrast to most CLM subgrid units, glacier_mec columns can be active (i.e., have model calculations run there) even if their area is zero. This is done because the ice sheet model may require a SMB even for some grid cells where CLM does not have glacier land units. To allow for this, grid overlap files have been pre-computed. For given resolutions of CLM and Glimmer-CISM, these files identify all land-covered grid cells that overlap any part of the ice sheet grid. In these overlapping cells, glacier_mec columns are defined in all elevation classes. Some columns may have zero area and are called "virtual" columns. These columns do not affect energy exchange between the land and the atmosphere, but are included for potential forcing of Glimmer-CISM.

10.3 Computation of the surface mass balance

The SMB of a glacier or ice sheet is the net annual accumulation/ablation of mass at the upper surface. Ablation is defined as the mass of water that runs off to the ocean. Not all the surface meltwater runs off; some of the melt percolates into the snow and

refreezes. Accumulation is primarily by snowfall and deposition, and ablation is primarily by melting and evaporation/sublimation. CLM uses a surface-energy-balance (SEB) scheme to compute the SMB. In this scheme, the melting depends on the sum of the radiative, turbulent, and conductive fluxes reaching the surface, as described elsewhere in this document.

CLM has a somewhat unrealistic treatment of accumulation and melting for standard glacier land units. The snow depth is limited to a prescribed depth of 1 m liquid water equivalent, with any additional snow assumed to run off to the ocean. (This amounts to a crude parameterization of iceberg calving.) Snow melting is treated in a realistic fashion, with meltwater percolating downward through snow layers as long as the snow is unsaturated. Once the underlying snow is saturated, any additional meltwater runs off. When glacier ice melts, however, the meltwater is assumed to remain in place until it refreezes. In warm parts of the ice sheet, the meltwater does not refreeze, but stays in place indefinitely.

In the modified glacier_mec columns, the treatment of melting and freezing depends on the logical variable *glc_dyntopo*. This variable controls whether CLM surface topography changes dynamically as the ice sheet evolves (i.e., whether the coupling is one-way or two-way). If *glc_dyntopo* is true, then CLM receives updated topographic information from the ice sheet model. In this case, snow in excess of the prescribed maximum depth is assumed to turn into ice, contributing a positive SMB to the ice sheet model. Melting ice is assumed to run off to the ocean, giving a negative SMB. The net SMB associated with ice formation (by conversion from snow) and melting/runoff is computed for each column, averaged over the coupling interval, and

sent to the coupler (*qice, mm/s*). If *glc_dyntopo* is false, then surface runoff for glacier_mec land units is computed as for glacier land units: (1) Any snow in excess of 1 m LWE runs off to the ocean, and (2) Melted ice remains in place until it refreezes. Excess snow and melted ice still contribute to positive and negative values, respectively, of *qice*, but only for the purpose of forcing Glimmer-CISM. Currently, *glc_dyntopo* = false is the default, and the only supported option.

Note that the SMB typically is defined as the total accumulation of ice and snow, minus the total ablation. The *qice* flux passed to Glimmer-CISM is the mass balance for ice alone, not snow. We can think of CLM as owning the snow, whereas Glimmer-CISM owns the underlying ice. Fluctuations in snow depth between 0 and 1 m LWE are not reflected in the SMB passed to Glimmer-CISM.

11. River Transport Model (RTM)

The RTM was developed to route total runoff from the land surface model to either the active ocean or marginal seas which enables the hydrologic cycle to be closed (Branstetter 2001, Branstetter and Famiglietti 1999). This is needed to model ocean convection and circulation, which is affected by freshwater input. It also provides another method of diagnosing the performance of the land model because the river flow can be directly compared to gauging station data (e.g., Dai and Trenberth 2002).

To improve global energy conservation when CLM is being run as part of the Community Climate System Model, runoff is split into two streams, a liquid water stream and an ice water stream (derived from excess snowfall in snow-capped grid cells, section 7.7). The liquid and ice streams are routed through the RTM, passed to, and dealt with by the ocean separately.

The RTM uses a linear transport scheme to route water from each grid cell to its downstream neighboring grid cell. The change in storage S of river water, whether it be liquid or ice, within a RTM grid cell ($m^3\ s^{-1}$) is

$$\frac{dS}{dt} = \sum F_{in} - F_{out} + R \tag{11.1}$$

where $\sum F_{in}$ is the sum of inflows of water from neighboring upstream grid cells ($m^3\ s^{-1}$), F_{out} is the flux of water leaving the grid cell in the downstream direction ($m^3\ s^{-1}$), and R is the total runoff generated by the land model grid cell ($m^3\ s^{-1}$). Downstream water flow direction in each grid cell is determined as one of eight compass points (north, northeast, east, southeast, south, southwest, west, and northwest) based on the steepest

downhill slope as determined from a digital elevation model (Graham et al. 1999). The flux of water leaving the grid cell F_{out} is

$$F_{out} = \frac{v}{d} S \tag{11.2}$$

where v is the effective water flow velocity (m s^{-1}), d is the distance between centers of neighboring grid cells (m), and S is the volume of river water stored within the grid cell (m^3). The effective water flow velocity can be estimated from Manning's equation, which is a function of surface water slope, the hydraulic radius of the river channel, and a channel roughness coefficient (Dingman, 2002). However, hydraulic radius and channel roughness data are not available globally, so a simplified effective flow velocity expression is used in RTM

$$v = \max\left(0.05, k\beta^{1/2}\right) \tag{11.2}$$

where β is the grid cell mean topographic slope, and $k = 1$.

The distance d between two grid cell centers depends on river direction, latitude, and longitude as

$$d = \sqrt{\Delta x^2 + \Delta y^2}\,. \tag{11.3}$$

The distance in the zonal direction Δx (m) is

$$\Delta x = \left(1 \times 10^3 \left|\theta_{i,j} - \theta_{i*,j*}\right| R_e\right)\left[0.5\left(\cos\phi_{i,j} + \cos\phi_{i*,j*}\right)\right] \tag{11.4}$$

where $\theta_{i,j}$ and $\theta_{i*,j*}$ are the latitudes (radians) of the upstream and downstream grid cells, $\phi_{i,j}$ and $\phi_{i*,j*}$ are the longitudes (radians) of the upstream and downstream grid cells, R_e is the radius of the earth (km) (Table 2.6), and i and j are grid cell indices. The distance in the meridional direction Δy (m) is

$$\Delta y = \left(1 \times 10^3 \left|\theta_{i,j} - \theta_{i*,j*}\right| R_e\right). \tag{11.5}$$

The RTM is generally run at a time step greater than that of the CLM because of computational constraints. The total runoff from the land model at each time step is accumulated until the RTM is invoked. The total liquid water runoff at the land model resolution (kg m^{-2} s^{-1}) is

$$R_{liq} = q_{over} + q_{drai} + q_{rgwl} \tag{11.6}$$

where q_{over} is surface runoff (section 7.3), q_{drai} is sub-surface drainage (section 7.6), and q_{rgwl} is liquid runoff from glaciers, wetlands, and lakes (all in kg m^{-2} s^{-1}) (sections 7.7 and 9.6.3). The total ice water runoff, also at the land model resolution is

$$R_{ice} = q_{snwcp,ice} \tag{11.7}$$

where $q_{snwcp,ice}$ is the ice runoff from snow-capped surfaces (section 7.7). The runoff at the land model resolution is interpolated to the resolution of RTM and converted to units of m^3 s^{-1} for use in equation (11.1) by multiplying by $1 \times 10^{-3} A$ where A is the area (m^2) of the RTM grid cell.

The RTM grid cells that are at river mouths, hence providing freshwater flux to the ocean, are identified by examining each RTM ocean grid cell and determining if a RTM land grid cell flows to that ocean grid cell. River mouth grid cells are also assigned if any overlapping grid cells at the land model resolution contain land. When used as part of the Community Climate System Model, the ocean freshwater liquid and ice fluxes at the RTM resolution are passed to the flux coupler which distributes the fluxes to the appropriate ocean grid cells. When used with the Community Atmosphere Model or

when run offline, RTM serves only as a diagnostic tool. The river-routing scheme conserves water globally as

$$\sum_{i,j}\left(\frac{dS}{dt}\right)_{i,j} = \sum_{i,j} R_{i,j} \,. \tag{11.8}$$

12. Urban Model (CLMU)

At the global scale, and at the coarse spatial resolution of current climate models, urbanization has negligible impact on climate. However, the urban parameterization (CLMU; Oleson et al. 2008b,c) allows simulation of the urban environment within a climate model, and particularly the temperature where people live. As such, the urban model allows scientific study of how climate change affects the urban heat island and possible urban planning and design strategies to mitigate warming (e.g., white roofs).

The urban model that was released as a component of CLM4.0 is separately described in the urban technical note (Oleson et al. 2010b). Here, we provide a brief overview of the urban model released as a component of CLM4.5. The main changes in the urban model from CLM4.0 to CLM4.5 are 1) an expansion of the single urban landunit to up to three landunits per grid cell stratified by urban density types, 2) the number of urban layers for roofs and walls is no longer constrained to be equal to the number of ground layers, 3) space heating and air conditioning wasteheat factors are now set to zero by default so that the user can customize these factors for their own application, 4) the elevation threshold used to eliminate urban areas in the surface dataset creation routines has been changed from 2200 meters to 2600 meters, 5) hydrologic and thermal calculations for the pervious road now follows CLM4.5 parameterizations.

Urban areas in CLM are represented by up to three urban landunits per gridcell according to density class. The urban landunit is based on the "urban canyon" concept of Oke (1987) in which the canyon geometry is described by building height (H) and street width (W) (Figure 12.1). The canyon system consists of roofs, walls, and canyon floor.

Walls are further divided into shaded and sunlit components. The canyon floor is divided into pervious (e.g., to represent residential lawns, parks) and impervious (e.g., to represent roads, parking lots, sidewalks) fractions. Vegetation is not explicitly modeled for the pervious fraction; instead evaporation is parameterized by a simplified bulk scheme.

Each of the five urban surfaces is treated as a column within the landunit (Figure 12.1). Radiation parameterizations account for trapping of solar and longwave radiation inside the canyon. Momentum fluxes are determined for the urban landunit using a roughness length and displacement height appropriate for the urban canyon and stability formulations from CLM. A one-dimensional heat conduction equation is solved numerically for a multiple-layer ($N_{levurb} = 5$) column to determine conduction fluxes into and out of canyon surfaces. The interior boundary conditions for roofs and walls are determined by an interior building temperature (T_{iB}) held between prescribed maximum and minimum temperatures ($T_{iB,\max}, T_{iB,\min}$), thus explicitly resolving space heating and air conditioning fluxes. Anthropogenic sources of waste heat ($Q_{H,waste}$) from air conditioning and space heating can be optionally incorporated as modifications to the canyon energy budget. Turbulent [sensible heat ($Q_{H,u}$) and latent heat ($Q_{E,u}$)] and storage ($Q_{S,u}$) heat fluxes and surface ($T_{u,s}$) and internal ($T_{u,i=1,N_{levgrnd}}$) temperatures are determined for each urban surface u. Hydrology on the roof and canyon floor is simulated and walls are hydrologically inactive. A snowpack can form on the active surfaces. A certain amount of liquid water is allowed to pond on these surfaces which

supports evaporation. Water in excess of the maximum ponding depth runs off (R_{roof}, $R_{imprvrd}$, R_{prvrd}).

The heat and moisture fluxes from each surface interact with each other through a bulk air mass that represents air in the urban canopy layer for which specific humidity (q_{ac}) and temperature (T_{ac}) are prognosed (Figure 12.2). The air temperature can be compared with that from surrounding vegetated/soil (rural) surfaces in the model to ascertain heat island characteristics. As with other landunits, the CLMU is forced either with output from a host atmospheric model (e.g., the Community Atmosphere Model (CAM)) or observed forcing (e.g., reanalysis or field observations). The urban model produces sensible, latent heat, and momentum fluxes, emitted longwave, and reflected solar radiation, which are area-averaged with fluxes from non-urban "landunits" (e.g., vegetation, lakes) to supply grid cell averaged fluxes to the atmospheric model.

Present day global urban extent and urban properties were developed by Jackson et al. (2010). Urban extent, defined for four classes [tall building district (TBD), and high, medium, and low density (HD, MD, LD)], was derived from LandScan 2004, a population density dataset derived from census data, nighttime lights satellite observations, road proximity, and slope (Dobson et al. 2000). The urban extent data for TBD, HD, and MD classes are aggregated from the original 1 km resolution to both a 0.05° by 0.05° global grid for high-resolution studies or a 0.5° by 0.5° grid. For the current implementation, the LD class is not used because it is highly rural and better modeled as a vegetated/soil surface. Although the TBD, HD, and MD classes are represented as individual urban landunits, urban model history output is currently a weighted average of the output for individual classes.

For each of 33 distinct regions across the globe, thermal (e.g., heat capacity and thermal conductivity), radiative (e.g., albedo and emissivity) and morphological (e.g., height to width ratio, roof fraction, average building height, and pervious fraction of the canyon floor) properties are provided for each of the density classes. Building interior minimum and maximum temperatures are prescribed based on climate and socioeconomic considerations. The surface dataset creation routines (see CLM4.5 User's Guide) aggregate the data to the desired resolution.

Figure 12.1. Schematic representation of the urban land unit.

See the text for description of notation. Incident, reflected, and net solar and longwave radiation are calculated for each individual surface but are not shown for clarity.

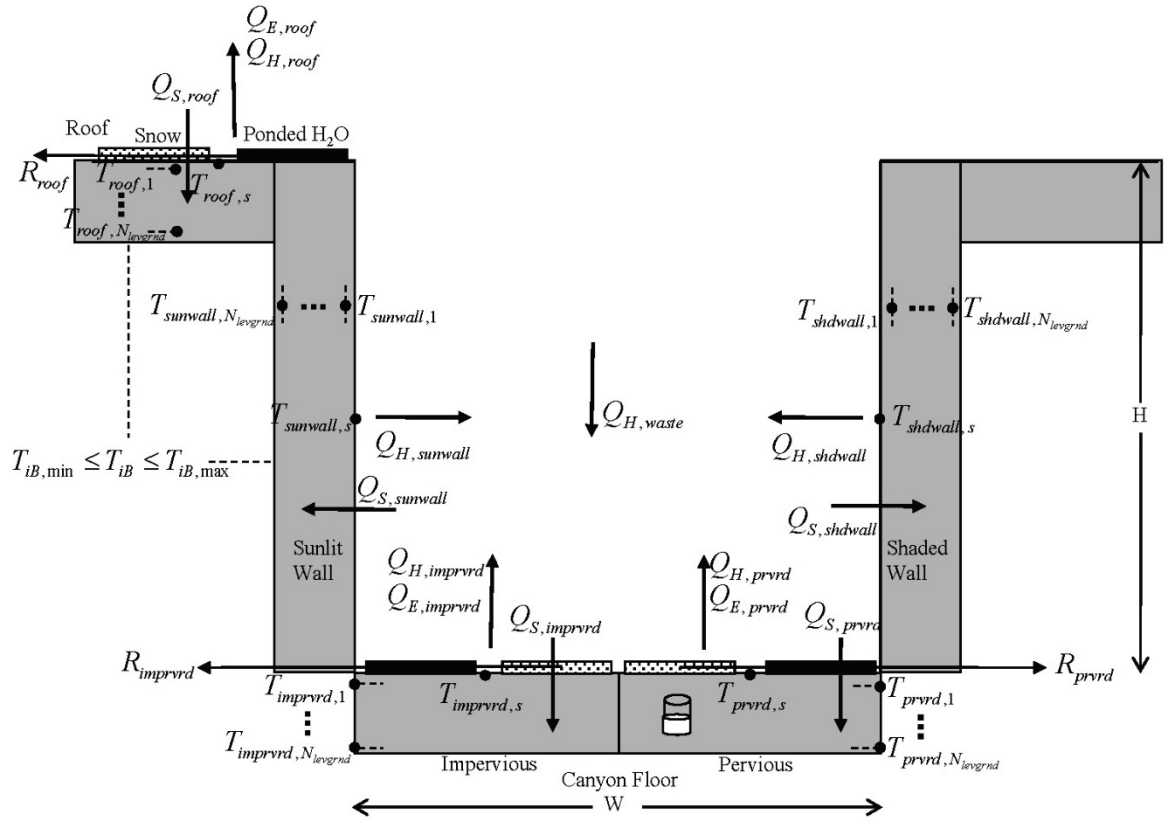

Figure 12.2. Schematic of urban and atmospheric model coupling.

The urban model is forced by the atmospheric model wind (u_{atm}), temperature (), specific humidity (q_{atm}), precipitation (P_{atm}), solar ($S_{atm}\downarrow$) and longwave ($L_{atm}\downarrow$) radiation at reference height z'_{atm} (section 2.2.1). Fluxes from the urban landunit to the atmosphere are turbulent sensible (H) and latent heat (λE), momentum (τ), albedo ($I\uparrow$), emitted longwave ($L\uparrow$), and absorbed shortwave ($\vec{S}$) radiation. Air temperature (T_{ac}), specific humidity (q_{ac}), and wind speed (u_c) within the urban canopy layer are diagnosed by the urban model. H is the average building height.

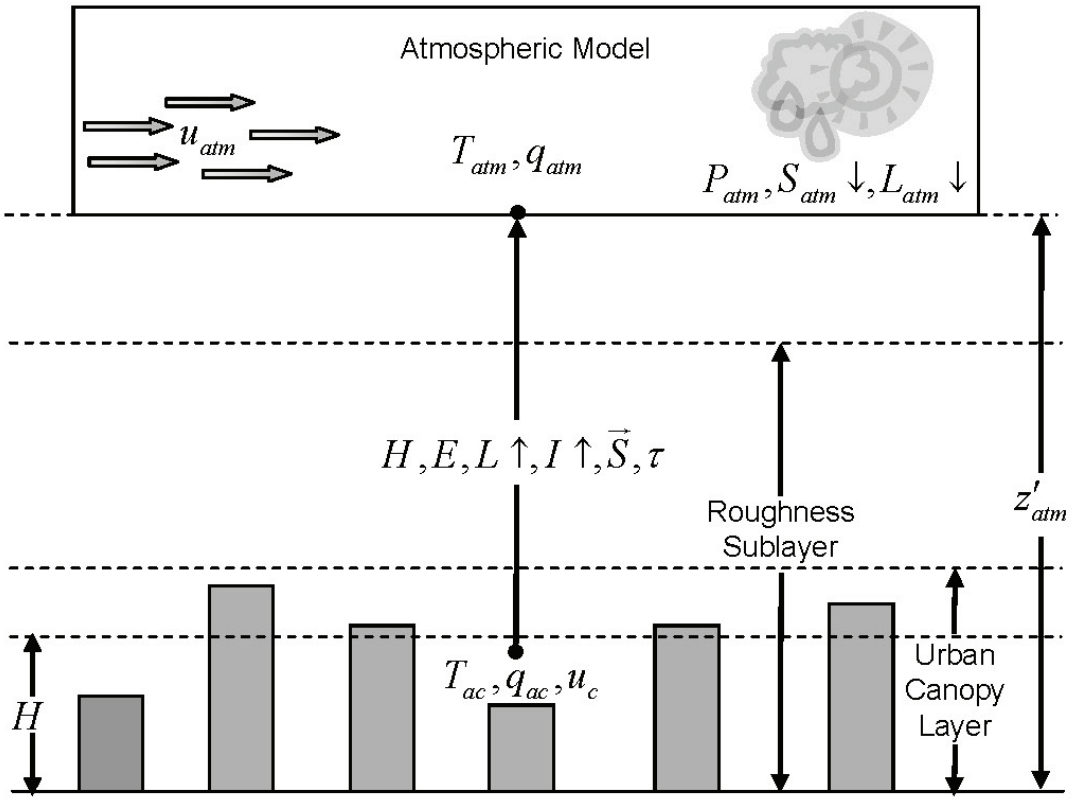

13. Carbon and Nitrogen Pools, Allocation, and Respiration

13.1 Introduction

CLM includes a fully-prognostic treatment of the terrestrial carbon and nitrogen cycles including interactions between these cycles as mediated by biological mechanisms of plants and soil heterotrophs. The model is fully prognostic with respect to all carbon and nitrogen state variables in the vegetation, litter, and soil organic matter. The seasonal timing of new vegetation growth and litterfall is also prognostic, responding to soil and air temperature, soil water availability, and daylength, in varying degrees depending on a specified phenology type for each PFT (see Chapter 14). The prognostic LAI, SAI, and vegetation heights are utilized by the biophysical model.

Separate state variables for C and N are tracked for leaf, live stem, dead stem, live coarse root, dead coarse root, and fine root pools (Figure 13.1 and 13.2). Each of these pools has two corresponding storage pools representing, respectively, short-term and long-term storage of non-structural carbohydrates and labile nitrogen. There are two additional carbon pools, one for the storage of growth respiration reserves, and another used to meet excess demand for maintenance respiration during periods with low photosynthesis. One additional nitrogen pool tracks retranslocated nitrogen, mobilized from leaf tissue prior to abscission and litterfall. Altogether there are 20 state variables for vegetation carbon, and 19 for vegetation nitrogen.

Figure 13.1. Vegetation fluxes and pools.

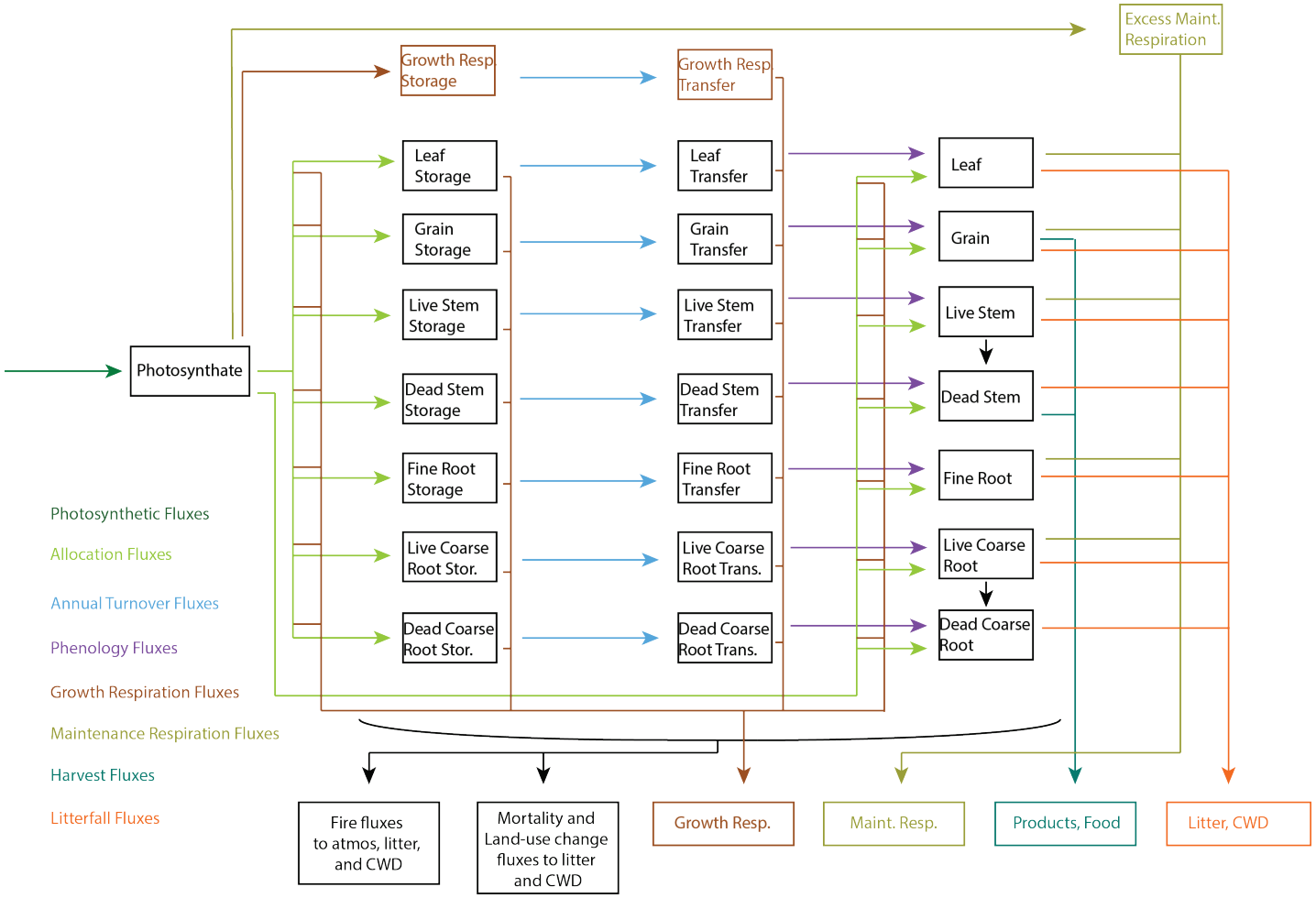

Figure 13.2: Carbon and nitrogen pools.

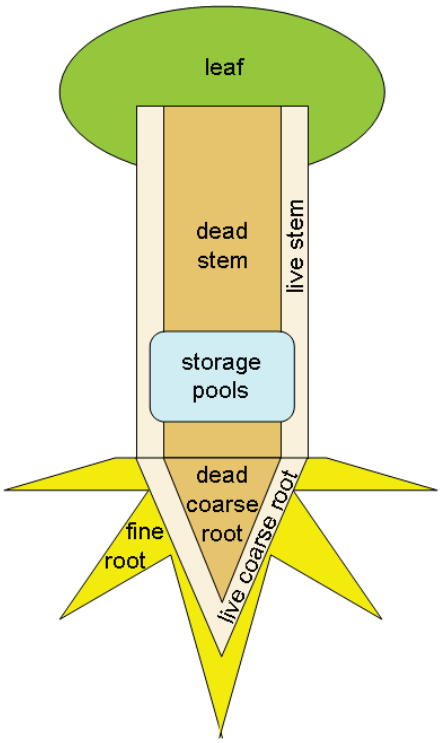

CLM vegetation state variables (pools):

C and N pools for each tissue (structural pools):

- Leaf
- Stem (live and dead)
- Coarse root (live and dead)
- Fine root

Each structural pool has two corresponding storage pools:

- Long-term storage (> 1 yr)
- Short-term storage (< 1 yr)

Additional pools:

- Growth respiration storage (C)
- Maintenance respiration reserve (C)
- Retranslocated nitrogen

Total number of pools…

Carbon: 6 + 12 + 2 = 20

Nitrogen: 6 + 12 + 1 = 19

13.2 Carbon Allocation for Maintenance Respiration Costs

The carbon and nitrogen allocation routines in CLM determine the fate of newly assimilated carbon, coming from the calculation of photosynthesis, and available mineral nitrogen, coming from plant uptake of mineral nitrogen in the soil or being drawn out of plant reserves. Allocation fluxes are determined in three steps: first CF_{GPPpot} is used to evaluate the potential allocation of carbon and nitrogen assuming an unlimited nitrogen supply, then the actual nitrogen supply is compared against the demand, and finally allocation of carbon and nitrogen are reduced, if necessary, to match nitrogen supply and demand.

Allocation of available carbon on each time step is prioritized, with first priority given to the demand for carbon to support maintenance respiration of live tissues (section 13.7). Second priority is to replenish the internal plant carbon pool that supports maintenance respiration during times when maintenance respiration exceeds photosynthesis (e.g. at night, during winter for perennial vegetation, or during periods of drought stress) (Sprugel et al., 1995). Third priority is to support growth of new tissues, including allocation to storage pools from which new growth will be displayed in subsequent time steps.

The total maintenance respiration demand (CF_{mr}, gC m^{-2} s^{-1}) is calculated as a function of tissue mass and nitrogen concentration, and temperature (section 13.7). The carbon supply to support this demand is composed of fluxes allocated from carbon assimilated in the current timestep ($CF_{GPP,mr}$, gC m^{-2} s^{-1}) and from a storage pool that is drawn down when total demand exceeds photosynthesis ($CF_{xs,mr}$, gC m^{-2} s^{-1}):

$$CF_{mr} = CF_{GPP,mr} + CF_{xs,mr} \tag{13.1}$$

$$CF_{GPP,mr} = \begin{cases} CF_{mr} & \text{for } CF_{mr} \le CF_{GPPpot} \\ CF_{GPPpot} & \text{for } CF_{mr} > CF_{GPPpot} \end{cases} \tag{13.2}$$

$$CF_{xs,mr} = \begin{cases} 0 & \text{for } CF_{mr} \le CF_{GPPpot} \\ CF_{mr} - CF_{GPPpot} & \text{for } CF_{mr} > CF_{GPPpot} \end{cases} \tag{13.3}$$

The storage pool that supplies carbon for maintenance respiration in excess of current CF_{GPPpot} (CS_{xs}, gC m^{-2}) is permitted to run a deficit (negative state), and the magnitude of this deficit determines an allocation demand which gradually replenishes CS_{xs}. The logic for allowing a negative state for this pool is to eliminate the need to know in advance what the total maintenance respiration demand will be for a particular

combination of climate and plant type. Using the deficit approach, the allocation to alleviate the deficit increases as the deficit increases, until the supply of carbon into the pool balances the demand for carbon leaving the pool in a quasi-steady state, with variability driven by the seasonal cycle, climate variation, disturbance, and internal dynamics of the plant-litter-soil system. In cases where the combination of climate and plant type are not suitable to sustained growth, the deficit in this pool increases until the available carbon is being allocated mostly to alleviate the deficit, and new growth approaches zero. The allocation flux to CS_{xs} ($CF_{GPP,xs}$, gC m^{-2} s^{-1}) is given as

$$CF_{GPP,xs,pot} = \begin{cases} 0 & \text{for } CS_{xs} \geq 0 \\ -CS_{xs} / (86400\tau_{xs}) & \text{for } CS_{xs} < 0 \end{cases} \quad (13.4)$$

$$CF_{GPP,xs} = \begin{cases} CF_{GPP,xs,pot} & \text{for } CF_{GPP,xs,pot} \leq CF_{GPPpot} - CF_{GPP,mr} \\ \max(CF_{GPPpot} - CF_{GPP,mr}, 0) & \text{for } CF_{GPP,xs,pot} > CF_{GPPpot} - CF_{GPP,mr} \end{cases} \quad (13.5)$$

where τ_{xs} is the time constant (currently set to 30 days) controlling the rate of replenishment of CS_{xs}.

Note that these two top-priority carbon allocation fluxes ($CF_{GPP,mr}$ and $CF_{GPP,xs}$) are not stoichiometrically associated with any nitrogen fluxes, and so this initial allocation step can proceed without reference to (or limitation from) the available mineral nitrogen supply.

13.3 Carbon and Nitrogen Stoichiometry of New Growth

After accounting for the carbon cost of maintenance respiration, the remaining carbon flux from photosynthesis which can be allocated to new growth (CF_{avail}, gC m^{-2} s^{-1}) is

$$CF_{avail\_alloc} = CF_{GPPpot} - CF_{GPP,mr} - CF_{GPP,xs}. \quad (13.6)$$

Potential allocation to new growth is calculated for all of the plant carbon and nitrogen state variables based on specified C:N ratios for each tissue type and allometric parameters that relate allocation between various tissue types. The allometric parameters are defined as follows:

$$\begin{aligned} a_1 &= \text{ ratio of new fine root : new leaf carbon allocation} \\ a_2 &= \text{ ratio of new coarse root : new stem carbon allocation} \\ a_3 &= \text{ ratio of new stem : new leaf carbon allocation} \\ a_4 &= \text{ ratio new live wood : new total wood allocation} \\ g_1 &= \text{ratio of growth respiration carbon : new growth carbon.} \end{aligned} \tag{13.7}$$

Parameters a_1, a_2, and a_4 are defined as constants for a given PFT (Table 13.1), while g_l = 0.3 (unitless) is prescribed as a constant for all PFTs, based on construction costs for a range of woody and non-woody tissues (Larcher, 1995).

The model includes a dynamic allocation scheme for woody vegetation (parameter a_3 = -1, Table 13.1), in which case the ratio for carbon allocation between new stem and new leaf increases with increasing net primary production (NPP), as

$$a_3 = \frac{2.7}{1 + e^{-0.004 NPP_{ann} - 300}} - 0.4 \tag{13.8}$$

where NPP_{ann} is the annual sum of NPP from the previous year. This mechanism has the effect of increasing woody allocation in favorable growth environments (Allen et al., 2005; Vanninen and Makela, 2005) and during the phase of stand growth prior to canopy closure (Axelsson and Axelsson, 1986).

Table 13.1. Allocation and carbon:nitrogen ratio parameters

Plant functional type	a_1	a_2	a_3	a_4	CN_{leaf}	CN_{fr}	CN_{lw}	CN_{dw}
NET Temperate	1	0.3	-1	0.1	35	42	50	500
NET Boreal	1	0.3	-1	0.1	40	42	50	500
NDT Boreal	1	0.3	-1	0.1	25	42	50	500
BET Tropical	1	0.3	-1	0.1	30	42	50	500
BET temperate	1	0.3	-1	0.1	30	42	50	500
BDT tropical	1	0.3	-1	0.1	25	42	50	500
BDT temperate	1	0.3	-1	0.1	25	42	50	500
BDT boreal	1	0.3	-1	0.1	25	42	50	500
BES temperate	1	0.3	0.2	0.5	30	42	50	500
BDS temperate	1	0.3	0.2	0.5	25	42	50	500
BDS boreal	1	0.3	0.2	0.1	25	42	50	500
C_3 arctic grass	1	0	0	0	25	42	0	0
C_3 grass	2	0	0	0	25	42	0	0
C_4 grass	2	0	0	0	25	42	0	0
Crop R	2	0	0	0	25	42	0	0
Crop I	2	0	0	0	25	42	0	0
Corn R	2	0	0	1	25	42	50	500
Corn I	2	0	0	1	25	42	50	500
Temp Cereal R	2	0	0	1	25	42	50	500
Temp Cereal I	2	0	0	1	25	42	50	500
Winter Cereal R	2	0	0	1	25	42	50	500
Winter Cereal I	2	0	0	1	25	42	50	500
Soybean R	2	0	0	1	25	42	50	500
Soybean I	2	0	0	1	25	42	50	500

Carbon to nitrogen ratios are defined for different tissue types as follows:

$$\begin{aligned} CN_{leaf} &= \text{C:N for leaf} \\ CN_{fr} &= \text{C:N for fine root} \\ CN_{lw} &= \text{C:N for live wood (in stem and coarse root)} \\ CN_{dw} &= \text{C:N for dead wood (in stem and coarse root)} \end{aligned} \tag{13.9}$$

where all C:N parameters are defined as constants for a given PFT (Table 13.1).

Given values for the parameters in (13.7) and (13.9), total carbon and nitrogen allocation to new growth (CF_{alloc}, gC m^{-2} s^{-1}, and NF_{alloc}, gN m^{-2} s^{-1}, respectively) can be expressed as functions of new leaf carbon allocation ($CF_{GPP,leaf}$, gC m^{-2} s^{-1}):

$$\begin{aligned} CF_{alloc} &= CF_{GPP,leaf}\, C_{allom} \\ NF_{alloc} &= CF_{GPP,leaf}\, N_{allom} \end{aligned} \tag{13.10}$$

where

$$C_{allom} = \begin{cases} \left(1+g_1\right)\left(1+a_1+a_3\left(1+a_2\right)\right) & \text{for woody PFT} \\ 1+g_1+a_1\left(1+g_1\right) & \text{for non-woody PFT} \end{cases} \tag{13.11}$$

$$N_{allom} = \begin{cases} \dfrac{1}{CN_{leaf}} + \dfrac{a_1}{CN_{fr}} + \dfrac{a_3 a_4\left(1+a_2\right)}{CN_{lw}} + \\ \qquad \dfrac{a_3\left(1-a_4\right)\left(1+a_2\right)}{CN_{dw}} & \text{for woody PFT} \\ \dfrac{1}{CN_{leaf}} + \dfrac{a_1}{CN_{fr}} & \text{for non-woody PFT.} \end{cases} \tag{13.12}$$

Since the C:N stoichiometry for new growth allocation is defined, from Eq. (13.10), as C_{allom}/N_{allom}, the total carbon available for new growth allocation (CF_{avail_alloc}) can be used to calculate the total plant nitrogen demand for new growth (NF_{plant_demand}, gN m^{-2} s^{-1}) as:

$$NF_{plant\_demand} = CF_{avail\_alloc} \frac{N_{allom}}{C_{allom}}. \quad (13.13)$$

13.4 Deployment of retranslocated nitrogen

In many plants, some portion of the nitrogen used to construct new tissues is mobilized from senescing tissues, especially leaves, and retained within the plant when the tissues are lost as litter. This store of retranslocated nitrogen is used to supply part of the nitrogen demand for subsequent growth (Magill et al., 1997; Oikawa et al., 2005; Son and Gower, 1991). CLM includes one pool of retranslocated nitrogen ($NS_{retrans}$, gN m^{-2}), and the availability of nitrogen from this pool to support new growth ($NF_{avail\_retrans}$, gN m^{-2} s^{-1}) is proportional to the plant nitrogen demand, as:

$$NF_{avail\_retrans} = \min\left(\frac{NF_{retrans\_ann} \dfrac{NF_{plant\_demand}}{NF_{plant\_demand\_ann}}}{\Delta t}, \frac{NS_{retrans}}{\Delta t} \right) \quad (13.14)$$

where $NF_{retrans\_ann}$ (gN m^{-2} y^{-1}) is the previous year's annual sum of retranslocated nitrogen extracted from senescing tissues, $NF_{plant\_demand\_ann}$ (gN m^{-2} y^{-1}) is the previous year's annual sum of NF_{plant_demand}, and Δt (s) is the model's biogeochemistry time step. This formulation produces an annual cycle in the extraction of nitrogen from $NS_{retrans}$ which corresponds to the annual cycle of plant nitrogen demand, and which is scaled to give $NS_{retrans}$ approximately a one-year turnover time. The minimum function prevents extraction of more than the remaining pool of retranslocated nitrogen, which can be an important constraint under conditions where high rates of mortality are modifying the size of the pool. During the first year of an initial simulation, before $NF_{plant\_demand\_ann}$ and $NF_{retrans\_ann}$ have valid values, $NF_{avail\_retrans}$ is set to 0.0.

The actual flux of nitrogen from the retranslocated N pool into allocation of new growth ($NF_{retrans,alloc}$, gN m^{-2} s^{-1}) is never greater than the plant demand for new nitrogen:

$$NF_{retrans,alloc} = \min\left(NF_{plant\_demand}, NF_{avail\_retrans}\right) \tag{13.15}$$

13.5 Plant nitrogen uptake from soil mineral nitrogen pool

The total plant nitrogen demand is reduced by the nitrogen flux from $NS_{retrans}$ to give the plant demand for mineral nitrogen from the soil ($NF_{plant\_demand\_soil}$, gN m^{-2} s^{-1}):

$$NF_{plant\_demand\_soil} = NF_{plant\_demand} - NF_{retrans,alloc}. \tag{13.16}$$

The combined demand from all PFTs sharing space on a soil column and the demand from the heterotrophic community in the soil (nitrogen immobilization demand) compete for the available soil mineral nitrogen pool. The result of this competition is passed back to the allocation algorithm as f_{plant_demand}, the fraction (from 0 to 1) of the plant nitrogen demand which can be met given the current soil mineral nitrogen supply and competition with heterotrophs. Plant uptake from the soil mineral nitrogen pool is then given as:

$$NF_{sminn,alloc} = NF_{plant\_demand\_soil} f_{plant\_demand} \tag{13.17}$$

13.6 Final carbon and nitrogen allocation

The total flux of allocated nitrogen is given as:

$$NF_{alloc} = NF_{retrans,alloc} + NF_{sminn,alloc} \tag{13.18}$$

From the stoichiometric relationship in Eq. (13.10), the associated carbon allocation flux is:

$$CF_{alloc} = NF_{alloc} \frac{C_{allom}}{N_{allom}}. \tag{13.19}$$

The downregulation of photosynthesis can then be calculated as:

$$f_{dreg} = \frac{CF_{alloc} - CF_{avail\_alloc}}{CF_{GPPpot}}. \quad (13.20)$$

Total allocation to new leaf carbon ($CF_{alloc,leaf\_tot}$, gC m^{-2} s^{-1}) is calculated as:

$$CF_{alloc,leaf\_tot} = \frac{CF_{alloc}}{C_{allom}}. \quad (13.21)$$

There are two carbon pools associated with each plant tissue – one which represents the currently displayed tissue, and another which represents carbon stored for display in a subsequent growth period. The nitrogen pools follow this same organization. The model keeps track of stored carbon according to which tissue type it will eventually be displayed as, and the separation between display in the current timestep and storage for later display depends on the parameter f_{cur} (values 0 to 1). Given $CF_{alloc,leaf}$ and f_{cur}, the allocation fluxes of carbon to display and storage pools (where storage is indicated with *_stor*) for the various tissue types are given as:

$$CF_{alloc,leaf} = CF_{alloc,leaf\_tot} f_{cur} \quad (13.22)$$

$$CF_{alloc,leaf\_stor} = CF_{alloc,leaf\_tot} \left(1 - f_{cur}\right) \quad (13.23)$$

$$CF_{alloc,froot} = CF_{alloc,leaf\_tot} a_1 f_{cur} \quad (13.24)$$

$$CF_{alloc,froot\_stor} = CF_{alloc,leaf\_tot} a_1 \left(1 - f_{cur}\right) \quad (13.25)$$

$$CF_{alloc,livestem} = CF_{alloc,leaf\_tot} a_3 a_4 f_{cur} \quad (13.26)$$

$$CF_{alloc,livestem\_stor} = CF_{alloc,leaf\_tot} a_3 a_4 \left(1 - f_{cur}\right) \quad (13.27)$$

$$CF_{alloc,deadstem} = CF_{alloc,leaf\_tot} a_3 \left(1 - a_4\right) f_{cur} \quad (13.28)$$

$$CF_{alloc,deadstem\_stor} = CF_{alloc,leaf\_tot} a_3 \left(1 - a_4\right)\left(1 - f_{cur}\right) \quad (13.29)$$

$$CF_{alloc,livecroot} = CF_{alloc,leaf\_tot} a_2 a_3 a_4 f_{cur} \quad (13.30)$$

$$CF_{alloc,livecroot\_stor} = CF_{alloc,leaf\_tot} a_2 a_3 a_4 \left(1 - f_{cur}\right) \tag{13.31}$$

$$CF_{alloc,deadcroot} = CF_{alloc,leaf\_tot} a_2 a_3 \left(1 - a_4\right) f_{cur} \tag{13.32}$$

$$CF_{alloc,deadcroot\_stor} = CF_{alloc,leaf\_tot} a_2 a_3 \left(1 - a_4\right)\left(1 - f_{cur}\right). \tag{13.33}$$

The corresponding nitrogen allocation fluxes are given as:

$$NF_{alloc,leaf} = \frac{CF_{alloc,leaf\_tot}}{CN_{leaf}} f_{cur} \tag{13.34}$$

$$NF_{alloc,leaf\_stor} = \frac{CF_{alloc,leaf\_tot}}{CN_{leaf}}\left(1 - f_{cur}\right) \tag{13.35}$$

$$NF_{alloc,froot} = \frac{CF_{alloc,leaf\_tot} a_1}{CN_{fr}} f_{cur} \tag{13.36}$$

$$NF_{alloc,froot\_stor} = \frac{CF_{alloc,leaf\_tot} a_1}{CN_{fr}}\left(1 - f_{cur}\right) \tag{13.37}$$

$$NF_{alloc,livestem} = \frac{CF_{alloc,leaf\_tot} a_3 a_4}{CN_{lw}} f_{cur} \tag{13.38}$$

$$NF_{alloc,livestem\_stor} = \frac{CF_{alloc,leaf\_tot} a_3 a_4}{CN_{lw}}\left(1 - f_{cur}\right) \tag{13.39}$$

$$NF_{alloc,deadstem} = \frac{CF_{alloc,leaf\_tot} a_3 \left(1 - a_4\right)}{CN_{dw}} f_{cur} \tag{13.40}$$

$$NF_{alloc,deadstem\_stor} = \frac{CF_{alloc,leaf\_tot} a_3 \left(1 - a_4\right)}{CN_{dw}}\left(1 - f_{cur}\right) \tag{13.41}$$

$$NF_{alloc,livecroot} = \frac{CF_{alloc,leaf\_tot} a_2 a_3 a_4}{CN_{lw}} f_{cur} \tag{13.42}$$

$$NF_{alloc,livecroot\_stor} = \frac{CF_{alloc,leaf\_tot} a_2 a_3 a_4}{CN_{lw}}\left(1 - f_{cur}\right) \tag{13.43}$$

$$NF_{alloc,deadcroot} = \frac{CF_{alloc,leaf\_tot} a_2 a_3 (1 - a_4)}{CN_{dw}} f_{cur} \quad (13.44)$$

$$NF_{alloc,deadcroot\_stor} = \frac{CF_{alloc,leaf} a_2 a_3 (1 - a_4)}{CN_{dw}} (1 - f_{cur}). \quad (13.45)$$

13.7 Autotrophic Respiration

The model treats maintenance and growth respiration fluxes separately, even though it is difficult to measure them as separate fluxes (Lavigne and Ryan, 1997; Sprugel et al., 1995). Maintenance respiration is defined as the carbon cost to support the metabolic activity of existing live tissue, while growth respiration is defined as the additional carbon cost for the synthesis of new growth.

13.7.1 Maintenance Respiration

Under the assumption that tissue nitrogen content is a suitable index of cellular metabolic rate, maintenance respiration costs for live tissues (leaf, live stem, live coarse root, and fine root) are calculated as functions tissue nitrogen content and the relevant temperature, following the empirical relationship reported by Ryan (1991):

$$CF_{mr\_leaf} = NS_{leaf} MR_{base} MR_{Q10}^{(T_{2m}-20)/10} \quad (13.46)$$

$$CF_{mr\_livestem} = NS_{livestem} MR_{base} MR_{Q10}^{(T_{2m}-20)/10} \quad (13.47)$$

$$CF_{mr\_livecroot} = NS_{livecroot} MR_{base} MR_{Q10}^{(T_{2m}-20)/10} \quad (13.48)$$

$$CF_{mr\_froot} = \sum_{j=1}^{nlevsoi} NS_{froot} rootfr_j MR_{base} MR_{Q10}^{(Ts_j-20)/10} \quad (13.49)$$

where MR_{base} (= 2.525e^{-6} gC gN^{-1} s^{-1}) is the base rate of maintenance respiration per unit nitrogen content, MR_{q10} (= 2.0) is the temperature sensitivity for maintenance respiration,

T_{2m} (°C) is the air temperature at 2m height, Ts_j (°C) is the soil temperature at level j, and $rootfr_j$ is the fraction of fine roots distributed in soil level j.

Note that, for woody vegetation, maintenance respiration costs are not calculated for the dead stem and dead coarse root components. These components are assumed to consist of dead xylem cells, with no metabolic function. By separating the small live component of the woody tissue (ray parenchyma, phloem, and sheathing lateral meristem cells) from the larger fraction of dead woody tissue, it is reasonable to assume a common base maintenance respiration rate for all live tissue types.

The total maintenance respiration cost is then given as:

$$CF_{mr} = CF_{mr\_leaf} + CF_{mr\_froot} + CF_{mr\_livestem} + CF_{mr\_livecroot}. \quad (13.50)$$

13.7.2 Growth Respiration

Growth respiration is calculated as a factor of 0.3 times the total carbon in new growth on a given timestep, based on construction costs for a range of woody and non-woody tissues (Larcher, 1995). For new carbon and nitrogen allocation that enters storage pools for subsequent display, it is not clear what fraction of the associated growth respiration should occur at the time of initial allocation, and what fraction should occur later, at the time of display of new growth from storage. Eddy covariance estimates of carbon fluxes in forest ecosystems suggest that the growth respiration associated with transfer of allocated carbon and nitrogen from storage into displayed tissue is not significant (Churkina et al., 2003), and so it is assumed in CLM that all of the growth respiration cost is incurred at the time of initial allocation, regardless of the fraction of allocation that is displayed immediately (i.e. regardless of the value of f_{cur}, section 13.5). This behavior is parameterized in such a way that if future research suggests that some

fraction of the growth respiration cost should be incurred at the time of display from storage, a simple parameter modification will effect the change.[1]

[1] Parameter *grpnow* in routines CNGResp and CNAllocation, currently set to 1.0, could be changed to a smaller value to transfer some portion (1-*grpnow*) of the growth respiration forward in time to occur at the time of growth display from storage.

14. Vegetation Phenology

The CLM phenology model consists of several algorithms controlling the transfer of stored carbon and nitrogen out of storage pools for the display of new growth and into litter pools for losses of displayed growth. PFTs are classified into three distinct phenological types that are represented by separate algorithms: an evergreen type, for which some fraction of annual leaf growth persists in the displayed pool for longer than one year; a seasonal-deciduous type with a single growing season per year, controlled mainly by temperature and daylength; and a stress-deciduous type with the potential for multiple growing seasons per year, controlled by temperature and soil moisture conditions.

The three phenology types share a common set of control variables. The calculation of the phenology fluxes is generalized, operating identically for all three phenology types, given a specification of the common control variables. The following sections describe first the general flux parameterization, followed by the algorithms for setting the control parameters for the three phenology types.

14.1 General Phenology Flux Parameterization

Fluxes of carbon and nitrogen from storage pools and into displayed tissue pools pass through a special transfer pool (denoted *_xfer*), maintained as a separate state variable for each tissue type. Storage (*_stor*) and transfer (*_xfer*) pools are maintained separately to reduce the complexity of accounting for transfers into and out of storage over the course of a single growing season.

Figure 14.1. Example of annual phenology cycle for seasonal deciduous.

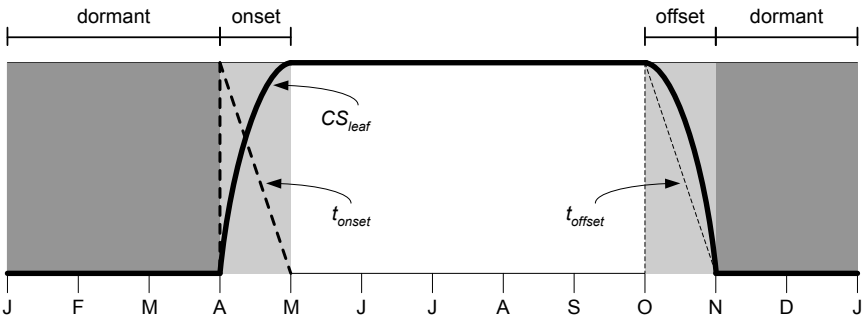

14.1.1 Onset Periods

The deciduous phenology algorithms specify the occurrence of onset growth periods (Figure 14.1). Carbon fluxes from the transfer pools into displayed growth are calculated during these periods as:

$$CF_{leaf\_xfer,leaf} = r_{xfer\_on} CS_{leaf\_xfer} \tag{14.1}$$

$$CF_{froot\_xfer,froot} = r_{xfer\_on} CS_{froot\_xfer} \tag{14.2}$$

$$CF_{livestem\_xfer,livestem} = r_{xfer\_on} CS_{livestem\_xfer} \tag{14.3}$$

$$CF_{deadstem\_xfer,deadstem} = r_{xfer\_on} CS_{deadstem\_xfer} \tag{14.4}$$

$$CF_{livecroot\_xfer,livecroot} = r_{xfer\_on} CS_{livecroot\_xfer} \tag{14.5}$$

$$CF_{deadcroot\_xfer,deadcroot} = r_{xfer\_on} CS_{deadcroot\_xfer}, \tag{14.6}$$

with corresponding nitrogen fluxes:

$$NF_{leaf\_xfer,leaf} = r_{xfer\_on} NS_{leaf\_xfer} \tag{14.7}$$

$$NF_{froot\_xfer,froot} = r_{xfer\_on} NS_{froot\_xfer} \tag{14.8}$$

$$NF_{livestem\_xfer,livestem} = r_{xfer\_on} NS_{livestem\_xfer} \tag{14.9}$$

$$NF_{deadstem\_xfer,deadstem} = r_{xfer\_on} NS_{deadstem\_xfer} \tag{14.10}$$

$$NF_{livecroot\_xfer,livecroot} = r_{xfer\_on} NS_{livecroot\_xfer} \tag{14.11}$$

$$NF_{deadcroot\_xfer,deadcroot} = r_{xfer\_on} NS_{deadcroot\_xfer}\,, \tag{14.12}$$

where CF is the carbon flux, CS is stored carbon, NF is the nitrogen flux, NS is stored nitrogen, r_{xfer_on} (s^{-1}) is a time-varying rate coefficient controlling flux out of the transfer pool:

$$r_{xfer\_on} = \begin{cases} 2/t_{onset} & \text{for } t_{onset} \neq \Delta t \\ 1/\Delta t & \text{for } t_{onset} = \Delta t \end{cases} \tag{14.13}$$

and t_{onset} (s) is the number of seconds remaining in the current phenology onset growth period (Figure 14.1). The form of Eq. (14.13) produces a flux from the transfer pool which declines linearly over the onset growth period, approaching zero flux in the final timestep.

14.1.2 Offset Periods

The deciduous phenology algorithms also specify the occurrence of litterfall during offset periods. In contrast to the onset periods, only leaf and fine root state variables are subject to litterfall fluxes. Carbon fluxes from display pools into litter are calculated during these periods as:

$$CF^{n}_{leaf,litter} = \begin{cases} CF^{n-1}_{leaf,litter} + r_{xfer\_off}\left(CS_{leaf} - CF^{n-1}_{leaf,litter} t_{offset}\right) & \text{for } t_{offset} \neq \Delta t \\ \left(CS_{leaf}/\Delta t\right) + CF_{alloc,leaf} & \text{for } t_{offset} = \Delta t \end{cases} \tag{14.14}$$

$$CF^{n}_{froot,litter} = \begin{cases} CF^{n-1}_{froot,litter} + r_{xfer\_off}\left(CS_{froot} - CF^{n-1}_{froot,litter} t_{offset}\right) & \text{for } t_{offset} \neq \Delta t \\ \left(CS_{froot}/\Delta t\right) + CF_{alloc,froot} & \text{for } t_{offset} = \Delta t \end{cases} \tag{14.15}$$

$$r_{xfer\_off} = \frac{2\Delta t}{t_{offset}^{2}} \tag{14.16}$$

where superscripts *n* and *n-1* refer to fluxes on the current and previous timesteps, respectively. The rate coefficient r_{xfer_off} varies with time to produce a linearly increasing litterfall rate throughout the offset period, and the special case for fluxes in the final litterfall timestep ($t_{offset} = \Delta t$) ensures that all of the displayed growth is sent to the litter pools for deciduous plant types.

Corresponding nitrogen fluxes during litterfall take into account retranslocation of nitrogen out of the displayed leaf pool prior to litterfall ($NF_{leaf,retrans}$, gN m^{-2} s^{-1}). Retranslocation of nitrogen out of fine roots is assumed to be negligible. The fluxes are:

$$NF_{leaf,litter} = CF_{leaf,litter} / CN_{leaf\_litter} \tag{14.17}$$

$$NF_{froot,litter} = CF_{leaf,litter} / CN_{froot} \tag{14.18}$$

$$NF_{leaf,retrans} = \left(CF_{leaf,litter} / CN_{leaf} \right) - NF_{leaf,litter} . \tag{14.19}$$

where CN is C:N.

14.1.3 Background Onset Growth

The stress-deciduous phenology algorithm includes a provision for the case when stress signals are absent, and the vegetation shifts from a deciduous habit to an evergreen habit, until the next occurrence of an offset stress trigger . In that case, the regular onset flux mechanism is switched off and a background onset growth algorithm is invoked ($r_{bgtr} > 0$). During this period, small fluxes of carbon and nitrogen from the storage pools into the associated transfer pools are calculated on each time step, and the entire contents of the transfer pool are added to the associated displayed growth pool on each time step. The carbon fluxes from transfer to display pools under these conditions are:

$$CF_{leaf\_xfer,leaf} = CS_{leaf\_xfer} / \Delta t \tag{14.20}$$

$$CF_{froot\_xfer,froot} = CS_{froot\_xfer} / \Delta t \quad (14.21)$$

$$CF_{livestem\_xfer,livestem} = CS_{livestem\_xfer} / \Delta t \quad (14.22)$$

$$CF_{deadstem\_xfer,deadstem} = CS_{deadstem\_xfer} / \Delta t \quad (14.23)$$

$$CF_{livecroot\_xfer,livecroot} = CS_{livecroot\_xfer} / \Delta t \quad (14.24)$$

$$CF_{deadcroot\_xfer,deadcroot} = CS_{deadcroot\_xfer} / \Delta t \,, \quad (14.25)$$

and the corresponding nitrogen fluxes are:

$$NF_{leaf\_xfer,leaf} = NS_{leaf\_xfer} / \Delta t \quad (14.26)$$

$$NF_{froot\_xfer,froot} = NS_{froot\_xfer} / \Delta t \quad (14.27)$$

$$NF_{livestem\_xfer,livestem} = NS_{livestem\_xfer} / \Delta t \quad (14.28)$$

$$NF_{deadstem\_xfer,deadstem} = NS_{deadstem\_xfer} / \Delta t \quad (14.29)$$

$$NF_{livecroot\_xfer,livecroot} = NS_{livecroot\_xfer} / \Delta t \quad (14.30)$$

$$NF_{deadcroot\_xfer,deadcroot} = NS_{deadcroot\_xfer} / \Delta t \,. \quad (14.31)$$

14.1.4 Background Litterfall

Both evergreen and stress-deciduous phenology algorithms can specify a litterfall flux that is not associated with a specific offset period, but which occurs instead at a slow rate over an extended period of time, referred to as background litterfall. For evergreen types the background litterfall is the only litterfall flux. For stress-deciduous types either the offset period litterfall or the background litterfall mechanism may be active, but not both at once. Given a specification of the background litterfall rate (r_{bglf}, s^{-1}), litterfall carbon fluxes are calculated as

$$CF_{leaf,litter} = r_{bglf} CS_{leaf} \quad (14.32)$$

$$CS_{froot,litter} = r_{bglf} CS_{froot}, \tag{14.33}$$

with corresponding nitrogen litterfall and retranslocation fluxes:

$$NF_{leaf,litter} = CF_{leaf,litter} / CN_{leaf\_litter} \tag{14.34}$$

$$NF_{froot,litter} = CF_{froot,litter} / CN_{froot} \tag{14.35}$$

$$NF_{leaf,retrans} = \left(CF_{leaf,litter} / CN_{leaf} \right) - NF_{leaf,litter}. \tag{14.36}$$

14.1.5 Livewood Turnover

The conceptualization of live wood vs. dead wood fractions for stem and coarse root pools is intended to capture the difference in maintenance respiration rates between these two physiologically distinct tissue types. Unlike displayed pools for leaf and fine root, which are lost to litterfall, live wood cells reaching the end of their lifespan are retained as a part of the dead woody structure of stems and coarse roots. A mechanism is therefore included in the phenology routine to effect the transfer of live wood to dead wood pools, which also takes into account the different nitrogen concentrations typical of these tissue types.

A live wood turnover rate (r_{lwt}, s^{-1}) is defined as

$$r_{lwt} = p_{lwt} / \left(365 \cdot 86400 \right) \tag{14.37}$$

where $p_{lwt} = 0.7$ is the assumed annual live wood turnover fraction. Carbon fluxes from live to dead wood pools are:

$$CF_{livestem,deadstem} = CS_{livestem} r_{lwt} \tag{14.38}$$

$$CF_{livecroot,deadcroot} = CS_{livecroot} r_{lwt}, \tag{14.39}$$

and the associated nitrogen fluxes, including retranslocation of nitrogen out of live wood during turnover, are:

$$NF_{livestem,deadstem} = CF_{livestem,deadstem} / CN_{dw} \quad (14.40)$$

$$NF_{livestem,retrans} = \left(CF_{livestem,deadstem} / CN_{lw} \right) - NF_{livestem,deadstem} \quad (14.41)$$

$$NF_{livecroot,deadcroot} = CF_{livecroot,deadcroot} / CN_{dw} \quad (14.42)$$

$$NF_{livecroot,retrans} = \left(CF_{livecroot,deadcroot} / CN_{lw} \right) - NF_{livecroot,deadcroot} . \quad (14.43)$$

14.2 Evergreen Phenology

The evergreen phenology algorithm is by far the simplest of the three possible types. It is assumed for all evergreen types that all carbon and nitrogen allocated for new growth in the current timestep goes immediately to the displayed growth pools (i.e. f_{cur} = 1.0 (Chapter 13)). As such, there is never an accumulation of carbon or nitrogen in the storage or transfer pools, and so the onset growth and background onset growth mechanisms are never invoked for this type. Litterfall is specified to occur only through the background litterfall mechanism – there are no distinct periods of litterfall for evergreen types, but rather a continuous (slow) shedding of foliage and fine roots. This is an obvious area for potential improvements in the model, since it is known, at least for evergreen needleleaf trees in the temperate and boreal zones, that there are distinct periods of higher and lower leaf litterfall (Ferrari, 1999; Gholz et al., 1985). The rate of background litterfall (r_{bglf}, section 14.1.4) depends on the specified leaf longevity (τ_{leaf}, y), as

$$r_{bglf} = \frac{1}{\tau_{leaf} \cdot 365 \cdot 86400} . \quad (14.44)$$

14.3 Seasonal-Deciduous Phenology

The seasonal-deciduous phenology algorithm derives directly from the treatment used in the offline model Biome-BGC v. 4.1.2, (Thornton et al., 2002), which in turn is

based on the parameterizations for leaf onset and offset for temperate deciduous broadleaf forest from White et al. (1997). Initiation of leaf onset is triggered when a common degree-day summation exceeds a critical value, and leaf litterfall is initiated when daylength is shorter than a critical value. Because of the dependence on daylength, the seasonal deciduous phenology algorithm is only valid for latitudes outside of the tropical zone, defined here as $|\text{latitude}| > 19.5°$. Neither the background onset nor background litterfall mechanism is invoked for the seasonal-deciduous phenology algorithm. The algorithm allows a maximum of one onset period and one offset period each year.

The algorithms for initiation of onset and offset periods use the winter and summer solstices as coordination signals. The period between winter and summer solstice is identified as $dayl_n > dayl_{n-1}$, and the period between summer and winter solstice is identified as $dayl_n < dayl_{n-1}$, where $dayl_n$ and $dayl_{n-1}$ are the daylength (s) calculated for the current and previous timesteps, respectively, using

$$dayl = 2 \cdot 13750.9871 \cdot \text{acos}\left(\frac{-\sin(lat)\sin(decl)}{\cos(lat)\cos(decl)} \right), \qquad (14.45)$$

where *lat* and *decl* are the latitude and solar declination (radians), respectively, and the factor 13750.9871 is the number of seconds per radian of hour-angle.

14.3.1 Seasonal-Deciduous Onset Trigger

The onset trigger for the seasonal-deciduous phenology algorithm is based on an accumulated growing-degree-day approach (White et al., 1997). The growing-degree-day summation (GDD_{sum}) is initiated (GDD_{sum} = 0) when the phenological state is

dormant and the model timestep crosses the winter solstice. Once these conditions are met, GDD_{sum} is updated on each timestep as

$$GDD_{sum}^{n} = \begin{cases} GDD_{sum}^{n-1} + \left(T_{s,3} - TKFRZ\right) f_{day} & \text{for } T_{s,3} > TKFRZ \\ GDD_{sum}^{n-1} & \text{for } T_{s,3} \le TKFRZ \end{cases} \tag{14.46}$$

where $T_{s,3}$ (K) is the temperature of the third soil layer, and $f_{day} = \Delta t / 86400$. The onset period is initiated if $GDD_{sum} > GDD_{sum\_crit}$, where

$$GDD_{sum\_crit} = \exp\left(4.8 + 0.13\left(T_{2m,ann\_avg} - TKFRZ\right)\right) \tag{14.47}$$

and where T_{2m,ann_avg} (K) is the annual average of the 2m air temperature, and TKFRZ is the freezing point of water (273.15 K). The following control variables are set when a new onset growth period is initiated:

$$GDD_{sum} = 0 \tag{14.48}$$

$$t_{onset} = 86400 \cdot n_{days\_on}, \tag{14.49}$$

where n_{days_on} is set to a constant value of 30 days. Fluxes from storage into transfer pools occur in the timestep when a new onset growth period is initiated. Carbon fluxes are:

$$CF_{leaf\_stor,leaf\_xfer} = f_{stor,xfer} CS_{leaf\_stor} / \Delta t \tag{14.50}$$

$$CF_{froot\_stor,froot\_xfer} = f_{stor,xfer} CS_{froot\_stor} / \Delta t \tag{14.51}$$

$$CF_{livestem\_stor,livestem\_xfer} = f_{stor,xfer} CS_{livestem\_stor} / \Delta t \tag{14.52}$$

$$CF_{deadstem\_stor,deadstem\_xfer} = f_{stor,xfer} CS_{deadstem\_stor} / \Delta t \tag{14.53}$$

$$CF_{livecroot\_stor,livecroot\_xfer} = f_{stor,xfer} CS_{livecroot\_stor} / \Delta t \tag{14.54}$$

$$CF_{deadcroot\_stor,deadcroot\_xfer} = f_{stor,xfer} CS_{deadcroot\_stor} / \Delta t \tag{14.55}$$

$$CF_{gresp\_stor,gresp\_xfer} = f_{stor,xfer} CS_{gresp\_stor} / \Delta t \tag{14.56}$$

and the associated nitrogen fluxes are:

$$NF_{leaf\_stor,leaf\_xfer} = f_{stor,xfer} NS_{leaf\_stor} / \Delta t \tag{14.57}$$

$$NF_{froot\_stor,froot\_xfer} = f_{stor,xfer} NS_{froot\_stor} / \Delta t \tag{14.58}$$

$$NF_{livestem\_stor,livestem\_xfer} = f_{stor,xfer} NS_{livestem\_stor} / \Delta t \tag{14.59}$$

$$NF_{deadstem\_stor,deadstem\_xfer} = f_{stor,xfer} NS_{deadstem\_stor} / \Delta t \tag{14.60}$$

$$NF_{livecroot\_stor,livecroot\_xfer} = f_{stor,xfer} NS_{livecroot\_stor} / \Delta t \tag{14.61}$$

$$NF_{deadcroot\_stor,deadcroot\_xfer} = f_{stor,xfer} NS_{deadcroot\_stor} / \Delta t \tag{14.62}$$

where $f_{stor,xfer}$ is the fraction of current storage pool moved into the transfer pool for display over the incipient onset period. This fraction is set to 0.5, based on the observation that seasonal deciduous trees are capable of replacing their canopies from storage reserves in the event of a severe early-season disturbance such as frost damage or defoliation due to insect herbivory.

If the onset criterion ($GDD_{sum} > GDD_{sum\_crit}$) is not met before the summer solstice, then GDD_{sum} is set to 0.0 and the growing-degree-day accumulation will not start again until the following winter solstice. This mechanism prevents the initiation of very short growing seasons late in the summer in cold climates. The onset counter is decremented on each time step after initiation of the onset period, until it reaches zero, signaling the end of the onset period:

$$t_{onfset}^{n} = t_{onfset}^{n-1} - \Delta t \tag{14.63}$$

14.3.2 Seasonal-Deciduous Offset Trigger

After the completion of an onset period, and once past the summer solstice, the offset (litterfall) period is triggered when daylength is shorter than 39300 s. The offset counter is set at the initiation of the offset period: $t_{offset} = 86400 \cdot n_{days\_off}$, where n_{days_off} is set to a constant value of 15 days. The offset counter is decremented on each time step after initiation of the offset period, until it reaches zero, signaling the end of the offset period:

$$t_{offset}^{n} = t_{offset}^{n-1} - \Delta t \tag{14.64}$$

14.4 Stress-Deciduous Phenology

The stress-deciduous phenology algorithm was developed specifically for the CLM based in part on the grass phenology model proposed by White et al. (1997). The algorithm handles phenology for vegetation types such as grasses and tropical drought-deciduous trees that respond to both cold and drought-stress signals, and that can have multiple growing seasons per year. The algorithm also allows for the possibility that leaves might persist year-round in the absence of a suitable stress trigger. In that case the phenology switches to an evergreen habit, maintaining a marginally-deciduous leaf longevity (one year) until the occurrence of the next stress trigger.

14.4.1 Stress-Deciduous Onset Triggers

In climates that are warm year-round, onset triggering depends on soil water availability. At the beginning of a dormant period (end of previous offset period), an accumulated soil water index (SWI_{sum}, d) is initialized (SWI_{sum} = 0), with subsequent accumulation calculated as:

$$SWI_{sum}^{n} = \begin{cases} SWI_{sum}^{n-1} + f_{day} & \text{for } \Psi_{s,3} \geq \Psi_{onset} \\ SWI_{sum}^{n-1} & \text{for } \Psi_{s,3} < \Psi_{onset} \end{cases} \tag{14.65}$$

where $\Psi_{s,3}$ is the soil water potential (MPa) in the third soil layer and Ψ_{onset} = -2 MPa is the onset soil water potential threshold. Onset triggering is possible once $SWI_{sum} > 15$. If the cold climate growing degree-day accumulator is not active at the time when this threshold is reached (see below), and if the daylength is greater than 6 hours, then onset is triggered. Except as noted below, SWI_{sum} continues to accumulate according to Eq. (14.65) during the dormant period if the daylength criterion prevents onset triggering, and onset is then triggered at the timestep when daylength exceeds 6 hours.

In climates with a cold season, onset triggering depends on both accumulated soil temperature summation and adequate soil moisture. At the beginning of a dormant period a freezing day accumulator (FD_{sum}, d) is initialized ($FD_{sum} = 0$), with subsequent accumulation calculated as:

$$FD_{sum}^{n} = \begin{cases} FD_{sum}^{n-1} + f_{day} & \text{for } T_{s,3} > TKFRZ \\ FD_{sum}^{n-1} & \text{for } T_{s,3} \leq TKFRZ \end{cases}. \tag{14.66}$$

If $FD_{sum} > 15$ during the dormant period, then a cold-climate onset triggering criterion is introduced, following exactly the growing degree-day summation (GDD_{sum}) logic of Eqs. (14.46) and (14.47). At that time SWI_{sum} is reset ($SWI_{sum} = 0$). Onset triggering under these conditions depends on meeting all three of the following criteria: $SWI_{sum} > 15$, $GDD_{sum} > GDD_{sum\_crit}$, and daylength greater than 6 hrs.

The following control variables are set when a new onset growth period is initiated: $SWI_{sum} = 0$, $FD_{sum} = 0$, $GDD_{sum} = 0$, $n_{days\_active} = 0$, and $t_{onset} = 86400 \cdot n_{days\_on}$, where n_{days_on} is set to a constant value of 30 days. Fluxes from storage into transfer pools occur

in the timestep when a new onset growth period is initiated, and are handled identically to Eqs. (14.50) - (14.56) for carbon fluxes, and to Eqs. (14.57) - (14.62) for nitrogen fluxes. The onset counter is decremented on each time step after initiation of the onset period, until it reaches zero, signaling the end of the onset period:

$$t_{onfset}^{n} = t_{onfset}^{n-1} - \Delta t \tag{14.67}$$

14.4.2 Stress-Deciduous Offset Triggers

Any one of the following three conditions is sufficient to initiate an offset period for the stress-deciduous phenology algorithm: sustained period of dry soil, sustained period of cold temperature, or daylength shorter than 6 hours. Offset triggering due to dry soil or cold temperature conditions is only allowed once the most recent onset period is complete. Dry soil condition is evaluated with an offset soil water index accumulator ($OSWI_{sum}$, d). To test for a sustained period of dry soils, this control variable can increase or decrease, as follows:

$$OSWI_{sum}^{n} = \begin{cases} OSWI_{sum}^{n-1} + f_{day} & \text{for } \Psi_{s,3} \le \Psi_{offset} \\ \max\left(OSWI_{sum}^{n-1} - f_{day}, 0\right) & \text{for } \Psi_{s,3} > \Psi_{onset} \end{cases} \tag{14.68}$$

where Ψ_{offset} = -2 MPa is the offset soil water potential threshold. An offset period is triggered if the previous onset period is complete and $OSWI_{sum} \ge OSWI_{sum\_crit}$, where $OSWI_{sum\_crit}$ = 15.

The cold temperature trigger is calculated with an offset freezing day accumulator (OFD_{sum}, d). To test for a sustained period of cold temperature, this variable can increase or decrease, as follows:

$$OFD_{sum}^{n} = \begin{cases} OFD_{sum}^{n-1} + f_{day} & \text{for } T_{s,3} \le TKFRZ \\ \max\left(OFD_{sum}^{n-1} - f_{day}, 0\right) & \text{for } T_{s,3} > TKFRZ \end{cases} \tag{14.69}$$

An offset period is triggered if the previous onset period is complete and $OFD_{sum} > OFD_{sum\_crit}$, where $OFD_{sum\_crit} = 15$.

The offset counter is set at the initiation of the offset period: $t_{offset} = 86400 \cdot n_{days\_off}$, where n_{days_off} is set to a constant value of 15 days. The offset counter is decremented on each time step after initiation of the offset period, until it reaches zero, signaling the end of the offset period:

$$t_{offset}^{n} = t_{offset}^{n-1} - \Delta t \tag{14.70}$$

14.4.3 Stress-Deciduous: Long Growing Season

Under conditions when the stress-deciduous conditions triggering offset are not met for one year or longer, the stress-deciduous algorithm shifts toward the evergreen behavior. This can happen in cases where a stress-deciduous vegetation type is assigned in a climate where suitably strong stresses occur less frequently than once per year. This condition is evaluated by tracking the number of days since the beginning of the most recent onset period (n_{days_active}, d). At the end of an offset period n_{days_active} is reset to 0. A long growing season control variable (LGS, range 0 to 1) is calculated as:

$$LGS = \begin{cases} 0 & \text{for } n_{days\_active} < 365 \\ \left(n_{days\_active} / 365\right) - 1 & \text{for } 365 \le n_{days\_active} < 730 \\ 1 & \text{for } n_{days\_active} \ge 730 \end{cases}. \tag{14.71}$$

The rate coefficient for background litterfall (r_{bglf}, s^{-1}) is calculated as a function of LGS:

$$r_{bglf} = \frac{LGS}{\tau_{leaf} \cdot 365 \cdot 86400} \tag{14.72}$$

where τ_{leaf} is the leaf longevity. The result is a shift to continuous litterfall as n_{days_active} increases from 365 to 730. When a new offset period is triggered r_{bglf} is set to 0.

The rate coefficient for background onset growth from the transfer pools (r_{bgtr}, s^{-1}) also depends on *LGS*, as:

$$r_{bgtr} = \frac{LGS}{365 \cdot 86400}. \tag{14.73}$$

On each timestep with $r_{bgtr} \neq 0$, carbon fluxes from storage to transfer pools are calculated as:

$$CF_{leaf\_stor,leaf\_xfer} = CS_{leaf\_stor} r_{bgtr} \tag{14.74}$$

$$CF_{froot\_stor,froot\_xfer} = CS_{froot\_stor} r_{bgtr} \tag{14.75}$$

$$CF_{livestem\_stor,livestem\_xfer} = CS_{livestem\_stor} r_{bgtr} \tag{14.76}$$

$$CF_{deadstem\_stor,deadstem\_xfer} = CS_{deadstem\_stor} r_{bgtr} \tag{14.77}$$

$$CF_{livecroot\_stor,livecroot\_xfer} = CS_{livecroot\_stor} r_{bgtr} \tag{14.78}$$

$$CF_{deadcroot\_stor,deadcroot\_xfer} = CS_{deadcroot\_stor} r_{bgtr}, \tag{14.79}$$

with corresponding nitrogen fluxes:

$$NF_{leaf\_stor,leaf\_xfer} = NS_{leaf\_stor} r_{bgtr} \tag{14.80}$$

$$NF_{froot\_stor,froot\_xfer} = NS_{froot\_stor} r_{bgtr} \tag{14.81}$$

$$NF_{livestem\_stor,livestem\_xfer} = NS_{livestem\_stor} r_{bgtr} \tag{14.82}$$

$$NF_{deadstem\_stor,deadstem\_xfer} = NS_{deadstem\_stor} r_{bgtr} \tag{14.83}$$

$$NF_{livecroot\_stor,livecroot\_xfer} = NS_{livecroot\_stor} r_{bgtr} \tag{14.84}$$

$$NF_{deadcroot\_stor,deadcroot\_xfer} = NS_{deadcroot\_stor} r_{bgtr}. \tag{14.85}$$

The result, in conjunction with the treatment of background onset growth, is a shift to continuous transfer from storage to display pools at a rate that would result in complete turnover of the storage pools in one year at steady state, once *LGS* reaches 1 (i.e. after

two years without stress-deciduous offset conditions). If and when conditions cause stress-deciduous triggering again, r_{bgtr} is rest to 0.

14.5 Litterfall Fluxes Merged to the Column Level

CLM uses three litter pools, defined on the basis of commonly measured chemical fractionation of fresh litter into labile (LIT1 = hot water and alcohol soluble fraction), cellulose/hemicellulose (LIT2 = acid soluble fraction) and remaining material, referred to here for convenience as lignin (LIT3 = acid insoluble fraction) (Aber et al., 1990; Taylor et al., 1989). While multiple plant functional types can coexist on a single CLM soil column, each soil column includes a single instance of the litter pools. Fluxes entering the litter pools due to litterfall are calculated using a weighted average of the fluxes originating at the PFT level. Carbon fluxes are calculated as:

$$CF_{leaf,lit1} = \sum_{p=0}^{npfts} CF_{leaf,litter} f_{lab\_leaf,p} wcol_p \tag{14.86}$$

$$CF_{leaf,lit2} = \sum_{p=0}^{npfts} CF_{leaf,litter} f_{cel\_leaf,p} wcol_p \tag{14.87}$$

$$CF_{leaf,lit3} = \sum_{p=0}^{npfts} CF_{leaf,litter} f_{lig\_leaf,p} wcol_p \tag{14.88}$$

$$CF_{froot,lit1} = \sum_{p=0}^{npfts} CF_{froot,litter} f_{lab\_froot,p} wcol_p \tag{14.89}$$

$$CF_{froot,lit2} = \sum_{p=0}^{npfts} CF_{froot,litter} f_{cel\_froot,p} wcol_p \tag{14.90}$$

$$CF_{froot,lit3} = \sum_{p=0}^{npfts} CF_{froot,litter} f_{lig\_froot,p} wcol_p \,, \tag{14.91}$$

where $f_{lab\_leaf,p}$, $f_{cel\_leaf,p}$, and $f_{lig\_leaf,p}$ are the labile, cellulose/hemicellulose, and lignin fractions of leaf litter for PFT p, $f_{lab\_froot,p}$, $f_{cel\_froot,p}$, and $f_{lig\_froot,p}$ are the labile,

cellulose/hemicellulose, and lignin fractions of fine root litter for PFT p, $wtcol_p$ is the weight relative to the column for PFT p, and p is an index through the plant functional types occurring on a column. Nitrogen fluxes to the litter pools are assumed to follow the C:N of the senescent tissue, and so are distributed using the same fractions used for carbon fluxes:

$$NF_{leaf,lit1} = \sum_{p=0}^{npfts} NF_{leaf,litter} f_{lab\_leaf,p} wcol_p \tag{14.92}$$

$$NF_{leaf,lit2} = \sum_{p=0}^{npfts} NF_{leaf,litter} f_{cel\_leaf,p} wcol_p \tag{14.93}$$

$$NF_{leaf,lit3} = \sum_{p=0}^{npfts} NF_{leaf,litter} f_{lig\_leaf,p} wcol_p \tag{14.94}$$

$$NF_{froot,lit1} = \sum_{p=0}^{npfts} NF_{froot,litter} f_{lab\_froot,p} wcol_p \tag{14.95}$$

$$NF_{froot,lit2} = \sum_{p=0}^{npfts} NF_{froot,litter} f_{cel\_froot,p} wcol_p \tag{14.96}$$

$$NF_{froot,lit3} = \sum_{p=0}^{npfts} NF_{froot,litter} f_{lig\_froot,p} wcol_p \ . \tag{14.97}$$

15. Decomposition

Decomposition of fresh litter material into progressively more recalcitrant forms of soil organic matter is represented in CLM is defined as a cascade of k_{tras} transformations between m_{pool} decomposing coarse woody debris (CWD), litter, and soil organic matter (SOM) pools, each defined at n_{lev} vertical levels. CLM allows the user to define, at compile time, between 2 contrasting hypotheses of decomposition as embodied by two separate decomposition submodels: the CLM-CN pool structure used in CLM4.0, or a second pool structure, characterized by slower decomposition rates, based on the Century model (Parton et al. 1988). In addition, the user can choose, at compile time, whether to allow n_{lev} to equal 1, as in CLM4.0, or to equal the number of soil levels used for the soil hydrology (default 10).

Figure 15.1. Schematic of decomposition model in CLM.

Model is structured to allow different representations of the soil C and N decomposition cascade, as well as a vertically-explicit treatment of soil biogeochemistry.

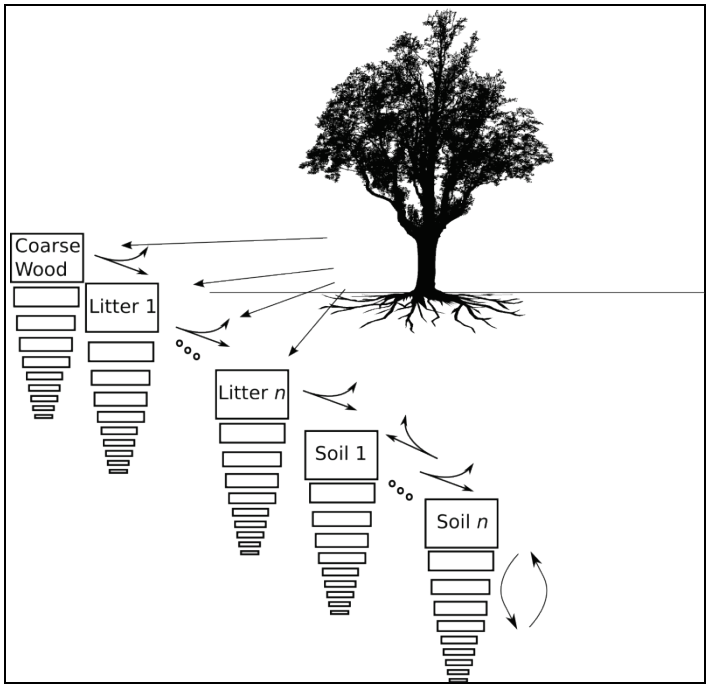

For the single-level model structure, the fundamental equation for carbon balance of the decomposing pools is:

$$\frac{\partial C_i}{\partial t} = R_i + \sum_{j \neq i} (i - r_j) T_{ji} k_j C_j - k_i C_i \qquad (15.1)$$

where C_i is the carbon content of pool i, R_i are the carbon inputs from plant tissues directly to pool i (only non-zero for CWD and litter pools), k_i is the decay constant of pool i; T_{ji} is the fraction of carbon directed from pool j to pool i with fraction r_j lost as a respiration flux along the way.

Adding the vertical dimension to the decomposing pools changes the balance equation to the following:

$$\frac{\partial C_i(z)}{\partial t} = R_i(z) + \sum_{i \neq j} \left(1 - r_j\right) T_{ji} k_j(z) C_j(z) - k_i(z) C_i(z) + \frac{\partial}{\partial z}\left(D(z) \frac{\partial C_i}{\partial z} \right) + \frac{\partial}{\partial z}\left(A(z) C_i \right) \tag{15.2}$$

where $C_i(z)$ is now defined at each model level, and in volumetric (gC m^{-3}) rather than areal (gC m^{-2}) units, along with $R_i(z)$ and $k_j(z)$. In addition, vertical transport is handled by the last two terms, for diffusive and advective transport. In the base model, advective transport is set to zero, leaving only a diffusive flux with diffusivity $D(z)$ defined for all decomposing carbon and nitrogen pools. Further discussion of the vertical distribution of carbon inputs $R_i(z)$, vertical turnover times $k_j(z)$, and vertical transport $D(z)$ is below. Discussion of the vertical model and analysis of both decomposition structures is in Koven et al (2013).

Figure 15.2. Pool structure, transitions, respired fractions (numbers at end of arrows), and turnover times (numbers in boxes) for the 2 alternate soil decomposition models included in CLM.

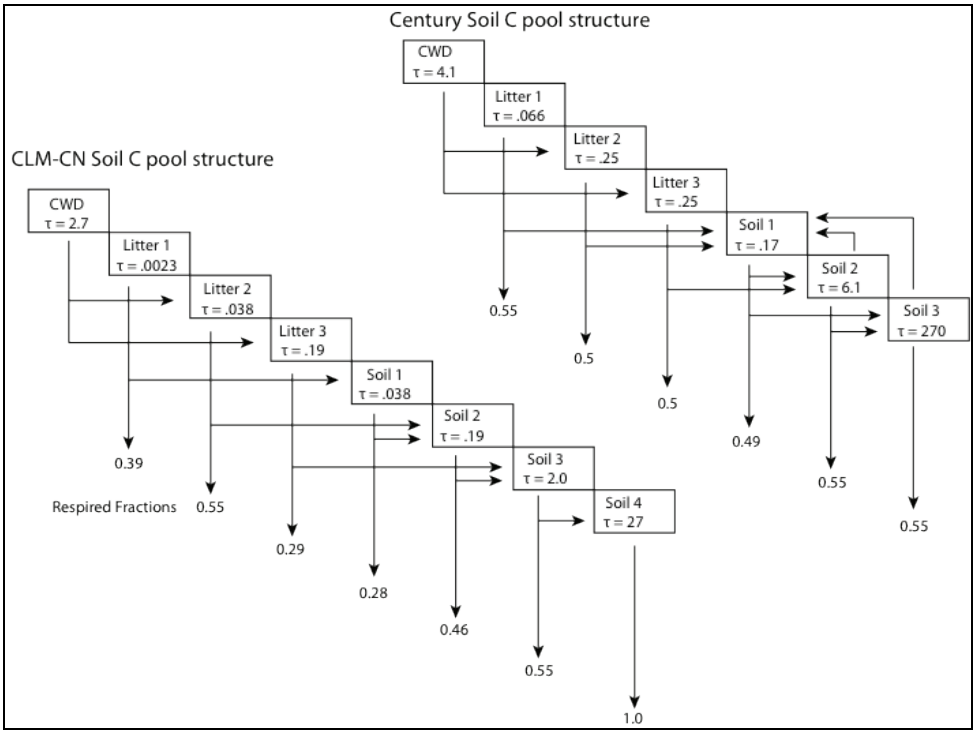

15.1 CLM-CN Pool Structure, Rate Constants and Parameters

The CLM-CN structure in CLM45 uses three state variables for fresh litter and four state variables for soil organic matter (SOM). The masses of carbon and nitrogen in the live microbial community are not modeled explicitly, but the activity of these organisms is represented by decomposition fluxes transferring mass between the litter and SOM pools, and heterotrophic respiration losses associated with these transformations. The litter and SOM pools in CLM-CN are arranged as a converging cascade (Figure 15.2), derived directly from the implementation in Biome-BGC v4.1.2 (Thornton et al. 2002; Thornton and Rosenbloom, 2005).

Model parameters are estimated based on a synthesis of microcosm decomposition studies using radio-labeled substrates (Degens and Sparling, 1996; Ladd et al. 1992; Martin et al. 1980; Mary et al. 1993; Saggar et al. 1994; Sørensen, 1981; van Veen et al. 1984). Multiple exponential models are fitted to data from the microcosm studies to estimate exponential decay rates and respiration fractions (Thornton, 1998). The microcosm experiments used for parameterization were all conducted at constant temperature and under moist conditions with relatively high mineral nitrogen concentrations, and so the resulting rate constants are assumed not limited by the availability of water or mineral nitrogen. Table 15.1 lists the base decomposition rates for each litter and SOM pool, as well as a base rate for physical fragmentation for the coarse woody debris pool (CWD).

Table 15.1. Decomposition rate constants for litter and SOM pools, C:N ratios, and acceleration parameters (see section 15.8 for explanation) for the CLM-CN decomposition pool structure.

	Biome-BGC	CLM-CN		
	k_{disc1} (d^{-1})	k_{disc2} (hr^{-1})	*C:N ratio*	*Acceleration term* (a_i)
k_{Lit1}	0.7	0.04892	-	1
k_{Lit2}	0.07	0.00302	-	1
k_{Lit3}	0.014	0.00059	-	1
k_{SOM1}	0.07	0.00302	12	1
k_{SOM2}	0.014	0.00059	12	1
k_{SOM3}	0.0014	0.00006	10	5
k_{SOM4}	0.0001	0.000004	10	70
k_{CWD}	0.001	0.00004	-	1

The first column of Table 15.1 gives the rates as used for the Biome-BGC model, which uses a discrete-time model with a daily timestep. The second column of Table 15.1 shows the rates transformed for a one-hour discrete timestep typical of CLM-CN. The transformation is based on the conversion of the initial discrete-time value (k_{disc1}) first to a continuous time value (k_{cont}), then to the new discrete-time value with a different timestep (k_{disc2}) , following Olson (1963):

$$k_{cont} = -\log\left(1 - k_{disc1}\right) \tag{15.3}$$

$$k_{disc2} = 1 - \exp\left(-k_{cont}\frac{\Delta t_2}{\Delta t_1}\right) \tag{15.4}$$

where Δt_1 (s) and Δt_2 (s) are the time steps of the initial and new discrete-time models, respectively.

Respiration fractions are parameterized for decomposition fluxes out of each litter and SOM pool. The respiration fraction (*rf*, unitless) is the fraction of the decomposition carbon flux leaving one of the litter or SOM pools that is released as CO_2 due to heterotrophic respiration. Respiration fractions and exponential decay rates are estimated simultaneously from the results of microcosm decomposition experiments (Thornton, 1998). The same values are used in CLM-CN and Biome-BGC (Table 15.2).

Table 15.2. Respiration fractions for litter and SOM pools

Pool	*rf*
rf_{Lit1}	0.39
rf_{Lit2}	0.55
rf_{Lit3}	0.29
rf_{SOM1}	0.28
rf_{SOM2}	0.46
rf_{SOM3}	0.55
rf_{SOM4}	1.0[a]

[a] The respiration fraction for pool SOM4 is 1.0 by definition: since there is no pool downstream of SOM4, the entire carbon flux leaving this pool is assumed to be respired as CO_2.

15.2 Century-based Pool Structure, Rate Constants and Parameters

The Century-based decomposition cascade is, like CLM-CN, a first-order decay model; the two structures differ in the number of pools, the connections between those pools, the turnover times of the pools, and the respired fraction during each transition (Figure 15.2). The turnover times are different for the Century-based pool structure, following those described in Parton et al. (1988) (Table 15.3).

Table 15.3. Turnover times, C:N ratios, and acceleration parameters (see section 15.8 for explanation) for the Century-based decomposition cascade.

	Turnover time (year)	C:N ratio	Acceleration term (a_i)
CWD	4.1	-	1
Litter 1	0.066	-	1
Litter 2	0.25	-	1
Litter 3	0.25	-	1
SOM 1	0.17	8	1
SOM 2	6.1	11	15
SOM 3	270	11	675

Likewise, values for the respiration fraction of Century-based structure are in Table 15.4.

Table 15.4. Respiration fractions for litter and SOM pools for Century-based structure

Pool	*rf*
rf_{Lit1}	0.55
rf_{Lit2}	0.5
rf_{Lit3}	0.5
rf_{SOM1}	f(txt)
rf_{SOM2}	0.55
rf_{SOM3}	0.55

15.3 Environmental modifiers on decomposition rate

These base rates are modified on each timestep by functions of the current soil environment. For the single-level model, there are two rate modifiers, temperature (r_{tsoil}, unitless) and moisture (r_{water}, unitless), both of which are calculated using the average environmental conditions of the top five model levels (top 29 cm of soil column). For the vertically-resolved model, two additional environmental modifiers are calculated beyond the temperature and moisture limitations: an oxygen scalar (r_{oxygen}, unitless), and a depth scalar (r_{depth}, unitless).

The Temperature scalar r_{tsoil} is calculated in CLM using a Q_{10} approach, with $Q_{10}=1.5$:

$$r_{tsoil} = Q_{10}^{\left(\frac{T_{soil,j}-T_{ref}}{10}\right)} \tag{15.5}$$

where j is the soil layer index, $T_{soil,j}$ (K) is the temperature of soil level j. The reference temperature T_{ref} = 25C.

The rate scalar for soil water potential (r_{water}, unitless) is calculated using a relationship from Andrén and Paustian (1987) and supported by additional data in Orchard and Cook (1983):

$$r_{water} = \sum_{j=1}^{5} \begin{cases} 0 & \text{for } \Psi_j < \Psi_{min} \\ \dfrac{\log\left(\Psi_{min}/\Psi_j\right)}{\log\left(\Psi_{min}/\Psi_{max}\right)} w_{soil,j} & \text{for } \Psi_{min} \le \Psi_j \le \Psi_{max} \\ 1 & \text{for } \Psi_j > \Psi_{max} \end{cases} \quad (15.6)$$

where Ψ_j is the soil water potential in layer j, Ψ_{min} is a lower limit for soil water potential control on decomposition rate (set to -10 MPa). $\Psi_{sat,j}$ (MPa) is the saturated soil water potential, calculated using the multivariate regression model from Cosby et al. (1984):

$$\Psi_{sat,j} = -(9.8\text{e-}5)\exp\left(\left(1.54 - 0.0095P_{sand,j} + 0.0063\left(100 - P_{sand,j} - P_{clay,j}\right)\right)\log(10)\right) \quad (15.7)$$

where $P_{sand,j}$ and $P_{clay,j}$ are the volume percentages of sand and clay in soil layer j.

For frozen soils, the bulk of the rapid dropoff in decomposition with decreasing temperature is due to the moisture limitation, since matric potential is limited by temperature in the supercooled water formulation of Niu and Yang (2006),

$$\psi(T) = -\frac{L_f(T - T_f)}{10^3 T} \quad (15.8)$$

An additional frozen decomposition limitation can be specified using a 'frozen Q_{10}' following Koven et al. (2011), however the default value of this is the same as the unfrozen Q_{10} value, and therefore the basic hypothesis is that frozen respiration is limited by liquid water availability, and can be modeled following the same approach as thawed but dry soils.

An additional rate scalar, r_{oxygen} is enabled when the CH_4 submodel is used (set equal to 1 for the single layer model or when the CH_4 submodel is disabled). This limits decomposition when there is insufficient molecular oxygen to satisfy stoichiometric demand (1 mol O_2 consumed per mol CO_2 produced) from heterotrophic decomposers, and supply from diffusion through soil layers (unsaturated and saturated) or aerenchyma (Chapter 19). A minimum value of r_{oxygen} is set at 0.2, with the assumption that oxygen within organic tissues can supply the necessary stoichiometric demand at this rate. This value lies between estimates of 0.025–0.1 (Frolking et al. 2001), and 0.35 (Wania et al. 2009); the large range of these estimates poses a large unresolved uncertainty.

Lastly, a possible explicit depth dependence, r_{depth}, (set equal to 1 for the single layer model) can be applied to soil C decomposition rates to account for processes other than temperature, moisture, and anoxia that can limit decomposition. This depth dependence of decomposition was shown by Jenkinson and Coleman (2008) to be an important term in fitting total C and 14C profiles, and implies that unresolved processes, such as priming effects, microscale anoxia, soil mineral surface and/or aggregate stabilization may be important in controlling the fate of carbon at depth (Koven et al. 2013). CLM includes these unresolved depth controls via an exponential decrease in the soil turnover time with depth:

$$r_{depth} = \exp\left(-\frac{z}{z_\tau}\right) \tag{15.9}$$

where z_τ is the e-folding depth for decomposition, set by default to 0.5m.

The combined decomposition rate scalar (r_{total}, unitless) is:

$$r_{total} = r_{tsoil} r_{water} r_{oxygen} r_{depth}. \tag{15.10}$$

15.4 N-limitation of Decomposition Fluxes

Decomposition rates can also be limited by the availability of mineral nitrogen, but calculation of this limitation depends on first estimating the potential rates of decomposition, assuming an unlimited mineral nitrogen supply. The general case is described here first, referring to a generic decomposition flux from an "upstream" pool (*u*) to a "downstream" pool (*d*), with an intervening loss due to respiration. The potential carbon flux out of the upstream pool ($CF_{pot,u}$, gC m^{-2} s^{-1}) is:

$$CF_{pot,u} = CS_u k_u \tag{15.11}$$

where CS_u (gC m^{-2}) is the initial mass in the upstream pool and k_u is the decay rate constant (s^{-1}) for the upstream pool, adjusted for temperature and moisture conditions. Depending on the C:N ratios of the upstream and downstream pools and the amount of carbon lost in the transformation due to respiration (the respiration fraction), the execution of this potential carbon flux can generate either a source or a sink of new mineral nitrogen ($NF_{pot\_min,u\to d}$, gN m^{-2} s^{-1}). The governing equation (Thornton and Rosenbloom, 2005) is:

$$NF_{pot\_min,u\to d} = \frac{CF_{pot,u}\left(1 - rf_u - \frac{CN_d}{CN_u}\right)}{CN_d} \tag{15.12}$$

where rf_u is the respiration fraction for fluxes leaving the upstream pool, CN_u and CN_d are the C:N ratios for upstream and downstream pools, respectively. Negative values of $NF_{pot\_min,u\to d}$ indicate that the decomposition flux results in a source of new mineral nitrogen, while positive values indicate that the potential decomposition flux results in a sink (demand) for mineral nitrogen.

Following from the general case, potential carbon fluxes leaving individual pools in the decomposition cascade, for the example of the CLM-CN pool structure, are given as:

$$CF_{pot,Lit1} = CS_{Lit1} k_{Lit1} r_{total} / \Delta t \tag{15.13}$$

$$CF_{pot,Lit2} = CS_{Lit2} k_{Lit2} r_{total} / \Delta t \tag{15.14}$$

$$CF_{pot,Lit3} = CS_{Lit3} k_{Lit3} r_{total} / \Delta t \tag{15.15}$$

$$CF_{pot,SOM1} = CS_{SOM1} k_{SOM1} r_{total} / \Delta t \tag{15.16}$$

$$CF_{pot,SOM2} = CS_{SOM2} k_{SOM2} r_{total} / \Delta t \tag{15.17}$$

$$CF_{pot,SOM3} = CS_{SOM3} k_{SOM3} r_{total} / \Delta t \tag{15.18}$$

$$CF_{pot,SOM4} = CS_{SOM4} k_{SOM4} r_{total} / \Delta t \tag{15.19}$$

where the factor ($1/\Delta t$) is included because the rate constant is calculated for the entire timestep (Eqs. (15.3) and (15.4)), but the convention is to express all fluxes on a per-second basis. Potential mineral nitrogen fluxes associated with these decomposition steps are, again for the example of the CLM-CN pool structure (the CENTURY structure will be similar but without the different terminal step):

$$NF_{pot\_min,Lit1 \rightarrow SOM1} = CF_{pot,Lit1} \left(1 - rf_{Lit1} - \frac{CN_{SOM1}}{CN_{Lit1}} \right) \Big/ CN_{SOM1} \tag{15.20}$$

$$NF_{pot\_min,Lit2 \rightarrow SOM2} = CF_{pot,Lit2} \left(1 - rf_{Lit2} - \frac{CN_{SOM2}}{CN_{Lit2}} \right) \Big/ CN_{SOM2} \tag{15.21}$$

$$NF_{pot\_min,Lit3 \rightarrow SOM3} = CF_{pot,Lit3} \left(1 - rf_{Lit3} - \frac{CN_{SOM3}}{CN_{Lit3}} \right) \Big/ CN_{SOM3} \tag{15.22}$$

$$NF_{pot\_min,SOM1 \rightarrow SOM2} = CF_{pot,SOM1} \left(1 - rf_{SOM1} - \frac{CN_{SOM2}}{CN_{SOM1}} \right) \Big/ CN_{SOM2} \tag{15.23}$$

$$NF_{pot\_min,SOM2\rightarrow SOM3} = CF_{pot,SOM2}\left(1 - rf_{SOM2} - \frac{CN_{SOM3}}{CN_{SOM2}}\right) \Big/ CN_{SOM3} \tag{15.24}$$

$$NF_{pot\_min,SOM3\rightarrow SOM4} = CF_{pot,SOM3}\left(1 - rf_{SOM3} - \frac{CN_{SOM4}}{CN_{SOM3}}\right) \Big/ CN_{SOM4} \tag{15.25}$$

$$NF_{pot\_min,SOM4} = -CF_{pot,SOM4} \Big/ CN_{SOM4} \tag{15.26}$$

where the special form of Eq. (15.26) arises because there is no SOM pool downstream of SOM4 in the converging cascade: all carbon fluxes leaving that pool are assumed to be in the form of respired CO_2, and all nitrogen fluxes leaving that pool are assumed to be sources of new mineral nitrogen.

Steps in the decomposition cascade that result in release of new mineral nitrogen (mineralization fluxes) are allowed to proceed at their potential rates, without modification for nitrogen availability. Steps that result in an uptake of mineral nitrogen (immobilization fluxes) are subject to rate limitation, depending on the availability of mineral nitrogen, the total immobilization demand, and the total demand for soil mineral nitrogen to support new plant growth. The potential mineral nitrogen fluxes from Eqs. (15.20) - (15.26) are evaluated, summing all the positive fluxes to generate the total potential nitrogen immobilization flux (NF_{immob_demand}, gN m^{-2} s^{-1}), and summing absolute values of all the negative fluxes to generate the total nitrogen mineralization flux (NF_{gross_nmin}, gN m^{-2} s^{-1}). Since NF_{griss_nmin} is a source of new mineral nitrogen to the soil mineral nitrogen pool it is not limited by the availability of soil mineral nitrogen, and is therefore an actual as opposed to a potential flux.

15.5 N Competition between plant uptake and soil immobilization fluxes

Once NF_{immob_demand} is known, the competition between plant and microbial nitrogen demand can be resolved. Mineral nitrogen in the soil pool (NS_{sminn}, gN m^{-2}) at the beginning of the timestep is considered the available supply. Total demand for mineral nitrogen from this pool (NF_{total_demand}, gN m^{-2} s^{-1}) is:

$$NF_{total\_demand} = NF_{immob\_demand} + NF_{plant\_demand\_soil} \tag{15.27}$$

If $NF_{total\_demand}\Delta t < NS_{sminn}$, then the available pool is large enough to meet both plant and microbial demand, and neither plant growth nor immobilization steps in the decomposition cascade are limited by nitrogen availability in the timestep. In that case, the signaling variables f_{plant_demand} and f_{immob_demand} are both set to 1.0, where f_{plant_demand} is defined and used in section 15.4, and f_{immob_demand} is the fraction of potential immobilization demand that can be met given current supply of mineral nitrogen.

If $NF_{total\_demand}\Delta t \geq NS_{sminn}$, then there is not enough mineral nitrogen to meet the combined demands for plant growth and heterotrophic immobilization, and both of these processes proceed at lower-than-potential rates, defined by the fractions f_{plant_demand} and f_{immob_demand}, where:

$$f_{plant\_demand} = f_{immob\_demand} = \frac{NS_{sminn}}{\Delta t\, NF_{total\_demand}} \tag{15.28}$$

This treatment of competition for nitrogen as a limiting resource is referred to a demand-based competition, where the fraction of the available resource that eventually flows to a particular process depends on the demand from that process in comparison to the total demand from all processes. Processes expressing a greater demand acquire a larger fraction of the available resource.

15.6 Final Decomposition Fluxes

With f_{immob_demand} known, final decomposition fluxes can be calculated. Actual carbon fluxes leaving the individual litter and SOM pools, again for the example of the CLM-CN pool structure (the CENTURY structure will be similar but, again without the different terminal step), are calculated as:

$$CF_{Lit1} = \begin{cases} CF_{pot,Lit1} f_{immob\_demand} & \text{for } NF_{pot\_min,Lit1 \rightarrow SOM1} > 0 \\ CF_{pot,Lit1} & \text{for } NF_{pot\_min,Lit1 \rightarrow SOM1} \leq 0 \end{cases} \quad (15.29)$$

$$CF_{Lit2} = \begin{cases} CF_{pot,Lit2} f_{immob\_demand} & \text{for } NF_{pot\_min,Lit2 \rightarrow SOM2} > 0 \\ CF_{pot,Lit2} & \text{for } NF_{pot\_min,Lit2 \rightarrow SOM2} \leq 0 \end{cases} \quad (15.30)$$

$$CF_{Lit3} = \begin{cases} CF_{pot,Lit3} f_{immob\_demand} & \text{for } NF_{pot\_min,Lit3 \rightarrow SOM3} > 0 \\ CF_{pot,Lit3} & \text{for } NF_{pot\_min,Lit3 \rightarrow SOM3} \leq 0 \end{cases} \quad (15.31)$$

$$CF_{SOM1} = \begin{cases} CF_{pot,SOM1} f_{immob\_demand} & \text{for } NF_{pot\_min,SOM1 \rightarrow SOM2} > 0 \\ CF_{pot,SOM1} & \text{for } NF_{pot\_min,SOM1 \rightarrow SOM2} \leq 0 \end{cases} \quad (15.32)$$

$$CF_{SOM2} = \begin{cases} CF_{pot,SOM2} f_{immob\_demand} & \text{for } NF_{pot\_min,SOM2 \rightarrow SOM3} > 0 \\ CF_{pot,SOM2} & \text{for } NF_{pot\_min,SOM2 \rightarrow SOM3} \leq 0 \end{cases} \quad (15.33)$$

$$CF_{SOM3} = \begin{cases} CF_{pot,SOM3} f_{immob\_demand} & \text{for } NF_{pot\_min,SOM3 \rightarrow SOM4} > 0 \\ CF_{pot,SOM3} & \text{for } NF_{pot\_min,SOM3 \rightarrow SOM4} \leq 0 \end{cases} \quad (15.34)$$

$$CF_{SOM4} = CF_{pot,SOM4} \quad (15.35)$$

Heterotrophic respiration fluxes (losses of carbon as CO_2 to the atmosphere) are:

$$CF_{Lit1,HR} = CF_{Lit1} rf_{Lit1} \quad (15.36)$$

$$CF_{Lit2,HR} = CF_{Lit2} rf_{Lit2} \quad (15.37)$$

$$CF_{Lit3,HR} = CF_{Lit3} rf_{Lit3} \quad (15.38)$$

$$CF_{SOM1,HR} = CF_{SOM1} rf_{SOM1} \quad (15.39)$$

$$CF_{SOM2,HR} = CF_{SOM2} rf_{SOM2} \tag{15.40}$$

$$CF_{SOM3,HR} = CF_{SOM3} rf_{SOM3} \tag{15.41}$$

$$CF_{SOM4,HR} = CF_{SOM4} rf_{SOM4} \tag{15.42}$$

Transfers of carbon from upstream to downstream pools in the decomposition cascade are given as:

$$CF_{Lit1,SOM1} = CF_{Lit1}\left(1 - rf_{Lit1}\right) \tag{15.43}$$

$$CF_{Lit2,SOM2} = CF_{Lit2}\left(1 - rf_{Lit2}\right) \tag{15.44}$$

$$CF_{Lit3,SOM3} = CF_{Lit3}\left(1 - rf_{Lit3}\right) \tag{15.45}$$

$$CF_{SOM1,SOM2} = CF_{SOM1}\left(1 - rf_{SOM1}\right) \tag{15.46}$$

$$CF_{SOM2,SOM3} = CF_{SOM2}\left(1 - rf_{SOM2}\right) \tag{15.47}$$

$$CF_{SOM3,SOM4} = CF_{SOM3}\left(1 - rf_{SOM3}\right) \tag{15.48}$$

In accounting for the fluxes of nitrogen between pools in the decomposition cascade and associated fluxes to or from the soil mineral nitrogen pool, the model first calculates a flux of nitrogen from an upstream pool to a downstream pool, then calculates a flux either from the soil mineral nitrogen pool to the downstream pool (immobilization) or from the downstream pool to the soil mineral nitrogen pool (mineralization). Transfers of nitrogen from upstream to downstream pools in the decomposition cascade are given as:

$$NF_{Lit1,SOM1} = CF_{Lit1} / CN_{Lit1} \tag{15.49}$$

$$NF_{Lit2,SOM2} = CF_{Lit2} / CN_{Lit2} \tag{15.50}$$

$$NF_{Lit3,SOM3} = CF_{Lit3} / CN_{Lit3} \tag{15.51}$$

$$NF_{SOM1,SOM2} = CF_{SOM1} / CN_{SOM1} \tag{15.52}$$

$$NF_{SOM2,SOM3} = CF_{SOM2} / CN_{SOM2} \quad (15.53)$$

$$NF_{SOM3,SOM4} = CF_{SOM3} / CN_{SOM3} \quad (15.54)$$

Corresponding fluxes to or from the soil mineral nitrogen pool depend on whether the decomposition step is an immobilization flux or a mineralization flux:

$$NF_{sminn,Lit1\rightarrow SOM1} = \begin{cases} NF_{pot\_min,Lit1\rightarrow SOM1} f_{immob\_demand} & \text{for } NF_{pot\_min,Lit1\rightarrow SOM1} > 0 \\ NF_{pot\_min,Lit1\rightarrow SOM1} & \text{for } NF_{pot\_min,Lit1\rightarrow SOM1} \leq 0 \end{cases} \quad (15.55)$$

$$NF_{sminn,Lit2\rightarrow SOM2} = \begin{cases} NF_{pot\_min,Lit2\rightarrow SOM2} f_{immob\_demand} & \text{for } NF_{pot\_min,Lit2\rightarrow SOM2} > 0 \\ NF_{pot\_min,Lit2\rightarrow SOM2} & \text{for } NF_{pot\_min,Lit2\rightarrow SOM2} \leq 0 \end{cases} \quad (15.56)$$

$$NF_{sminn,Lit3\rightarrow SOM3} = \begin{cases} NF_{pot\_min,Lit3\rightarrow SOM3} f_{immob\_demand} & \text{for } NF_{pot\_min,Lit3\rightarrow SOM3} > 0 \\ NF_{pot\_min,Lit3\rightarrow SOM3} & \text{for } NF_{pot\_min,Lit3\rightarrow SOM3} \leq 0 \end{cases} \quad (15.57)$$

$$NF_{sminn,SOM1\rightarrow SOM2} = \begin{cases} NF_{pot\_min,SOM1\rightarrow SOM2} f_{immob\_demand} & \text{for } NF_{pot\_min,SOM1\rightarrow SOM2} > 0 \\ NF_{pot\_min,SOM1\rightarrow SOM2} & \text{for } NF_{pot\_min,SOM1\rightarrow SOM2} \leq 0 \end{cases} \quad (15.58)$$

$$NF_{sminn,SOM2\rightarrow SOM3} = \begin{cases} NF_{pot\_min,SOM2\rightarrow SOM3} f_{immob\_demand} & \text{for } NF_{pot\_min,SOM2\rightarrow SOM3} > 0 \\ NF_{pot\_min,SOM2\rightarrow SOM3} & \text{for } NF_{pot\_min,SOM2\rightarrow SOM3} \leq 0 \end{cases} \quad (15.59)$$

$$NF_{sminn,SOM3\rightarrow SOM4} = \begin{cases} NF_{pot\_min,SOM3\rightarrow SOM4} f_{immob\_demand} & \text{for } NF_{pot\_min,SOM3\rightarrow SOM4} > 0 \\ NF_{pot\_min,SOM3\rightarrow SOM4} & \text{for } NF_{pot\_min,SOM3\rightarrow SOM4} \leq 0 \end{cases} \quad (15.60)$$

$$NF_{sminn,SOM4} = NF_{pot\_min,SOM4} \quad (15.61)$$

15.7 Vertical Distribution and Transport of Decomposing C and N pools

Additional terms are needed to calculate the vertically-resolved soil C and N budget: the initial vertical distribution of C and N from PFTs delivered to the litter and CWD pools, and the vertical transport of C and N pools.

For initial vertical inputs, CLM uses separate profiles for aboveground (leaf, stem) and belowground (root) inputs. Aboveground inputs are given a single exponential with

default e-folding depth = 0.1m. Belowground inputs are distributed according to rooting profiles with default values based on the Jackson et al. (1996) exponential parameterization.

Vertical mixing is accomplished by an advection-diffusion equation. The goal of this is to consider slow, soild- and adsorbed-phase transport due to bioturbation, cryoturbation, and erosion. Faster aqueous-phase transport is not included in CLM, but has been developed as part of the CLM-BeTR suite of parameterizations (Tang and Riley 2013). The default value of the advection term is 0 cm/yr, such that transport is purely diffusive. Diffusive transport differs in rate between permafrost soils (where cryoturbation is the dominant transport term) and non-permafrost soils (where bioturbation dominates). For permafrost soils, a parameterization based on that of Koven et al. (2009) is used: the diffusivity parameter is constant through the active layer, and decreases linearly from the base of the active layer to zero at a set depth (default 3m); the default permafrost diffusivity is 5 cm^2/yr. For non-permafrost soils, the default diffusivity is 1 cm^2/yr.

15.8 Model Equilibration

Because of the coupling between the slowest SOM pools and productivity through N downregulation of photosynthesis, equilibration of the model for initialization purposes will take an extremely long time in the standard mode. This is particularly true for the CENTURY-based decomposition cascade, which includes a passive pool. In order to rapidly equilibrate the model, a modified version of the "accelerated decomposition" (Thornton and Rosenbloom, 2005) is used. The fundamental idea of this approach is to allow fluxes between the various pools (both turnover-defined and vertically-defined

fluxes) adjust rapidly, while keeping the pool sizes themselves small so that they can fill quickly. To do this, the base decomposition rate k_i for each pool i is accelerated by a term a_i such that the slow pools are collapsed onto an approximately annual timescale (Koven et al. 2013). Accelerating the pools beyond this timescale distorts the seasonal and/or diurnal cycles of decomposition and N mineralization, thus leading to a substantially different ecosystem productivity than the full model. For the vertical model, the vertical transport terms are also accelerated by the same term a_i, as is the radioactive decay when ^{14}C is enabled, following the same principle of keeping fluxes between pools (or fluxes lost to decay) close to the full model while keeping the pools sizes small. When leaving the accelerated decomposition mode, the concentration of C and N in pools that had been accelerated are multiplied by the same term a_i, to bring the model into approximate equilibrium. Note that in CLM, the model can also transition into accelerated decomposition mode from the standard mode (by dividing the pools by a_i), and that the transitions into and out of accelerated decomposition mode are handled automatically by CLM upon loading from restart files (which preserve information about the mode of the model when restart files were written).

The acceleration terms for the two decomposition cascades are shown in Tables 15.1 and 15.3.

16. External Nitrogen Cycle

In addition to the relatively rapid cycling of nitrogen within the plant – litter – soil organic matter system, CLM also represents several slow processes which couple the internal nitrogen cycle to external sources and sinks. Inputs of new mineral nitrogen are from atmospheric deposition and biological nitrogen fixation. Losses of mineral nitrogen are due to nitrification, denitrification, leaching, and losses in fire. While the short-term dynamics of nitrogen limitation depend on the behavior of the internal nitrogen cycle, establishment of total ecosystem nitrogen stocks depends on the balance between sources and sinks in the external nitrogen cycle.

CLM includes two separate treatments of the slow nitrogen cycle. The first is the original CLM-CN formulations, which includes a single soil mineral nitrogen pool to represent both NO_3^- and NH_4^+, and with nitrogen losses via denitrification calculated as a constant fraction of mineralization plus a fixed first-order loss of unutilized mineral nitrogen at the end of every timestep. The second is based on the Century N-gas model; this includes separate NH_4^+ and NO_3^- pools, as well as environmentally controlled nitrification and denitrification rates. Both are described below.

16.1 Atmospheric Nitrogen Deposition

CLM uses a single variable to represent the total deposition of mineral nitrogen onto the land surface, combining wet and dry deposition of NO_y and NH_x as a single flux (NF_{ndep_sminn}, gN m^{-2} s^{-1}). This flux is intended to represent total reactive nitrogen deposited to the land surface which originates from the following natural and anthropogenic sources (Galloway et al. 2004): formation of NO_x during lightning, NO_x

and NH_3 emission from wildfire, NO_x emission from natural soils, NH_3 emission from natural soils, vegetation, and wild animals, NO_x and NH_3 emission during fossil fuel combustion (both thermal and fuel NO_x production), NO_x and NH_3 emission from other industrial processes, NO_x and NH_3 emission from fire associated with deforestation, NO_x and NH_3 emission from agricultural burning, NO_x emission from agricultural soils, NH_3 emission from agricultural crops, NH_3 emission from agricultural animal waste, and NH_3 emission from human waste and waste water. The deposition flux is provided as a spatially and (potentially) temporally varying dataset (see section 2.2.3 for a description of the default input dataset).

In the CLM-CN mineral N pool model, the nitrogen deposition flux is assumed to enter the soil mineral nitrogen pool (NS_{sminn}) directly; while in the Century-based model, all of the nitrogen is assumed to enter the NH_4^+ pool. Real pathways for wet and dry nitrogen deposition can be more complex than currently represented in the CLM-CN, including release from melting snowpack and direct foliar uptake of deposited NO_y (e.g. Tye et al. 2005; Vallano and Sparks, 2007).

16.2 Biological Nitrogen Fixation

The fixation of new reactive nitrogen from atmospheric N_2 by soil microorganisms is an important component of both preindustrial and modern-day nitrogen budgets, but a mechanistic understanding of global-scale controls on biological nitrogen fixation (BNF) is still only poorly developed (Cleveland et al. 1999; Galloway et al. 2004). Cleveland et al. (1999) suggested empirical relationships that predict BNF as a function of either evapotranspiration rate or net primary productivity for natural vegetation. CLM assumes that BNF is a function of net primary production (CF_{ann_NPP}, gC m^{-2} y^{-1}). The rationale

for choosing net primary production over evapotranspiration as the predictor is that the two are well-correlated (Parton et al. 1993; Running et al. 1989), and the use of primary production also introduces a known dependence of BNF on the carbon supply to nitrogen fixing microorganisms (Cleveland et al. 1999). The expression used is:

$$NF_{nfix,sminn} = 1.8\left(1 - \exp\left(-0.003 CF_{ann\_NPP}\right)\right) \Big/ \left(86400 \cdot 365\right) \qquad (16.1)$$

where $NF_{nfix,sminn}$ (gN m^{-2} s^{-1}) is the rate of BNF. Eq. (16.1) is plotted over a range of annual NPP in Figure 16.1.

Figure 16.1. Biological nitrogen fixation as a function of annual net primary production.

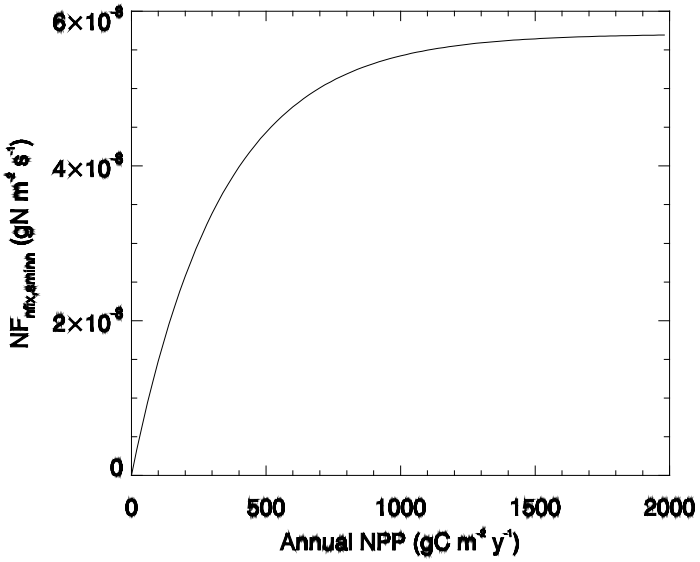

Because of the empirical nature of this NPP-BNF relationship, the timescale for calculating NPP and thus BNF is unconstrained. Using annual NPP, as in CLM4.0, introduces an error at high latitudes because the aseasonal BNF inputs mean that much of the nitrogen is added when the vegetation is dormant and may be lost before it is ever taken up by vegetation. Thus an option was added to CLM to allow for an exponential

relaxation (with default e-folding time of 10 days) calculation of NPP, and BNF calculated from that using equation 16.1.

As with Atmospheric N deposition, BNF N inputs are added directly to the mineral N pools. In the CLM-CN N model, this is the single mineral N pool; in the Century-based model, this is the NH_4^+ pool.

16.3 Nitrification and Denitrification Losses of Nitrogen

In order to better understand the structural uncertainty in biogeochemical responses to climate change, CLM includes two alternate representations of the mineral N transformations and losses that define the slow N cycle. Each of these is described below.

16.3.1 CLM-CN formulation

Under aerobic conditions in the soil oxygen is the preferred electron acceptor supporting the metabolism of heterotrophs, but anaerobic conditions favor the activity of soil heterotrophs which use nitrate as an electron acceptor (e.g. *Pseudomonas* and *Clostridium*) supporting respiration. This process, known as denitrification, results in the transformation of nitrate to gaseous N_2, with smaller associated production of NO_x and N_2O. It is typically assumed that nitrogen fixation and denitrification were approximately balanced in the preindustrial biosphere (Galloway et al. 2004). It is likely that denitrification can occur within anaerobic microsites within an otherwise aerobic soil environment, leading to large global denitrification fluxes even when fluxes per unit area are rather low (Galloway et al. 2004).

Because the vertical distribution of soil organic matter is not resolved explicitly in CLM-CN, a simple denitrification parameterization is used that treats denitrification as a

constant fraction of gross nitrogen mineralization. At each step in the decomposition cascade, if the transformation from an upstream to a downstream pool is predicted to mineralize (as opposed to immobilize) nitrogen, then a constant fraction of the nitrogen mineralization flux is assumed to be lost via denitrification. Due to large uncertainties in the mechanistic understanding of the environmental controls on denitrification, no modifications to the denitrification fraction are made for different soil moisture conditions. This is identified as a high-priority area for future model development.

Denitrification fluxes associated with gross mineralization in the decomposition cascade are calculated as follows:

$$NF_{denit,Lit1\rightarrow SOM1} = \begin{cases} 0 & \text{for } NF_{pot\_min,Lit1\rightarrow SOM1} > 0 \\ -NF_{pot\_min,Lit1\rightarrow SOM1} f_{denit} & \text{for } NF_{pot\_min,Lit1\rightarrow SOM1} \leq 0 \end{cases} \quad (16.2)$$

$$NF_{denit,Lit2\rightarrow SOM2} = \begin{cases} 0 & \text{for } NF_{pot\_min,Lit2\rightarrow SOM2} > 0 \\ -NF_{pot\_min,Lit2\rightarrow SOM2} f_{denit} & \text{for } NF_{pot\_min,Lit2\rightarrow SOM2} \leq 0 \end{cases} \quad (16.3)$$

$$NF_{denit,Lit3\rightarrow SOM3} = \begin{cases} 0 & \text{for } NF_{pot\_min,Lit3\rightarrow SOM3} > 0 \\ -NF_{pot\_min,Lit3\rightarrow SOM3} f_{denit} & \text{for } NF_{pot\_min,Lit3\rightarrow SOM3} \leq 0 \end{cases} \quad (16.4)$$

$$NF_{denit,SOM1\rightarrow SOM2} = \begin{cases} 0 & \text{for } NF_{pot\_min,SOM1\rightarrow SOM2} > 0 \\ -NF_{pot\_min,SOM1\rightarrow SOM2} f_{denit} & \text{for } NF_{pot\_min,SOM1\rightarrow SOM2} \leq 0 \end{cases} \quad (16.5)$$

$$NF_{denit,SOM2\rightarrow SOM3} = \begin{cases} 0 & \text{for } NF_{pot\_min,SOM2\rightarrow SOM3} > 0 \\ -NF_{pot\_min,SOM2\rightarrow SOM3} f_{denit} & \text{for } NF_{pot\_min,SOM2\rightarrow SOM3} \leq 0 \end{cases} \quad (16.6)$$

$$NF_{denit,SOM3\rightarrow SOM4} = \begin{cases} 0 & \text{for } NF_{pot\_min,SOM3\rightarrow SOM4} > 0 \\ -NF_{pot\_min,SOM3\rightarrow SOM4} f_{denit} & \text{for } NF_{pot\_min,SOM3\rightarrow SOM4} \leq 0 \end{cases} \quad (16.7)$$

$$NF_{denit,SOM4} = -NF_{pot\_min,SOM4} \quad (16.8)$$

where f_{denit} = 0.01 is the constant denitrification fraction of gross mineralization, and the denitrification fluxes are assumed to be leaving the soil mineral nitrogen pool (NS_{sminn})

and entering the atmosphere. The speciation of gaseous nitrogen fluxes entering the atmosphere (e.g. N_2 vs. NO_x or N_2O) is not specified. Providing an explicit speciation of these nitrogen losses is another high-priority area for future model development.

The model includes one other denitrification pathway, intended to represent the observed losses of mineral nitrogen in systems experiencing nitrogen saturation. One reason this mechanism has been included is in anticipation of an agricultural fertilization flux, provided either through a prescribed dataset or through a prognostic agricultural management routine. The model does not currently include an explicit representation of the fertilization flux, but when it is introduced, it will be necessary to account for the substantial denitrification losses associated with high nitrate concentrations in some heavily fertilized agricultural soils. Nitrogen saturation can also occur in natural vegetation systems, especially under conditions of high atmospheric nitrogen deposition, and so this mechanism plays a useful role even prior to the introduction within the model of agricultural fertilization.

For the purpose of this calculation, nitrogen saturation is evaluated on each timestep, by comparing the total demand for new mineral nitrogen from plants and immobilization with the available soil mineral nitrogen pool. The denitrification of excess soil mineral nitrogen is non-zero whenever the supply of mineral nitrogen exceeds the demand:

$$NF_{sminn,denit} = \begin{cases} \left(\frac{NS_{sminn}}{\Delta t} \right) - NF_{total\_demand} f_{dnx} & \text{for } NF_{total\_demand} \Delta t < NS_{sminn} \\ 0 & \text{for } NF_{total\_demand} \Delta t \geq NS_{sminn} \end{cases} \quad (16.9)$$

where f_{dnx} (unitless) is the fraction of excess soil mineral nitrogen subject to denitrification on each timestep. This fraction is parameterized such that 50% of any excess soil mineral nitrogen would be lost to denitrification per day:

$$f_{dnx} = 0.5\frac{\Delta t}{86400} \tag{16.10}$$

16.3.2 Century-based formulation

CLM includes a detailed representation of nitrification and denitrification based on the Century N model (Parton et al. 1996, 2001; del Grosso et al. 2000). In this approach, nitrification of NH_4^+ to NO_3^- is a function of temperature, moisture, and pH:

$$f_{nitr,p} = [NH_4]k_{nitr}f(T)f(H_2O)f(pH) \tag{16.11}$$

where $f_{nitr,p}$ is the potential nitrification rate (prior to competition for NH_4^+ by plant uptake and N immobilization), k_{nitr} is the maximum nitrification rate (10 % day^{-1}, (Parton et al. 2001)), and *f(T)* and $f(H_2O)$ are rate modifiers for temperature and moisture content. CLM uses the same rate modifiers as are used in the decomposition routine. *f(pH)* is a rate modifier for pH; however, because CLM does not calculate pH, instead a fixed pH value of 6.5 is used in the pH function of Parton et al. (1996).

The potential denitrification rate is co-limited by NO^{-3} concentration and C consumption rates, and occurs only in the anoxic fraction of soils:

$$f_{denitr,p} = \min\left(f(decomp), f\left([NO_3^-]\right)\right)frac_{anox} \tag{16.12}$$

where $f_{denitr,p}$ is the potential denitrification rate and *f(decomp)* and $f([NO_3^-])$ are the carbon- and nitrate- limited denitrification rate functions, respectively, (del Grosso et al. 2000). Because the modified CLM includes explicit treatment of soil biogeochemical vertical profiles, including diffusion of the trace gases O_2 and CH_4 (Riley et al. 2011a), the calculation of anoxic fraction $frac_{anox}$ uses this information following the anoxic microsite formulation of Arah and Vinten (1995):

$$frac_{anox} = \exp\left(-aR_{\psi}^{-\alpha}V^{-\beta}C^{\gamma}\left[\theta + \chi\varepsilon\right]^{\delta}\right) \tag{16.13}$$

where *a, α, β, γ,* and δ are constants (equal to 1.5×10^{-10}, 1.26, 0.6, 0.6, and 0.85, respectively), R_ψ is the radius of a typical pore space at moisture content ψ, V is the O_2 consumption rate, C is the O_2 concentration, θ is the water-filled pore space, χ is the ratio of diffusivity of oxygen in water to that in air, and ε is the air-filled pore space (Arah and Vinten, 1995). These parameters are all calculated separately at each layer to define a profile of anoxic porespace fraction in the soil.

The nitrification/denitrification models used here also predict fluxes of N_2O via a "hole-in-the-pipe" approach (Firestone and Davidson, 1989). A constant fraction ($6 * 10^{-4}$, Li et al. 2000) of the nitrification flux is assumed to be N_2O, while the fraction of denitrification going to N_2O, $P_{N2:N2O}$, is variable, following the Century (del Grosso et al. 2000) approach:

$$P_{N_2:N_2O} = \max\left(0.16k_1, k_1 \exp\left(-0.8P_{NO_3:CO_2}\right)\right) f_{WFPS} \tag{16.14}$$

where $P_{NO3:CO2}$ is the ratio of CO_2 production in a given soil layer to the NO_3^- concentration, k_1 is a function of d_g, the gas diffusivity through the soil matrix:

$$k_1 = \max\left(1.7, 38.4 - 350 * d_g\right) \tag{16.15}$$

and f_{WFPS} is a function of the water filled pore space *WFPS:*

$$f_{WFPS} = \max\left(0.1, 0.015 \times WFPS - 0.32\right) \tag{16.16}$$

16.4 Leaching Losses of Nitrogen

Soil mineral nitrogen remaining after plant uptake, immobilization, and denitrification is subject to loss as a dissolved component of hydrologic outflow from the soil column (leaching). This leaching loss ($NF_{leached}$, gN m^{-2} s^{-1}) depends on the concentration of dissolved mineral (inorganic) nitrogen in soil water solution (*DIN*, gN

kgH_2O), and the rate of hydrologic discharge from the soil column to streamflow (Q_{dis}, $kgH_2O\ m^{-2}\ s^{-1}$, section 7.6), as

$$NF_{leached} = DIN \cdot Q_{dis}. \tag{16.17}$$

DIN is calculated assuming that a constant fraction (*sf*, proportion) of the remaining soil mineral N pool is in soluble form, and that this entire fraction is dissolved in the total soil water. For the CLM-CN soil model, it is further assumed that *sf* = 0.1, representing an estimated 10% of the total NS_{sminn} pool as soluble nitrate, with the remaining 90% as less soluble ammonia; for the Century-based formulation, the leaching acts only on the NO_3^- pool (which is assumed to be 100% soluble), while the NH_4^+ pool is assumed to be 100% adsorbed onto mineral surfaces and unaffected by leaching. *DIN* is then given as

$$DIN = \frac{NS_{sminn} sf}{WS_{tot\_soil}} \tag{16.18}$$

where WS_{tot_soil} ($kgH_2O\ m^{-2}$) is the total mass of soil water content integrated over the column. The total mineral nitrogen leaching flux is limited on each time step to not exceed the soluble fraction of NS_{sminn}

$$NF_{leached} = \min\left(NF_{leached}, \frac{NS_{sminn} sf}{\Delta t} \right). \tag{16.19}$$

The CLM-CN parameterization of the soluble fraction is poorly constrained by observations. Fraction of total soil mineral N pool present as nitrate will vary spatially and temporally, depending on oxygen status of soils and rates of nitrification. A calibration of this parameterization against observations of dissolved nitrate in headwater streams might be an effective method for imposing better observational constraints at broad spatial scales.

16.5 Losses of Nitrogen Due to Fire

The final pathway for nitrogen loss is through combustion, also known as pyrodenitrification. Detailed equations are provided, together with the effects of fire on the carbon budget, in Chapter 18. It is assumed in CLM-CN that losses of N due to fire are restricted to vegetation and litter pools (including coarse woody debris). Loss rates of N are determined by the fraction of biomass lost to combustion, assuming that most of the nitrogen in the burned biomass is lost to the atmosphere (Schlesinger, 1997; Smith et al. 2005). It is assumed that soil organic matter pools of carbon and nitrogen are not directly affected by fire (Neff et al. 2005).

17. Plant Mortality

Plant mortality as described here applies to perennial vegetation types, and is intended to represent the death of individuals from a stand of plants due to the aggregate of processes such as wind throw, insect attack, disease, extreme temperatures or drought, and age-related decline in vigor. These processes are referred to in aggregate as "gap-phase" mortality. Mortality due to fire and anthropogenic land cover change are treated separately (see Chapters 18 and 21, respectively).

17.1 Mortality Fluxes Leaving Vegetation Pools

Whole-plant mortality is parameterized very simply, assuming a mortality rate of 2% yr^{-1} for all vegetation types. This is clearly a gross oversimplification of an important process, and additional work is required to better constrain this process in different climate zones (Keller et al. 2004; Sollins 1982), for different species mixtures (Gomes et al. 2003), and for different size and age classes (Busing 2005; Law et al. 2003). Literature values for forest mortality rates range from at least 0.7% to 3.0% yr^{-1}. Taking the annual rate of mortality (*am*, proportion yr^{-1}) as 0.02, a mortality rate per second (*m*) is calculated as $m = am/(365 \cdot 86400)$. All vegetation carbon and nitrogen pools for display, storage, and transfer are affected at rate *m*, with mortality fluxes out of vegetation pools eventually merged to the column level and deposited in litter pools. Mortality (*mort*) fluxes out of displayed vegetation carbon and nitrogen pools are

$$CF_{leaf\_mort} = CS_{leaf} m \tag{17.1}$$

$$CF_{froot\_mort} = CS_{froot} m \tag{17.2}$$

$$CF_{livestem\_mort} = CS_{livestem} m \tag{17.3}$$

$$CF_{deadstem\_mort} = CS_{deadstem} m \quad (17.4)$$

$$CF_{livecroot\_mort} = CS_{livecroot} m \quad (17.5)$$

$$CF_{deadcroot\_mort} = CS_{deadcroot} m \quad (17.6)$$

$$NF_{leaf\_mort} = NS_{leaf} m \quad (17.7)$$

$$NF_{froot\_mort} = NS_{froot} m \quad (17.8)$$

$$NF_{livestem\_mort} = NS_{livestem} m \quad (17.9)$$

$$NF_{deadstem\_mort} = NS_{deadstem} m \quad (17.10)$$

$$NF_{livecroot\_mort} = NS_{livecroot} m \quad (17.11)$$

$$NF_{deadcroot\_mort} = NS_{deadcroot} m \quad (17.12)$$

$$NF_{retrans\_mort} = NS_{retrans} m \, . \quad (17.13)$$

where CF are carbon fluxes, CS is carbon storage, NF are nitrogen fluxes, NS is nitrogen storage, *croot* refers to coarse roots, *froot* refers to fine roots, and *retrans* refers to retranslocated.

Mortality fluxes out of carbon and nitrogen storage (*stor)* pools are

$$CF_{leaf\_stor\_mort} = CS_{leaf\_stor} m \quad (17.14)$$

$$CF_{froot\_stor\_mort} = CS_{froot\_stor} m \quad (17.15)$$

$$CF_{livestem\_stor\_mort} = CS_{livestem\_stor} m \quad (17.16)$$

$$CF_{deadstem\_stor\_mort} = CS_{deadstem\_stor} m \quad (17.17)$$

$$CF_{livecroot\_stor\_mort} = CS_{livecroot\_stor} m \quad (17.18)$$

$$CF_{deadcroot\_stor\_mort} = CS_{deadcroot\_stor} m \quad (17.19)$$

$$CF_{gresp\_stor\_mort} = CS_{gresp\_stor} m \tag{17.20}$$

$$NF_{leaf\_stor\_mort} = NS_{leaf\_stor} m \tag{17.21}$$

$$NF_{froot\_stor\_mort} = NS_{froot\_stor} m \tag{17.22}$$

$$NF_{livestem\_stor\_mort} = NS_{livestem\_stor} m \tag{17.23}$$

$$NF_{deadstem\_stor\_mort} = NS_{deadstem\_stor} m \tag{17.24}$$

$$NF_{livecroot\_stor\_mort} = NS_{livecroot\_stor} m \tag{17.25}$$

$$NF_{deadcroot\_stor\_mort} = NS_{deadcroot\_stor} m \tag{17.26}$$

where *gresp* refers to growth respiration.

Mortality fluxes out of carbon and nitrogen transfer (*xfer)* growth pools are

$$CF_{leaf\_xfer\_mort} = CS_{leaf\_xfer} m \tag{17.27}$$

$$CF_{froot\_xfer\_mort} = CS_{froot\_xfer} m \tag{17.28}$$

$$CF_{livestem\_xfer\_mort} = CS_{livestem\_xfer} m \tag{17.29}$$

$$CF_{deadstem\_xfer\_mort} = CS_{deadstem\_xfer} m \tag{17.30}$$

$$CF_{livecroot\_xfer\_mort} = CS_{livecroot\_xfer} m \tag{17.31}$$

$$CF_{deadcroot\_xfer\_mort} = CS_{deadcroot\_xfer} m \tag{17.32}$$

$$CF_{gresp\_xfer\_mort} = CS_{gresp\_xfer} m \tag{17.33}$$

$$NF_{leaf\_xfer\_mort} = NS_{leaf\_xfer} m \tag{17.34}$$

$$NF_{froot\_xfer\_mort} = NS_{froot\_xfer} m \tag{17.35}$$

$$NF_{livestem\_xfer\_mort} = NS_{livestem\_xfer} m \tag{17.36}$$

$$NF_{deadstem\_xfer\_mort} = NS_{deadstem\_xfer} m \tag{17.37}$$

$$NF_{livecroot\_xfer\_mort} = NS_{livecroot\_xfer} m \tag{17.38}$$

$$NF_{deadcroot\_xfer\_mort} = NS_{deadcroot\_xfer} m \tag{17.39}$$

17.2 Mortality Fluxes Merged to the Column Level

Analogous to the treatment of litterfall fluxes, mortality fluxes leaving the vegetation pools are merged to the column level according to the weighted distribution of PFTs on the column ($wcol_p$), and deposited in litter and coarse woody debris pools, which are defined at the column level. Carbon and nitrogen fluxes from mortality of displayed leaf and fine root into litter pools are calculated as

$$CF_{leaf\_mort,lit1} = \sum_{p=0}^{npfts} CF_{leaf\_mort} f_{lab\_leaf,p} wcol_p \tag{17.40}$$

$$CF_{leaf\_mort,lit2} = \sum_{p=0}^{npfts} CF_{leaf\_mort} f_{cel\_leaf,p} wcol_p \tag{17.41}$$

$$CF_{leaf\_mort,lit3} = \sum_{p=0}^{npfts} CF_{leaf\_mort} f_{lig\_leaf,p} wcol_p \tag{17.42}$$

$$CF_{froot\_mort,lit1} = \sum_{p=0}^{npfts} CF_{froot\_mort} f_{lab\_froot,p} wcol_p \tag{17.43}$$

$$CF_{froot\_mort,lit2} = \sum_{p=0}^{npfts} CF_{froot\_mort} f_{cel\_froot,p} wcol_p \tag{17.44}$$

$$CF_{froot\_mort,lit3} = \sum_{p=0}^{npfts} CF_{froot\_mort} f_{lig\_froot,p} wcol_p \tag{17.45}$$

$$NF_{leaf\_mort,lit1} = \sum_{p=0}^{npfts} NF_{leaf\_mort} f_{lab\_leaf,p} wcol_p \tag{17.46}$$

$$NF_{leaf\_mort,lit2} = \sum_{p=0}^{npfts} NF_{leaf\_mort} f_{cel\_leaf,p} wcol_p \tag{17.47}$$

$$NF_{leaf\_mort,lit3} = \sum_{p=0}^{npfts} NF_{leaf\_mort} f_{lig\_leaf,p} wcol_p \tag{17.48}$$

$$NF_{froot\_mort,lit1} = \sum_{p=0}^{npfts} NF_{froot\_mort} f_{lab\_froot,p} wcol_p \tag{17.49}$$

$$NF_{froot\_mort,lit2} = \sum_{p=0}^{npfts} NF_{froot\_mort} f_{cel\_froot,p} wcol_p \tag{17.50}$$

$$NF_{froot\_mort,lit3} = \sum_{p=0}^{npfts} NF_{froot\_mort} f_{lig\_froot,p} wcol_p \ . \tag{17.51}$$

where *lab* refers to labile, *cel* refers to cellulose, and *lig* refers to lignin. Carbon and nitrogen mortality fluxes from displayed live and dead stem and coarse root pools are merged to the column level and deposited in the coarse woody debris (*cwd*) pools:

$$CF_{livestem\_mort,cwd} = \sum_{p=0}^{npfts} CF_{livestem\_mort} wcol_p \tag{17.52}$$

$$CF_{deadstem\_mort,cwd} = \sum_{p=0}^{npfts} CF_{deadstem\_mort} wcol_p \tag{17.53}$$

$$CF_{livecroot\_mort,cwd} = \sum_{p=0}^{npfts} CF_{livecroot\_mort} wcol_p \tag{17.54}$$

$$CF_{deadcroot\_mort,cwd} = \sum_{p=0}^{npfts} CF_{deadcroot\_mort} wcol_p \tag{17.55}$$

$$NF_{livestem\_mort,cwd} = \sum_{p=0}^{npfts} NF_{livestem\_mort} wcol_p \tag{17.56}$$

$$NF_{deadstem\_mort,cwd} = \sum_{p=0}^{npfts} NF_{deadstem\_mort} wcol_p \tag{17.57}$$

$$NF_{livecroot\_mort,cwd} = \sum_{p=0}^{npfts} NF_{livecroot\_mort} wcol_p \tag{17.58}$$

$$NF_{deadcroot\_mort,cwd} = \sum_{p=0}^{npfts} NF_{deadcroot\_mort} wcol_p \quad (17.59)$$

All vegetation storage and transfer pools for carbon and nitrogen are assumed to exist as labile pools within the plant (e.g. as carbohydrate stores, in the case of carbon pools). This assumption applies to storage and transfer pools for both non-woody and woody tissues. The mortality fluxes from these pools are therefore assumed to be deposited in the labile litter pools (CS_{lit1}, NS_{lit1}), after being merged to the column level. Carbon mortality fluxes out of storage and transfer pools are:

$$CF_{leaf\_stor\_mort,lit1} = \sum_{p=0}^{npfts} CF_{leaf\_stor\_mort} wcol_p \quad (17.60)$$

$$CF_{froot\_stor\_mort,lit1} = \sum_{p=0}^{npfts} CF_{froot\_stor\_mort} wcol_p \quad (17.61)$$

$$CF_{livestem\_stor\_mort,lit1} = \sum_{p=0}^{npfts} CF_{livestem\_stor\_mort} wcol_p \quad (17.62)$$

$$CF_{deadstem\_stor\_mort,lit1} = \sum_{p=0}^{npfts} CF_{deadstem\_stor\_mort} wcol_p \quad (17.63)$$

$$CF_{livecroot\_stor\_mort,lit1} = \sum_{p=0}^{npfts} CF_{livecroot\_stor\_mort} wcol_p \quad (17.64)$$

$$CF_{deadcroot\_stor\_mort,lit1} = \sum_{p=0}^{npfts} CF_{deadcroot\_stor\_mort} wcol_p \quad (17.65)$$

$$CF_{gresp\_stor\_mort,lit1} = \sum_{p=0}^{npfts} CF_{gresp\_stor\_mort} wcol_p \quad (17.66)$$

$$CF_{leaf\_xfer\_mort,lit1} = \sum_{p=0}^{npfts} CF_{leaf\_xfer\_mort} wcol_p \quad (17.67)$$

$$CF_{froot\_xfer\_mort,lit1} = \sum_{p=0}^{npfts} CF_{froot\_xfer\_mort} wcol_p \quad (17.68)$$

$$CF_{livestem\_xfer\_mort,lit1} = \sum_{p=0}^{npfts} CF_{livestem\_xfer\_mort} wcol_p \quad (17.69)$$

$$CF_{deadstem\_xfer\_mort,lit1} = \sum_{p=0}^{npfts} CF_{deadstem\_xfer\_mort} wcol_p \quad (17.70)$$

$$CF_{livecroot\_xfer\_mort,lit1} = \sum_{p=0}^{npfts} CF_{livecroot\_xfer\_mort} wcol_p \quad (17.71)$$

$$CF_{deadcroot\_xfer\_mort,lit1} = \sum_{p=0}^{npfts} CF_{deadcroot\_xfer\_mort} wcol_p \quad (17.72)$$

$$CF_{gresp\_xfer\_mort,lit1} = \sum_{p=0}^{npfts} CF_{gresp\_xfer\_mort} wcol_p \; . \quad (17.73)$$

Nitrogen mortality fluxes out of storage and transfer pools, including the storage pool for retranslocated nitrogen, are calculated as:

$$NF_{leaf\_stor\_mort,lit1} = \sum_{p=0}^{npfts} NF_{leaf\_stor\_mort} wcol_p \quad (17.74)$$

$$NF_{froot\_stor\_mort,lit1} = \sum_{p=0}^{npfts} NF_{froot\_stor\_mort} wcol_p \quad (17.75)$$

$$NF_{livestem\_stor\_mort,lit1} = \sum_{p=0}^{npfts} NF_{livestem\_stor\_mort} wcol_p \quad (17.76)$$

$$NF_{deadstem\_stor\_mort,lit1} = \sum_{p=0}^{npfts} NF_{deadstem\_stor\_mort} wcol_p \quad (17.77)$$

$$NF_{livecroot\_stor\_mort,lit1} = \sum_{p=0}^{npfts} NF_{livecroot\_stor\_mort} wcol_p \quad (17.78)$$

$$NF_{deadcroot\_stor\_mort,lit1} = \sum_{p=0}^{npfts} NF_{deadcroot\_stor\_mort} wcol_p \quad (17.79)$$

$$NF_{retrans\_mort,lit1} = \sum_{p=0}^{npfts} NF_{retrans\_mort} wcol_p \quad (17.80)$$

$$NF_{leaf\_xfer\_mort,lit1} = \sum_{p=0}^{npfts} NF_{leaf\_xfer\_mort} wcol_p \quad (17.81)$$

$$NF_{froot\_xfer\_mort,lit1} = \sum_{p=0}^{npfts} NF_{froot\_xfer\_mort} wcol_p \quad (17.82)$$

$$NF_{livestem\_xfer\_mort,lit1} = \sum_{p=0}^{npfts} NF_{livestem\_xfer\_mort} wcol_p \quad (17.83)$$

$$NF_{deadstem\_xfer\_mort,lit1} = \sum_{p=0}^{npfts} NF_{deadstem\_xfer\_mort} wcol_p \quad (17.84)$$

$$NF_{livecroot\_xfer\_mort,lit1} = \sum_{p=0}^{npfts} NF_{livecroot\_xfer\_mort} wcol_p \quad (17.85)$$

$$NF_{deadcroot\_xfer\_mort,lit1} = \sum_{p=0}^{npfts} NF_{deadcroot\_xfer\_mort} wcol_p \ . \quad (17.86)$$

18. Fire

The fire parameterization in CLM contains four components: non-peat fires outside cropland and tropical closed forests, agricultural fires, deforestation fires in the tropical closed forests, and peat fires (Li et al. 2012a, b, 2013a). In this fire parameterization, burned area is affected by climate and weather conditions, vegetation composition and structure, and human activities. After burned area is calculated, we estimate the fire impact, including biomass and peat burning, fire-induced vegetation mortality, and the adjustment of the carbon and nitrogen (C/N) pools. Justification for all equations and parameter values is given by Li et al. (2012a, b; 2013a) in detail.

18.1 Non-peat fires outside cropland and tropical closed forest

Burned area in a grid cell per time step, A_b (km^2 (time step)$^{-1}$), is determined by

$$A_b = N_f a \tag{18.1}$$

where N_f (count (time step)$^{-1}$) is fire counts in the grid cell; a (km^2) is average fire spread area of a fire.

18.1.1 Fire counts

Fire counts N_f is taken as

$$N_f = N_i f_b f_m f_{se,o} \tag{18.2}$$

where N_i (count (time step)$^{-1}$) is the number of ignition sources due to natural causes and human activities; f_b and f_m (fractions) represent the availability and combustibility of

fuel, respectively; $f_{se,o}$ is the fraction of anthropogenic and natural fires unsuppressed by humans and related to the socioeconomic conditions.

N_i (count (time step)$^{-1}$) is given as

$$N_i = (I_n + I_a) A_g \tag{18.3}$$

where I_n (count km^{-2} (time step)$^{-1}$) and I_a (count km^{-2} (time step)$^{-1}$) are the number of natural and anthropogenic ignitions per km^2, respectively; A_g is the area of the grid cell (km^2). I_n is estimated by

$$I_n = \gamma \psi I_l \tag{18.4}$$

where γ=0.25 is ignition efficiency of cloud-to-ground lightning; $\psi = \frac{1}{5.16 + 2.16\cos(3\lambda)}$ is the cloud-to-ground lightning fraction and depends on the latitude λ; I_l (flash km^{-2} (time step)$^{-1}$) is the total lightning flashes. I_a, is modeled as a monotonic increasing function of population density:

$$I_a = \frac{\alpha D_P k(D_P)}{n} \tag{18.5}$$

where $\alpha = 0.0035$ (count person^{-1} mon^{-1}) is the number of potential ignition sources by a person per month; D_P (person km^{-2}) is the population density; $k(D_P) = 6.8 D_P^{-0.6}$ represents anthropogenic ignition potential as a function of human population density D_P; n is the number of time steps in a month.

Fuel availability f_b is given as

$$f_b = \begin{cases} 0 & B_{ag} < B_{low} \\ \dfrac{B_{ag} - B_{low}}{B_{up} - B_{low}}, & B_{low} \le B_{ag} \le B_{up} \\ 1 & B_{ag} > B_{up} \end{cases} \tag{18.6}$$

where B_{ag} (g C m^{-2}) is the aboveground biomass of combined leaf, stem and aboveground litter (leaf litter and woody debris) pools; B_{low}=155 g C m^{-2} is the lower fuel threshold below which fire does not occur; B_{up}= 1050 g C m^{-2} is the upper fuel threshold above which fire occurrence is not limited by fuel availability.

Fuel combustibility f_m is estimated by

$$f_m = f_{RH} f_\theta f_T \tag{18.7}$$

where f_{RH}, f_θ, f_T represent the dependence of fuel combustibility on relative humidity *RH* (%), surface soil wetness θ, and surface air temperature *T* (ºC), respectively. f_{RH} is calculated by

$$f_{RH} = \begin{cases} 1 & RH \le RH_{low} \\ \dfrac{RH_{up} - RH}{RH_{up} - RH_{low}}, & RH_{low} < RH < RH_{up} \\ 0 & RH \ge RH_{up} \end{cases} \tag{18.8}$$

RH_{low}=30% and RH_{up}=70% are used as the lower and upper thresholds of relative humidity. f_θ is given by

$$f_\theta = \exp[-\pi(\frac{\theta}{\theta_e})^2] \tag{18.9}$$

where θ is the soil wetness defined as volumetric soil moisture relative to that at saturation; θ_e=0.69 is the extinction coefficient of soil wetness. f_T is given by

$$f_T = \max[0, \min(1, \frac{T+10}{10})] \quad (18.9)$$

consistent with the fact that temperature is the main constraint for fire occurrence when temperature is below freezing, and fire generally does not occur when the temperature is less than -10 ºC.

For scarcely populated regions ($D_p \le 0.1$ person km^{-2}), we assume that anthropogenic suppression on fire occurrence is negligible, i.e., $f_{se,o} = 1.0$. In regions of $D_p > 0.1$ person km^{-2}, we parameterize the fraction of anthropogenic and natural fires unsuppressed by human activities as

$$f_{se,o} = f_d f_e \quad (18.10)$$

where f_d and f_e are the effects of the demographic and economic conditions on fire occurrence. The demographic influence on fire occurrence is

$$f_d = 0.01 + 0.98\exp(-0.025 D_P). \quad (18.11)$$

For shrub and grass PFTs, the economic influence on fire occurrence is parameterized as a function of Gross Domestic Product GDP (k 1995US$ capita^{-1}):

$$f_e = 0.1 + 0.9 \times \exp[-\pi(\frac{GDP}{8})^{0.5}] \quad (18.12)$$

which captures 73% of the observed MODIS fire counts with variable GDP in regions where shrub and grass PFTs are dominant (fractional coverage of shrub and grass PFTs > 50%). In regions outside tropical closed forests and dominated by trees (fractional coverage of tree PFTs > 50%), we divide the MODIS fire counts into only two bins (

$GDP \geq 20$ k 1995US$ capita^{-1}, and $GDP < 20$ k 1995US$ capita^{-1}) and parameterize the economic influence on fire occurrence for tree PFTs as

$$f_e = \begin{cases} 0.39, & GDP \geq 20 \\ 1 & GDP < 20 \end{cases} \tag{18.13}$$

to reproduce that the MODIS fire counts in tree-dominated regions of GDP ≥ 20 k 1995US$ capita^{-1} is 39% of that in other tree-dominated regions.

18.1.2 Average spread area of a fire

Fire fighting capacity depends on socioeconomic conditions and affects fire spread area. Due to a lack of observations, we consider the socioeconomic impact on the average burned area rather than separately on fire spread rate and fire duration:

$$a = a^* F_{se} \tag{18.14}$$

where a^* is the average burned area of a fire without anthropogenic suppression and F_{se} is the socioeconomic effect on fire spread area.

Average burned area of a fire without anthropogenic suppression is assumed elliptical in shape with the wind direction along the major axis and the point of ignition at one of the foci. According to the area formula for an ellipse, average burned area of a fire can be represented as:

$$a^* = \pi \frac{l}{2} \frac{w}{2} \times 10^{-6} = \frac{\pi u_p^2 \tau^2}{4 L_B} (1 + \frac{1}{H_B})^2 \times 10^{-6} \tag{18.15}$$

where u_p (m s^{-1}) is the fire spread rate in the downwind direction; τ (s) is average fire duration; L_B and H_B are length-to-breadth ratio and head-to-back ratio of the ellipse; 10^{-6} converts m^2 to km^2.

According to Arora and Boer (2005),

$$L_B = 1.0 + 10.0[1 - \exp(-0.06W)] \tag{18.16}$$

where W (m s^{-1}) is the wind speed. According to the mathematical properties of the ellipse, the head-to-back ratio H_B is

$$H_B = \frac{u_p}{u_b} = \frac{L_B + (L_B{}^2 - 1)^{0.5}}{L_B - (L_B{}^2 - 1)^{0.5}}. \tag{18.17}$$

The fire spread rate in the downwind direction is represented as

$$u_p = u_{\max} C_m g(W) \tag{18.18}$$

(Arora and Boer, 2005), where $u_{\max}$ (m s^{-1}) is the PFT-dependent average maximum fire spread rate in natural vegetation regions; C_m and $g(W)$ represent the dependence of u_p on fuel wetness and wind speed W, respectively. $u_{\max}$ is set to 0.55 m s^{-1} for grass PFTs, 0.46 m s^{-1} for shrub PFTs, 0.43 m s^{-1} for needleleaf tree PFTs, and 0.40 m s^{-1} for other tree PFTs. $C_m = C_\beta C_{RH}$ is estimated by the dependence of u_p on root zone soil wetness (C_β) and relative humidity (C_{RH}). Here, β is a root zone soil moisture limitation function. Due to a lack of observations to calibrate C_β, we adopt a simple linear function, where β_{low}=0.3 and β_{up}=0.7 are the lower and upper thresholds of root zone soil wetness, respectively. C_{RH} is set equal to f_{RH}. $g(W)$ is derived from the mathematical properties of the ellipse and Eqs (18.16) and (18.17)

$$g(W) = \frac{2L_B}{1+\frac{1}{H_B}} g(0) . \quad (18.19)$$

Since g(W)=1.0, and L_B and H_B are at their maxima $L_B^{\max} = 11.0$ and $H_B^{\max} = 482.0$ when $W \to \infty$, g(0) can be derived as

$$g(0) = \frac{1+\frac{1}{H_B^{\max}}}{2L_B^{\max}} = 0.05 . \quad (18.20)$$

In the absence of globally gridded data on barriers to fire (e.g. rivers, lakes, roads, firebreaks) and human fire-fighting efforts, average fire duration is simply assumed equal to 1 which is the observed 2001–2004 mean persistence of most fires in the world (Giglio et al. 2006).

As with the socioeconomic influence on fire occurrence, we assume that the socioeconomic influence on fire spreading is negligible in regions of $D_p \le 0.1$ person km^{-2}, i.e., $F_{se} = 1.0$. In regions of $D_p > 0.1$ person km^{-2}, we parameterize such socioeconomic influence as:

$$F_{se} = F_d F_e \quad (18.21)$$

where F_d and F_e are effects of the demographic and economic conditions on the average spread area of a fire, and are identified by maximizing the explained variability of the GFED3 burned area fraction with both socioeconomic indices in grid cells with various dominant vegetation types. For shrub and grass PFTs, the demographic impact factor is

$$F_d = 0.2 + 0.8 \times \exp[-\pi(\frac{D_p}{450})^{0.5}] \quad (18.22)$$

and the economic impact factor is

$$F_e = 0.2 + 0.8 \times \exp(-\pi \frac{GDP}{7}). \tag{18.23}$$

For tree PFTs outside tropical closed forests, the demographic and economic impact factors are given as

$$F_d = 0.4 + 0.6 \times \exp(-\pi \frac{D_p}{125}) \tag{18.24}$$

and

$$F_e = \begin{cases} 0.62, & GDP > 20 \\ 0.83, & 8 < GDP \le 20 \\ 1, & GDP \le 8 \end{cases}. \tag{18.25}$$

Eqs. (18.22)-(18.25) reflect that more developed and more densely populated regions have a higher fire fighting capability.

18.1.3 Fire impact

In post-fire regions, we calculate PFT-level fire carbon emissions from the *j*th PFT, φ_j (g C (time step)$^{-1}$), as

$$\varphi_j = A_{b,j} \mathbf{C_j} \bullet \mathbf{CC_j} \tag{18.26}$$

where $A_{b,j}$ (km^2 (time step)$^{-1}$) is burned area for the *j*th PFT; $\boldsymbol{C_j}$=(C_{leaf}, C_{stem}, C_{root}, C_{ts})$_j$ is a vector with carbon density (g C km^{-2}) for leaf, stem (live and dead stem), root (fine, live coarse and dead coarse root), and transfer and storage carbon pools as elements; $\boldsymbol{CC_j}$=(CC_{leaf}, CC_{stem}, CC_{root}, CC_{ts})$_j$ is the corresponding combustion completeness factor vector (Table 18.1). Moreover, we assume that 30% and 20% of column-level litter and

coarse woody debris are burned and the corresponding carbon is transferred to atmosphere.

Tissue mortality due to fire leads to carbon transfers in two ways. First, carbon from uncombusted leaf, live stem, dead stem, root, and transfer and storage pools $\mathbf{C}'_{j1} = (C_{\text{leaf}}(1-CC_{\text{leaf}}), C_{\text{livestem}}(1-CC_{\text{stem}}), C_{\text{deadstem}}(1-CC_{\text{stem}}), C_{\text{root}}(1-CC_{\text{root}}), C_{\text{ts}}(1-CC_{\text{ts}}))_j$ (g C km^{-2}) is transferred to litter as

$$\Psi_{j1} = \frac{A_{b,j}}{f_j A_g} \mathbf{C}'_{\mathbf{j}1} \bullet \mathbf{M}_{\mathbf{j}1} \tag{18.27}$$

where $M_{\mathbf{j}1} = (M_{\text{leaf}}, M_{\text{livestem,1}}, M_{\text{deadstem}}, M_{\text{root}}, M_{\text{ts}})_j$ is the corresponding mortality factor vector (Table 18.1). Second, carbon from uncombusted live stems is transferred to dead stems as:

$$\Psi_{j2} = \frac{A_{b,j}}{f_j A_g} C_{\text{livestem}}(1-CC_{\text{stem}}) M_{\text{livestem,2}} \tag{18.28}$$

where $M_{\text{livestem,2}}$ is the corresponding mortality factor (Table 18.1).

Fire nitrogen emissions and nitrogen transfers due to fire-induced mortality are calculated the same way as for carbon, using the same values for combustion completeness and mortality factors. With CLM's dynamic vegetation option enabled, the number of tree PFT individuals killed by fire per km^2 (individual km^{-2} (time step)$^{-1}$) is given by

$$P_{disturb,j} = \frac{A_{b,j}}{f_j A_g} P_j \xi_j \tag{18.29}$$

where P_j (individual km^{-2}) is the population density for the *j*th tree PFT and ξ_j is the whole-plant mortality factor (Table 18.1).

18.2 Agricultural fires

The burned area of cropland (km^2 (time step)$^{-1}$) is taken as A_b:

$$A_b = a_1 f_b f_{se} f_t f_{crop} A_g \tag{18.30}$$

where a_1 ((time step)$^{-1}$) is a constant; f_b is the fuel availability factor; f_{se} represents the socioeconomic effect on fires; f_t determines the seasonality of agricultural fires; f_{crop} is the fractional coverage of cropland. $a_1 = 0.31$ hr^{-1} is estimated using an inverse method, by matching 1997-2004 simulations from an unreleased CLM4.5 version driven by Qian et al. (2006) atmospheric forcing and climatological lightning data to the analysis of van der Werf et al. (2010) that shows the 2001-2009 average contribution of cropland fires is 4.7% of the total global burned area.

We assume the same fuel-load requirement for all fires, so f_b is set by Eq. (18.6). The socioeconomic factor f_{se} is given as follows:

$$f_{se} = f_d f_e \,. \tag{18.31}$$

Here

$$f_d = 0.04 + 0.96 \times \exp[-\pi (\frac{D_p}{350})^{0.5}] \tag{18.32}$$

and

$$f_e = 0.01 + 0.99 \times \exp(-\pi \frac{GDP}{10}) \tag{18.33}$$

are the effects of population density and GDP on burned area, derived in a similar way to Eqs. (18.22) and (18.23). f_t is set to 1 during the climatological peak month for agricultural fires (van der Werf et al. 2010) in time steps with no precipitation and $T>T_f$ if no agricultural fires occurred earlier in the year; f_t is set to 0 otherwise. Peak month in this dataset correlates with the month after harvesting or the month before planting. In CLM we use this dataset the same way whether the CROP option is active or not, without regard to the CROP option's simulated planting and harvesting dates.

In the post-fire region, fire impact is parameterized similar to section 18.1.3 but with combustion completeness factors and tissue mortality factors for crop PFTs (Table 18.1).

18.3 Deforestation fires

CLM focuses on deforestation fires in tropical closed forests. Tropical closed forests are defined as grid cells with tropical tree coverage >60% according to the FAO classification. Deforestation fires are defined as fires caused by deforestation, including escaped deforestation fires, termed degradation fires. Deforestation and degradation fires are assumed to occur outside of cropland areas in these grid cells. Burned area is controlled by the deforestation rate and climate:

$$A_b = bf_{lu} f_{cli,d} A_g \tag{18.34}$$

where b (time step)$^{-1}$ is a global constant; f_{lu} (fraction) represents the effect of decreasing fractional coverage of tree PFTs derived from land use data; and $f_{cli,d}$ (fraction) represents the effect of climate conditions on the burned area.

Constants b and f_{lu} are calibrated based on observations and reanalysis datasets in the Amazon rainforest (tropical closed forests within 15°S–5°N, 80.5°W–91°W). b=0.035 d^{-1} and f_{lu} is defined as

$$f_{lu} = \max(0.0005, 0.19D - 0.0011) \tag{18.35}$$

where D (yr^{-1}) is the annual loss of tree cover based on CLM4's land use and land cover change data.

The effect of climate on deforestation fires is parameterized as:

$$f_{cli,d} = \max[0, \min(1, \frac{b_2 - P_{60d}}{b_2})]^{0.5} \max[0, \min(1, \frac{b_3 - P_{10d}}{b_3})]^{0.5} \max[0, \min(1, \frac{0.25 - P}{0.25})] \tag{18.36}$$

where P (mm d^{-1}) is instantaneous precipitation, while P_{60d} (mm d^{-1}) and P_{10d} (mm d^{-1}) are 60-day and 10-day running means of precipitation, respectively; b_2 (mm d^{-1}) and b_3 (mm d^{-1}) are the grid-cell dependent thresholds of P_{60d} and P_{10d}; 0.25 mm d^{-1} is the maximum precipitation rate for drizzle. Le Page et al. (2010) analyzed the relationship between large-scale deforestation fire counts and precipitation during 2003–2006 in southern Amazonia where tropical evergreen trees (BET Tropical) are dominant. Figure 2 in Le Page et al. (2010) showed that fires generally occurred if both P_{60d} and P_{10d} were less than about 4.0 mm d^{-1}, and fires occurred more frequently in a drier environment.

Based on the 30-yr (1985−2004) precipitation data in Qian et al. (2006), the climatological precipitation of dry months (P<4.0 mm d^{-1}) in a year over tropical deciduous tree (BDT Tropical) dominated regions is 46% of that over BET Tropical dominated regions, so we set the PFT-dependent thresholds of P_{60d} and P_{10d} as 4.0 mm d^{-1} for BET Tropical and 1.8 mm d^{-1} (= 4.0 mm d^{-1} × 46%) for BDT Tropical, and b_2 and b_3 are the average of thresholds of BET Tropical and BDT Tropical weighted by their coverage.

The post-fire area due to deforestation is not limited to land-type conversion regions. In the tree-reduced region, the maximum fire carbon emissions are assumed to be 80% of the total conversion flux. According to the fraction of conversion flux for tropical trees in the tree-reduced region (60%) assigned by CLM, to reach the maximum fire carbon emissions in a conversion region requires burning this region about twice when we set PFT-dependent combustion completeness factors to about 0.3 for stem [the mean of 0.2−0.4 used in van der Werf (2010)]. Therefore, when the burned area calculated from Eq. (18.36) is no more than twice the tree-reduced area, we assume no escaped fires outside the land-type conversion region, and the fire-related fraction of the total conversion flux is estimated as $\frac{A_b / A_g}{2D}$. Otherwise, 80% of the total conversion flux is assumed to be fire carbon emissions, and the biomass combustion and vegetation

mortality outside the tree-reduced regions with an area fraction of $\frac{A_b}{A_g} - 2D$ are set as in section 18.1.3.

18.4 Peat fires

The burned area due to peat fires is given as A_b:

$$A_b = cf_{cli,p} f_{peat}(1 - f_{sat}) A_g \tag{18.37}$$

where c (time step)$^{-1}$ is a constant; $f_{cli,p}$ represents the effect of climate on the burned area; f_{peat} is the fractional coverage of peatland in the grid cell; and f_{sat} is the fraction of the grid cell with a water table at the surface or higher. c=1.0×10^{-3} hr^{-1} for tropical peat fires and c=4.2×10^{-5} hr^{-1} for boreal peat fires are derived using an inverse method, by matching simulations from an unreleased CLM4.5 version driven by Qian et al. (2006) atmospheric forcing and climatological lightning data to earlier studies: about 2.4 Mha peatland was burned over Indonesia in 1997 (Page et al. 2002) and the average burned area of peat fires in Western Canada was 0.2 Mha yr^{-1} for 1980–1999 (Turetsky et al. 2004).

For tropical peat fires, $f_{cli,p}$ is set as a function of long-term precipitation P_{60d}:

$$f_{cli,p} = \max[0, \min(1, \frac{4 - P_{60d}}{4})]^2 . \tag{18.38}$$

For boreal peat fires, $f_{cli,p}$ is set to

$$f_{cli,p} = \exp(-\pi \frac{\theta_{17cm}}{0.3}) \cdot \max[0, \min(1, \frac{T_{17cm} - T_f}{10})] \tag{18.39}$$

where θ_{17cm} and T_{17cm} are the wetness and temperature of the top 17 cm of soil; T_f =273.15 K is the freezing temperature.

Peat fires lead to peat combustion and the combustion and mortality of vegetation in peatlands. For tropical peat fires, based on Page et al. (2002), about 6% of the peat carbon loss from stored carbon is caused by 33.9% of the peatland burned. Carbon emissions due to peat combustion (g C m^{-2} (time step)$^{-1}$) are therefore set as the product of 6%/33.9%, by burned area fraction of peat fire ((time step)$^{-1}$), by soil organic carbon (g C m^{-2}). For boreal peat fires, the carbon emissions due to peat combustion are set as 2.2 kg C m^{-2} peat fire area (Turetsky et al. 2002). Biomass combustion and vegetation mortality in post-fire peatlands are set the same as section 18.1.3 for non-crop PFTs and as section 18.2 for crops PFTs.

Table 18.1. PFT-specific combustion completeness and fire mortality factors.

PFT	CC_{leaf}	CC_{stem}	CC_{root}	CC_{ts}	M_{leaf}	$M_{livestem}$	$M_{deadstem}$	M_{root}	M_{ts}	$M_{livestem}$	ξ_j
NET Temperate	0.80	0.25	0.00	0.50	0.80	0.15	0.15	0.15	0.50	0.35	0.15
NET Boreal	0.80	0.25	0.00	0.50	0.80	0.15	0.15	0.15	0.50	0.35	0.15
NDT Boreal	-	-	-	-	-	-	-	-	-	-	-
BET Tropical	0.80	0.22	0.00	0.45	0.80	0.13	0.13	0.13	0.45	0.32	0.13
BET Temperate	0.80	0.22	0.00	0.45	0.80	0.13	0.13	0.13	0.45	0.32	0.13
BDT Tropical	0.80	0.22	0.00	0.45	0.80	0.10	0.10	0.10	0.35	0.25	0.10
BDT Temperate	0.80	0.22	0.00	0.45	0.80	0.10	0.10	0.10	0.35	0.25	0.10
BDT Boreal	0.80	0.22	0.00	0.45	0.80	0.13	0.13	0.13	0.45	0.32	0.13
BES Temperate	-	-	-	-	-	-	-	-	-	-	-
BDS Temperate	0.80	0.30	0.00	0.55	0.80	0.17	0.17	0.17	0.55	0.38	0.17
BDS Boreal	0.80	0.30	0.00	0.55	0.80	0.17	0.17	0.17	0.55	0.38	0.17
C_3 Grass Arctic	0.80	0.80	0.00	0.80	0.80	0.20	0.20	0.20	0.80	0.60	-
C_3 Grass	0.80	0.80	0.00	0.80	0.80	0.20	0.20	0.20	0.80	0.60	-
C_4 Grass	0.80	0.80	0.00	0.80	0.80	0.20	0.20	0.20	0.80	0.60	-
Crop 1	0.80	0.80	0.00	0.80	0.80	0.20	0.20	0.20	0.80	0.60	-
Crop 2	-	-	-	-	-	-	-	-	-	-	-

Leaves (CC_{leaf}), stems (CC_{stem}), roots (CC_{root}), and transfer and storage carbon (CC_{ts}); mortality factors for leaves (M_{leaf}), live stems ($M_{livestem,1}$), dead stems ($M_{deadstem}$), roots (M_{root}), and transfer and storage carbon (M_{ts}) related to the carbon transfers from these pools to litter pool; mortality factors for live stems ($M_{livestem,2}$) related to the carbon transfer from live stems to dead stems; whole-plant mortality factor (ξ_j). Parameters are calibrated in an unreleased CLM4.5 version driven by Qian et al. (2006) atmospheric forcing and climatological lightning data.

19. Methane Model

The representation of processes in the methane biogeochemical model integrated in CLM [CLM4Me; (Riley et al. 2011a)] is based on several previously published models (Cao et al. 1996; Petrescu et al. 2010; Tian et al. 2010; Walter et al. 2001; Wania et al. 2010; Zhang et al. 2002; Zhuang et al. 2004). Although the model has similarities with these precursor models, a number of new process representations and parameterization have been integrated into CLM.

Mechanistically modeling net surface CH_4 emissions requires representing a complex and interacting series of processes. We first (section 19.1) describe the overall model structure and flow of information in the CH_4 model, then describe the methods used to represent: (19.2) CH_4 mass balance; (19.3) CH_4 production; (19.4) ebullition; (19.5) aerenchyma transport; (19.6) CH_4 oxidation; (19.7) reactive transport solution, including boundary conditions, numerical solution, water table interface, etc.; (19.8) seasonal inundation effects; and (19.9) impact of seasonal inundation on CH_4 production.

19.1 Methane Model Structure and Flow

The driver routine for the methane biogeochemistry calculations (ch4, in ch4Mod.F) controls the (1) initialization of boundary conditions, inundation, and impact of redox conditions; (2) calls to routines to calculate CH_4 production, oxidation, transport through aerenchyma, ebullition, and the overall mass balance (for unsaturated and saturated soils and, if desired, lakes); (3) resolves changes to CH_4 calculations associated with a changing inundated fraction; (4) performs a mass balance check; and (5) calculates the average gridcell CH_4 production, oxidation, and exchanges with the atmosphere.

19.2 Governing Mass-Balance Relationship

The model (Figure 19.1) accounts for CH_4 production in the anaerobic fraction of soil (P, mol m^{-3} s^{-1}), ebullition (E, mol m^{-3} s^{-1}), aerenchyma transport (A, mol m^{-3} s^{-1}), aqueous and gaseous diffusion (F_D, mol m^{-2} s^{-1}), and oxidation (O, mol m^{-3} s^{-1}) via a transient reaction diffusion equation:

$$\frac{\partial(RC)}{\partial t} = \frac{\partial F_D}{\partial z} + P(z,t) - E(z,t) - A(z,t) - O(z,t) \tag{19.1}$$

Here z (m) represents the vertical dimension, t (s) is time, and R accounts for gas in both the aqueous and gaseous phases: $R = \varepsilon_a + K_H \varepsilon_w$, with ε_a, ε_w, and K_H (-) the air-filled porosity, water-filled porosity, and partitioning coefficient for the species of interest, respectively, and C represents CH_4 or O_2 concentration with respect to water volume (mol m^{-3}).

An analogous version of equation (19.1) is concurrently solved for O_2, but with the following differences relative to CH_4: $P = E = 0$ (i.e., no production or ebullition), and the oxidation sink includes the O_2 demanded by methanotrophs, heterotroph decomposers, nitrifiers, and autotrophic root respiration.

As currently implemented, each gridcell contains an inundated and a non-inundated fraction. Therefore, equation (19.1) is solved four times for each gridcell and time step: in the inundated and non-inundated fractions, and for CH_4 and O_2. If desired, the CH_4 and O_2 mass balance equation is solved again for lakes (Chapter 9). For non-inundated areas, the water table interface is defined at the deepest transition from greater than 95% saturated to less than 95% saturated that occurs above frozen soil layers. The inundated fraction is allowed to change at each time step, and the total soil CH_4 quantity is conserved by evolving CH_4 to the atmosphere when the inundated fraction decreases, and

averaging a portion of the non-inundated concentration into the inundated concentration when the inundated fraction increases.

Figure 19.1. Schematic representation of biological and physical processes integrated in CLM that affect the net CH_4 surface flux (Riley et al. 2011a). (left) Fully inundated portion of a CLM gridcell and (right) variably saturated portion of a gridcell.

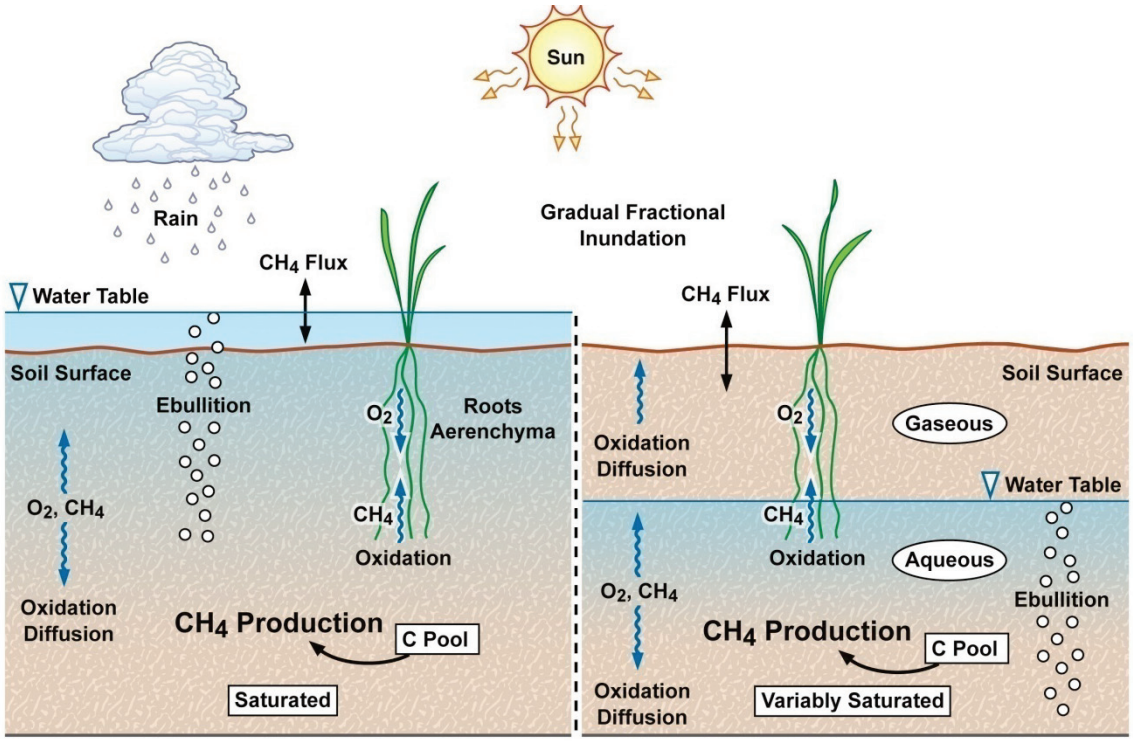

19.3 CH_4 Production

Because CLM does not currently specifically represent wetland plant functional types or soil biogeochemical processes, we used gridcell-averaged decomposition rates as proxies. Thus, the upland (default) heterotrophic respiration is used to estimate the wetland decomposition rate after first dividing off the O_2 limitation. The O_2 consumption associated with anaerobic decomposition is then set to the unlimited version so that it will

be reduced appropriately during O_2 competition. CH_4 production at each soil level in the anaerobic portion (i.e., below the water table) of the column is related to the gridcell estimate of heterotrophic respiration from soil and litter (R_H; mol C m^{-2} s^{-1}) corrected for its soil temperature (T_s) dependence, soil temperature through a Q_{10} factor (f_T), pH (f_{pH}), redox potential (f_{pE}), and a factor accounting for the seasonal inundation fraction (S, described below):

$$P = R_H f_{CH_4} f_T f_{pH} f_{pE} S \,. \tag{19.2}$$

Here, f_{CH_4} is the baseline ratio between CO_2 and CH_4 production (all parameters values are given in Table 19.1). Currently, f_{CH_4} is modified to account for our assumptions that methanogens (1) may have a higher Q_{10} than aerobic decomposers; (2) are not N limited; and (3) do not have a low-moisture limitation.

When the single BGC soil level is used in CLM (Chapter 15), the temperature factor, f_T, is set to 0 for temperatures equal to or below freezing, even though CLM allows heterotrophic respiration below freezing. However, if the vertically resolved BGC soil column is used, CH_4 production continues below freezing because liquid water stress limits decomposition. The base temperature for the Q_{10} factor, T_B, is 22 °C and effectively modified the base f_{CH_4} value.

For the single-layer BGC version, R_H is distributed among soil levels by assuming that 50% is associated with the roots (using the CLM PFT-specific rooting distribution) and the rest is evenly divided among the top 0.28 m of soil (to be consistent with CLM's soil decomposition algorithm). For the vertically resolved BGC version, the prognosed distribution of R_H is used to estimate CH_4 production.

The factor f_{pH} is nominally set to 1, although a static spatial map of *pH* can be used to determine this factor (Dunfield et al. 1993) by applying:

$$f_{pH} = 10^{-0.2235\,pH^2 + 2.7727\,pH - 8.6} \quad (19.3)$$

.

The f_{pE} factor assumes that alternative electron acceptors are reduced with an e-folding time of 30 days after inundation. The default version of the model applies this factor to horizontal changes in inundated area but not to vertical changes in the water table depth in the upland fraction of the gridcell. We consider both f_{pH} and f_{pE} to be poorly constrained in the model and identify these controllers as important areas for model improvement.

As a non-default option to account for CH_4 production in anoxic microsites above the water table, we apply the Arah and Stephen (1998) estimate of anaerobic fraction:

$$\varphi = \frac{1}{1 + \eta C_{O_2}}. \quad (19.4)$$

Here, φ is the factor by which production is inhibited above the water table (compared to production as calculated in equation (19.2), C_{O_2} (mol m^{-3}) is the bulk soil oxygen concentration, and η = 400 mol m^{-3}.

The O_2 required to facilitate the vertically resolved heterotrophic decomposition and root respiration is estimated assuming 1 mol O_2 is required per mol CO_2 produced. The model also calculates the O_2 required during nitrification, and the total O_2 demand is used in the O_2 mass balance solution.

Table 19.1. Parameter descriptions and sensitivity analysis ranges applied in the methane model.

Mechanism	Parameter	Baseline Value	Range for Sensitivity Analysis	Units	Description
Production	Q_{10}	2	1.5 – 4	-	CH_4 production Q_{10}
	f_{pH}	1	On, off	-	Impact of pH on CH_4 production
	f_{pE}	1	On, off	-	Impact of redox potential on CH_4 production
	S	Varies	NA	-	Seasonal inundation factor
	β	0.2	NA	-	Effect of anoxia on decomposition rate (used to calculate S only)
	f_{CH_4}	0.2	NA	-	Ratio between CH_4 and CO_2 production below the water table
Ebullition	$C_{e,max}$	0.15	NA	mol m^{-3}	CH_4 concentration to start ebullition
	$C_{e,min}$	0.15	NA	-	CH_4 concentration to end ebullition
Diffusion	f_{D_0}	1	1, 10	m^2 s^{-1}	Diffusion coefficient multiplier (Table 19.2)
Aerenchyma	p	0.3	NA	-	Grass aerenchyma porosity
	R	2.9×10^{-3} m	NA	m	Aerenchyma radius
	r_L	3	NA	-	Root length to depth ratio
	F_a	1	0.5 – 1.5	-	Aerenchyma conductance multiplier
Oxidation	K_{CH_4}	5×10^{-3}	5×10^{-4} - 5×10^{-2}	mol m^{-3}	CH_4 half-saturation oxidation coefficient (wetlands)
	K_{O_2}	2×10^{-2}	2×10^{-3} - 2×10^{-1}	mol m^{-3}	O_2 half-saturation oxidation coefficient
	$R_{o,\max}$	1.25×10^{-5}	1.25×10^{-6} - 1.25×10^{-4}	mol m^{-3} s^{-1}	Maximum oxidation rate (wetlands)

19.4 Ebullition

Briefly, the simulated aqueous CH_4 concentration in each soil level is used to estimate the expected equilibrium gaseous partial pressure (C_e), as a function of temperature and depth below the water table, by first estimating the Henry's law partitioning coefficient (k_h^C) by the method described in Wania et al. (2010):

$$\log\left(\frac{1}{k_H}\right) = \log k_H^s - \frac{1}{C_H}\left(\frac{1}{T} - \frac{1}{T^s}\right) \tag{19.5}$$

$$k_h^C = T k_H R_g \tag{19.6}$$

$$C_e = \frac{C_w R_g T}{\theta_s k_H^C p} \tag{19.7}$$

where C_H is a constant, R_g is the universal gas constant, k_H^s is Henry's law partitioning coefficient at standard temperature (T^s), C_w is local aqueous CH_4 concentration, and p is pressure.

The local pressure is calculated as the sum of the ambient pressure, water pressure down to the local depth, and pressure from surface ponding (if applicable). When the CH_4 partial pressure exceeds 15% of the local pressure (Baird et al. 2004; Strack et al. 2006; Wania et al. 2010), bubbling occurs to remove CH_4 to below this value, modified by the fraction of CH_4 in the bubbles [taken as 57%; (Kellner et al. 2006; Wania et al. 2010)]. Bubbles are immediately added to the surface flux for saturated columns and are placed immediately above the water table interface in unsaturated columns.

19.5 Aerenchyma Transport

Aerenchyma transport is modeled in CLM as gaseous diffusion driven by a concentration gradient between the specific soil layer and the atmosphere and, if

specified, by vertical advection with the transpiration stream. There is evidence that pressure driven flow can also occur, but we did not include that mechanism in the current model.

The diffusive transport through aerenchyma (A, mol m^{-2} s^{-1}) from each soil layer is represented in the model as:

$$A = \frac{C(z) - C_a}{r_L z / D + r_a} pT\rho_r , \tag{19.8}$$

where D is the free-air gas diffusion coefficient (m^2 s^{-1}); $C(z)$ (mol m^{-3}) is the gaseous concentration at depth z (m); r_L is the ratio of root length to depth; p is the porosity (-); T is specific aerenchyma area (m^2 m^{-2}); r_a is the aerodynamic resistance between the surface and the atmospheric reference height (s m^{-1}); and ρ_r is the rooting density as a function of depth (-). The gaseous concentration is calculated with Henry's law as described in equation (19.6).

Based on the ranges reported in Colmer (2003), we have chosen baseline aerenchyma porosity values of 0.3 for grass and crop PFTs and 0.1 for tree and shrub PFTs. The aerenchyma area varies over the course of the growing season; we parameterize this dependency using the simulated leaf area index L (m^2 m^{-2}), as in Wania et al. (2010):

$$T = \frac{f_N N_a L}{0.22} \pi R^2 . \tag{19.9}$$

Here N_a is annual net primary production (NPP, mol m^{-2} s^{-1}); R is the aerenchyma radius (2.9×10^{-3} m); f_N is the belowground fraction of annual NPP; and the 0.22 factor represents the amount of C per tiller. O_2 can also diffuse in from the atmosphere to the soil layer via the reverse of the same pathway, with the same representation as Equation (19.8) but with the gas diffusivity of oxygen.

CLM also simulates the direct emission of CH_4 from leaves to the atmosphere via transpiration of dissolved methane. We calculate this flux (F_{CH_4-T}; mol m^{-2} s^{-1}) using the simulated soil water methane concentration ($C_{CH_4,j}$ (mol m^{-3})) in each soil layer *j* and the CLM predicted transpiration (F_T) for each PFT, assuming that no methane was oxidized inside the plant tissue:

$$F_{CH_4-T} = \sum_j \rho_{r,j} F_T C_{CH_4,j} . \tag{19.10}$$

19.6 CH_4 Oxidation

CLM represents CH_4 oxidation with double Michaelis-Menten kinetics (Arah and Stephen 1998; Segers 1998), dependent on both the gaseous CH_4 and O_2 concentrations:

$$R_{oxic} = R_{o,\max}\left[\frac{C_{CH_4}}{K_{CH_4}+C_{CH_4}}\right]\left[\frac{C_{O_2}}{K_{O_2}+C_{O_2}}\right]Q_{10}F_g \tag{19.11}$$

where K_{CH_4} and K_{O_2} are the half saturation coefficients (mol m^{-3}) with respect to CH_4 and O_2 concentrations, respectively; $R_{o,\max}$ is the maximum oxidation rate (mol m^{-3} s^{-1}); and Q_{10} specifies the temperature dependence of the reaction with a base temperature set to 12 °C. The soil moisture limitation factor F_g is applied above the water table to represent water stress for methanotrophs. Based on the data in Schnell and King (1996), we take $F_g = e^{-P/P_c}$, where *P* is the soil moisture potential and P_c = -2.4×10^5 mm.

19.7 Reactive Transport Solution

The solution to equation (19.1) is solved in several sequential steps: (1) resolve competition for CH_4 and O_2 (section 19.7.1); (2) add the ebullition flux into the layer directly above the water table or into the atmosphere; (3) calculate the overall CH_4 or O_2

source term based on production, aerenchyma transport, ebullition, and oxidation; (4) establish boundary conditions, including surface conductance to account for snow, ponding, and turbulent conductances and bottom flux condition (section 19.7.2); (5) calculate diffusivity (section 19.7.3); and (6) solve the resulting mass balance using a tridiagonal solver (section 19.7.5).

19.7.1 Competition for CH_4 and O_2

For each time step, the unlimited CH_4 and O_2 demands in each model depth interval are computed. If the total demand over a time step for one of the species exceeds the amount available in a particular control volume, the demand from each process associated with the sink is scaled by the fraction required to ensure non-negative concentrations. Since the methanotrophs are limited by both CH_4 and O_2, the stricter limitation is applied to methanotroph oxidation, and then the limitations are scaled back for the other processes. The competition is designed so that the sinks must not exceed the available concentration over the time step, and if any limitation exists, the sinks must sum to this value. Because the sinks are calculated explicitly while the transport is semi-implicit, negative concentrations can occur after the tridiagonal solution. When this condition occurs for O_2, the concentrations are reset to zero; if it occurs for CH_4, the surface flux is adjusted and the concentration is set to zero if the adjustment is not too large.

19.7.2 CH_4 and O_2 Source Terms

The overall CH_4 net source term consists of production, oxidation at the base of aerenchyma, transport through aerenchyma, methanotrophic oxidation, and ebullition (either to the control volume above the water table if unsaturated or directly to the

atmosphere if saturated). For O_2 below the top control volume, the net source term consists of O_2 losses from methanotrophy, SOM decomposition, and autotrophic respiration, and an O_2 source through aerenchyma.

19.7.3 Aqueous and Gaseous Diffusion

For gaseous diffusion, we adopted the temperature dependence of molecular free-air diffusion coefficients (D_0 (m^2 s^{-1})) as described by Lerman et al. (1979) and applied by Wania et al. (2010) (Table 19.2).

Table 19.2. Temperature dependence of aqueous and gaseous diffusion coefficients for CH_4 and O_2.

D_0 (m^2 s^{-1})	CH_4	O_2
Aqueous	$0.9798 + 0.02986T + 0.0004381T^2$	$1.172 + 0.03443T + 0.0005048T^2$
Gaseous	$0.1875 + 0.0013T$	$0.1759 + 0.0011T$

Gaseous diffusivity in soils also depends on the molecular diffusivity, soil structure, porosity, and organic matter content. Moldrup et al. (2003), using observations across a range of unsaturated mineral soils, showed that the relationship between effective diffusivity (D_e (m^2 s^{-1})) and soil properties can be represented as:

$$D_e = D_0 \theta_a^2 \left(\frac{\theta_a}{\theta_s} \right)^{3/b}, \tag{19.12}$$

where θ_a and θ_s are the air-filled and total (saturated water-filled) porosities (-), respectively, and b is the slope of the water retention curve (-). However, Iiyama and

Hasegawa (2005) have shown that the original Millington-Quirk (Millington and Quirk 1961) relationship matched measurements more closely in unsaturated peat soils:

$$D_e = D_0 \frac{\theta_a^{10/3}}{\theta_s^2} \tag{19.13}$$

In CLM, we applied equation (19.12) for soils with zero organic matter content and equation (19.13) for soils with more than 130 kg m^{-3} organic matter content. A linear interpolation between these two limits is applied for soils with SOM content below 130 kg m^{-3}. For aqueous diffusion in the saturated part of the soil column, we applied (Moldrup et al. 2003):

$$D_e = D_0 \theta_s^2 . \tag{19.14}$$

To simplify the solution, we assumed that gaseous diffusion dominates above the water table interface and aqueous diffusion below the water table interface. Descriptions, baseline values, and dimensions for parameters specific to the CH_4 model are given in Table 19.1. For freezing or frozen soils below the water table, diffusion is limited to the remaining liquid (CLM allows for some freezing point depression), and the diffusion coefficients are scaled by the volume-fraction of liquid. For unsaturated soils, Henry's law equilibrium is assumed at the interface with the water table.

19.7.4 Boundary Conditions

We assume the CH_4 and O_2 surface fluxes can be calculated from an effective conductance and a gaseous concentration gradient between the atmospheric concentration and either the gaseous concentration in the first soil layer (unsaturated soils) or in equilibrium with the water (saturated soil $w\left(C_1^n - C_a\right)$ and $w\left(C_1^{n+1} - C_a\right)$ for the fully explicit and fully implicit cases, respectively (however, see Tang and Riley (2013) for a

more complete representation of this process). Here, w is the surface boundary layer conductance as calculated in the existing CLM surface latent heat calculations. If the top layer is not fully saturated, the $\frac{D_{m1}}{\Delta x_{m1}}$ term is replaced with a series combination: $\left[\frac{1}{w}+\frac{\Delta x_1}{D_1}\right]^{-1}$, and if the top layer is saturated, this term is replaced with $\left[\frac{K_H}{w}+\frac{\frac{1}{2}\Delta x_1}{D_1}\right]^{-1}$, where K_H is the Henry's law equilibrium constant.

When snow is present, a resistance is added to account for diffusion through the snow based on the Millington-Quirk expression (equation (19.13)) and CLM's prediction of the liquid water, ice, and air fractions of each snow layer. When the soil is ponded, the diffusivity is assumed to be that of methane in pure water, and the resistance as the ratio of the ponding depth to diffusivity. The overall conductance is taken as the series combination of surface, snow, and ponding resistances. We assume a zero flux gradient at the bottom of the soil column.

19.7.5 Crank-Nicholson Solution

Equation (19.1) is solved using a Crank-Nicholson solution (Press et al. 1992), which combines fully explicit and implicit representations of the mass balance. The fully explicit decomposition of equation (19.1) can be written as

$$\frac{R_j^{n+1}C_j^{n+1}-R_j^nC_j^n}{\Delta t}=\frac{1}{\Delta x_j}\left[\frac{D_{p1}^n}{\Delta x_{p1}}\left(C_{j+1}^n-C_j^n\right)-\frac{D_{m1}^n}{\Delta x_{m1}}\left(C_j^n-C_{j-1}^n\right)\right]+S_j^n, \qquad (19.15)$$

where j refers to the cell in the vertically discretized soil column (increasing downward), n refers to the current time step, Δt is the time step (s), $p1$ is $j+½$, $m1$ is $j-½$, and S_j^n is the

net source at time step n and position j, i.e., $S_j^n = P(j,n) - E(j,n) - A(j,n) - O(j,n)$. The diffusivity coefficients are calculated as harmonic means of values from the adjacent cells. Equation (19.15) is solved for gaseous and aqueous concentrations above and below the water table, respectively. The R term ensure the total mass balance in both phases is properly accounted for. An analogous relationship can be generated for the fully implicit case by replacing n by $n+1$ on the C and S terms of equation (19.15). Using an average of the fully implicit and fully explicit relationships gives:

$$-\frac{1}{2\Delta x_j}\frac{D_{m1}}{\Delta x_{m1}}C_{j-1}^{n+1} + \left[\frac{R_j^{n+1}}{\Delta t} + \frac{1}{2\Delta x_j}\left(\frac{D_{p1}}{\Delta x_{p1}} + \frac{D_{m1}}{\Delta x_{m1}}\right)\right]C_j^{n+1} - \frac{1}{2\Delta x_j}\frac{D_{p1}}{\Delta x_{p1}}C_{j+1}^{n+1} = \frac{R_j^n}{\Delta t} + \frac{1}{2\Delta x_j}\left[\frac{D_{p1}}{\Delta x_{p1}}\left(C_{j+1}^n - C_j^n\right) - \frac{D_{m1}}{\Delta x_{m1}}\left(C_j^n - C_{j-1}^n\right)\right] + \frac{1}{2}\left[S_j^n + S_j^{n+1}\right], \quad (19.16)$$

Equation (19.16) is solved with a standard tridiagonal solver, i.e.:

$$aC_{j-1}^{n+1} + bC_j^{n+1} + cC_{j+1}^{n+1} = r, \quad (19.17)$$

with coefficients specified in equation (19.16).

Two methane balance checks are performed at each timestep to insure that the diffusion solution and the time-varying aggregation over inundated and non-inundated areas strictly conserves methane molecules (except for production minus consumption) and carbon atoms.

19.7.6 Interface between water table and unsaturated zone

We assume Henry's Law equilibrium at the interface between the saturated and unsaturated zone and constant flux from the soil element below the interface to the center of the soil element above the interface. In this case, the coefficients are the same as described above, except for the soil element above the interface:

$$\frac{D_{p1}}{\Delta x_{p1}} = \left[K_H \frac{\Delta x_j}{2D_j} + \frac{\Delta x_{j+1}}{2D_{j+1}} \right]^{-1}$$

$$b = \left[\frac{R_j^{n+1}}{\Delta t} + \frac{1}{2\Delta x_j} \left(K_H \frac{D_{p1}}{\Delta x_{p1}} + \frac{D_{m1}}{\Delta x_{m1}} \right) \right]$$

$$r = \frac{R_j^n}{\Delta t} C_j^n + \frac{1}{2\Delta x_j} \left[\frac{D_{p1}}{\Delta x_{p1}} \left(C_{j+1}^n - K_H C_j^n \right) - \frac{D_{m1}}{\Delta x_{m1}} \left(C_j^n - C_{j-1}^n \right) \right] + \frac{1}{2} \left[S_j^n + S_j^{n+1} \right] \quad (19.18)$$

and the soil element below the interface:

$$\frac{D_{m1}}{\Delta x_{m1}} = \left[K_H \frac{\Delta x_{j-1}}{2D_{j-1}} + \frac{\Delta x_j}{2D_j} \right]^{-1}$$

$$a = -K_H \frac{1}{2\Delta x_j} \frac{D_{m1}}{\Delta x_{m1}}$$

$$r = \frac{R_j^n}{\Delta t} + C_j^n + \frac{1}{2\Delta x_j} \left[\frac{D_{p1}}{\Delta x_{p1}} \left(C_{j+1}^n - C_j^n \right) - \frac{D_{m1}}{\Delta x_{m1}} \left(C_j^n - K_H C_{j-1}^n \right) \right] + \frac{1}{2} \left[S_j^n + S_j^{n+1} \right] \quad (19.19)$$

19.8 Inundated Fraction Prediction

We developed a simplified dynamic representation of spatial inundation based on recent work by Prigent et al. (2007), who described a multi-satellite approach to estimate the global monthly inundated fraction (F_i) over an equal area grid (0.25°×0.25° at the equator) from 1993 - 2000. They suggested that the IGBP estimate for inundation could be used as a measure of sensitivity of their detection approach at low inundation. We therefore used the sum of their satellite-derived F_i and the constant IGBP estimate when it was less than 10% to perform a simple inversion for the inundated fraction for methane production (f_s). The method optimized three parameters (p_1, p_2, p_3) for each grid cell in a simple model based on simulated water table depth (z_w) and surface runoff (Q_r (mm s^{-1})):

$$f_s = P_1 e^{-z_w / p_2} + p_3 Q_r . \quad (19.20)$$

These parameters were evaluated at the 0.5° resolution, and aggregated for coarser simulations. We expect that ongoing work in the hydrology submodel of CLM will alleviate the need for this crude simplification of inundated fraction in future model versions.

19.9 Seasonal Inundation

We have developed a simplified scaling factor to mimic the impact of seasonal inundation on CH_4 production (see appendix B in Riley et al. (2011a) for a discussion of this simplified expression):

$$S = \frac{\beta\left(f - \overline{f}\right) + \overline{f}}{f}, S \le 1. \quad (19.21)$$

Here, f is the instantaneous inundated fraction, $\overline{f}$ is the annual average inundated fraction (evaluated for the previous calendar year) weighted by heterotrophic respiration, and β is the anoxia factor that relates the fully anoxic decomposition rate to the fully oxygen-unlimited decomposition rate, all other conditions being equal.

20. Crops and Irrigation

20.1 Summary of CLM4.5 updates relative to the CLM4.0

We describe here the complete crop and irrigation parameterizations that appear in CLM4.5. Corresponding information for CLM4.0 appeared on the CLM4.0 web site in a pdf document independent of the CLM4.0 Technical Note (Oleson et al. 2010a). The CLM4.0 crop model description also appeared in Levis et al. (2012).

CLM4.5 includes the following updates to the CROP option, where CROP refers to the interactive crop management model:

- Interactive irrigation
- Interactive fertilization
- Biological nitrogen fixation for soybeans
- Modified C:N ratios for crops
- Nitrogen retranslocation for crops
- Separate reproductive pool

These updates appear in detail in section 20.4. Most also appear in Drewniak et al. (2013).

20.2 The crop model

20.2.1 Introduction

Groups developing Earth System Models generally account for the human footprint on the landscape in simulations of historical and future climates. Traditionally we have represented this footprint with natural vegetation types and particularly grasses because they resemble many common crops. Most modeling efforts have not incorporated more

explicit representations of land management such as crop type, planting, harvesting, tillage, fertilization, and irrigation, because global scale datasets of these factors have lagged behind vegetation mapping. As this begins to change, we increasingly find models that will simulate the biogeophysical and biogeochemical effects not only of natural but also human-managed land cover.

AgroIBIS is a state-of-the-art land surface model with options to simulate dynamic vegetation (Kucharik et al. 2000) and interactive crop management (Kucharik and Brye 2003). The interactive crop management parameterizations from AgroIBIS (March 2003 version) were coupled as a proof-of-concept to the Community Land Model version 3 [CLM3.0, Oleson et al. (2004)] (not published), then coupled to the CLM3.5 (Levis et al. 2009) and later released to the community with CLM4CN (Levis et al. 2012).

With interactive crop management and, therefore, a more accurate representation of agricultural landscapes, we hope to improve the CLM's simulated biogeophysics and biogeochemistry. These advances may improve fully coupled simulations with the Community Earth System Model (CESM), while helping human societies answer questions about changing food, energy, and water resources in response to climate, environmental, land use, and land management change (e.g., Kucharik and Brye 2003; Lobell et al. 2006).

20.2.2 Crop plant functional types

CLM's default list of plant functional types (pfts) includes an unmanaged crop (Table 2.1) treated as a second C3 grass. The unmanaged crop has grid cell coverage assigned from satellite data, as do all natural pfts when CLM's dynamic vegetation model (CNDV; Castillo et al. 2012) is not active.

The new crop pfts used in the CLM get grid cell coverage from the present-day crop dataset of Portmann et al. (2010). We assign these managed crops in the proportions given by Portmann et al. (2010) without exceeding the area previously assigned to the unmanaged crop. The unmanaged crop continues to occupy any of its original area that remains and continues to be handled just by the carbon/nitrogen cycling part of the CLM (i.e., CN). The managed crop types (corn, soybean, and temperate cereals) were chosen based on the availability of corresponding algorithms in AgroIBIS. Temperate cereals include wheat, barley, and rye here. We treat all temperate cereals as summer crops (like spring wheat, for example) at this time. We may introduce winter cereals (such as winter wheat) in a future version of the model.

To allow crops to coexist with natural vegetation in a grid cell and be treated by separate models (i.e., CLM4.5CNcrop versus CLM4.5CNDV), we separate the vegetated land unit into a naturally vegetated land unit and a human managed land unit. Plant functional types in the naturally vegetated land unit share one soil column and compete for water (default CLM setting). Managed crop PFTs in the human managed land unit do not share soil columns and thus permit for differences in land management between crops.

20.2.3 Phenology

CLM4.5CN includes evergreen, seasonally deciduous (responding to changes in day length), and stress deciduous (responding to changes in temperature and/or soil moisture) phenology algorithms (Chapter 14). In CLM4.5CNcrop we have added the AgroIBIS crop phenology algorithm, consisting of three distinct phases.

Phase 1 starts at planting and ends with leaf emergence, phase 2 continues from leaf emergence to the beginning of grain fill, and phase 3 starts from the beginning of grain fill and ends with physiological maturity and harvest.

20.2.3.1 Planting

Corn and temperate cereals must meet the following requirements between April 1st and June 14th for planting in the northern hemisphere (NH):

$$\begin{aligned} &T_{10d} > T_p \\ &T_{10d}^{\min} > T_p^{\min} \\ &GDD_8 \geq GDD_{\min} \end{aligned} \tag{20.1}$$

where T_{10d} is the 10-day running mean of T_{2m}, (the simulated 2-m air temperature at every model time step) and $T_{10d}^{\min}$ is the 10-day running mean of $T_{2m}^{\min}$ (the daily minimum of T_{2m}). T_p and $T_p^{\min}$ are crop-specific coldest planting temperatures (Table 20.1), GDD_8 is the 20-year running mean growing degree-days (units are degree-days or °days) tracked from April through September (NH) base 8°C with maximum daily increments of 30°days (see Eq. (20.3)), and $GDD_{\min}$ is the minimum growing degree day requirement (Table 20.1). Soy must meet the same requirements but between May 1st and June 14th for planting. If the requirements in Eq. (20.1) are not met by June 14th, then corn, soybean, and temperate cereals are still planted on June 15th as long as $GDD_8>0$. In the southern hemisphere (SH) the NH requirements apply 6 months later.

GDD_8 does not change as quickly as T_{10d} and $T_{10d}^{\min}$, so it determines whether the crop can be planted in a grid cell, while the two faster-changing variables determine when the crop may be planted.

At planting, each crop is assigned 1 g leaf C m^{-2} pft column area to be transferred to the leaves upon leaf emergence. An equivalent amount of seed leaf N is assigned given the pft's C to N ratio for leaves (CN_{leaf}). (This differs from AgroIBIS, which uses a seed leaf area index instead of seed C.)

At planting, the model updates the average growing degree-days necessary for the crop to reach vegetative and physiological maturity, GDD_{mat}, according to the following AgroIBIS rules:

$$\begin{aligned} GDD_{\text{mat}}^{\text{corn}} &= 0.85 GDD_8 \quad \text{and} \quad 950 < GDD_{\text{mat}}^{\text{corn}} < 1850°\text{days} \\ GDD_{\text{mat}}^{\text{temp. cereals}} &= GDD_0 \quad \text{and} \quad GDD_{\text{mat}}^{\text{temp. cereals}} < 1700°\text{days} \\ GDD_{\text{mat}}^{\text{soy}} &= GDD_{10} \quad \text{and} \quad GDD_{\text{mat}}^{\text{soy}} < 1700°\text{days} \end{aligned} \tag{20.2}$$

where GDD_{10} is the 20-year running mean growing degree-days tracked from April through September (NH) base 10°C with maximum daily increments of 30°days. Eq. (20.3) shows how we calculate GDD_0, GDD_8, and GDD_{10}:

$$\begin{aligned} GDD_0 &= GDD_0 + T_{2\text{m}} - T_f \quad \text{where} \quad 0 \le T_{2\text{m}} - T_f \le 26°\text{days} \\ GDD_8 &= GDD_8 + T_{2\text{m}} - T_f - 8 \quad \text{where} \quad 0 \le T_{2\text{m}} - T_f - 8 \le 30°\text{days} \\ GDD_{10} &= GDD_{10} + T_{2\text{m}} - T_f - 10 \quad \text{where} \quad 0 \le T_{2\text{m}} - T_f - 10 \le 30°\text{days} \end{aligned} \tag{20.3}$$

where, if $T_{2\text{m}}$ - T_f takes on values outside the above ranges, then it equals the minimum or maximum value in the range. Also T_f equals 273.15 K, $T_{2\text{m}}$ has units of K, and GDD has units of °days.

20.2.3.2 Leaf emergence

According to AgroIBIS, leaves may emerge when the growing degree-days of soil temperature to 0.05 m depth tracked since planting ($GDD_{T_{soi}}$) reaches 3 to 5% of GDD_{mat} (Table 20.1). $GDD_{T_{soi}}$ is base 8, 0, and 10°C for corn, soybean, and temperate cereals. Leaf onset, as defined in the CN part of the model, occurs in the first time step of phase 2,

at which moment all seed C is transferred to leaf C. Subsequently, the leaf area index generally increases and reaches a maximum value during phase 2.

20.2.3.3 Grain fill

Phase 3 begins in a similar way to phase 2. A variable tracked since planting like $GDD_{T_{soi}}$ but for 2-m air temperature, $GDD_{T_{2m}}$, must reach a heat unit threshold, *h*, of 40 to 70% of GDD_{mat} (Table 20.1). For corn the percentage itself is an empirical function of GDD_{mat} (not shown). In phase 3, the leaf area index begins to decline in response to a background litterfall rate calculated as the inverse of leaf longevity for the pft as done in the CN part of the model.

20.2.3.4 Harvest

Harvest is assumed to occur as soon as the crop reaches maturity. When $GDD_{T_{2m}}$ reaches 100% of GDD_{mat} or the number of days past planting reaches a crop-specific maximum (Table 20.1), then the crop is harvested. Harvest occurs in one time step using CN's leaf offset algorithm. New variables track the flow of grain C and N to food and of live stem C and N to litter. Currently, food C and N are routed directly to litter using the labile, cellulose, and lignin fractions for leaves. The same fractions for leaves are used for the flow of live stem C and N to litter for corn, soybean, and temperate cereals. This is in contrast to the approach for unmanaged PFTs which puts live stem C and N to dead stems first, rather than to litter.

20.2.4 Allocation

Allocation responds to the same phases as phenology (section 20.2.3). Simulated C assimilation begins every year upon leaf emergence in phase 2 and ends with harvest at

the end of phase 3; therefore, so does the allocation of such C to the crop's leaf, live stem, fine root, and reproductive pools.

20.2.4.1 Leaf emergence to grain fill

During phase 2, the allocation coefficients (fraction of available C) to each C pool are defined as:

$$
\begin{aligned}
a_{repr} &= 0 \\
a_{froot} &= a^{i}_{froot} - (a^{i}_{froot} - a^{f}_{froot})\frac{GDD_{T_{2m}}}{GDD_{\text{mat}}} \quad \text{where} \quad \frac{GDD_{T_{2m}}}{GDD_{\text{mat}}} \le 1 \\
a_{leaf} &= (1 - a_{froot}) \cdot \frac{a^{i}_{leaf}(e^{-b} - e^{-b\frac{GDD_{T_{2m}}}{h}})}{e^{-b} - 1} \quad \text{where} \quad b = 0.1 \\
a_{livestem} &= 1 - a_{repr} - a_{froot} - a_{leaf}
\end{aligned}
\tag{20.4}
$$

where a^{i}_{leaf}, a^{i}_{froot}, and a^{f}_{froot} are initial and final values of these coefficients (Table 20.2), and h is a heat unit threshold defined in section 20.2.3. At a crop-specific maximum leaf area index, $L_{\max}$ (Table 20.2), carbon allocation is directed exclusively to the fine roots.

20.2.4.2 Grain fill to harvest

The calculation of a_{froot} remains the same from phase 2 to phase 3. Other allocation coefficients change to:

$$
\begin{aligned}
a_{leaf} &= a^{i,3}_{leaf} \quad \text{when} \quad a^{i,3}_{leaf} \le a^{f}_{leaf} \quad \text{else...} \\
a_{leaf} &= a_{leaf}\left(1 - \frac{GDD_{T_{2m}} - h}{GDD_{\text{mat}} d_L - h}\right)^{d^{leaf}_{alloc}} \ge a^{f}_{leaf} \quad \text{where} \quad \frac{GDD_{T_{2m}} - h}{GDD_{\text{mat}} d_L - h} \le 1 \\
a_{livestem} &= a^{i,3}_{livestem} \quad \text{when} \quad a^{i,3}_{livestem} \le a^{f}_{livestem} \quad \text{else...} \\
a_{livestem} &= a_{livestem}\left(1 - \frac{GDD_{T_{2m}} - h}{GDD_{\text{mat}} d_L - h}\right)^{d^{stem}_{alloc}} \ge a^{f}_{livestem} \quad \text{where} \quad \frac{GDD_{T_{2m}} - h}{GDD_{\text{mat}} d_L - h} \le 1 \\
a_{repr} &= 1 - a_{froot} - a_{livestem} - a_{leaf}
\end{aligned}
\tag{20.5}
$$

where $a_{leaf}^{i,3}$ and $a_{livestem}^{i,3}$ (initial values) equal the last a_{leaf} and $a_{livestem}$ calculated in phase 2, d_L, d_{alloc}^{leaf} and d_{alloc}^{stem} are leaf area index and leaf and stem allocation decline factors, and a_{leaf}^{f} and $a_{livestem}^{f}$ are final values of these allocation coefficients (Table 20.2).

20.2.5 General comments

C and N accounting now includes new pools and fluxes pertaining to live stems and reproductive tissues. For example, the calculations of growth respiration, above ground net primary production, litter fall, and displayed vegetation all now account for reproductive C.

We track allocation to reproductive C separately from CN's allocation to other C pools but within the CN framework. CN uses $\frac{a_{root}}{a_{leaf}}$ and $\frac{a_{livestem}}{a_{leaf}}$ to calculate C and N allometry and plant N demand.

Stem area index (S) is equal to $0.1L$ for corn and $0.2L$ for other crops, as in AgroIBIS, where L is the leaf area index. All live C and N pools go to 0 after crop harvest, but the S is kept at 0.25 to simulate a post-harvest "stubble" on the ground.

Crop heights at the top and bottom of the canopy, z_{top} and z_{bot} (m), come from the AgroIBIS formulation:

$$z_{top} = z_{top}^{\max}\left(\frac{L}{L_{\max}-1}\right)^2 \geq 0.05 \text{ where } \frac{L}{L_{\max}-1} \leq 1 \qquad (20.6)$$
$$z_{bot} = 0.02\text{m}$$

The CN part of the model keeps track of a term representing excess maintenance respiration that for perennial pfts or pfts with C storage may be extracted from later gross primary production. Later extraction cannot continue to happen after harvest for annual crops, so at harvest we turn the excess respiration pool into a flux that extracts CO_2

directly from the atmosphere. This way we eliminate any excess maintenance respiration remaining at harvest as if such respiration had not taken place.

In the list of plant physiological and other parameters used by the CLM, we started the managed crops with the existing values assigned to the unmanaged C3 crop. Then we changed the following parameters to distinguish corn, soybean, and temperate cereals from the unmanaged C3 crop and from each other:

- Growth respiration coefficient from 0.30 to the AgroIBIS value of 0.25.
- Fraction of leaf N in the Rubisco enzyme from 0.1 to 0.2 g N Rubisco g^{-1} N leaf for temperate cereals to increase productivity (not chosen based on AgroIBIS).
- Fraction of current photosynthesis displayed as growth changed from 0.5 to 1 (not chosen based on AgroIBIS).
- CLM4.5CN curve for the effect of temperature on photosynthesis instead of crop-specific curves from AgroIBIS.
- Quantum efficiency at 25°C, α, from 0.06 to 0.04 μmol CO_2 μmol^{-1} photon for C4 crops (corn and unmanaged C4 crop), using CLM4.5CN's C4 grass value.
- Slope, *m*, of conductance-to-photosynthesis relationship from 9 to 4 for C4 crops as in AgroIBIS.
- Specific leaf areas, *SLA*, to the AgroIBIS values (Table 20.1).
- Leaf orientation, χ_L, to the AgroIBIS values (Table 20.1).
- Soil moisture photosynthesis limitation factor, β_t, for soybeans multiplied as in AgroIBIS by 1.25 for increased drought tolerance.

Table 20.1. Crop plant functional types (pfts) in CLM4.5CNcrop and their parameters relating to phenology and morphology.

Numbers in the first column correspond to the list of pfts in Table 2.1.

Number and pft corresponding or added to CLM's list of pfts		Phenological Type	T_p K	T_p^{min} K	GDD_{min} ºdays	GDD_{mat} ºdays	Phase 2 $\%GDD_{mat}$	Phase 3 $\%GDD_{mat}$	Harvest: days past planting	z_{top}^{max} m	*SLA* m^2leaf $g^{-1}C$	χ_L index
15.	C_3 unmanaged rainfed crop	Stress Deciduous									0.03	-0.30
16.	C_3 unmanaged irrigated crop	Stress Deciduous									0.03	-0.30
17.	Rainfed Corn (also known as Maize)	Crop/Managed	283.15	279.15	50	950-1850	3	55-65	≤165	2.50	0.05	-0.50
18.	Irrigated Corn (also known as Maize)	Crop/Managed	283.15	279.15	50	950-1850	3	55-65	≤165	2.50	0.05	-0.50
19.	Rainfed Temperate Cereals	Crop/Managed	280.15	272.15	50	≤1700	5	60	≤150	1.20	0.07	0.65
20.	Irrigated Temperate Cereals	Crop/Managed	280.15	272.15	50	≤1700	5	60	≤150	1.20	0.07	0.65
21.	Rainfed Winter cereals (place holder)	Crop/Managed		278.15	50	1900	5	40	≤265	1.20	0.07	0.65
22.	Irrigated Winter cereals (place holder)	Crop/Managed		278.15	50	1900	5	40	≤265	1.20	0.07	0.65
23.	Rainfed Soybean	Crop/Managed	286.15	279.15	50	≤1700	3	70	≤150	0.75	0.07	-0.50
24.	Irrigated Soybean	Crop/Managed	286.15	279.15	50	≤1700	3	70	≤150	0.75	0.07	-0.50

Notes: T_p and T_p^{min} are coldest planting temperatures but for winter cereals T_p^{min} is a warmest planting temperature. GDD_{min} is the lowest (for planting) 20-year running mean growing degree-days base 0ºC (winter cereals) or 8 (other crops) tracked from April to

September (NH). GDD_{mat} is a crop's 20-year running mean growing degree-days needed for vegetative and physiological maturity. Harvest occurs at 100%GDD_{mat} or when the days past planting reach the number in the 10$^{\text{th}}$ column. Crop growth phases are described in the text. $z_{top}^{\max}$ is the maximum top-of-canopy height of a crop, *SLA* is specific leaf area, and leaf orientation index, χ_L, equals -1 for vertical, 0 for random, and 1 for horizontal leaf orientation.

Table 20.2. Crop pfts in CLM4.5CNcrop and their parameters relating to allocation. Numbers in the first column correspond to the list of pfts in Table 2.1.

Number and pft corresponding or added to CLM's list of pfts	Phase 2		Phases 2 and 3		Phase 3				
	a^i_{leaf}	$L_{\max}$	a^i_{froot}	a^f_{froot}	a^f_{leaf}	$a^f_{livestem}$	d_L	d^{stem}_{alloc}	d^{leaf}_{alloc}
	fraction	$m^2\ m^{-2}$	Fraction		Fraction		dimensionless		
17. Rainfed Corn (also referred to as Maize)	0.800	5	0.400	0.050	0.000	0.000	1.05	2	5
18. Irrigated Corn (also referred to as Maize)	0.800	5	0.400	0.050	0.000	0.000	1.05	2	5
19. Rainfed Temperate Cereals	0.750	7	0.300	0.000	0.000	0.050	1.05	1	3
20. Irrigated Temperate Cereals	0.750	7	0.300	0.000	0.000	0.050	1.05	1	3
21. Rainfed Winter cereals (place holder)	0.425	7	0.300	0.000	0.000	0.050	1.05	1	3
22. Irrigated Winter cereals (place holder)	0.425	7	0.300	0.000	0.000	0.050	1.05	1	3
23. Rainfed Soybean	0.850	6	0.500	0.200	0.000	0.300	1.05	5	2
24. Irrigated Soybean	0.850	6	0.500	0.200	0.000	0.300	1.05	5	2

Notes: Crop growth phases and corresponding variables are described in the text

20.3 The irrigation model

The CLM includes the option to irrigate cropland areas that are equipped for irrigation. The application of irrigation responds dynamically to the soil moisture conditions simulated by the CLM. This irrigation algorithm is based loosely on the implementation of Ozdogan et al. (2010).

When irrigation is enabled, the crop areas of each grid cell are divided into irrigated and rainfed fractions according to a dataset of areas equipped for irrigation (Portmann et al. 2010). Irrigated and rainfed crops are placed on separate soil columns, so that irrigation is only applied to the soil beneath irrigated crops.

In irrigated croplands, a check is made once per day to determine whether irrigation is required on that day. This check is made in the first time step after 6 AM local time. Irrigation is required if (1) crop leaf area > 0, and (2) $\beta_t < 1$, i.e., water is limiting for photosynthesis (see section 8.4).

If irrigation is required, the model computes the deficit between the current soil moisture content and a target soil moisture content; this deficit is the amount of water that will be added through irrigation. The target soil moisture content in each soil layer i ($w_{target,i}$, kg m^{-2}) is a weighted average of (1) the minimum soil moisture content that results in no water stress in that layer ($w_{o,i}$, kg m^{-2}) and (2) the soil moisture content at saturation in that layer ($w_{sat,i}$, kg m^{-2}):

$$w_{target,i} = (1-0.7) \cdot w_{o,i} + 0.7 \cdot w_{sat,i} \tag{20.7}$$

$w_{o,i}$ is determined by inverting equation 8.19 in Oleson et al. (2010a) to solve for the value of s_i (soil wetness) that makes $\Psi_i = \Psi_o$ (where Ψ_i is the soil water matric potential and Ψ_o is the soil water potential when stomata are fully open), and then converting this

value to units of kg m^{-2}. $w_{sat,i}$ is calculated simply by converting effective porosity (section 7.4) to units of kg m^{-2}. The value 0.7 was determined empirically, in order to give global, annual irrigation amounts that approximately match observed gross irrigation water use around the year 2000 (i.e., total water withdrawals for irrigation: ~ 2500 – 3000 km^3 $year^{-1}$ (Shiklomanov 2000)). The total water deficit ($w_{deficit}$, kg m^{-2}) of the column is then determined by:

$$w_{deficit} = \sum_i \max\left(w_{target,i} - w_{liq,i}, 0\right) \tag{20.8}$$

where $w_{liq,i}$ (kg m^{-2}) is the current soil water content of layer i (Chapter 7). The max function means that a surplus in one layer cannot make up for a deficit in another layer. The sum is taken only over soil layers that contain roots. In addition, if the temperature of any soil layer is below freezing, then the sum only includes layers above the top-most frozen soil layer.

The amount of water added to this column through irrigation is then equal to $w_{deficit}$. This irrigation is applied at a constant rate over the following four hours. Irrigation water is applied directly to the ground surface, bypassing canopy interception (i.e., added to $q_{grnd,liq}$: section 7.1). Added irrigation is removed from total liquid runoff (R_{liq}: Chapter 11), simulating removal from nearby rivers.

20.4 The details about what is new in CLM4.5

20.4.1 Interactive irrigation for corn, temperate cereals, and soybean

CLM4.0 included interactive irrigation only for the generic C3 crops, i.e. plant functional types (pfts) 15 (rainfed) and 16 (irrigated) in the CLM list of pfts and not for the additional crops of the interactive crop management model (CROP). Irrigation and CROP were mutually exclusive in CLM4.0.

In CLM4.5 we have reversed this situation. Now the irrigation model can be used only while running with CROP. To accomplish this we downloaded data of percent irrigated and percent rainfed corn, soybean, and temperate cereals (wheat, barley, and rye) (Portmann et al. 2010), available online from *ftp://ftp.rz.uni-frankfurt.de/pub/uni-frankfurt/physische_geographie/hydrologie/public/data/MIRCA2000/harvested_area_grids.*

We embedded this data in CLM's high-resolution pft data for use with the tool mksurfdat to generate surface datasets at any desired resolution. Now this data includes percent cover for 24 pfts:

1-16 as in the standard list of pfts, plus six more:

17 corn

18 irrigated_corn

19 spring_temperate_cereal

20 irrigated_spring_temperate_cereal

21 winter_temperate_cereal

22 irrigated_winter_temperate_cereal

23 soybean

24 irrigated_soybean

We intend surface datasets with 24 pfts only for CROP simulations with or without irrigation. In simulations without irrigation, the rainfed and irrigated crops merge into just rainfed crops at run time. Surface datasets with 16 pfts can be used for all other CLM simulations.

20.4.2 Interactive fertilization

CLM adds nitrogen directly to the soil mineral nitrogen pool to meet crop nitrogen demands. CLM's separate crop land unit ensures that natural vegetation will not access the fertilizer applied to crops. Fertilizer amounts are obtained from the Agro-IBIS model (Kucharik and Brye 2003), but can be modified in CLM's pft-physiology input dataset. Fertilizer is reported in g N/m^2 by plant functional type. Total nitrogen fertilizer amounts are 150 g N/m^2 for maize, 80 g N/m^2 for temperate cereals, and 25 g N/m^2 for soybean, representative of central U.S. annual fertilizer application amounts. Since CLM's denitrification rate is high and results in a 50% loss of the unused available nitrogen each day, fertilizer is applied slowly to minimize the loss and maximize plant uptake. Fertilizer application begins during the emergence phase of crop development and continues for 20 days, which helps reduce large losses of nitrogen from leaching and denitrification during the early stage of crop development. The 20-day period is chosen as an optimization to limit fertilizer application to the emergence stage. A fertilizer counter in seconds, f, is set as soon as the onset growth for crops initiates:

$$f = n * 86400 \tag{20.9}$$

where n is set to 20 fertilizer application days. When the crop enters phase 2 (leaf emergence to the beginning of grain fill) of its growth cycle, fertilizer application begins by initializing fertilizer amount to the total fertilizer divided by the initialized f. Fertilizer is applied and f is decremented each time step until a zero balance on the counter is reached.

The crop fertilization scheme was developed in versions of the CLM prior to CLM4.5. In CLM4.5, crops with fertilization may be simulated over productive.

20.4.3 Biological nitrogen fixation for soybeans

Nitrogen fixation by soybeans is similar to that in the SWAT model (Neitsch et al. 2005) and depends on soil moisture, nitrogen availability, and growth stage. Soybean fixation is calculated only for unmet nitrogen demand; if soil nitrogen meets soybean demand, there will be no fixation during the time step. Soybean fixation is determined by

$$N_{fix} = N_{plant\_ndemand} * min\left(1, fxw, fxn\right) * fxg \tag{20.10}$$

where N_{plant_demand} is the balance of nitrogen needed to reach potential growth that cannot be supplied from the soil mineral nitrogen pool, *fxw* is the soil water factor, *fxn* is the soil nitrogen factor, and *fxg* is the growth stage factor calculated by

$$fxw = \frac{wf}{0.85} \tag{20.11}$$

$$fxn = \begin{cases} 0 & \text{for } sminn \le 10 \\ 1.5 - 0.005\left(sminn \times 10\right) & \text{for } 10 < sminn \ \ge 30 \\ 1 & \text{for } sminn > 30 \end{cases} \tag{20.12}$$

$$fxg = \begin{cases} 0 & \text{for } GDD_{T_{2m}} \le 0.15 \\ 6.67 \times GDD_{T_{2m}} - 1 & \text{for } 0.15 < GDD_{T_{2m}} \ge 0.30 \\ 1 & \text{for } 0.30 < GDD_{T_{2m}} \ge 0.55 \\ 3.75 - 5 \times GDD_{T_{2m}} & \text{for } 0.55 < GDD_{T_{2m}} \ge 0.75 \\ 0 & \text{for } GDD_{T_{2m}} > 0.75 \end{cases} \tag{20.13}$$

where *wf* is the soil water content as a fraction of the water holding capacity for the top 0.05 m, *sminn* is the total nitrogen in the soil pool (g/m^2), and $GDD_{T_{2m}}$ is the fraction of growing degree-days accumulated during the growing season. N_{fix} is added directly to the soil mineral nitrogen pool for use that time step. Nitrogen fixation occurs after the plant has accumulated 15%GDD_{mat} and before 75%GDD_{mat}, so before grain fill begins.

20.4.4 Modified C:N ratios for crops

Typically, C:N ratios in plant tissue vary throughout the growing season and tend to be lower during early growth stages and higher in later growth stages. In order to account for this change, two sets of C:N ratios are established in CLM for the leaf, stem, and fine root of crops. This modified C:N ratio approach accounts for the nitrogen retranslocation that occurs during phase 3 of crop growth. Leaf and stem (and root for temperate cereals) C:N ratios for phases 1 and 2 are lower than measurements (Table 20.3) to allow excess nitrogen storage in plant tissue. During grain fill (phase 3) of the crop growth cycle, the nitrogen in the plant tissues is moved to a storage pool to fulfill nitrogen demands of organ (reproductive pool) development, such that the resulting C:N ratio of the plant tissue is reflective of measurements at harvest. All C:N ratios were determined by calibration process, through comparisons of model output versus observations of plant carbon throughout the growth season.

20.4.5 Nitrogen retranslocation for crops

Nitrogen retranslocation in crops occurs when nitrogen that was used for tissue growth of leaves, stems, and fine roots during the early growth season is remobilized and used for grain development (Pollmer et al. 1979; Crawford et al. 1982; Simpson et al. 1983; Ta and Weiland 1992; Barbottin et al. 2005; Gallais et al. 2006, 2007). Nitrogen allocation for crops follows that of natural vegetation, is supplied in CLM by the soil mineral nitrogen pool, and depends on C:N ratios for leaves, stems, roots, and organs. Nitrogen demand during organ development is fulfilled through retranslocation from leaves, stems, and roots. Nitrogen retranslocation is initiated at the beginning of the grain fill stage for corn and temperate cereals, but not until after LAI decline in soybean. Nitrogen stored in the leaf and stem is moved into a storage retranslocation pool. For

temperate cereals, nitrogen in roots is also released into the retranslocation storage pool. The quantity of nitrogen mobilized depends on the C:N ratio of the plant tissue, and is calculated as

$$leaf\_to\_retransn = \frac{c_{leaf}}{CN_{leaf}} - \frac{c_{leaf}}{CN_{leaf}^{f}} \tag{20.14}$$

$$stemn\_to\_retransn = \frac{c_{stem}}{CN_{stem}} - \frac{c_{stem}}{CN_{stem}^{f}} \tag{20.15}$$

$$frootn\_to\_retransn = \frac{c_{froot}}{CN_{froot}} - \frac{c_{froot}}{CN_{froot}^{f}} \tag{20.16}$$

where C_{leaf}, C_{stem}, and C_{froot} is the carbon in the plant leaf, stem, and fine root, respectively, CN_{leaf}, CN_{stem}, and CN_{froot} is the pre-grain fill C:N ratio of the leaf, stem, and fine root respectively, and CN_{leaf}^{f}, CN_{stem}^{f}, and CN_{froot}^{f} is the post-grain fill C:N ratio of the leaf, stem, and fine root respectively (Table 20.3). Since C:N measurements are taken from mature crops, pre-grain development C:N ratios for leaves, stems, and roots are optimized to allow maximum nitrogen accumulation for later use during organ development. Post-grain fill C:N ratios are assigned the same as crop residue. Once excess nitrogen is moved into the retranslocated pool, during the remainder of the growing season the retranslocated pool is used first to meet plant nitrogen demand by assigning the available nitrogen from the retranslocated pool equal to the plant nitrogen demand. Once the retranslocation pool is depleted, soil mineral nitrogen pool is used to fulfill plant nitrogen demands.

Table 20.3. Pre- and post-grain fill C:N ratios for crop leaf, stem, fine root, and reproductive pools.

Pre-grain fill stage	Corn	Temperate Cereals	Soybean
CN_{leaf}	10	15	25
CN_{stem}	50	50	50
CN_{froot}	42	30	42
Post-grain fill stage			
CN^{f}_{leaf}	65	65	65
CN^{f}_{stem}	120	100	130
CN^{f}_{froot}	42	40	42
CN^{f}_{repr}	50	40	60

20.4.6 Separate reproductive pool

One notable difference between natural vegetation and crops is the presence of a reproductive carbon pool (and nitrogen pool). Accounting for the reproductive pool helps determine whether crops are performing reasonably, through yield calculations, seasonal GPP and NEE changes, etc. The reproductive pool is maintained similarly to the leaf, stem, and fine root pools, but allocation of carbon and nitrogen does not begin until the grain fill stage of crop development. Eq. (20.5) shows the carbon and nitrogen allocation coefficients to the reproductive pool. In the CLM4.0, allocation of carbon to the reproductive pool was calculated but merged with the stem pool. In the model, as

allocation declines during the grain fill stage of growth, increasing amounts of carbon and nitrogen are available for grain development.

21. Transient Landcover Change

CLM includes a treatment of mass and energy fluxes associated with prescribed temporal change in land cover. Using an annual time series of the spatial distribution of PFTs and wood harvest, CLM diagnoses the change in area for PFTs at each model time step and then performs mass and energy balance accounting necessary to represent the expansion and contraction of PFT area. This implementation currently only pertains to the case where all PFTs for a particular grid cell coexist on a single soil/snow column. In this case, the only biogeophysical state variable affected is canopy water (W_{can}). The biogeochemical impacts of land use and land cover change are simulated through changes in CLM carbon pools and fluxes as shown in Figure 21.1 and described further in Chapter 13. Other implementations are possible, such as changing the area of soil/snow columns or land unit area, however these require additional consideration of conservation of mass and energy among the soil/snow columns and land units which will be implemented in future versions of CLM.

21.1 Annual Transient Land Cover Data and Time Interpolation

The changes in area over time associated with individual PFTs are prescribed through a forcing dataset, referred to here as the *dynpft* dataset. The *dynpft* dataset consists of an annual time series of global grids, where each annual time slice describes the fractional area occupied by all PFTs and the annual wood harvest within each grid cell. Changes in area and wood harvest for each PFT within a grid cell at each model time step are inferred from a time-interpolation of the area information for the PFT from the two bracketing annual time slices in the *dynpft* dataset.

As a special case, when the time dimension of the *dynpft* dataset starts at a later year than the current model time step, the first time slice from the *dynpft* dataset is used to represent the current time step PFT fractional area distributions. Similarly, when the time dimension of the *dynpft* dataset stops at an earlier year than the current model time step, the last time slice of the *dynpft* dataset is used. Thus, the simulation will have invariant representations of PFT distributions through time for the periods prior to and following the time duration of the *dynpft* dataset, with transient PFT distributions during the period covered by the *dynpft* dataset.

The following equations capture this logic, where $year_{cur}$ is the calendar year for the current timestep, $dynpft\_year(1)$ and $dynpft\_year(nyears)$ are the first and last calendar years in the *dynpft* dataset, respectively, $nyears$ is the number of years in the *dynpft* dataset, nt_1 and nt_2 are the two bracketing years used in the interpolation algorithm, and n is the index value for the $dynpft\_year$ array corresponding to $dynpft\_year(n) = year_{cur}$:

$$nt_1 = \begin{cases} 1 & \text{for} \quad year_{cur} < dynpft\_year(1) \\ n & \text{for} \quad dynpft\_year(1) \le year_{cur} < dynpft\_year(nyears) \\ nyears & \text{for} \quad year_{cur} \ge dynpft\_year(nyears) \end{cases} \quad (21.1)$$

$$nt_2 = \begin{cases} 1 & \text{for} \quad year_{cur} < dynpft\_year(1) \\ n+1 & \text{for} \quad dynpft\_year(1) \le year_{cur} < dynpft\_year(nyears) \\ nyears & \text{for} \quad year_{cur} \ge dynpft\_year(nyears) \end{cases} \quad (21.2)$$

Interpolation of PFT weights between annual time slices in the *dynpft* dataset uses a simple linear algorithm, based on the conversion of the current time step information into a floating-point value for the number of calendar days since January 1 of the current model year ($cday$). The interpolation weight for the current time step tw_{cday} is

$$tw_{cday} = \frac{366 - cday}{365} \tag{21.3}$$

where the numerator is 366 instead of 365 because the time manager function for CLM returns a value of $cday = 1.0$ for midnight Greenwich mean time on January 1. With weights $w_p(nt_1)$ and $w_p(nt_2)$ obtained from the *dynpft* dataset for PFT *p* at the bracketing annual time slices nt_1 and nt_2, the interpolated PFT weight for the current time step ($w_{p,t}$) is

$$w_{p,t} = tw_{cday}\left[w_p\left(nt_1\right) - w_p\left(nt_2\right)\right] + w_p\left(nt_2\right) \tag{21.4}$$

The form of this equation is designed to improve roundoff accuracy performance, and guarantees $w_{p,t}$ stays in the range [0,1]. Note that values for $w_p(nt_1)$, $w_p(nt_2)$, and $w_{p,t}$ are fractional weights at the column level of the subgrid hierarchy.

The change in weight for a PFT between the current and previous time steps (Δw_p) is

$$\Delta w_p = w_p^n - w_p^{n-1} \tag{21.5}$$

where *n* denotes the current time step. The area of a given PFT increases for $\Delta w_p > 0$ and decreases for $\Delta w_p < 0$.

21.2 Mass and Energy Conservation

Mass conservation is maintained across a PFT weight transition by summing up all the water state variables to get the total vegetated land unit water content before ($W_{tot,1}$) and after ($W_{tot,2}$) new PFT weights are calculated. For example, $W_{tot,1}$ is

$$W_{tot,1} = W_a + W_{sno} + \sum_{i=1}^{N_{levgrnd}}\left(w_{liq,i} + w_{ice,i}\right) + \sum_{j=1}^{npft}\left(W_{can,j} wt_{j,1}\right) \tag{21.6}$$

where W_a is the aquifer water, W_{sno} is the snow water, $w_{liq,i}$ and $w_{ice,i}$ are the liquid and ice soil water contents, $W_{can,j}$ is the canopy water content for PFT j, and $wt_{j,1}$ is the PFT weight for PFT j. For the situation where only PFT weights are changing and all other land unit fractions are constant, any difference between $W_{tot,1}$ and $W_{tot,2}$ can only be due to differences in the total canopy water before and after the PFT weight change. To ensure water conservation, the typically very small difference between $W_{tot,2}$ and $W_{tot,1}$ is subtracted from the grid cell runoff

$$R_{liq} = R_{liq} + W_{tot,2} - W_{tot,1}. \quad (21.7)$$

Total energy is unperturbed in this case and therefore an energy conservation treatment is not required. As noted above, other implementations are possible and will be desirable in the future, such as changing the area of soil/snow columns or land unit area, for example in a situation in which crops are implemented on a separate soil column. These would require additional consideration of conservation of mass and energy among the soil/snow columns and land units.

21.3 Annual Transient Land Cover Dataset Development

This section describes the development of the d*ynpft* dataset. Development of this dataset requires adapting for use with the CLM a harmonized dataset of land cover change for the historical period and for different representations of the scenario period.

21.3.1 UNH Transient Land Use and Land Cover Change Dataset

To coordinate the processing and consistency of land use and land cover change data between the historical period (1850-2005) and the four IPCC representative concentration pathways (RCPs) derived from integrated assessment models (IAM), the

University of New Hampshire (UNH) research group (Louise Chini, George Hurtt, Steve Frolking; luh.unh.edu) produced a harmonized transient dataset for use in climate change simulations. The historical component of the transient land use and land cover change dataset is Version 1 of the Land-Use History A product (LUHa.v1) covering the period 1850-2005. The RCP transient land use and land cover change components (2005-2100) are referred to as the Future Land-Use Harmonization A products. Version 1 (LUHa.v1_future.v1) is used for the AIM, MESSAGE, and MiniCAM IAMs; Version 1.1 (LUHa.v1_future.v1.1) is used for the IMAGE IAM. The land cover information is provided at 0.5 degree grid resolution and includes fractional grid cell coverage by crops, pasture, and primary and secondary natural vegetation.

The crop fraction of the grid cell represents the area of the grid cell used to grow any type of crop. Similarly, pasture represents the fraction of a grid cell used for grazing livestock. The remaining area in a half degree grid cell is partitioned into primary and secondary vegetation. Primary vegetation represents the fractional area of a grid cell with vegetation undisturbed by human activities. Secondary vegetation represents vegetated areas that have recovered from some human disturbance; this could include re-vegetation of pasture and crop areas as well as primary vegetation areas that have been logged.

The UNH dataset provides a transition matrix that describes the annual fraction of land that is transformed from one category to another (e.g. primary land to crop, pasture to crop, etc.; Hurtt et al. 2006). Included in these transitions is the conversion of secondary land to secondary land, representing the logging on land recovering from an earlier disturbance. These transitions provide information on all changes in land cover through the sum of all transitions in a given year. Harmonized prescriptions of CMIP5

wood harvest statistics also are provided by (Hurtt et al. 2011) for the historical and RCP time series. The wood harvest is prescribed spatially on the same 0.5 degree grid as the land use class transitions for each year.

To ensure consistency with the various land use classes wood harvest is prescribed as both the area of land harvested and the amount of carbon extracted in the grid cell for a particular year. To account for the differences in standing amount of wood carbon as well as the differences in harvest intensity associated with the different land units, the harvest area and carbon amounts are prescribed for the five classes of: Primary Forest, Primary Non-Forest, Secondary Mature Forest, Secondary Young Forest, and Secondary Non-Forest.

21.3.2 Representing Land Use and Land Cover Change in CLM

CLM represents the land surface as a hierarchy of sub-grid types: glacier; lake; wetland; urban; and vegetated land. The vegetated land is further divided into a mosaic of PFTs. To represent the UNH transient land use and land cover change dataset in CLM, the annual fractional composition of crop, pasture, primary vegetation, and secondary vegetation land units specified in the UNH dataset needs to be faithfully represented with a corresponding PFT mosaic in CLM using the methods described in Lawrence et al (2012). This method translated each of the UNH land units into fractional PFT values based on current day and potential vegetation CLM land surface parameters for that grid cell and for that year, as shown in Figure 21.2.

The methodology for creating the transient PFT dataset is based on four steps which are applied across the time series. First, crop PFT composition is directly specified from the crop land unit fractional area. Second, pasture PFTs are assigned based on grass

PFTs found in the potential vegetation and current day CLM land surface parameters scaled by the area of pasture. Third, potential vegetation PFTs are assigned to the grid cell scaled by the fractional area of the primary land unit. Last, current day non-crop and non-pasture PFTs are assigned to the grid cell scaled by the fractional area of the secondary land unit. The annual tree harvest values also are calculated from the harvest information of the UNH dataset used in conjunction with transient tree PFT values. Separate datasets representing the extent of water, wetland, ice and urban land cover are used to compile the final land cover present in each CLM grid cell. These additional non-vegetated land cover fractions are held constant throughout the time series. All datasets are resolved at the half degree grid resolution.

21.3.3 Present Day PFT Dataset

The present day dataset is based on the methodology of Lawrence and Chase (2007) and uses a variety of satellite products to develop present day PFT distributions with matching leaf area index values. The dataset initially derives fractions of bare ground and tree cover from the Moderate Resolution Imaging Spectroradiometer (MODIS) vegetation continuous fields product (Hansen et al. 2003). To further distinguish tree types, the tree fraction is divided into broadleaf/needleleaf and evergreen/deciduous types based on the Advanced Very High Resolution Radiometer (AVHRR) continuous fields tree cover (DeFries et al. 2000). The remaining grid cell area is assumed to be herbaceous grasses and shrubs, including crops. The area of crop is initially determined from Ramankutty et al. (2008) circa 2000 global crop land areas, and the remaining grass and shrub fractions are derived from the MODIS land cover (Friedl et al. 2002). Further subdivisions of grass, shrub and tree PFTs into tropical, temperate and

boreal types were based on the physiology and climate rules from Nemani and Running (1996), and for C3/C4 photosynthetic pathways based on MODIS derived leaf area index values and the mapping methods of Still et al. (2003). In contrast to Lawrence and Chase (2007), the understory grasses of forested areas have been replaced with trees for the dataset. Some advantages of this dataset are that it reproduces the physical properties as observed by the MODIS land surface data (e.g. grid cell albedo and leaf area index values) while maintaining the multiple PFT representation.

21.3.4 Potential PFT Distribution

Essential to any reconstruction of past vegetation distributions is the need to know the potential vegetation that would be there prior to human activities. Many researchers have worked to estimate potential vegetation types at regional and global scales from remnant vegetation and other field data or from bioclimatic models. The CLM potential PFT distribution is derived from Ramankutty et al. (2008) at 5 arc-minute resolution. However, this product is based on a biome type classification system that is not directly compatible with the CLM PFT distributions.

The CLM potential vegetation is described by Lawrence and Chase (2010). This reconstruction describes potential PFT distributions extrapolated from the current day PFT composition of remnant natural biomes as mapped by Ramankutty et al. (2008). The current day remnant natural PFT parameters were taken from the Lawrence and Chase (2007) dataset with the same forest understory changes as described above to ensure consistency between the two datasets. The current day remnant natural PFT biome compositions were spatially extrapolated to the potential vegetation biome distributions provided by Ramankutty et al. (2008) using inverse distance weighted methods. The

resulting product is a CLM PFT distribution that may have existed prior to human disturbance under current day climate conditions.

21.3.5 Transient Land Cover Change Dataset

For each year from 1850 to 2005 and to 2100 for each of the four RCPs, PFT distributions and wood harvest are adjusted based on the UNH dataset. Initially the grid cell is checked to adjust the crop area based on the UNH crop area. If the crop area exceeds the available land area (i.e. the grid cell area minus the area assigned to glacier, wetlands, lake and urban areas) then all the available area is allocated to crops and no other PFTs are added. After the crop area is assigned, any remaining area is considered available for pasture.

As the pasture data from the UNH dataset represents grazing, pasture areas are assigned in the present day based on the availability of grasses (C3, C4 and boreal C3 PFTs) and shrubs relative to the bare soil fraction. If the grazing area exceeds the total vegetated area from both the potential and current day PFT data, then the grazed area is limited to the larger of the potential or current day vegetated area. This is done to prevent representing sparsely vegetated grazing areas as 100% vegetated pastures. Once the grazing area is less than or equal to the total vegetated area, then grazing areas are assigned to the C3 and C4 grass areas based on their potential vegetation and current day fractions. In areas where the grazing area cannot be met through the current day or potential vegetation grass fraction alone, the current day tree PFTs are converted to grass PFTs, with the remaining shrub PFTs included as being grazed.

Once crop and pasture areas are assigned to a grid cell, the remaining area is assigned to primary and secondary natural vegetation. Primary vegetation is assumed to

be undisturbed and reflects the potential vegetation PFT distributions. In the secondary region, the PFT distributions are based on the current day non-crop and non-pasture PFTs in the grid cell. This process ensures that the PFT distributions are kept consistent with the original current day and potential vegetation CLM parameters, while remaining faithful to the UNH assigned areas.

21.3.6 Forest Harvest Dataset Changes

Discussions following the initial analysis of CCSM4 land cover change experiments found there were very high wood harvest areas compared to wood harvest carbon in the RCP 6.0 and RCP 8.5 time series. The high wood harvest areas were traced to using gridded spatially explicit wood harvest targets from the MESSAGE and AIM groups for these two time series, rather than using regional targets with spatial downscaling in GLM as done with the other three time periods. As a result of these discussions new amended wood harvest targets were generated with regional targets through GLM for the RCP 6.0 and RCP 8.5 time series as described in Lawrence et al. (2012).

Figure 21.1. Schematic of land cover change impacts on CLM carbon pools and fluxes.

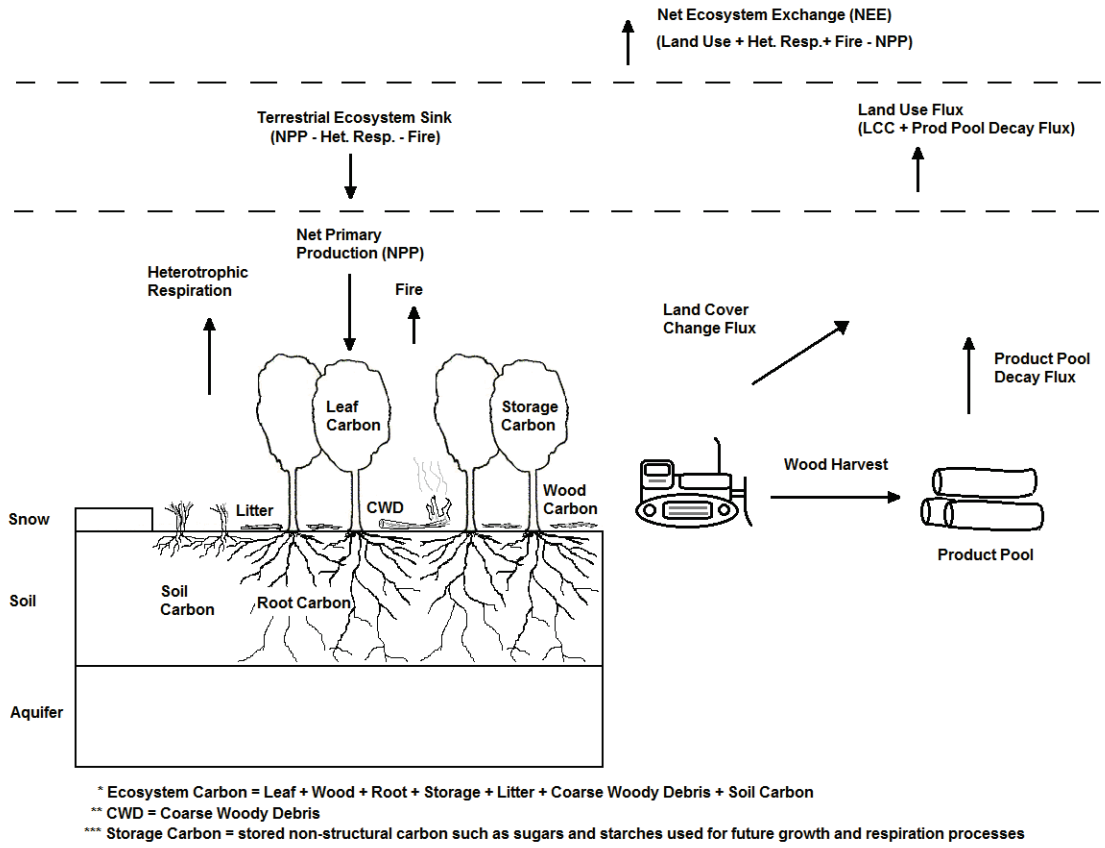

Figure 21.2. Schematic of translation of annual UNH land units to CLM4 plant functional types.

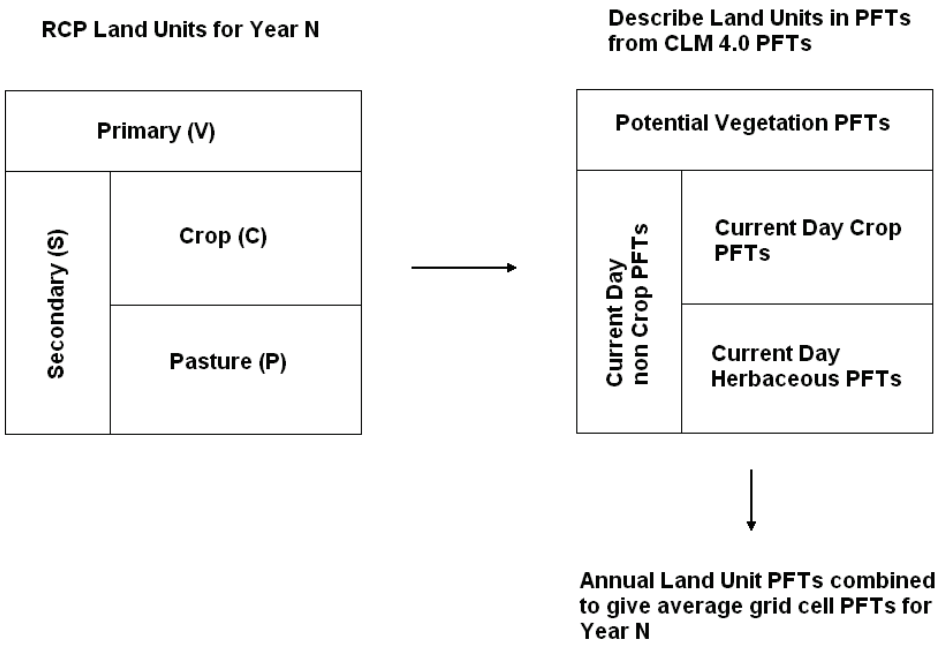

22. Dynamic Global Vegetation Model

In CLM the user may choose to run the CN model as a dgvm (dynamic global vegetation model) (CNDV). Note that CN must be active to run the dgvm in CLM. In this section, a general description of the dgvm processes and how they integrate with CN are provided. Further details are available in the CLM3DGVM Technical Note (Levis et al. 2004). The focus here is on the differences relative to the corresponding processes in the CLM3DGVM.

As with the CLM3DGVM, CNDV can simulate biogeographical changes only for natural vegetation. Although the vegetated land unit may be separated into naturally vegetated and human managed land units to permit a coexistence of natural and human managed vegetation, CNDV only works if the human managed land units are fixed. CLM's transient land cover and land use change capability (see Chapter 21), which permits transitions between natural and human managed plant functional types (PFTs), is incompatible with the CNDV option at this time.

CNDV was implemented by introducing CLM3DGVM code to the hourly CN framework only to the extent necessary to simulate annual biogeography updates. This includes the annual processes of light competition, establishment, and survival [see sections 2.7 and 2.10, Levis et al. (2004)] as they pertain to the calculations of PFT cover (FPC) and population (P) but not processes related to carbon pools, leaf area index (LAI), or canopy height. In CNDV we added complexity to the gap mortality calculation with annual heat stress and growth efficiency considerations from the corresponding CLM3DGVM algorithm [section 2.8, Levis et al. (2004)]. All other ecosystem processes

(allocation, phenology, fire, etc.) are handled by CN modules. Unlike in the CLM3DGVM, in CNDV, annual biogeography updates are interpolated to hourly intervals.

22.1 Establishment and survival

The PFT distribution in the vegetated land unit is typically prescribed in CLM (see section 2.1.2) except for the case when CNDV is active. In CNDV the model begins with no PFT information per grid cell and evaluates whether or not a PFT may establish or survive according to the PFT's bioclimatic limits (Table 22.1). Shrub PFTs are treated as trees at establishment.

CNDV omits the CLM3DGVM's annual introduction of saplings when a PFT can establish. The CLM3DGVM merged sapling carbon pools with a PFT's existing carbon. The resultant leaf carbon (annual maximum value) would update the FPC, i.e. the foliar projective cover or fraction of the vegetated land unit occupied by the PFT [section 2.10, Levis et al. (2004)]. Instead, CNDV updates the FPC using the PFT's annual maximum leaf carbon without an addition from saplings. For newly established PFTs, CNDV assigns seed leaf carbon equal to 1 g C m^{-2} of land unit area and seed FPC equal to 0.05 for grasses and 0.000844 for trees (values determined from CLM3DGVM simulations). The addition of establishing individuals to *P*, a PFT's population, is handled as in the CLM3DGVM.

FPC changes annually as in the CLM3DGVM but now is interpolated to an hourly increment using the algorithms designed to conserve energy and mass in the CLM's dynamic land use option.

22.2 Light competition

In CNDV's order of annual processes, light competition is invoked before establishment and survival. However, light competition does not affect a simulation starting from bare ground until the vegetation fills the land unit (a few years at least).

Light competition starts with a calculation updating *FPC*. For reference, this update was included at the end of allocation in the CLM3DGVM [section 2.6, Levis et al. (2004)].

Due to their height advantage, trees will cover up to 95% of the land unit when their productivity permits, as in the CLM3DGVM, regardless of grass and shrub productivity. Grasses get second priority, as in the CLM3DGVM, even with shrubs included now. Shrubs, then, have access to the remaining space and follow the tree algorithm for self thinning [section 2.7, Levis et al. (2004)]. As a result, trees typically dominate in the most productive regions, grasses in less productive regions, and shrubs in the least productive non-desert regions (Zeng et al. 2008).

22.3 CN processes modified for the CNDV coupling

Gap mortality and mortality from fire: Constant annual mortality rate of 0.02 is changed for trees and shrubs to an annual rate calculated as in the CLM3DGVM accounting for background and stress mortality [section 2.8, Levis et al. (2004)]. The CN module converts the annual rate to hourly.

The CLM3DGVM used the concepts of average plant individual and PFT population, *P*. CNDV retains these concepts in the light competition, establishment, and survival calculations. In CNDV we account for the individuals removed hourly from *P* in response to CN's fire and gap mortality, while the carbon pools per individual and FPC remain constant. Ultimately, *P* updates should only affect the annual processes of light

competition, establishment, and survival, so the *P* update may be moved to the end of the year in a future version of CNDV.

Vegetation Structure Update: CN stocking is a constant, while in CNDV stocking changes as P and FPC change. This affects the top-of-canopy height calculation. CN specific leaf area and stem diameter calculations are kept, while the height calculation is replaced with the CLM3DGVM's [section 2.6, Levis et al. (2004)]. CN stem area index (SAI) is kept.

Allocation: CN calculates a PFT's fraction of currently allocated carbon relative to the total allocation instead of obtaining a constant value from CLM's PFT-physiology file. In CNDV, we returned to the constant values in the old PFT-physiology file to get a reasonable simulation of PFTs. For CNDV to use the calculated fraction, we will need to change the algorithm for PFTs in early stages of growth.

Table 22.1. Plant functional type (PFT) biogeography rules with respect to climate. Adapted from Table 1 of Levis et al. (2004) to include shrub PFTs. $T_{c,\min}$, coldest minimum monthly air temperature for survival of previously established PFTs; $T_{c,\max}$, warmest minimum monthly air temperature for establishment of new PFTs; $GDD_{\min}$, minimum annual growing degree-days above 5°C for establishment of new PFTs. Levis et al. (2004) include an explanation of these variables and their use.

PFT and PFT number corresponding to the list of PFTs in Table 2.1		Survival	Establishment	
		$T_{c,\min}$ (°C)	$T_{c,\max}$ (°C)	$GDD_{\min}$
Tropical broadleaf evergreen tree (BET)	(4)	15.5	No limit	0
Tropical broadleaf deciduous tree (BDT)	(6)	15.5	No limit	0
Temperate needleleaf evergreen tree (NET)	(1)	-2.0	22.0	900
Temperate broadleaf evergreen tree (BET)	(5)	3.0	18.8	1200
Temperate broadleaf deciduous tree (BDT)	(7)	-17.0	15.5	1200
Boreal needleleaf evergreen tree (NET)	(2)	-32.5	-2.0	600
Boreal deciduous tree	(8)	No limit	-2.0	350
Temperate broadleaf deciduous shrub (BDS)	(10)	-17.0	No limit	1200
Boreal broadleaf deciduous shrub (BDS)	(11)	No limit	-2.0	350
C_4	(14)	15.5	No limit	0
C_3	(13)	-17.0	15.5	0
C_3 arctic	(12)	No limit	-17.0	0

23. Biogenic Volatile Organic Compounds (BVOCs)

This chapter briefly describes the biogenic volatile organic compound (BVOC) emissions model implemented in CLM. The CLM3 version (Levis et al. 2003; Oleson et al. 2004) was based on Guenther et al. (1995). Heald et al. (2008) updated this scheme in CLM4 based on Guenther et al. (2006). The current version in CLM4.5 is based on MEGAN2.1 discussed in detail in Guenther et al. (2012). This update of MEGAN incorporates four main features: (1) expansion to 147 chemical compounds (2) the treatment of the light-dependent fraction (LDF) for each compound (3) inclusion of the inhibition of isoprene emission by atmospheric CO_2 and (4) emission factors mapped to the specific PFTs of the CLM.

MEGAN2.1 now describes the emissions of speciated monoterpenes, sesquiterpenes, oxygenated VOC as well as isoprene. A flexible scheme has been implemented in the CLM to specify a subset of emissions. This allows for additional flexibility in grouping chemical compounds to form the lumped species frequently used in atmospheric chemistry. The mapping or grouping are therefore defined through a namelist parameter in drv_flds_in, e.g. megan_specifier = 'ISOP = isoprene', 'BIGALK = pentane + hexane + heptane + tricyclene'.

Terrestrial BVOC emissions from plants to the atmosphere are expressed as a flux, F_i (μg C m^{-2} ground area h^{-1}), for emission of chemical compound i

$$F_i = \gamma_i \rho \sum_j \varepsilon_{i,j} \left(wt \right)_j \tag{23.1}$$

where γ_i is the emission activity factor accounting for responses to meteorological and phenological conditions, ρ is the canopy loss and production factor also known as

escape efficiency (set to 1), and $\varepsilon_{i,j}$ (μg C m^{-2} ground area h^{-1}) is the emission factor at standard conditions of light, temperature, and leaf area for plant functional type *j* with fractional coverage $(wt)_j$ (Guenther et al. 2012). The emission activity factor γ_i depends on plant functional type, temperature, LAI, leaf age, and soil moisture (Guenther et al. 2012). For isoprene only, the effect of CO_2 inhibition is now included as described by Heald et al. (2009). Previously, only isoprene was treated as a light-dependent emission. In MEGAN2.1, each chemical compound is assigned a LDF (ranging from 1.0 for isoprene to 0.2 for some monoterpenes, VOCs and acetone). The activity factor for the light response of emissions is therefore estimated as:

$$\gamma_{P,i} = (1 - LDF_i) + \gamma_{P\_LDF} LDF_i \tag{23.2}$$

where the LDF activity factor (γ_{P_LDF}) is specified as a function of PAR as in previous versions of MEGAN.

The values for each emission factor $\varepsilon_{i,j}$ are now available for each of the 15 plant functional types in the CLM and each chemical compound. This information is distributed through an external file, allowing for more frequent and easier updates.

24. Dust Model

Atmospheric dust is mobilized from the land by wind in the CLM. The most important factors determining soil erodibility and dust emission include the wind friction speed, the vegetation cover, and the soil moisture. The CLM dust mobilization scheme (Mahowald et al. 2006) accounts for these factors based on the DEAD (Dust Entrainment and Deposition) model of Zender et al. (2003). Please refer to the Zender et al. (2003) article for additional information regarding the equations presented in this section.

The total vertical mass flux of dust, F_j (kg m^{-2} s^{-1}), from the ground into transport bin j is given by

$$F_j = TSf_m \alpha Q_s \sum_{i=1}^{I} M_{i,j} \tag{24.1}$$

where T is a global factor that compensates for the DEAD model's sensitivity to horizontal and temporal resolution and equals 5 x 10^{-4} in the CLM instead of 7 x 10^{-4} in Zender et al. (2003). S is the source erodibility factor set to 1 in the CLM and serves as a place holder at this time.

The grid cell fraction of exposed bare soil suitable for dust mobilization f_m is given by

$$f_m = \left(1 - f_{lake} - f_{wetl}\right)\left(1 - f_{sno}\right)\left(1 - f_v\right)\frac{w_{liq,1}}{w_{liq,1} + w_{ice,1}} \tag{24.2}$$

where f_{lake} and f_{wetl} and f_{sno} are the CLM grid cell fractions of lake and wetland (section 2.2.3) and snow cover (section 7.2.1), all ranging from zero to one. Not mentioned by Zender et al. (2003), $w_{liq,1}$ and $w_{ice,1}$ are the CLM top soil layer liquid water

and ice contents (mm) entered as a ratio expressing the decreasing ability of dust to mobilize from increasingly frozen soil. The grid cell fraction of vegetation cover, f_v, is defined as

$$0 \le f_v = \frac{L+S}{(L+S)_t} \le 1 \quad \text{where } (L+S)_t = 0.3 \text{ m}^2\text{m}^{-2} \tag{24.3}$$

where equation (24.3) applies only for dust mobilization and is not related to the plant functional type fractions prescribed from the CLM input data or simulated by the CLM dynamic vegetation model (Chapter 22). L and S are the CLM leaf and stem area index values (m^2 m^{-2}) averaged at the land unit level so as to include all the pfts and the bare ground present in a vegetated land unit. L and S may be prescribed from the CLM input data (section 2.1.4) or simulated by the CLM biogeochemistry model (Chapter 13).

The sandblasting mass efficiency α (m^{-1}) is calculated as

$$\alpha = 100e^{(13.4M_{clay}-6.0)\ln 10} \quad \begin{cases} M_{clay} = \%clay \times 0.01 & 0 \le \%clay \le 20 \\ M_{clay} = 20 \times 0.01 & 20 < \%clay \le 100 \end{cases} \tag{24.4}$$

where M_{clay} is the mass fraction of clay particles in the soil and %clay is determined from the surface dataset (section 2.2.3). $M_{clay} = 0$ corresponds to sand and $M_{clay} = 0.2$ to sandy loam.

Q_s is the total horizontally saltating mass flux (kg m^{-1} s^{-1}) of "large" particles (Table 24.1), also referred to as the vertically integrated streamwise mass flux

$$Q_s = \begin{cases} \dfrac{c_s \rho_{atm} u_{*s}^3}{g}\left(1-\dfrac{u_{*t}}{u_{*s}}\right)\left(1+\dfrac{u_{*t}}{u_{*s}}\right)^2 & \text{for } u_{*t} < u_{*s} \\ 0 & \text{for } u_{*t} \ge u_{*s} \end{cases} \tag{24.5}$$

where the saltation constant c_s equals 2.61 and ρ_{atm} is the atmospheric density (kg m^{-3}) (Table 2.3), g the acceleration of gravity (m s^{-2}) (Table 2.6). The threshold wind friction speed for saltation u_{*t} (m s^{-1}) is

$$u_{*_t} = f_z \left[\mathrm{Re}_{*_t}^{f} \, \rho_{osp} g D_{osp} \left(1 + \frac{6 \times 10^{-7}}{\rho_{osp} g D_{osp}^{2.5}} \right) \right]^{\frac{1}{2}} \rho_{atm}^{-\frac{1}{2}} f_w \tag{24.6}$$

where f_z is a factor dependent on surface roughness but set to 1 as a place holder for now, ρ_{osp} and D_{osp} are the density (2650 kg m^{-3}) and diameter (75 x 10^{-6} m) of optimal saltation particles, and f_w is a factor dependent on soil moisture:

$$f_w = \begin{cases} 1 & \text{for } w \le w_t \\ \sqrt{1 + 1.21 \left[100 \left(w - w_t \right) \right]^{0.68}} & \text{for } w > w_t \end{cases} \tag{24.7}$$

where

$$w_t = a \left(0.17 M_{clay} + 0.14 M_{clay}^2 \right) \qquad 0 \le M_{clay} = \%clay \times 0.01 \le 1 \tag{24.8}$$

and

$$w = \frac{\theta_1 \rho_{liq}}{\rho_{d,1}} \tag{24.9}$$

where $a = M_{clay}^{-1}$ for tuning purposes, θ_1 is the volumetric soil moisture in the top soil layer (m^3 m^{-3}) (section 7.4), ρ_{liq} is the density of liquid water (kg m^{-3}) (Table 2.6), and $\rho_{d,1}$ is the bulk density of soil in the top soil layer (kg m^{-3}) defined as in section 6.3 rather than as in Zender et al. (2003). $\mathrm{Re}_{*_t}^{f}$ from equation (24.6) is the threshold friction Reynolds factor

$$\mathrm{Re}_{*t}^{f} = \begin{cases} \dfrac{0.1291^2}{-1+1.928\,\mathrm{Re}_{*t}} & \text{for } 0.03 \le \mathrm{Re}_{*t} \le 10 \\ 0.12^2\left(1-0.0858e^{-0.0617(\mathrm{Re}_{*t}-10)}\right)^2 & \text{for } \mathrm{Re}_{*t} > 10 \end{cases} \tag{24.10}$$

and Re_{*t} is the threshold friction Reynolds number approximation for optimally sized particles

$$\mathrm{Re}_{*t} = 0.38 + 1331\left(100 D_{osp}\right)^{1.56} \tag{24.11}$$

In equation (24.5), u_{*s} is defined as the wind friction speed (m s^{-1}) accounting for the Owen effect (Owen 1964)

$$u_{*s} = \begin{cases} u_* & \text{for } U_{10} < U_{10,t} \\ u_* + 0.003\left(U_{10} - U_{10,t}\right)^2 & \text{for } U_{10} \ge U_{10,t} \end{cases} \tag{24.12}$$

where u_* is the CLM wind friction speed (m s^{-1}), also known as friction velocity (section 5.1), U_{10} is the 10-m wind speed (m s^{-1}) calculated as the wind speed at the top of the canopy in section 4.3 of Bonan (1996) but here for 10 m above the ground, and $U_{10,t}$ is the threshold wind speed at 10 m (m s^{-1})

$$U_{10,t} = u_{*t}\frac{U_{10}}{u_*} \tag{24.13}$$

In equation (24.1) we sum $M_{i,j}$ over $I = 3$ source modes i where $M_{i,j}$ is the mass fraction of each source mode i carried in each of $J = 4$ transport bins j

$$M_{i,j} = \frac{m_i}{2}\left[\mathrm{erf}\left(\frac{\ln\frac{D_{j,\max}}{\tilde{D}_{v,i}}}{\sqrt{2}\ln\sigma_{g,i}}\right) - \mathrm{erf}\left(\frac{\ln\frac{D_{j,\min}}{\tilde{D}_{v,i}}}{\sqrt{2}\ln\sigma_{g,i}}\right)\right] \tag{24.14}$$

where m_i, $\tilde{D}_{v,i}$, and $\sigma_{g,i}$ are the mass fraction, mass median diameter, and geometric standard deviation assigned to each particle source mode i (Table 24.1), while $D_{j,\min}$ and $D_{j,\max}$ are the minimum and maximum diameters (m) in each transport bin j (Table 24.2).

Table 24.1. Mass fraction m_i, mass median diameter $\tilde{D}_{v,i}$, and geometric standard deviation $\sigma_{g,i}$, per dust source mode i

i	m_i (fraction)	$\tilde{D}_{v,i}$ (m)	$\sigma_{g,i}$
1	0.036	0.832×10^{-6}	2.1
2	0.957	4.820×10^{-6}	1.9
3	0.007	19.38×10^{-6}	1.6

Table 24.2. Minimum and maximum particle diameters in each dust transport bin j

j	$D_{j,\min}$ (m)	$D_{j,\max}$ (m)
1	0.1×10^{-6}	1.0×10^{-6}
2	1.0×10^{-6}	2.5×10^{-6}
3	2.5×10^{-6}	5.0×10^{-6}
4	5.0×10^{-6}	10.0×10^{-6}

25. Carbon Isotopes

CLM includes a fully prognostic representation of the fluxes, storage, and isotopic discrimination of the carbon isotopes ^{13}C and ^{14}C. The implementation of the C isotopes capability takes advantage of the CLM hierarchical data structures, replicating the carbon state and flux variable structures at the column and PFT level to track total carbon and both C isotopes separately (see description of data structure hierarchy in Chapter 2). For the most part, fluxes and associated updates to carbon state variables for ^{13}C are calculated directly from the corresponding total C fluxes. Separate calculations are required in a few special cases, such as where isotopic discrimination occurs, or where the necessary isotopic ratios are undefined. The general approach for ^{13}C flux and state variable calculation is described here, followed by a description of all the places where special calculations are required.

25.1 General Form for Calculating ^{13}C and ^{14}C Flux

In general, the flux of ^{13}C and corresponding to a given flux of total C (CF_{13C} and CF_{totC}, respectively) is determined by CF_{totC}, the masses of ^{13}C and total C in the upstream pools (CS_{13C_up} and CS_{totC_up}, respectively, i.e. the pools *from which* the fluxes of ^{13}C and total C originate), and a fractionation factor, f_{frac}:

$$CF_{13C} = \begin{cases} CF_{totC} \dfrac{CS_{13C\_up}}{CS_{totC\_up}} f_{frac} & \text{for } CS_{totC} \neq 0 \\ 0 & \text{for } CS_{totC} = 0 \end{cases} \tag{25.1}$$

If the f_{frac} = 1.0 (no fractionation), then the fluxes CF_{13C} and CF_{totC} will be in simple proportion to the masses CS_{13C_up} and CS_{totC_up}. Values of f_{frac} < 1.0 indicate a

discrimination against the heavier isotope (^{13}C) in the flux-generating process, while f_{frac} > 1.0 would indicate a preference for the heavier isotope. Currently, in all cases where Eq. (25.1) is used to calculate a ^{13}C flux, f_{frac} is set to 1.0.

For ^{14}C, no fractionation is used in either the initial photosynthetic step, nor in subsequent fluxes from upstream to downstream pools; as discussed below, this is because observations of ^{14}C are typically described in units that implicitly correct out the fractionation of ^{14}C by referencing them to ^{13}C ratios.

25.2 Isotope Symbols, Units, and Reference Standards

Carbon has two primary stable isotopes, ^{12}C and ^{13}C. ^{12}C is the most abundant, comprising about 99% of all carbon. The isotope ratio of a compound, R_A, is the mass ratio of the rare isotope to the abundant isotope

$$R_A = \frac{^{13}C_A}{^{12}C_A}. \tag{25.2}$$

Carbon isotope ratios are often expressed using delta notation, δ. The $\delta^{13}C$ value of a compound A, $\delta^{13}C_A$, is the difference between the isotope ratio of the compound, R_A, and that of the Pee Dee Belemnite standard, R_{PDB}, in parts per thousand

$$\delta^{13}C_A = \left(\frac{R_A}{R_{PDB}} - 1 \right) \times 1000 \tag{25.3}$$

where R_{PDB} = 0.0112372, and units of δ are per mil (‰).

Isotopic fractionation can be expressed in several ways. One expression of the fractionation factor is with alpha (α) notation. For example, the equilibrium fractionation between two reservoirs A and B can be written as:

$$\alpha_{A-B} = \frac{R_A}{R_B} = \frac{\delta_A + 1000}{\delta_B + 1000}. \tag{25.4}$$

This can also be expressed using epsilon notation (ε), where

$$\alpha_{A-B} = \frac{\varepsilon_{A-B}}{1000} + 1 \tag{25.5}$$

In other words, if $\varepsilon_{A-B} = 4.4‰$, then $\alpha_{A\text{-}B}=1.0044$.

In addition to the stable isotopes ^{12}C and ^{13}C, the unstable isotope ^{14}C is included in CLM. ^{14}C can also be described using the delta notation:

$$\delta^{14}C = \left(\frac{A_s}{A_{abs}} - 1 \right) \times 1000 \tag{25.6}$$

However, observations of ^{14}C are typically fractionation-corrected using the following notation:

$$\Delta^{14}C = 1000 \times \left(\left(1 + \frac{\delta^{14}C}{1000} \right) \frac{0.975^2}{\left(1 + \frac{\delta^{13}C}{1000} \right)^2} - 1 \right) \tag{25.7}$$

where $\delta^{14}C$ is the measured isotopic fraction and $\Delta^{14}C$ corrects for mass-dependent isotopic fractionation processes (assumed to be 0.975 for fractionation of ^{13}C by photosynthesis). CLM assumes a background preindustrial atmospheric ^{14}C /C ratio of 10^{-12}, which is used for A_{abs}. For the reference standard A_{abs}, which is a plant tissue and has a $\delta^{13}C$ value is −25 ‰ due to photosynthetic discrimination, $\delta^{14}C = \Delta^{14}C$. For CLM, in order to use the ^{14}C model independently of the ^{13}C model, for the ^{14}C calculations, this fractionation is set to zero, such that the 0.975 term becomes 1, the $\delta^{13}C$ term (for the calculation of $\delta^{14}C$ only) becomes 0, and thus $\delta^{14}C = \Delta^{14}C$.

25.3 Carbon Isotope Discrimination During Photosynthesis

Photosynthesis is modeled in CLM as a two-step process: diffusion of CO_2 into the stomatal cavity, followed by enzymatic fixation (Chapter 8). Each step is associated with a kinetic isotope effect. The kinetic isotope effect during diffusion of CO_2 through the stomatal opening is 4.4‰. The kinetic isotope effect during fixation of CO_2 with Rubisco is ~30‰; however, since about 5-10% of carbon in C3 plants reacts with phosphoenolpyruvate carboxylase (PEPC) (Melzer and O'Leary, 1987), the net kinetic isotope effect during fixation is ~27‰ for C3 plants. In C4 plant photosynthesis, only the diffusion effect is important. The fractionation factor equations for C3 and C4 plants are given below:

For C4 plants,

$$\alpha_{psn} = 1 + \frac{4.4}{1000} \tag{25.8}$$

For C3 plants,

$$\alpha_{psn} = 1 + \frac{4.4 + 22.6\dfrac{c_i^*}{pCO_2}}{1000} \tag{25.9}$$

where α_{psn} is the fractionation factor, and c_i^* and pCO_2 are the revised intracellular and atmospheric CO_2 partial pressure, respectively.

As can be seen from the above equation, kinetic isotope effect during fixation of CO_2 is dependent on the intracellular CO_2 concentration, which in turn depends on the net carbon assimilation. That is calculated during the photosynthesis calculation as follows:

$$c_i = pCO_2 - a_n p \frac{(1.4g_s) + (1.6g_b)}{g_b g_s} \tag{25.10}$$

and

$$c_i^* = pCO_2 - a_n\left(1-d\right)p\frac{\left(1.4g_s\right)+\left(1.6g_b\right)}{g_b g_s} \tag{25.11}$$

where a_n is net carbon assimilation during photosynthesis, d is downscaling factor due to nitrogen limitation, p is atmospheric pressure, g_b is leaf boundary layer conductance, and g_s is leaf stomatal conductance.

The fractionation factor α_{psn} and net assimilation a_n are calculated during the radiation time-step in CanopyFluxesMod.F90, whereas the downscaling factor d is not calculated until after the nitrogen limitation is computed in CNAllocationMod.F90. That results in a difference between the actual photosynthesis, which is downscaled by d, and the potential photosynthesis. In order to overcome this mismatch, downscaling due to nitrogen limitation is factored in the calculation of the kinetic isotope effect during fixation by defining a downscaled version of intracellular CO_2 (c_i^*), as a first order approximation. However, since nitrogen down-regulation is calculated after the photosynthesis calculation, down-regulation coefficient calculated in the previous time step needs to be used.

Isotopic fractionation code is compatible with multi-layered canopy parameterization; i.e., it is possible to calculate varying discrimination rates for each layer of a multi-layered canopy. However, as with the rest of the photosynthesis model, the number of canopy layers is currently set to one by default.

25.4 ^{14}C radioactive decay and historical atmospheric ^{14}C concentrations

In the preindustrial biosphere, radioactive decay of ^{14}C in carbon pools allows dating of long-term age since photosynthetic uptake; while over the 20th century, radiocarbon in the atmosphere was first diluted by radiocarbon-free fossil fuels and then enriched by aboveground thermonuclear testing to approximately double its long-term mean concentration. CLM includes both of these processes to allow comparison of carbon that may vary on multiple timescales with observed values.

For radioactive decay, at each timestep all ^{14}C pools are reduced at a rate of $-\log(0.5)/\tau$, where τ is the half-life (Libby half-life value of 5568 years). In order to rapidly equilibrate the long-lived pools during accelerated decomposition spinup, the radioactive decay of the accelerated pools is also accelerated by the same degree as the decomposition, such that the ^{14}C value of these pools is in equilibrium when taken out of the spinup mode.

For variation of atmospheric ^{14}C over the historical period, $\Delta^{14}C$ values can be set to either fixed concentration ($\Delta^{14}C = 0‰$) or time-varying concentrations read in from a file. A default file is provided that is based on a spline fit through several observational datasets spanning the 20th century: (Levin and Kromer, 2004; Manning and Melhuish, 1994; Nydal and Lövseth, 1996; Turnbull et al. 2007). This is shown in Figure 25.1.

Figure 25.1. Atmospheric $\Delta^{14}C$ used to drive ^{14}C model over the historical period.

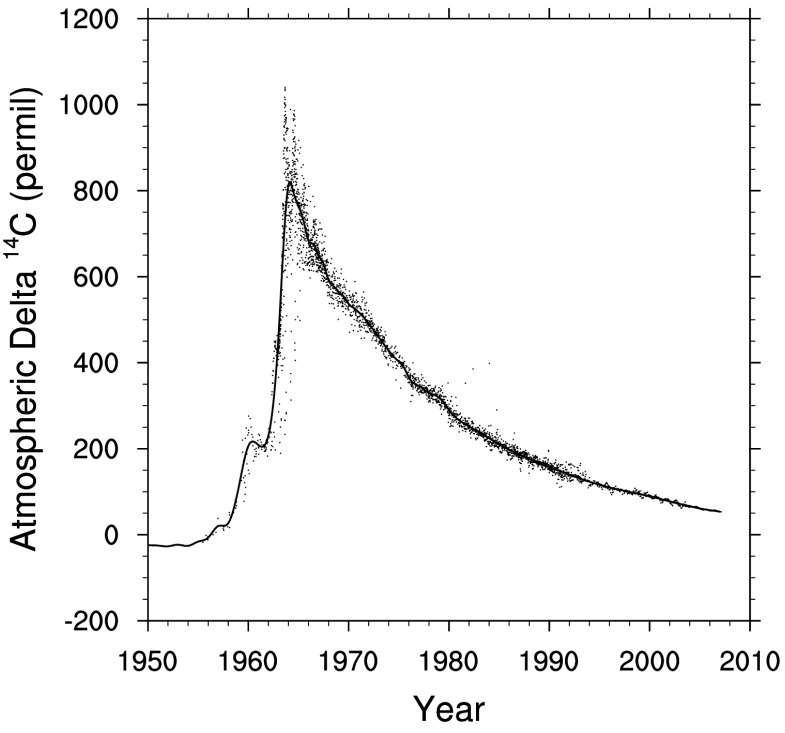

26. Offline Mode

In offline mode (uncoupled to an atmospheric model), the atmospheric forcing required by CLM (Table 2.3) is supplied by observed datasets. The standard forcing provided with the model is a 110-year (1901-2010) dataset (CRUNCEP; Viovy 2011) that is a combination of two existing datasets; the CRU TS3.2 0.5° X 0.5° monthly data covering the period 1901 to 2002 (Mitchell and Jones 2005) and the NCEP reanalysis 2.5° X 2.5° 6-hourly data covering the period 1948 to 2010. The CRUNCEP dataset has been used to force CLM for studies of vegetation growth, evapotranspiration, and gross primary production (Mao et al. 2012, Mao et al. 2013, Shi et al. 2013) and for the TRENDY (trends in net land-atmosphere carbon exchange over the period 1980-2010) project (Piao et al. 2012). Version 4 is used here (Viovy 2011). Alternative forcing datasets can also be used (e.g., the Qian et al. (2006) dataset used for previous versions of CLM is still available).

Here, the CRUNCEP dataset, which does not include data over oceans, lakes, and Antarctica is modified. This missing data is filled with Qian et al. (2006) data from 1948 that is interpolated by the data atmosphere model to the 0.5° CRUNCEP grid. This allows the model to be run over Antarctica and ensures data is available along coastlines regardless of model resolution.

The forcing data is ingested into a data atmosphere model in three "streams"; precipitation (P) (mm s^{-1}), solar radiation (S_{atm}) (W m^{-2}), and four other fields [atmospheric pressure P_{atm} (Pa), atmospheric specific humidity q_{atm} (kg kg^{-1}), atmospheric temperature T_{atm} (K), and atmospheric wind W_{atm} (m s^{-1})]. These are

separate streams because they are handled differently according to the type of field. In the CRUNCEP dataset, the precipitation stream is provided at six hour intervals and the data atmosphere model prescribes the same precipitation rate for each model time step within the six hour period. The four fields that are grouped together in another stream (pressure, humidity, temperature, and wind) are provided at six hour intervals and the data atmosphere model linearly interpolates these fields to the time step of the model.

The total solar radiation is also provided at six hour intervals. The data is fit to the model time step using a diurnal function that depends on the cosine of the solar zenith angle μ to provide a smoother diurnal cycle of solar radiation and to ensure that all of the solar radiation supplied by the six-hourly forcing data is actually used. The solar radiation at model time step t_M is

$$S_{atm}\left(t_M\right) = \frac{\frac{\Delta t_{FD}}{\Delta t_M} S_{atm}\left(t_{FD}\right)\mu\left(t_M\right)}{\sum_{i=1}^{\frac{\Delta t_{FD}}{\Delta t_M}} \mu\left(t_{M_i}\right)} \qquad \text{for } \mu\left(t_M\right) > 0.001$$
$$S_{atm}\left(t_M\right) = 0 \qquad \text{for } \mu\left(t_M\right) \le 0.001 \tag{26.1}$$

where Δt_{FD} is the time step of the forcing data (6 hours $\times$ 3600 seconds hour^{-1} = 21600 seconds), Δt_M is the model time step (seconds), $S_{atm}\left(t_{FD}\right)$ is the six-hourly solar radiation from the forcing data (W m^{-2}), and $\mu\left(t_M\right)$ is the cosine of the solar zenith angle at model time step t_M (section 3.3). The term in the denominator of equation (26.1) is the sum of the cosine of the solar zenith angle for each model time step falling within the six hour period. For numerical purposes, $\mu\left(t_{M_i}\right) \ge 0.001$.

The total incident solar radiation S_{atm} at the model time step t_M is then split into near-infrared and visible radiation and partitioned into direct and diffuse according to factors derived from one year's worth of hourly CAM output from CAM version cam3_5_55 as

$$S_{atm}\downarrow_{vis}^{\mu} = R_{vis}\left(\alpha S_{atm}\right) \tag{26.2}$$

$$S_{atm}\downarrow_{nir}^{\mu} = R_{nir}\left[\left(1-\alpha\right)S_{atm}\right] \tag{26.3}$$

$$S_{atm}\downarrow_{vis} = \left(1-R_{vis}\right)\left(\alpha S_{atm}\right) \tag{26.4}$$

$$S_{atm}\downarrow_{nir} = \left(1-R_{nir}\right)\left[\left(1-\alpha\right)S_{atm}\right]. \tag{26.5}$$

where α, the ratio of visible to total incident solar radiation, is assumed to be

$$\alpha = \frac{S_{atm}\downarrow_{vis}^{\mu} + S_{atm}\downarrow_{vis}}{S_{atm}} = 0.5\,. \tag{26.6}$$

The ratio of direct to total incident radiation in the visible R_{vis} is

$$R_{vis} = a_0 + a_1\times\alpha S_{atm} + a_2\times\left(\alpha S_{atm}\right)^2 + a_3\times\left(\alpha S_{atm}\right)^3 \quad 0.01 \le R_{vis} \le 0.99 \tag{26.7}$$

and in the near-infrared R_{nir} is

$$R_{nir} = b_0 + b_1\times\left(1-\alpha\right)S_{atm} + b_2\times\left[\left(1-\alpha\right)S_{atm}\right]^2 + b_3\times\left[\left(1-\alpha\right)S_{atm}\right]^3 \quad 0.01 \le R_{nir} \le 0.99 \tag{26.8}$$

where $a_0 = 0.17639, a_1 = 0.00380, a_2 = -9.0039\times10^{-6}, a_3 = 8.1351\times10^{-9}$ and $b_0 = 0.29548, b_1 = 0.00504, b_2 = -1.4957\times10^{-5}, b_3 = 1.4881\times10^{-8}$ are coefficients from polynomial fits to the CAM data.

The additional atmospheric forcing variables required by Table 2.3 are derived as follows. The atmospheric reference height z'_{atm} (m) is set to 30 m. The directional wind components are derived as $u_{atm} = v_{atm} = W_{atm}/\sqrt{2}$. The potential temperature $\overline{\theta_{atm}}$ (K) is set to the atmospheric temperature T_{atm}. The atmospheric longwave radiation $L_{atm}\downarrow$ (W

m^{-2}) is derived from the atmospheric vapor pressure e_{atm} and temperature T_{atm} (Idso 1981) as

$$L_{atm}\downarrow = \left[0.70 + 5.95\times10^{-5}\times 0.01 e_{atm}\exp\left(\frac{1500}{T_{atm}}\right)\right]\sigma T_{atm}^{4} \tag{26.9}$$

where

$$e_{atm} = \frac{P_{atm} q_{atm}}{0.622 + 0.378 q_{atm}} \tag{26.10}$$

and σ is the Stefan-Boltzmann constant (W m^{-2} K^{-4}) (Table 2.6). The fraction of precipitation P (mm s^{-1}) falling as rain and/or snow is

$$q_{rain} = P\left(f_P\right), \tag{26.11}$$

$$q_{snow} = P\left(1 - f_P\right) \tag{26.12}$$

where

$$f_P = 0 < 0.5\left(T_{atm} - T_f\right) < 1. \tag{26.13}$$

The aerosol deposition rates D_{sp} (14 rates as described in Table 2.3) are provided by a time-varying, globally-gridded aerosol deposition file developed by Lamarque et al. (2010).

If the user wishes to provide atmospheric forcing data from another source, the data format outlined above will need to be followed with the following exceptions. The data atmosphere model will accept a user-supplied relative humidity RH (%) and derive specific humidity q_{atm} (kg kg^{-1}) from

$$q_{atm} = \frac{0.622 e_{atm}}{P_{atm} - 0.378 e_{atm}} \tag{26.14}$$

where the atmospheric vapor pressure e_{atm} (Pa) is derived from the water ($T_{atm} > T_f$) or ice ($T_{atm} \le T_f$) saturation vapor pressure $e_{sat}^{T_{atm}}$ as $e_{atm} = \frac{RH}{100} e_{sat}^{T_{atm}}$ where T_f is the freezing temperature of water (K) (Table 2.6), and P_{atm} is the pressure at height z_{atm} (Pa). The data atmosphere model will also accept a user-supplied dew point temperature T_{dew} (K) and derive specific humidity q_{atm} from

$$q_{atm} = \frac{0.622 e_{sat}^{T_{dew}}}{P_{atm} - 0.378 e_{sat}^{T_{dew}}}. \tag{26.15}$$

Here, e_{sat}^{T}, the saturation vapor pressure as a function of temperature, is derived from Lowe's (1977) polynomials. If not provided by the user, the atmospheric pressure P_{atm} (Pa) is set equal to the standard atmospheric pressure $P_{std} = 101325$ Pa, and surface pressure P_{srf} (Pa) is set equal to P_{atm}.

The user may provide the total direct and diffuse solar radiation, $S_{atm}\downarrow^{\mu}$ and $S_{atm}\downarrow$. These will be time-interpolated using the procedure described above and then each term equally apportioned into the visible and near-infrared wavebands (e.g., $S_{atm}\downarrow_{vis}^{\mu} = 0.5 S_{atm}\downarrow^{\mu}$, $S_{atm}\downarrow_{nir}^{\mu} = 0.5 S_{atm}\downarrow^{\mu}$).

27. References

Aber, J.D., Melillo, J.M. and McClaugherty, C.A., 1990. Predicting long-term patterns of mass loss, nitrogen dynamics, and soil organic matter formation from initial fime litter chemistry in temperate forest ecosystems. Canadian Journal of Botany, 68: 2201-2208.

Aber, J.D., Goodale, C.L., Ollinger, S.V., Smith, M.-L., Magill, A.H., Martin, M.E., Hallett, R.A., and Stoddard, J.L. 2003. Is nitrogen deposition altering the nitrogen status of northeastern forests? BioScience 53:375-389.

Allen, C.B., Will, R.E., and Jacobson, M.A. 2005. Production efficiency and radiation use efficiency of four tree species receiving irrigation and fertilization. Forest Science 51:556-569.

Anderson, E.A. 1976. A point energy and mass balance model of a snow cover. NOAA Technical Report NWS 19, Office of Hydrology, National Weather Service, Silver Spring, MD.

André, J.-C., Goutorbe, J.-P., and Perrier, A. 1986. HAPEX-MOBILHY: A hydrologic atmosphere experiment for the study of water budget and evaporation flux at the climatic scale. Bull. Amer. Meteor. Soc. 67:138-144.

Andrén, O. and Paustian, K., 1987. Barley straw decomposition in the field: a comparison of models. Ecology 68(5):1190-1200.

Arah, J.R.M. and Stephen, K.D., 1998. A model of the processes leading to methane emission from peatland. Atmos. Environ. 32(19):3257-3264.

Arah, J. and Vinten, A., 1995. Simplified models of anoxia and denitrification in aggregated and simple-structured soils. European Journal of Soil Science 46(4):507-517.

Arendt, A., et al. 2012. Randolph Glacier Inventory: A Dataset of Global Glacier Outlines Version: 1.0, Global Land Ice Measurements from Space, Boulder Colorado, USA. Digital Media.

Arora, V.K. and Boer, G.J. 2005. Fire as an interactive component of dynamic vegetation models. J. Geophys. Res. 110:G02008. DOI:10.1029/2005JG000042.

Arya, S.P. 2001. Introduction to Meteorology. Academic Press, San Diego, CA.

Asner, G.P., Wessman, C.A., Schimel, D.S., and Archer, S. 1998. Variability in leaf and litter optical properties: implications for BRDF model inversions using AVHRR, MODIS, and MISR. Remote Sens. Environ. 63:243-257.

Axelsson, E., and Axelsson, B. 1986. Changes in carbon allocation patterns in spruce and pine trees following irrigation and fertilization. Tree Phys. 2:189-204.

Baird, A.J., Beckwith, C.W., Waldron, S. and Waddington, J.M., 2004. Ebullition of methane-containing gas bubbles from near-surface Sphagnum peat. Geophys. Res. Lett. 31(21). DOI:10.1029/2004GL021157.

Baldocchi, D., et al. 2001. FLUXNET: A new tool to study the temporal and spatial variability of ecosystem-scale carbon dioxide, water vapor, and energy flux densities. Bull. Amer. Meteor. Soc. 82:2415-2433.

Barbottin, A., Lecomte, C., Bouchard, C., and Jeuffroy, M.-H. 2005. Nitrogen remobilization during grain filling in wheat: Genotypic and environmental effects. Crop Sci. 45:1141-1150.

Batjes, N.H., 2006. ISRIC-WISE derived soil properties on a 5 by 5 arc-minutes global grid. Report 2006/02 (available through : http://www.isric.org)

Berger, A.L. 1978a. Long-term variations of daily insolation and quaternary climatic changes. J. Atmos. Sci. 35:2362-2367.

Berger, A.L. 1978b. A simple algorithm to compute long-term variations of daily or monthly insolation. Contribution de l'Institut d'Astronomie et de Géophysique, Université Catholique de Louvain, Louvain-la-Neuve, No. 18.

Berger, A., Loutre, M.-F., and Tricot, C. 1993. Insolation and Earth's orbital periods. J. Geophys. Res. 98:10341-10362.

Berkowitz, B., and Balberg, I. 1992. Percolation approach to the problem of hydraulic conductivity in porous media. Transport in Porous Media 9:275–286.

Beven, K.J., and Kirkby, M.J. 1979. A physically based variable contributing area model of basin hydrology. Hydrol. Sci. Bull. 24:43-69.

Bohren, C. F., and Huffman, D. R. 1983. Absorption and scattering of light by small particles. John Wiley & Sons, New York, NY.

Bonan, G.B. 1996. A land surface model (LSM version 1.0) for ecological, hydrological, and atmospheric studies: Technical description and user's guide. NCAR Technical Note NCAR/TN-417+STR, National Center for Atmospheric Research, Boulder, CO, 150 pp.

Bonan, G.B. 1998. The land surface climatology of the NCAR Land Surface Model coupled to the NCAR Community Climate Model. J. Climate 11:1307-1326.

Bonan, G.B. 2002. Ecological Climatology: Concepts and Applications. Cambridge University Press.

Bonan, G.B., Oleson, K.W., Vertenstein, M., Levis, S., Zeng, X., Dai, Y., Dickinson, R.E., and Yang, Z.-L. 2002a. The land surface climatology of the Community Land Model coupled to the NCAR Community Climate Model. J. Climate 15: 3123-3149.

Bonan, G.B., Levis, S., Kergoat, L., and Oleson, K.W. 2002b. Landscapes as patches of plant functional types: An integrating concept for climate and ecosystem models. Global Biogeochem. Cycles 16: 5.1-5.23.

Bonan, G.B., and Levis, S. 2006. Evaluating aspects of the Community Land and Atmosphere Models (CLM3 and CAM3) using a dynamic global vegetation model. J. Climate 19:2290-2301.

Bonan, G.B., Lawrence P.J., Oleson K.W., Levis S., Jung M., Reichstein M., Lawrence, D.M., and Swenson, S.C. 2011. Improving canopy processes in the Community Land Model (CLM4) using global flux fields empirically inferred from FLUXNET data. J. Geophys. Res. 116, G02014. DOI:10.1029/2010JG001593.

Bonan, G. B., Oleson, K.W., Fisher, R.A., Lasslop, G., and Reichstein, M. 2012. Reconciling leaf physiological traits and canopy flux data: Use of the TRY and FLUXNET databases in the Community Land Model version 4, J. Geophys. Res., 117, G02026. DOI:10.1029/2011JG001913.

Branstetter, M.L., and Famiglietti, J.S. 1999. Testing the sensitivity of GCM-simulated runoff to climate model resolution using a parallel river transport algorithm. Preprints, 14th Conference on Hydrology, Dallas, TX, Amer. Meteor. Soc., 391-392.

Branstetter, M.L. 2001. Development of a parallel river transport algorithm and applications to climate studies. Ph.D. dissertation, University of Texas at Austin.

Brun, E. 1989. Investigation of wet-snow metamorphism in respect of liquid water content. Ann. Glaciol. 13:22-26.

Bugmann, H., and Solomon, A.M. 2000. Explaining forest composition and biomass across multiple biogeographical regions. Ecol. Appl. 10:95-114.

Busing, R.T. 2005. Tree mortality, canopy turnover, and woody detritus in old cove forests of the southern Appalachians. Ecology 86:73-84.

Campbell, G.S., and Norman, J.M. 1998. An Introduction to Environmental Biophysics (2nd edition). Springer-Verlag, New York.

Castillo, G., Kendra, C., Levis, S., and Thornton, P. 2012. Evaluation of the new CNDV option of the Community Land Model: effects of dynamic vegetation and interactive nitrogen on CLM4 means and variability. J. Climate 25:3702–3714.

Cao, M., Marshall, S. and Gregson, K., 1996. Global carbon exchange and methane emissions from natural wetlands: Application of a process-based model. J. Geophys. Res. 101(D9):14,399-14,414.

Churkina, G. et al., 2003. Analyzing the ecosystem carbon dynamics of four European coniferous forests using a biogeochemistry model. Ecosystems, 6: 168-184.

CIESIN: Gridded population of the world version 3 (GPWv3), 2005. Population density grids, Technical report, Socioeconomic Data and Applications Center (SEDAC), Columbia University, Palisades, New York, USA.

Clapp, R.B., and Hornberger, G.M. 1978. Empirical equations for some soil hydraulic properties. Water Resour. Res. 14:601-604.

Clauser, C., and Huenges, E. 1995. Thermal conductivity of rocks and minerals. pp. 105-126. In: T. J. Ahrens (editor) Rock Physics and Phase Relations: A Handbook of Physical Constants. Washington, D.C.

Cleveland, C.C., Townsend, A.R., Schimel, D.S., Fisher, H., Howarth, R.W., Hedin, L.O., Perakis, S.S., Latty, E.F., Von Fischer, J.C., Elseroad, A., and Wasson, M.F. 1999. Global patterns of terrestrial biological nitrogen (N2) fixation in natural ecosystems. Global Biogeochem. Cycles 13:623-645.

Collatz, G.J., Ball, J.T., Grivet, C., and Berry, J.A. 1991. Physiological and environmental regulation of stomatal conductance, photosynthesis, and transpiration: A model that includes a laminar boundary layer. Agric. For. Meteor. 54:107-136.

Collatz, G.J., Ribas-Carbo, M., and Berry, J.A. 1992. Coupled photosynthesis-stomatal conductance model for leaves of C_4 plants. Aust. J. Plant Physiol. 19:519-538.

Colmer, T.D., 2003. Long-distance transport of gases in plants: a perspective on internal aeration and radial oxygen loss from roots. Plant Cell and Environment 26(1):17-36.

Conway, H., Gades, A., and Raymond, C.F. 1996. Albedo of dirty snow during conditions of melt. Water Resour. Res. 32:1713-1718.

Cosby, B.J., Hornberger, G.M., Clapp, R.B., and Ginn, T.R. 1984. A statistical exploration of the relationships of soil moisture characteristics to the physical properties of soils. Water Resour. Res. 20:682-690.

Crawford, T. W., Rendig, V. V., and Broadent, F. E. 1982. Sources, fluxes, and sinks of nitrogen during early reproductive growth of maize (Zea mays L.). Plant Physiol. 70:1645-1660.

Dai, Y., and Zeng, Q. 1997. A land surface model (IAP94) for climate studies. Part I: formulation and validation in off-line experiments. Adv. Atmos. Sci. 14:433-460.

Dai, Y., et al. 2001. Common Land Model: Technical documentation and user's guide [Available online at http://climate.eas.gatech.edu/dai/clmdoc.pdf].

Dai, Y., Zeng, X., Dickinson, R.E., Baker, I., Bonan, G.B., Bosilovich, M.G., Denning, A.S., Dirmeyer, P.A., Houser, P.R., Niu, G., Oleson, K.W., Schlosser, C.A., and Yang, Z.-L. 2003. The Common Land Model. Bull. Amer. Meteor. Soc. 84:1013-1023.

Dai, Y., Dickinson, R.E., and Wang, Y.-P. 2004. A two-big-leaf model for canopy temperature, photosynthesis, and stomatal conductance. J. Climate 17:2281-2299.

Dai, A., and Trenberth, K.E. 2002. Estimates of freshwater discharge from continents: Latitudinal and seasonal variations. J. Hydrometeor. 3:660-687.

DeFries, R.S., Hansen, M.C., Townshend, J.R.G., Janetos, A.C., and Loveland, T.R. 2000. A new global 1-km dataset of percentage tree cover derived from remote sensing. Global Change Biol. 6:247-254.

Degens, B. and Sparling, G., 1996. Changes in aggregation do not correspond with changes in labile organic C fractions in soil amended with ^{14}C-glucose. Soil Biology and Biochemistry, 28(4/5): 453-462.

de Vries, D.A. 1963. Thermal Properties of Soils. In: W.R. van Wijk (editor) Physics of the Plant Environment. North-Holland, Amsterdam.

Dickinson, R.E. 1983. Land surface processes and climate-surface albedos and energy balance. Adv. Geophys. 25:305-353.

Dickinson, R.E., Henderson-Sellers, A., and Kennedy, P.J. 1993. Biosphere-Atmosphere Transfer Scheme (BATS) version 1e as coupled to the NCAR Community Climate Model. NCAR Technical Note NCAR/TN-387+STR. National Center for Atmospheric Research, Boulder, CO.

Dickinson, R.E., Oleson, K.W., Bonan, G., Hoffman, F., Thornton, P., Vertenstein, M., Yang, Z.-L., and Zeng, X. 2006. The Community Land Model and its climate statistics as a component of the Community Climate System Model. J. Climate 19:2302-2324.

Dingman, S.L. 2002. Physical Hydrology. Second Edition. Prentice Hall, NJ.

Dirmeyer, P.A., Dolman, A.J., and Sato, N. 1999. The pilot phase of the Global Soil Wetness Project. Bull. Amer. Meteor. Soc. 80:851-878.

Dobson, J.E., Bright, E.A., Coleman, P.R., Durfee, R.C., and Worley, B.A. 2000. LandScan: A global population database for estimating populations at risk. Photogramm. Eng. Rem. Sens. 66:849-857.

Dorman, J.L., and Sellers, P.J. 1989. A global climatology of albedo, roughness length and stomatal resistance for atmospheric general circulation models as represented by the simple biosphere model (SiB). J. Appl. Meteor. 28:833-855.

Dougherty, R.L., Bradford, J.A., Coyne, P.I., and Sims, P.L. 1994. Applying an empirical model of stomatal conductance to three C4 grasses. Agric. For. Meteor. 67:269-290.

Drewniak, B., Song, J., Prell, J., Kotamarthi, V.R., and Jacob, R. 2013. Modeling agriculture in the Community Land Model. Geosci. Model Dev. 6:495-515. DOI:10.5194/gmd-6-495-2013.

Dunfield, P., Knowles, R., Dumont, R. and Moore, T.R., 1993. Methane Production and Consumption in Temperate and Sub-Arctic Peat Soils - Response to Temperature and Ph. Soil Biology & Biochemistry 25(3):321-326.

Entekhabi, D., and Eagleson, P.S. 1989. Land surface hydrology parameterization for atmospheric general circulation models including subgrid scale spatial variability. J. Climate 2:816-831.

Fang, X. and Stefan, H.G., 1996. Long-term lake water temperature and ice cover simulations/measurements. Cold Regions Science and Technology 24(3):289-304.

Farouki, O.T. 1981. The thermal properties of soils in cold regions. Cold Regions Sci. and Tech. 5:67-75.

Farquhar, G.D., von Caemmerer, S., and Berry, J.A. 1980. A biochemical model of photosynthetic CO_2 assimilation in leaves of C_3 species. Planta 149:78-90.

Farquhar, G.D., and von Caemmerer, S. 1982. Modeling of photosynthetic response to environmental conditions. pp. 549-587. In: O.L. Lange, P.S. Nobel, C.B. Osmond, and H. Zeigler (editors) Encyclopedia of Plant Physiology. Vol. 12B. Physiological Plant Ecology. II. Water Relations and Carbon Assimilation. Springer-Verlag, New York.

Ferrari, J.B., 1999. Fine-scale patterns of leaf litterfall and nitrogen cycling in an old-growth forest. Canadian Journal of Forest Research, 29: 291-302.

Firestone, M.K. and Davidson, E.A. 1989. Exchange of Trace Gases between Terrestrial Ecosystems and the Atmosphere. In: M.O. Andreae and D.S. Schimel (Editors). John Wiley and Sons, pp. 7-21.

Flanner, M.G., and Zender. C.S. 2005. Snowpack radiative heating: Influence on Tibetan Plateau climate. Geophys. Res. Lett. 32:L06501. DOI:10.1029/2004GL022076.

Flanner, M.G., and Zender, C.S. 2006. Linking snowpack microphysics and albedo evolution. J. Geophys. Res. 111:D12208. DOI:10.1029/2005JD006834.

Flanner, M.G., Zender, C.S., Randerson, J.T., and Rasch, P.J. 2007. Present day climate forcing and response from black carbon in snow. J. Geophys. Res. 112:D11202. DOI:10.1029/2006JD008003.

Flatau, P.J., Walko, R.L., and Cotton, W.R. 1992. Polynomial fits to saturation vapor pressure. J. Appl. Meteor. 31:1507-1513.

Friedl, M.A., McIver, D.K., Hodges, J.C.F., Zhang, X.Y., Muchoney, D., Strahler, A.H., Woodcock, C.E., Gopal, S., Schneider, A., Cooper, A., Baccini, A., Gao, F., and Schaaf, C. 2002. Global land cover mapping from MODIS: algorithms and early results. Remote Sens. Environ. 83:287-302.

Frolking, S., et al. 2001. Modeling Northern Peatland Decomposition and Peat Accumulation. Ecosystems. 4(5):479-498.

Gallais, A., Coque, M. Quillere, I., Prioul, J., and Hirel, B. 2006. Modeling postsilking nitrogen fluxes in maize (Zea mays) using 15N-labeling field experiments. New Phytologist 172:696-707.

Gallais, A., Coque, M., Gouis, J. L., Prioul, J. L., Hirel, B., and Quillere, I. 2007. Estimating the proportion of nitrogen remobilization and of postsilking nitrogen uptake allocated to maize kernels by Nitrogen-15 labeling. Crop Sci. 47:685-693.

Galloway, J.N., et al. 2004. Nitrogen cycles: past, present, and future. Biogeochem. 70:153-226.

Garcia, R.L., Kanemasu, E.T., Blad, B.L., Bauer, A., Hatfield, J.L., Major, D.A., Reginato, R.J., and Hubbard, K.G. 1988. Interception and use efficiency of light in winter wheat under different nitrogen regimes. Agric. For. Meteor. 44:175-186.

Gash, J.H.C., Nobre, C.A., Roberts, J.M., and Victoria, R.L. 1996. An overview of ABRACOS. pp. 1-14. In: J.H.C. Gash, C.A. Nobre, J.M. Roberts, and R.L. Victoria (editors) Amazonian Deforestation and Climate. John Wiley and Sons, Chichester, England.

Gholz, H.L., Perry, C.S., Cropper, W.P., Jr. and Hendry, L.C., 1985. Litterfall, decomposition, and nitrogen and phosphorous dynamics in a chronosequence of slash pine (*Pinus elliottii*) plantations. Forest Science, 31(2): 463-478.

Giglio, L., Csiszar, I., and Justice, C.O. 2006. Global distribution and seasonality of active fires as observed with the Terra and Aqua Moderate Resolution Imaging Spectroradiometer (MODIS) sensors. J. Geophys. Res. 111:G02016. DOI:10.1029/2005JG000142.

Global Soil Data Task 2000. Global soil data products CD-ROM (IGBP-DIS). International Geosphere-Biosphere Programme-Data and Information Available Services [Available online at http://www.daac.ornl.gov].

Gomes, E.P.C., Mantovani, W., and Kageyama, P.Y. 2003. Mortality and recruitment of trees in a secondary montane rain forest in southeastern Brazil. Brazilian Journal of Biology 63:47-60.

Gosz, J.R., Likens, G.E., and Bormann, F.H. 1973. Nutrient release from decomposing leaf and branch litter in the Hubbard Brook Forest, New Hampshire. Ecological Monographs 43:173-191.

Gotangco Castillo C., Levis S., and Thornton P. 2012. Evaluation of the new CNDV option of the Community Land Model: Effects of dynamic vegetation and interactive nitrogen on CLM4 means and variability. J. Climate 25:3702-3714. DOI:10.1175/JCLID-11-00372.1.

Graham, S.T., Famiglietti, J.S., and Maidment, D.R. 1999. Five-minute, 1/2º, and 1º data sets of continental watersheds and river networks for use in regional and global hydrologic and climate system modeling studies. Water Resour. Res. 35:583-587.

Grenfell, T.C., and Warren, S.G. 1999. Representation of a nonspherical ice particle by a collection of independent spheres for scattering and absorption of radiation. J. Geophys. Res. 104(D24):37697-37709.

del Grosso, S.J., et al. 2000. General model for N2O and N2 gas emissions from soils due to dentrification. Global Biogeochem. Cycles 14(4):1045-1060.

Guenther, A., Hewitt, C.N., Erickson, D., Fall, R., Geron, C., Graedel, T., Harley, P., Klinger, L., Lerdau, M., McKay, W.A., Pierce, T., Scholes, B., Steinbrecher, R., Tallamraju, R., Taylor, J., and Zimmerman, P. 1995. A global model of natural volatile organic compound emissions. J. Geophys. Res. 100:8873-8892.

Guenther, A., Karl, T., Harley, P., Wiedinmyer, C., Palmer. P.I., and Geron, C. 2006. Estimates of global terrestrial isoprene emissions using MEGAN (Model of Emissions of Gases and Aerosols from Nature). Atmos. Chem. Phys. 6:3181–3210.

Guenther, A. B., Jiang, X., Heald, C. L., Sakulyanontvittaya, T., Duhl, T., Emmons, L. K., & Wang, X., 2012. The Model of Emissions of Gases and Aerosols from Nature version 2.1 (MEGAN2.1): an extended and updated framework for modeling biogenic emissions, Geosci. Model Dev., 5, 1471–1492. DOI:10.5194.

Hack, J.J., Caron, J.M., Yeager, S.G., Oleson, K.W., Holland, M.M., Truesdale, J.E., and Rasch, P.J. 2006. Simulation of the global hydrological cycle in the CCSM Community Atmosphere Model version 3 (CAM3): mean features. J. Climate 19:2199-2221.

Hansen, M., DeFries, R.S., Townshend, J.R.G., Carroll, M., Dimiceli, C., and Sohlberg, R.A. 2003. Global percent tree cover at a spatial resolution of 500 meters: first results of the MODIS vegetation continuous fields algorithm. Earth Interactions 7(10):1-15.

Hastings, D.A., Dunbar, P.K., Elphingstone, G.M., Bootz, M., Murakami, H., Maruyama, H., Masaharu, H., Holland, P., Payne, J., Bryant, N.A., Logan, T.L., Muller, J.-P., Schreier, G., and MacDonald, J.S., eds., 1999. The Global Land One-kilometer Base Elevation (GLOBE) Digital Elevation Model, Version 1.0. National Oceanic and Atmospheric Administration, National Geophysical Data Center, 325 Broadway, Boulder, Colorado 80305-3328, U.S.A.

Heald, C.L., Henze, D.K., Horowitz, L.W., Feddema, J., Lamarque, J.-F., Guenther, A., Hess, P.G., Vitt, F., Seinfeld, J.H., Goldstein, A.H., and Fung, I. 2008. Predicted change in global secondary organic aerosol concentrations in response to future climate, emissions, and land use change. J. Geophys. Res. 113:D05211. DOI:10.1029/2007JD009092.

Heald, C.L., Wilkinson, M.J., Monson, R.K., Alo, C.A., Wang, G.L., and Guenther, A. 2009. Response of isoprene emission to ambient CO_2 changes and implications for global budgets. Global Change Biol. 15:1127-1140. DOI:10.1111/j.1365-2486.2008.01802.x

Henderson-Sellers, B. 1985. New formulation of eddy diffusion thermocline models. Appl. Math. Modelling 9:441-446.

Henderson-Sellers, B. 1986. Calculating the surface energy balance for lake and reservoir modeling: A review. Rev. Geophys. 24:625-649.

Henderson-Sellers, A., Yang, Z.-L., and Dickinson, R.E. 1993. The project for intercomparison of land-surface parameterization schemes. Bull. Amer. Meteor. Soc. 74: 1335-1349.

Hostetler, S.W., and Bartlein, P.J. 1990. Simulation of lake evaporation with application to modeling lake level variations of Harney-Malheur Lake, Oregon. Water Resour. Res. 26:2603-2612.

Hostetler, S.W., Bates, G.T., and Giorgi, F. 1993. Interactive coupling of a lake thermal model with a regional climate model. J. Geophys. Res. 98:5045-5057.

Hostetler, S.W., Giorgi, F., Bates, G.T., and Bartlein, P.J. 1994. Lake-atmosphere feedbacks associated with paleolakes Bonneville and Lahontan. Science 263:665-668.

Hou, Z., Huang, M., Leung, L.R., Lin, G., and Ricciuto, D.M. 2012. Sensitivity of surface flux simulations to hydrologic parameters based on an uncertainty quantification framework applied to the Community Land Model. J. Geophys. Res. 117:D15108.

Huang, M., and Liang, X. 2006. On the assessment of the impact of reducing parameters and identification of parameter uncertainties for a hydrologic model with applications to ungauged basins. J. Hydrol. 320:37-61.

Hugelius, G., C. Tarnocai, G. Broll, J.G. Canadell, P. Kuhry, adn D.K. Swanson, 2012. The Northern Circumpolar Soil Carbon Database: spatially distributed datasets of soil coverage and soil carbon storage in the northern permafrost regions. Earth Syst. Sci. Data Discuss., 5, 707-733 (available online at (http://dev1.geo.su.se/bbcc/dev/ncscd/).

Hunt, H.W., Ingham, E.R., Coleman, D.C., Elliott, E.T., and Reid, C.P.P. 1988. Nitrogen limitation of production and decomposition in prairie, mountain meadow, and pine forest. Ecology 69:1009-1016.

Hunt, E.R., Jr. and Running, S.W., 1992. Simulated dry matter yields for aspen and spruce stands in the north american boreal forest. Canadian Journal of Remote Sensing, 18(3): 126-133.

Hunt, E.R., Jr. et al., 1996. Global net carbon exchange and intra-annual atmospheric CO_2 concentrations predicted by an ecosystem process model and three-dimensional atmospheric transport model. Global Biogeochemical Cycles, 10(3): 431-456.

Hurtt, G.C., Frolking, S., Fearon, M.G., Moore, B., Shevliakova, E., Malyshev, S., Pacala, S.W., and Houghton, R.A. 2006. The underpinnings of land-use history: three centuries of global gridded land-use transitions, wood-harvest activity, and resulting secondary lands. Global Change Biol. 12:1208-1229.

Hurtt, G.C., et al. 2011. Harmonization of land-use scenarios for the period 1500-2100: 600 years of global gridded annual land-use transitions, wood harvest, and resulting secondary lands. Climatic Change 109:117-161. DOI:10.1007/s10584-011-0153-2.

Idso, S.B. 1981. A set of equations for full spectrum and 8- to 14- μm and 10.5- to 12.5- μm thermal radiation from cloudless skies. Water Resour. Res. 17:295-304.

Iiyama, I. and Hasegawa, S., 2005. Gas diffusion coefficient of undisturbed peat soils. Soil Science and Plant Nutrition 51(3):431-435.

Jackson, R. B., Canadell, J., Ehleringer, J. R., Mooney, H. A., Sala, O. E., and Schulze, E. D. 1996. A global analysis of root distributions for terrestrial biomes Oecologia 108:389–411. DOI:10.1007/BF00333714.

Jackson, T.L., Feddema, J.J., Oleson, K.W., Bonan, G.B., and Bauer, J.T. 2010. Parameterization of urban characteristics for global climate modeling. Annals of the Association of American Geographers. 100(4):848-865.

Jenkinson, D. and Coleman, K. 2008. The turnover of organic carbon in subsoils. Part 2. Modelling carbon turnover. European Journal of Soil Science 59(2):400-413.

Jordan, R. 1991. A One-dimensional Temperature Model for a Snow Cover: Technical Documentation for SNTHERM.89. U.S. Army Cold Regions Research and Engineering Laboratory, Special Report 91-16.

Kattge, J., and Knorr, W. 2007. Temperature acclimation in a biochemical model of photosynthesis: a reanalysis of data from 36 species. Plant Cell Environ. 30:1176-1190. DOI:10.1111/j.1365-3040.2007.01690.x.

Kattge, J., Knorr, W., Raddatz, T., and Wirth C. 2009: Quantifying photosynthetic capacity and its relationship to leaf nitrogen content for global–scale terrestrial biosphere models. Global Change Biol. 15:976–991.

Keller, M., Palace, M., Asner, G.P., Pereira, R., Jr. and Silva, J.N.M., 2004. Coarse woody debris in undisturbed and logged forests in the eastern Brazilian Amazon. Global Change Biology, 10: 784-795.

Kellner, E., Baird, A.J., Oosterwoud, M., Harrison, K. and Waddington, J.M., 2006. Effect of temperature and atmospheric pressure on methane (CH4) ebullition from near-surface peats. Geophys. Res. Lett. 33(18). DOI:10.1029/2006GL027509.

Kimball, J.S., Thornton, P.E., White, M.A. and Running, S.W. 1997. Simulating forest productivity and surface-atmosphere exchange in the BOREAS study region. Tree Physiology 17:589-599.

Kohyama, T., Suzuki, E., Partomihardjo, T., and Yamada, T. 2001. Dynamic steady state of patch-mosaic tree size structure of a mixed diptocarp forest regulated by local crowding. Ecological Research 16:85-98.

Kourzeneva, E., 2009. Global dataset for the parameterization of lakes in Numerical Weather Prediction and Climate modeling. ALADIN Newsletter, No 37, July-December, 2009, F. Bouttier and C. Fischer, Eds., Meteo-France, Toulouse, France, 46-53.

Kourzeneva, E., 2010: External data for lake parameterization in Numerical Weather Prediction and climate modeling. Boreal Environment Research, 15, 165-177.

Kourzeneva, E., Asensio, H., Martin, E. and Faroux, S., 2012. Global gridded dataset of lake coverage and lake depth for use in numerical weather prediction and climate modelling. Tellus A 64.

Koven, C., et al. 2009. On the formation of high-latitude soil carbon stocks: The effects of cryoturbation and insulation by organic matter in a land surface model. Geophys. Res. Lett. 36: L21501.

Koven, C.D., et al. 2011. Permafrost carbon-climate feedbacks accelerate global warming. Proceedings of the National Academy of Sciences 108(36):14769-14774.

Koven, C.D. et al. 2013. The effect of vertically-resolved soil biogeochemistry and alternate soil C and N models on C dynamics of CLM4. Biogeosciences Discussions 10(4):7201-7256.

Kucharik, C.J., Foley, J.A., Delire, C., Fisher, V.A., Coe, M.T., Lenters, J.D., Young-Molling, C., and Ramankutty, N. 2000. Testing the performance of a dynamic global ecosystem model: water balance, carbon balance, and vegetation structure. Global Biogeochem. Cycles 14: 795–825.

Kucharik, C.J., and Brye, K.R. 2003. Integrated BIosphere Simulator (IBIS) yield and nitrate loss predictions for Wisconsin maize receiving varied amounts of nitrogen fertilizer. Journal of Environmental Quality 32: 247–268.

Ladd, J.N., Jocteur-Monrozier, L. and Amato, M., 1992. Carbon turnover and nitrogen transformations in an alfisol and vertisol amended with [U-^{14}C] glucose and [^{15}N] ammonium sulfate. Soil Biology and Biochemistry, 24(4): 359-371.

Lamarque, J.-F., et al. 2010. Historical (1850-2000) gridded anthropogenic and biomass burning emissions of reactive gases and aerosols: methodology and application. Atmos. Chem. Phys. Discuss. 10:4963-5019. DOI:10.5194/acpd-10-4963-2010.

Larcher, W. 1995. Physiological Plant Ecology, Springer-Verlag, Berlin Heidelberg.

Lavigne, M.B., and Ryan, M.G. 1997. Growth and maintenance respiration rates of aspen, black spruce, and jack pine stems at northern and southern BOREAS sites. Tree Phys. 17:543-551.

Law, B.E., Sun, O.J., Campbell, J., Van Tuyl, S. and Thornton, P.E. 2003. Changes in carbon storage and fluxes in a chronosequence of ponderosa pine. Global Change Biology, 9(4): 510-514.

Lawrence, D.M., Thornton, P.E., Oleson, K.W., and Bonan, G.B. 2007. The partitioning of evapotranspiration into transpiration, soil evaporation, and canopy evaporation in a GCM: Impacts on land-atmosphere interaction. J. Hydrometeor. 8:862-880.

Lawrence, D.M., and Slater, A.G. 2008. Incorporating organic soil into a global climate model. Clim. Dyn. 30. DOI:10.1007/s00382-007-0278-1.

Lawrence, D.M., Slater, A.G., Romanovsky, V.E., and Nicolsky, D.J. 2008. The sensitivity of a model projection of near-surface permafrost degradation to soil column depth and inclusion of soil organic matter. J. Geophys. Res. 113:F02011. DOI:10.1029/2007JF000883.

Lawrence, D.M., K.W. Oleson, M.G. Flanner, P.E. Thornton, S.C. Swenson, P.J. Lawrence, X. Zeng, Z.-L. Yang, S. Levis, K. Sakaguchi, G.B. Bonan, and A.G. Slater, 2011. Parameterization improvements and

functional and structural advances in version 4 of the Community Land Model. J. Adv. Model. Earth Sys. 3. DOI:10.1029/2011MS000045.

Lawrence, P.J., and Chase, T.N. 2007. Representing a MODIS consistent land surface in the Community Land Model (CLM 3.0). J. Geophys. Res. 112:G01023. DOI:10.1029/2006JG000168.

Lawrence, P.J., and Chase, T.N. 2010. Investigating the climate impacts of global land cover change in the Community Climate System Model. Int. J. Climatol. 30:2066-2087. DOI:10.1002/joc.2061.

Lawrence, P.J., et al. 2012. Simulating the biogeochemical and biogeophysical impacts of transient land cover change and wood harvest in the Community Climate System Model (CCSM4) from 1850 to 2100. J. Climate 25:3071-3095. DOI:10.1175/JCLI-D-11-00256.1.

Lehner, B. and Döll, P., 2004. Development and validation of a global database of lakes, reservoirs and wetlands, J. Hydrol., 296, 1–22.

Le Page, Y., van der Werf, G.R., Morton, D.C., and Pereira, J.M.C. 2010. Modeling fire-driven deforestation potential in Amazonia under current and projected climate conditions. J. Geophys. Res. 115:G03012. DOI:10.1029/2009JG001190.

Lerman, A., 1979. Geochemical processes: Water and sediment environments. John Wiley and Sons, New York, N.Y.

Letts, M.G., Roulet, N.T., Comer, N.T., Skarupa, M.R., and Verseghy, D.L. 2000. Parametrization of peatland hydraulic properties for the Canadian Land Surface Scheme. Atmos.-Ocean 38:141-160.

Levin, I. and Kromer, B. 2004. The tropospheric 14CO2 level in mid-latitudes of the Northern Hemisphere (1959-2003) Radiocarbon 46(3):1.

Levis, S., Wiedinmyer, C., Bonan, G.B., and Guenther, A. 2003. Simulating biogenic volatile organic compound emissions in the Community Climate System Model. J. Geophys. Res. 108:4659. DOI:10.1029/2002JD003203.

Levis, S., Bonan, G.B., Vertenstein, M., and Oleson, K.W. 2004. The community land model's dynamic global vegetation model (CLM-DGVM): technical description and user's guide. NCAR Technical Note NCAR/TN-459+STR. National Center for Atmospheric Research, Boulder, Colorado. 50 pp.

Levis, S., Thornton, P., Bonan, G., and Kucharik, C. 2009. Modeling land use and land management with the Community Land Model. iLeaps newsletter, No. 7.

Levis, S., Bonan, G., Kluzek, E., Thornton, P., Jones, A., Sacks, W., and Kucharik, C 2012. Interactive crop management in the Community Earth System Model (CESM1): Seasonal influences on land-atmosphere fluxes. J. Climate 25: 4839-4859. DOI:10.1175/JCLI-D-11-00446.1.

Li, C., Aber, J., Stange, F., Butterbach-Bahl, K. and Papen, H. 2000. A process-oriented model of N2O and NO emissions from forest soils: 1. Model development. J. Geophys. Res. 105(D4):4369-4384.

Li, F., Zeng, X.-D., and Levis, S. 2012a. A process-based fire parameterization of intermediate complexity in a Dynamic Global Vegetation Model. Biogeosciences 9:2761-2780.

Li, F., Zeng, X. D., and Levis, S. 2012b. Corrigendum to "A process-based fire parameterization of intermediate complexity in a Dynamic Global Vegetation Model" published in Biogeosciences, 9, 2761–2780, 2012". Biogeosciences 9: 4771-4772.

Li, F., Levis, S., and Ward, D. S. 2013a. Quantifying the role of fire in the Earth system – Part 1: Improved global fire modeling in the Community Earth System Model (CESM1). Biogeosciences 10:2293-2314.

Li, H.-Y., Huang, M., Tesfa, T., Ke, Y., Sun, Y., Liu, Y., and Leung, L. R. 2013b. A subbasin-based framework to represent land surface processes in an Earth System Model, Geosci. Model Dev. Discuss. 6:2699-2730. DOI:10.5194/gmdd-6-2699-2013.

Li, H., Huang, M., Wigmosta, M.S., Ke, Y., Coleman, A.M., Leung, L.R., Wang, A., and Ricciuto, D.M. 2011. Evaluating runoff simulations from the Community Land Model 4.0 using observations from

flux towers and a mountainous watershed. J. Geophys. Res. 116:D24120. DOI:10.1029/2011JD016276.

Liang, X., Lettenmaier, D.P., Wood, E.F., and Burges, S.J. 1994. A simple hydrologically based model of land surface water and energy fluxes for GSMs. J. Geophys. Res. 99(D7):14,415–14,428.

Lipscomb, W., and Sacks, W. 2012. The CESM land ice model documentation and user's guide. 46 pp. [Available online at http://www.cesm.ucar.edu/models/cesm1.1/cism/].

Lloyd, J. and Taylor, J.A., 1994. On the temperature dependence of soil respiration. Functional Ecology, 8: 315-323.

Lloyd, J., et al. 2010. Optimisation of photosynthetic carbon gain and within-canopy gradients of associated foliar traits for Amazon forest trees. Biogeosci. 7:1833-1859. DOI:10.5194/bg-7-1833-2010.

Lobell, D.B., Bala, G., and Duffy, P.B. 2006. Biogeophysical impacts of cropland management changes on climate. Geophys. Res. Lett. 33:L06708. DOI:10.1029/2005GL025492.

Loveland, T.R., Reed, B.C., Brown, J.F., Ohlen, D.O., Zhu, Z., Yang, L., and Merchant, J.W. 2000. Development of a global land cover characteristics database and IGBP DISCover from 1 km AVHRR data. Int. J. Remote Sens. 21:1303-1330.

Lowe, P.R. 1977. An approximating polynomial for the computation of saturation vapor pressure. J. Appl. Meteor. 16:100-103.

Luo, Y., Hui, D., and Zhang, D. 2006. Elevated CO2 stimulates net accumulations of carbon and nitrogen in land ecosystems: a meta-analysis. Ecology 87:53-63.

Magill, A.H. et al., 1997. Biogeochemical response of forest ecosystems to simulated chronic nitrogen deposition. Ecological Applications, 7(2): 402-415.

Mahowald, N.M., Muhs, D.R., Levis, S., Rasch, P.J., Yoshioka, M., Zender, C.S., and Luo, C. 2006. Change in atmospheric mineral aerosols in response to climate: last glacial period, pre-industrial, modern and doubled CO_2 climates. J. Geophys. Res. 111:D10202. DOI:10.1029/2005JD006653.

Makela, A. 2002. Derivation of stem taper from the pipe model theory in a carbon balance framework. Tree Phys. 22:891-905.

Manning, M.R. and Melhuish, W.H. 1994. Trends: A Compendium of Data on Global Change. Carbon Dioxide Information Analysis Center,. Oak Ridge National Laboratory, U.S. Department of Energy, Oak Ridge, Tenn., U.S.A.

Mao, J., Thornton, P.E., Shi, X., Zhao, M., and Post, W.M. 2012. Remote sensing evaluation of CLM4 GPP for the period 2000 to 2009. J. Climate 25:5327-5342.

Mao, J., Shi, X., Thornton, P.E., Hoffman, F.M., Zhu, Z., and Ranga B. Myneni, R.B. 2013. Global latitudinal-asymmetric vegetation growth trends and their driving mechanisms: 1982-2009. Remote Sensing 5(3):1484-1497.

Martin, J.P., Haider, K. and Kassim, G., 1980. Biodegradation and stabilization after 2 years of specific crop, lignin, and polysaccharide carbons in soils. Soil Science Society of America Journal 44:1250-1255.

Mary, B., Fresneau, C., Morel, J.L. and Mariotti, A., 1993. C and N cycling during decomposition of root mucilage, roots and glucose in soil. Soil Biology and Biochemistry 25(8):1005-1014.

McGuire, A.D., Melillo, J.M., Joyce, L.A., Kicklighter, D.W., Grace, A.L., Moore III, B., and Vorosmarty, C.J. 1992. Interactions between carbon and nitrogen dynamics in estimating net primary productivity for potential vegetation in North America. Global Biogeochem. Cycles 6:101-124.

Melzer, E., and O'Leary, M.H. 1987. Anapleurotic CO2 Fixation by Phosphoenolpyruvate Carboxylase in C3 Plants. Plant. Physiol. 84:58.

Miller, J.R., Russell, G.L., and Caliri, G. 1994. Continental-scale river flow in climate models. J. Climate 7:914-928.

Millington, R. and Quirk, J.P., 1961. Permeability of Porous Solids. Transactions of the Faraday Society 57(8):1200-1207.

Mironov, D. et al., 2010. Implementation of the lake parameterisation scheme FLake into the numerical weather prediction model COSMO. Boreal Environment Research 15(2):218-230.

Mitchell, T.D., and Jones, P.D. 2005. An improved method of constructing a database of monthly climate observations and associated high-resolution grids. Int. J. Climatol. 25:693-712.

Moldrup, P. et al. 2003. Modeling diffusion and reaction in soils: X. A unifying model for solute and gas diffusivity in unsaturated soil. Soil Science 168(5):321-337.

Myneni, R.B., et al. 2002. Global products of vegetation leaf area and fraction absorbed PAR from year one of MODIS data. Remote Sens. Environ. 83:214-231.

Neff, J.C., Harden, J.W. and Gleixner, G. 2005. Fire effects on soil organic matter content, composition, and nutrients in boreal interior Alaska. Canadian Journal of Forest Research-Revue Canadienne De Recherche Forestiere 35(9):2178-2187.

Neitsch, S.L., Arnold, J.G., Kiniry, J.R., and Williams J.R. 2005. Soil and Water Assessment Tool, Theoretical Documentation: Version 2005. Temple, TX. USDA Agricultural Research Service and Texas A&M Blackland Research Center.

Nemani, R.R., and Running, S.W. 1996. Implementation of a hierarchical global vegetation classification in ecosystem function models. J. Veg. Sci. 7:337-346.

Niinemets, U., Kull, O., and Tenhunen, J.D. 1998. An analysis of light effects on foliar morphology, physiology, and light interception in temperate deciduous woody species of contrasting shade tolerance. Tree Phys. 18:681-696.

Niu, G.-Y., Yang, Z.-L., Dickinson, R.E., and Gulden, L.E. 2005. A simple TOPMODEL-based runoff parameterization (SIMTOP) for use in global climate models. J. Geophys. Res. 110:D21106. DOI:10.1029/2005JD006111.

Niu, G.-Y., and Yang, Z.-L. 2006. Effects of frozen soil on snowmelt runoff and soil water storage at a continental scale. J. Hydrometeor. 7:937-952.

Niu, G.-Y., Yang, Z.-L., Dickinson, R.E., Gulden, L.E., and Su, H. 2007. Development of a simple groundwater model for use in climate models and evaluation with Gravity Recovery and Climate Experiment data. J. Geophys. Res. 112:D07103. DOI:10.1029/2006JD007522.

Niu, G.-Y., and Yang, Z.-L. 2007. An observation-based formulation of snow cover fraction and its evaluation over large North American river basins. J. Geophys. Res. 112:D21101. DOI:10.1029/2007JD008674.

Nydal, R. and Lövseth, K. 1996. Carbon-14 Measurements In Atmospheric CO2 From Northern And Southern Hemisphere Sites, 1962-1993, Carbon Dioxide Information Analysis Center.

Oikawa, S., Hikosaka, K. and Hirose, T., 2005. Dynamics of leaf area and nitrogen in the canopy of an annual herb, Xanthium canadense. Oecologia, 143(4): 517-526.

Oke, T. 1987. Boundary Layer Climates (2nd edition). Routledge, London and New York.

Oleson, K.W., and Bonan, G.B. 2000. The effects of remotely-sensed plant functional type and leaf area index on simulations of boreal forest surface fluxes by the NCAR land surface model. J. Hydrometeor. 1:431-446.

Oleson, K.W., Dai, Y., Bonan, G., Bosilovich, M., Dickinson, R., Dirmeyer, P., Hoffman, F., Houser, P., Levis, S., Niu, G.-Y., Thornton, P., Vertenstein, M., Yang, Z.-L., and Zeng. X. 2004. Technical description of the Community Land Model (CLM). NCAR Technical Note NCAR/TN-461+STR. National Center for Atmospheric Research, Boulder, Colorado. 173 pp.

Oleson, K.W., Niu, G.-Y., Yang, Z.-L., Lawrence, D.M., Thornton, P.E., Lawrence, P.J., Stöckli, R., Dickinson, R.E., Bonan, G.B., Levis, S., Dai, A., and Qian, T. 2008a. Improvements to the Community

Land Model and their impact on the hydrological cycle. J. Geophys. Res. 113:G01021. DOI:10.1029/2007JG000563.

Oleson, K.W., Bonan, G.B., Feddema, J., Vertenstein, M., and Grimmond, C.S.B. 2008b. An urban parameterization for a global climate model. 1. Formulation and evaluation for two cities. J. Appl. Meteor. Clim. 47:1038-1060.

Oleson, K.W., Bonan, G.B., Feddema, J., and Vertenstein, M. 2008c. An urban parameterization for a global climate model. 2. Sensitivity to input parameters and the simulated urban heat island in offline simulations. J. Appl. Meteor. Clim. 47:1061-1076.

Oleson, K.W., et al. 2010a. Technical description of version 4.0 of the Community Land model (CLM). NCAR Technical Note NCAR/TN-478+STR, National Center for Atmospheric Research, Boulder, CO, 257 pp.

Oleson, K.W., Bonan, G.B., Feddema, J., Vertenstein, M., and Kluzek, E. 2010b. Technical description of an urban parameterization for the Community Land Model (CLMU). NCAR Technical Note NCAR/TN-480+STR, National Center for Atmospheric Research, Boulder, CO, 169 pp.

Olson, J.S., 1963. Energy storage and the balance of producers and decomposers in ecological systems. Ecology 44(2):322-331.

Olson, D.M., Dinerstein, E., Wikramanayake, E.D., Burgess, N.D., Powell, G.V.N., Underwood, E.C., D'Amico, J.A., Itoua, I., Strand, H. E., Morrison, J. C., Loucks, C. J., Allnutt, T. F., Ricketts, T. H., Kura, Y., Lamoreux, J. F., Wettengel, W. W., Heda, P., and Kassem, K. R., 2001. Terrestrial ecoregions of the world a new map of life on earth, Bioscience, 51, 933–938.

Orchard, V.A. and Cook, F.J., 1983. Relationship between soil respiration and soil moisture. Soil Biology and Biochemistry, 15(4): 447-453.

Owen, P.R. 1964. Saltation of uniform grains in air. J. Fluid Mech. 20:225-242.

Ozdogan, M., Rodell, M., Beaudoing, H.K., and Toll, D.L. 2010. Simulating the effects of irrigation over the United States in a land surface model based on satellite-derived agricultural data. Journal of Hydrometeorology 11:171-184.

Page, S.E., Siegert, F., Rieley, J.O., Boehm, H-D.V., Jaya, A., and Limin, S. 2002. The amount of carbon released from peat and forest fires in Indonesia in 1997. Nature 420:61-65.

Panofsky, H.A., and Dutton, J.A. 1984. Atmospheric Turbulence: Models and Methods for Engineering Applications. John Wiley and Sons, New York.

Parton, W., Stewart, J. and Cole, C., 1988. Dynamics of C, N, P And S in Grassland Soils - A Model. Biogeochemistry 5:109-131.

Parton, W.J., et al. 1993. Observations and modeling of biomass and soil organic matter dynamics for the grassland biome worlwide. Global Biogeochemical Cycles 7(4):785-809.

Parton, W. et al. 1996. Generalized model for N2 and N2O production from nitrification and denitrification. Global Biogeochemical Cycles 10(3):401-412.

Parton, W.J. et al. 2001. Generalized model for NOx and N2O emissions from soils. J. Geophys. Res. 106(D15):17403-17419.

Paterson, W.S.B., 1994. The Physics of Glaciers. Elsevier Science Inc., New York, 480 pp.

Petrescu, A.M.R. et al. 2010. Modeling regional to global CH4 emissions of boreal and arctic wetlands. Global Biogeochemical Cycles, 24(GB4009).

Philip, J.R. 1957. Evaporation, and moisture and heat fields in the soil. J. Meteor. 14:354-366.

Piao, S.L., et al. 2012. The carbon budget of terrestrial ecosystems in East Asia over the last two decades. Biogeosciences 9:3571-3586.

Pivovarov, A.A., 1972. Thermal Conditions in Freezing Lakes and Reservoirs. John Wiley, New York.

Pollmer, W.G., Eberhard, D., Klein, D., and Dhillon, B.S. 1979. Genetic control of nitrogen uptake and translocation in maize. Crop Sci. 19:82-86.

Portmann, F.T., Siebert, S., and Döll, P. 2010. MIRCA2000 - Global monthly irrigated and rainfed crop areas around the year 2000: A new high-resolution data set for agricultural and hydrological modeling. Global Biogeochem. Cycles. 24, GB1011. DOI:10.1029/2008GB003435.

Press, W.H., Teukolsky, S.A., Vetterling, W.T., and Flannery, B.P. 1992. Numerical Recipes in FORTRAN: The Art of Scientific Computing. Cambridge University Press, New York.

Prigent, C., Papa, F., Aires, F., Rossow, W.B. and Matthews, E. 2007. Global inundation dynamics inferred from multiple satellite observations, 1993-2000. J. Geophys. Res. 112(D12).

Pritchard, M.S., Bush, A.B.G., and Marshall, S.J. 2008. Neglecting ice-atmosphere interactions underestimates ice sheet melt in millennial-scale deglaciation simulations. Geophys. Res. Lett. 35:L01503. DOI:10.1029/2007GL031738.

Qian, T., Dai, A., Trenberth, K.E., and Oleson, K.W. 2006. Simulation of global land surface conditions from 1948 to 2004: Part I: Forcing data and evaluations. J. Hydrometeor. 7:953-975.

Ramankutty, N., and Foley, J. A., 1998. Characterizing patterns of global land use: An analysis of global croplands data. Global Biogeochemical Cycles, 12(4), 667-685.

Ramankutty, N., Evan, A., Monfreda, C., and Foley, J.A. 2008. Farming the Planet. Part 1: The Geographic Distribution of Global Agricultural Lands in the Year 2000. Global Biogeochem. Cycles. 22:GB1003. DOI:10.1029/2007GB002952.

Randlett, D.L., Zak, D.R., Pregitzer, K.S., and Curtis, P.S. 1996. Elevated atmospheric carbon dioxide and leaf litter chemistry: Influences on microbial respiration and net nitrogen mineralization. Soil Sci. Soc. Am. J. 60:1571-1577.

Rastetter, E.B., Ryan, M.G., Shaver, G.R., Melillo, J.M., Nadelhoffer, K.J., Hobbie, J.E., and Aber, J.D. 1991. A general biogeochemical model describing the responses of the C and N cycles in terrestrial ecosystems to changes in CO2, climate and N deposition. Tree Phys. 9:101-126.

Rastner, P., Bolch, T., Mölg, N., Machguth, H., and Paul, F., 2012. The first complete glacier inventory for the whole of Greenland, The Cryosphere Discuss., 6, 2399-2436, 10.5194/tcd-6-2399-2012.

Riley, W. J., Z. M. Subin, D. M. Lawrence, S. C. Swenson, M. S. Torn, L. Meng, N. Mahowald, and P. Hess, 2011a. Barriers to predicting global terrestrial methane fluxes: Analyses using a methane biogeochemistry model integrated in CESM. Biogeosciences, 8, 1925–1953. DOI:10.5194/bg-8-1925-2011.

Riley, W.J. et al. 2011b. CLM4Me, a Methane Biogeochemistry Model Integrated in CESM, Land and Biogeochemistry Model Working Group Meeting, Boulder, CO.

Ryan, M. G. 1991. A simple method for estimating gross carbon budgets for vegetation in forest ecosystems. Tree Phys. 9:255-266.

Running, S.W. and Coughlan, J.C., 1988. A general model of forest ecosystem processes for regional applications. I. Hydrological balance, canopy gas exchange and primary production processes. Ecological Modelling, 42: 125-154.

Running, S.W. et al., 1989. Mapping regional forest evapotranspiration and photosynthesis by coupling satellite data with ecosystem simlation. Ecology, 70(4): 1090-1101.

Running, S.W. and Gower, S.T., 1991. FOREST BGC, A general model of forest ecosystem processes for regional applications. II. Dynamic carbon allocation and nitrogen budgets. Tree Physiology, 9: 147-160.

Running, S.W. and Hunt, E.R., Jr., 1993. Generalization of a forest ecosystem process model for other biomes, BIOME-BGC, and an applicationfor global-scale models. In: J.R. Ehleringer and C. Field (Editors), Scaling Physiological Processes: Leaf to Globe. Academic Press, San Diego, CA, pp. 141-158.

Sacks, W. J., Cook, B. I., Buenning, N., Levis, S., and Helkowski, J. H. 2009. Effects of global irrigation on the near-surface climate. Climate Dyn., 33, 159–175. DOI:10.1007/s00382-008-0445-z.

Saggar, S., Tate, K.R., Feltham, C.W., Childs, C.W. and Parshotam, A., 1994. Carbon turnover in a range of allophanic soils amended with ^{14}C-labelled glucose. Soil Biology and Biochemistry, 26(9): 1263-1271.

Sakaguchi, K., and Zeng, X. 2009. Effects of soil wetness, plant litter, and under-canopy atmospheric stability on ground evaporation in the Community Land Model (CLM3.5). J. Geophys. Res. 114:D01107. DOI:10.1029/2008JD010834.

Schaaf, C.B., Gao, F., Strahler, A.H., Lucht, W., Li, X., Tsang, T., Strugnell, N.C., Zhang, X., Jin, Y., and Muller, J.-P. 2002. First operational BRDF, albedo nadir reflectance products from MODIS. Remote Sens. Environ. 83:135-148.

Schlesinger, W.H., 1997. Biogeochemistry: an analysis of global change. Academic Press, London, 588 pp.

Schnell, S. and King, G.M., 1996. Responses of methanotrophic activity in soils and cultures to water stress. Applied and Environmental Microbiology 62(9):3203-3209.

Segers, R., 1998. Methane production and methane consumption: a review of processes underlying wetland methane fluxes. Biogeochemistry 41(1):23-51.

Sellers, P.J. 1985. Canopy reflectance, photosynthesis and transpiration. Int. J. Remote Sens. 6:1335-1372.

Sellers, P.J., Mintz, Y., Sud, Y.C., and Dalcher, A. 1986. A simple biosphere model (SiB) for use within general circulation models. J. Atmos. Sci. 43:505-531.

Sellers, P.J., Hall, F.G., Asrar, G., Strebel, D.E., and Murphy, R.E. 1988. The First ISLSCP Field Experiment (FIFE). Bull. Amer. Meteor. Soc. 69:22-27.

Sellers, P.J., Berry, J.A., Collatz, G.J., Field, C.B., and Hall, F.G. 1992. Canopy reflectance, photosynthesis, and transpiration. III. A reanalysis using improved leaf models and a new canopy integration scheme. Remote Sens. Environ. 42:187-216.

Sellers, P.J., et al. 1995. The Boreal Ecosystem-Atmosphere Study (BOREAS): An overview and early results from the 1994 field year. Bull. Amer. Meteor. Soc. 76:1549-1577.

Sellers, P.J., Randall, D.A., Collatz, G.J., Berry, J.A., Field, C.B., Dazlich, D.A., Zhang, C., Collelo, G.D., and Bounoua, L. 1996. A revised land surface parameterization (SiB2) for atmospheric GCMs. Part I: Model formulation. J. Climate 9:676-705.

Shi, X., Mao, J., Thornton, P.E., and Huang, M. 2013. Spatiotemporal patterns of evapotranspiration in response to multiple environmental factors simulated by the Community Land Model. Environ. Res. Lett. 8(2):024012.

Shiklomanov, I.A. 2000. Appraisal and assessment of world water resources. Water International 25:11-32.

Siebert, S., Döll, P., Hoogeveen, J., Faures, J.M., Frenken, K., Feick, S., 2005. Development and validation of the global map of irrigation areas. Hydrol Earth Syst Sc 9:535–547

Simpson, R.J., Lambers, H., and Dalling, M.J. 1983. Nitrogen redistribution during grain growth in wheat (Triticum avestivum L.). Plant Physiol. 71:7-14.

Smith, A.M.S., Wooster, M.J., Drake, N.A., Dipotso, F.M. and Perry, G.L.W., 2005. Fire in African savanna: Testing the impact of incomplete combustion on pyrogenic emissions estimates. Ecological Applications, 15(3): 1074-1082.

Sollins, P., 1982. Input and decay of coarse woody debris in coniferous stands in western Oregon and Washington. Canadian Journal of Forest Research, 12: 18-28.

Son, Y. and Gower, S.T., 1991. Aboveground nitrogen and phosphorus use by five plantation-grown trees with different leaf longevities. Biogeochemistry, 14: 167-191.

Sørensen, L.H., 1981. Carbon-nitrogen relationships during the humification of cellulose in soils containing different amounts of clay. Soil Biology and Biochemistry, 13: 313-321.

Sprugel, D.G., Ryan, M.G., Brooks, J.R., Vogt, K.A., and Martin, T.A. 1995. Respiration from the organ level to stand level. pp. 255-299. In: W. K. Smith and T. M. Hinkley (editors) Resource Physiology of Conifers. Academic Press, San Diego,CA.

Stauffer, D., and Aharony, A. 1994. Introduction to Percolation Theory. Taylor and Francis, London.

Still, C.J., Berry, J.A., Collatz, G.J., and DeFries, R.S. 2003. Global distribution of C3 and C4 vegetation: carbon cycle implications. Global Biogeochem. Cycles 17:1006. DOI:10.1029/2001GB001807.

Stöckli, R., Lawrence, D.M., Niu, G.-Y., Oleson, K.W., Thornton, P.E., Yang, Z.-L., Bonan, G.B., Denning, A.S., and Running, S.W. 2008. Use of FLUXNET in the Community Land Model development. J. Geophys. Res. 113:G01025. DOI:10.1029/2007JG000562.

Strack, M., Kellner, E. and Waddington, J.M., 2006. Effect of entrapped gas on peatland surface level fluctuations. Hydrological Processes 20(17):3611-3622.

Strahler, A.H., Muchoney, D., Borak, J., Friedl, M., Gopal, S., Lambin, E., and Moody. A. 1999. MODIS Land Cover Product: Algorithm Theoretical Basis Document (Version 5.0). Boston University, Boston.

Stull, R.B. 1988. An Introduction to Boundary Layer Meteorology. Kluwer Academic Publishers, Dordrecht.

Subin, Z.M., Riley, W.J. and Mironov, D. 2012a. Improved lake model for climate simulations, J. Adv. Model. Earth Syst., 4, M02001. DOI:10.1029/2011MS000072.

Subin, Z.M., Murphy, L.N., Li, F., Bonfils, C. and Riley, W.J., 2012b. Boreal lakes moderate seasonal and diurnal temperature variation and perturb atmospheric circulation: analyses in the Community Earth System Model 1 (CESM1). Tellus A, North America, 64.

Sun, Y., Gu, L., and Dickinson, R. E. 2012. A numerical issue in calculating the coupled carbon and water fluxes in a climate model, J. Geophys. Res., 117, D22103. DOI:10.1029/2012JD018059.

Swenson, S.C., Lawrence, D.M., and Lee, H. 2012. Improved Simulation of the Terrestrial Hydrological Cycle in Permafrost Regions by the Community Land Model. JAMES, 4, M08002. DOI:10.1029/2012MS000165.

Swenson, S.C. and Lawrence, D.M. 2012. A New Fractional Snow Covered Area Parameterization for the Community Land Model and its Effect on the Surface Energy Balance. JGR, 117, D21107. DOI:10.1029/2012JD018178.

Ta, C.T. and Weiland, R.T. 1992. Nitrogen partitioning in maize during ear development. Crop Sci. 32:443-451.

Tang, J.Y. and Riley, W.J. 2013. A new top boundary condition for modeling surface diffusive exchange of a generic volatile tracer: Theoretical analysis and application to soil evaporation. Hydrol. Earth Syst. Sci. 17:873-893.

Tarnocai, C., Kettles, I. M., and Lacelle, B., 2011. Peatlands of Canada, Geological Survey of Canada, Open File 6561, CD-ROM. DOI:10.495/288786.

Taylor, B.R., Parkinson, D. and Parsons, W.F.J., 1989. Nitrogen and lignin content as predictors of litter decay rates: A microcosm test. Ecology, 70(1): 97-104.

Thonicke, K., Venevsky, S., Sitch, S., and Cramer, W. 2001. The role of fire disturbance for global vegetation dynamics: coupling fire into a Dynamic Global Vegetation Model. Global Ecology and Biogeography 10:661-667.

Thornton, P.E., 1998. Regional ecosystem simulation: combining surface- and satellite-based observations to study linkages between terrestrial energy and mass budgets. Ph.D. Thesis, The University of Montana, Missoula, 280 pp.

Thornton, P.E., Law, B.E., Gholz, H.L., Clark, K.L., Falge, E., Ellsworth, D.S., Goldstein, A.H., Monson, R.K., Hollinger, D., Falk, M., Chen, J., and Sparks, J.P. 2002. Modeling and measuring the effects of disturbance history and climate on carbon and water budgets in evergreen needleleaf forests. Agric. For. Meteor. 113:185-222.

Thornton, P.E., and Rosenbloom, N.A. 2005. Ecosystem model spin-up: estimating steady state conditions in a coupled terrestrial carbon and nitrogen cycle model. Ecological Modelling 189:25-48.

Thornton, P.E., and Zimmermann, N.E. 2007. An improved canopy integration scheme for a land surface model with prognostic canopy structure. J. Climate 20:3902-3923.

Thornton, P.E., Lamarque, J.-F., Rosenbloom, N.A., and Mahowald, N.M. 2007. Influence of carbon-nitrogen cycle coupling on land model response to CO_2 fertilization and climate variability. Global Biogeochem. Cycles 21:GB4018.

Thornton, P.E., Doney, S.C., Lindsay, K., Moore, J.K., Mahowald, N., Randerson, J.T., Fung, I., Lamarque, J.F., Feddema, J.J., and Lee, Y.H. 2009. Carbon-nitrogen interactions regulate climate-carbon cycle feedbacks: results from an atmosphere-ocean general circulation model. Biogeosci. 6:2099-2120.

Tian, H. et al. 2010. Spatial and temporal patterns of CH4 and N2O fluxes in terrestrial ecosystems of North America during 1979-2008: application of a global biogeochemistry model. Biogeosciences 7:2673-2694.

Toon, O.B., McKay, C.P., Ackerman, T.P., and Santhanam, K. 1989. Rapid calculation of radiative heating rates and photodissociation rates in inhomogeneous multiple scattering atmospheres. J. Geophys. Res. 94(D13):16,287-16,301.

Turetsky, M.R., Wieder, R.K., Halsey, L.A., and Vitt, D.H. 2002. Current disturbance and the diminishing peatland carbon sink. Geophys. Res. Lett. 29:1526. DOI:10.1029/2001GL014000.

Turetsky, M.R., Amiro, B.D., Bosch, E., andBhatti, J.S. 2004. Historical burn area in western Canadian peatlands and its relationship to fire weather indices. Global Biogeochem. Cycles 18:GB4014. DOI:10.1029/2004GB002222.

Turnbull, J.C. et al. 2007. A new high precision (CO2)-C-14 time series for North American continental air. Journal of Geophysical Research-Atmospheres 112(D11).

Tye, A.M., et al. 2005. The fate of N-15 added to high Arctic tundra to mimic increased inputs of atmospheric nitrogen released from a melting snowpack. Global Change Biology 11(10):1640-1654.

Unland, H.E., Houser, P.R., Shuttleworth, W.J., and Yang, Z.-L. 1996. Surface flux measurement and modeling at a semi-arid Sonoran Desert site. Agric. For. Meteor. 82:119-153.

UNSTAT, 2005. National Accounts Main Aggregates Database, United Nations Statistics Division.

Vallano, D.M. and Sparks, J.P. 2007. Quantifying foliar uptake of gaseous itrogen dioxide using enriched foliar δ^{15}N values. New Phytologist 177:946-955.

van der Werf, G.R., Randerson, J.T., Giglio, L., Collatz, G.J., Mu, M., Kasibhatla, S.P., Morton, D.C., DeFries, R.S., Jin, Y., van Leeuwen, T.T. 2010. Global fire emissions and the contribution of deforestation, savanna, forest, agricultural, and peat fires (1997-2009) Atmos. Chem. Phys. 10:11707-11735.

van Veen, J.A., Ladd, J.N. and Frissel, M.J., 1984. Modelling C and N turnover through the microbial biomass in soil. Plant and Soil, 76: 257-274.

Van Vuuren, D.P., Lucas, P.S., and Hilderink, H.B.M., 2006. Downscaling drivers of global environmental change: enabling use of global SRES scenarios at the national and grid levels, Report 550025001, Netherlands Environmental Assessment Agency, 45 pp.

Vanninen, P., and Makela, A. 2005. Carbon budget for Scots pine trees: effects of size, competition and site fertility on growth allocation and production. Tree Phys. 25:17-30.

Verdin, K. L., and S. K. Greenlee, 1996. Development of continental scale digital elevation models and extraction of hydrographic features, paper presented at the Third International Conference/Workshop on Integrating GIS and Environmental Modeling, Santa Fe, New Mexico, 21–26 January, Natl. Cent. for Geogr. Inf. and Anal., Santa Barbara, Calif.

Viovy, N. 2011. CRUNCEP dataset. [Description available at http://dods.extra.cea.fr/data/p529viov/cruncep/readme.htm. Data available at http://dods.extra.cea.fr/store/p529viov/cruncep/V4_1901_2011/].

Vitousek, P.M., and Howarth, R.W. 1991. Nitrogen limitation on land and in the sea: How can it occur? Biogeochem. 13:87-115.

Walter, B.P., Heimann, M. and Matthews, E., 2001. Modeling modern methane emissions from natural wetlands 1. Model description and results. J. Geophys. Res. 106(D24):34189-34206.

Wania, R., Ross, I. and Prentice, I.C. 2009. Integrating peatlands and permafrost into a dynamic global vegetation model: 2. Evaluation and sensitivity of vegetation and carbon cycle processes. Global Biogeochem. Cycles 23(3).

Wania, R., Ross, I. and Prentice, I.C. 2010. Implementation and evaluation of a new methane model within a dynamic global vegetation model LPJ-WHyMe v1.3. Geoscientific Model Development Discussions 3:1-59.

Wang, A., and Zeng, X. 2009. Improving the treatment of vertical snow burial fraction over short vegetation in the NCAR CLM3. Adv. Atmos. Sci. 26:877-886. DOI:10.1007/s00376-009-8098-3.

White, M.A., Thornton, P.E., and Running, S.W. 1997. A continental phenology model for monitoring vegetation responses to interannual climatic variability. Global Biogeochem. Cycles 11:217-234.

White, M.A., Thornton, P.E., Running, S.W., and Nemani, R.R. 2000. Parameterization and sensitivity analysis of the Biome-BGC terrestrial ecosystem model: net primary production controls. Earth Interactions 4:1-85.

Wiscombe, W.J., and Warren, S.G. 1980. A model for the spectral albedo of snow. I. Pure snow. J. Atmos. Sci. 37:2712-2733.

Wood, E.F., Lettenmaier, D.P., and Zartarian, V.G. 1992. A land-surface hydrology parameterization with subgrid variability for general circulation models. J. Geophys. Res. 97(D3):2717–2728. DOI:10.1029/91JD01786.

World Bank, 2004. World development indicators 2004, Oxford University Press, New York, 416 pp.

Yang, Z.-L. 1998. Technical note of a 10-layer soil moisture and temperature model. Unpublished manuscript.

Zender, C.S., Bian, H., and Newman, D. 2003. Mineral dust entrainment and deposition (DEAD) model: Description and 1990s dust climatology. J. Geophys. Res. 108(D14):4416. DOI:10.1029/2002JD002775.

Zeng, X., and Dickinson, R.E. 1998. Effect of surface sublayer on surface skin temperature and fluxes. J.Climate 11:537-550.

Zeng, X., Zhao, M., and Dickinson, R.E. 1998. Intercomparison of bulk aerodynamic algorithms for the computation of sea surface fluxes using the TOGA COARE and TAO data. J. Climate 11:2628-2644.

Zeng, X. 2001. Global vegetation root distribution for land modeling. J. Hydrometeor. 2:525-530.

Zeng, X., Shaikh, M., Dai, Y., Dickinson, R.E., and Myneni, R. 2002. Coupling of the Common Land Model to the NCAR Community Climate Model. J. Climate 15:1832-1854.

Zeng, X., Dickinson, R.E., Barlage, M., Dai, Y., Wang, G., and Oleson, K. 2005. Treatment of under-canopy turbulence in land models. J. Climate 18:5086-5094.

Zeng, X., and Wang, A. 2007. Consistent parameterization of roughness length and displacement height for sparse and dense canopies in land models. J. Hydrometeor. 8:730-737.

Zeng, X., and Decker, M. 2009. Improving the numerical solution of soil moisture-based Richards equation for land models with a deep or shallow water table. J. Hydrometeor. 10:308-319.

Zeng, X., Zeng, X., and Barlage, M. 2008. Growing temperate shrubs over arid and semiarid regions in the Community Land Model - Dynamic Global Vegetation Model. Global Biogeochem. Cycles 22:GB3003. DOI:10.1029/2007GB003014.

Zhang, Y., Li, C.S., Trettin, C.C., Li, H. and Sun, G., 2002. An integrated model of soil, hydrology, and vegetation for carbon dynamics in wetland ecosystems. Global Biogeochemical Cycles 16(4). DOI:10.1029/2001GB001838.

Zhuang, Q., et al. 2004. Methane fluxes between terrestrial ecosystems and the atmosphere at northern high latitudes during the past century: A retrospective analysis with a process-based biogeochemistry model. Global Biogeochemical Cycles 18(3). DOI:10.1029/2004GB002239.

Zilitinkevich, S.S. 1970. Dynamics of the Atmospheric Boundary Layer. Leningrad Gidrometeor.